Optimized Resource Allocation for Future Wireless Communication Systems

Optimierte Ressourcenzuweisung für zukünftige drahtlose Kommunikationssysteme

Der Technischen Fakultät
der Friedrich-Alexander-Universität Erlangen-Nürnberg
zur Erlangung des doktorgrades

Doktor-Ingenieur

vorgelegt von

Dongfang Xu

aus Shandong, China

Als Dissertation genehmigt von
der Technischen Fakultät
der Friedrich-Alexander-Universität Erlangen-Nürnberg

Tag der mündlichen Prüfung:	20.12.2022
Gutachter:	Prof. Dr.-Ing. Robert Schober
	Prof. Dr. Yuanwei Liu

To my parents

Acknowledgment

First and foremost, I would like to express my sincere gratitude to my supervisor Professor Robert Schober, for his attentive enlightening, and immense support during my master and Ph.D. study. His interesting and comprehensive lecture "Digital Communications" attracted me to the path of research. His broad vision and lenient mind also taught me to look at problems peacefully and tolerate a diverse world. As a top-notch scholar and distinguished lecturer, Robert's words and deeds encourage me to investigate scientific problems in a stringent and logical manner, face life optimistically and positively, and devote myself to a beloved career tirelessly and conscientiously. I am truly appreciative of his visionary suggestion for my career and I believe, I will benefit from this precious studying experience with him forever.

Moreover, I would like to earnestly thank Professor Derrick Wing Kwan Ng, for providing professional and thoughtful suggestions for my research. As an expert in both wireless communications and mathematical optimization, he can always help me broaden my view and deepen my understanding of research. Although there is jet lag between Australia and Germany, he is always so generous to assign his precious early mornings to clear up my doubts and boost my enthusiasm for research and life.

Furthermore, I feel very lucky to get acquainted with Professor Xianghao Yu, one outstanding young scholar, and my bosom friend, at the initial stage of my research career. During our collaboration in Germany, he selflessly shared his academic experiences with me and provided much valuable feedback on my research.

I also really appreciate the China Scholarship Council which financially supported me during my Ph.D. study and makes my dream come true. Many thanks go to my lovely colleagues at the Institute of Digital Communications, for the enjoyable time and every cherishing memory we shared together.

Last but not least, I am very grateful to my parents who care about me all the time and support me unconditionally throughout my 8-year study in Germany.

Zusammenfassung

Future wireless networks are envisioned to provide ubiquitous reliable high data-rate communication services. Unmanned aerial vehicles (UAVs) and intelligent reflecting surfaces (IRSs) are two promising means for meeting these requirements. To achieve the performance gains promised by these new technologies, they have to be delicately designed along with the other components of the wireless network. This thesis studies advanced resource allocation design for UAV- and IRS-based communications with the design objective of facilitating reliable power- and spectral-efficient communications in future wireless networks. In particular, we make five specific contributions.

First, we consider a practical UAV communication application scenario where a rotary-wing UAV acts as a flying base station (BS) to provide reliable communication services to multiple ground users in an uncertain environment with no-fly zones. To this end, we propose two novel and robust online resource allocation algorithms which produce a power-efficient UAV trajectory, velocity, and beamforming policy. In particular, we exploit monotonic optimization theory to develop the optimal resource allocation algorithm which provides a performance upper bound for the considered system. Furthermore, we propose a successive convex approximation (SCA)-based suboptimal algorithm whose complexity is affordable for the real-time design of practical UAV systems.

Second, we propose to exploit the programmability of IRSs to overcome undesired wireless channel conditions and to mitigate the various interferences occurring in full-duplex (FD) cognitive radio (CR) networks. We focus on an underlay CR network and aim to maximize the throughput of the FD secondary system without causing severe interference leakage to the incumbent users of the primary system. To this end, we develop an FD design framework for IRS-aided CR systems where the downlink and uplink beamforming at the secondary FD BS, the reflection matrix at the IRS as well as the transmit power for the uplink users are jointly optimized. Exploiting block coordinate descent theory, we construct three optimization blocks and solve the resulting three subproblems in an alternating manner. The developed algorithm produces a high-quality solution to the considered optimization problem with guaranteed convergence.

Third, we focus on large IRS-assisted simultaneous wireless information and power transfer (SWIPT) systems. Since the conventional element-wise IRS optimization frameworks result in a heavy computational burden for practical IRS sizes, we employ a scalable cascaded optimization framework comprising an offline and an online stage to facilitate low-complexity IRS design. For a given transmission mode set constructed in the offline stage, we first develop two criteria to remove less favorable transmission modes from the set, accounting for user fairness and the specific features of SWIPT systems, respectively. Then, we optimize the beamforming vectors and select the best transmission mode among all remaining candidates to minimize the system transmit power while satisfying the quality-of-service (QoS) requirements of the users. We reveal a performance upper bound for the considered system by developing a branch-and-bound-based optimal enumerating algorithm. Subsequently, to facilitate real-time design for practical IRS systems, we leverage the penalty method to develop an efficient algorithm which yields a local optimum of the considered problem in polynomial time.

Fourth, we propose to joint apply an IRS and artificial noise (AN) to enhance the physical layer security of a multiuser communication system and study the resulting resource allocation design. We ensure secure communication for the considered system by jointly optimizing the reflection pattern of the IRS and the beamforming vectors and AN covariance matrix at the BS. We divide the original optimization problem into two subproblems and develop a computationally-efficient suboptimal algorithm which sequentially solves the two subproblems by employing SCA and manifold optimization methods, respectively.

Fifth, to combat the conventional passive IRS-induced double path loss effect, active IRSs, a novel IRS structure that can simultaneously vary the phase and the magnitude of the reflected signal with the support of an additional power source, are considered. To facilitate green communication, we investigate the joint design of the IRS reflection matrix and the BS beamforming vectors for minimization of the BS transmit power taking into account the maximum power budget of the active IRS and the QoS requirements of the users. We propose a bilinear transformation-based computationally-efficient algorithm which produces a locally optimal solution of the formulated problem.

Zusammenfassung (in German)

Zukünftige drahtlose Kommunikationsnetzwerke sollen überall zuverlässige Kommunikationsdienste mit hoher Datenrate zur Verfügung stellen. „Unmanned Aerial Vehicles“(UAVs) und „Intelligent Reflecting Surfaces“(IRSs) sind zwei vielversprechende Ansätze, um dieses Ziel zu erreichen. Damit die Leistungssteigerungen, die diese neuen Techniken versprechen, erzielt werden können, ist die sorgfältige Optimierung der Techniken gemeinsam mit den anderen Komponenten von drahtlosen Kommunikationsnetzwerken erforderlich. Diese Dissertation untersucht neue Methoden für die Ressourcenzuweisung in UAV- und IRS-basierten Kommunikationsnetzen mit dem Ziel, zuverlässige power- und spektral-effiziente Kommunikation zu ermöglichen. Es werden fünf Aspekte besonders herausgestellt.

Zuerst betrachten wir ein praktisches Anwendungsszenario, bei dem ein Drehflügel-UAV als fliegende Basisstation (BS) fungiert. Das UAV soll zuverlässige Kommunikationsdienste für mehrere Nutzer am Boden bereitstellen und dabei Flugverbotszonen beachten. Zu diesem Zweck schlagen wir zwei neuartige und robuste Online-Algorithmen zur Ressourcenzuweisung vor, die energieeffiziente Richtlinien für die Flugbahn, die Geschwindigkeit und das Beamforming des UAV generieren. Dabei nutzen wir die Optimierungstheorie für monotone Funktionen, um einen Algorithmus für die optimale Ressourcenzuweisung zu entwickeln. Durch dessen Anwendung bestimmen wir eine obere Schranke der Leistungsfähigkeit des Kommunikationsnetzes. Anschließend schlagen wir einen suboptimalen Algorithmus vor, der auf „successive convex approximation“(SCA) basiert und aufgrund geringer Komplexität für UAV-Echtzeit-Anwendungen geeignet ist.

Weiterhin nutzen wir die Programmierbarkeit von IRSs, um die Auswirkungen von Fading und Interferenzen in „full duplex“(FD) „cognitive radio“(CR) Systemen abzuschwächen. Wir betrachten ein CR-Kommunikationsnetz und zielen drauf ab, den Datendurchsatz des sekundären FD-Systems zu maximieren, ohne die Leistung des primären Systems wesentlich zu beeinträchtigung. Dazu entwickeln wir ein FD-Design-Framework für IRS-gestützte CR-Systeme, bei dem das Uplink-und Downlink-Beamforming der sekundären FD-BS, die Reflexionsmatrix des IRS und die Sendeleistung der Uplink-Nutzer gemeinsam optimiert werden. Das Framework nutzt die „block coordinate descent theory“, um drei Optimierungsblöcke für drei Unterproble-

me zu definieren, die abwechselnd gelöst werden. Dieser Algorithmus konvergiert zu einer qualitativ hochwertigen Lösung des ursprünglichen Problems.

Anschließend betrachten wir IRS-gestützte „simultaneous wireless information and power transfer“(SWIPT) Systeme. Wegen der hohen Rechenkomplexität, die bei elementweiser Optimierung von typischerweise großen IRSs entsteht, verwenden wir ein skalierbares Optimierungsframework, das aus einer Offline-Phase und einer Online-Phase besteht. Dadurch wird ein IRS-Design mit geringer Komplexität ermöglicht. In der Offline-Phase wird eine Menge von Übertragungsmodi definiert, die zunächst so gefiltert wird, dass nur Modi erhalten bleiben, die Nutzer-Fairness und spezifische SWIPT Eigenschaften garantieren. Anschließend werden die Beamforming-Vektoren optimiert und derjenige Übertragungsmodus ausgewählt, der die Sendeleistung minimiert und gleichzeitig die Qualitätsanforderungen der Nutzer gewährleistet. Wir entwickeln einen Branch-and-Bound-Algorithmus, mit dem eine obere Schranke der Leistungsfähigkeit des Systems ermittelt wird. Schließlich nutzen wir die Penalty-Methode, um einen effizienten Algorithmus zuentwerfen, der ein lokales Optimum für das Optimierungsproblem in polynomialer-Zeit berechnet.

Außerdem fokussieren wir uns auf das Ressourcenzuweisung problem in Mehrnutzer-Kommunikationsnetzen und schlagen die gemeinsame Verwendung von IRS und „artificial noise“(AN) vor, um die Sicherheit auf der physikalischen Schicht zu verbessern. Mittels gemeinsamer Optimierung des Reflexionsmusters der IRS, der Beamforming-Vektoren und der AN-Kovarianzmatrix an der BS wird sichere Kommunikation erreicht. Das ursprüngliche Optimierungsproblem wird in zwei Teilprobleme unterteilt und mit einem rechen-effizienten Algorithmus gelöst, wobei SCA und Methoden der „manifold optimization“zum Einsatz kommen.

Zuletzt widmen wir uns aktiven IRSs, einer neuartigen IRS-Struktur, die mit einer zusätzlichen Energiequelle sowohl die Phase als auch den Betrag des reflektierten Signals ändert, um damit dem Effekt des doppelten Pfadverlusts bei konventionellen IRSs entgegenzutreten. Gleichzeitig sollen grüne Kommunikationsnetze ermöglicht werden, weshalb wir die Qualitätsanforderungen der Nutzer und das Leistungsbudget des aktiven IRS in Betracht ziehen, um die IRS-Reflexionsmatrix und die BS-Beamforming-Vektoren für minimale Sendeleistung zu optimieren. Dafür schlagen wir einen rechen-effizienten Algorithmus vor, der auf bilinearer Transformation basiert und eine lokal-optimale Lösung des Problems findet.

Preface

I hereby declare that I am the author of this thesis. Appendices B-F are based on works performed under the supervision of Professor Robert Schober and in collaboration with Professor Derrick Wing Kwan Ng from the University of New South Wales, Australia, Professor Xianghao Yu from the Hong Kong University of Science and Technology, Hong Kong, China, Professor Vahid Jamali from the Technical University of Darmstadt, Germany, and Doctor Yan Sun from Huawei Technologies, China.

For all publications, I had the original idea, reviewed the related literature, formulated the system models, solved the optimization problems, implemented the simulation code, and **wrote the manuscripts**. My supervisor guided the direction of the research, validated the optimization solutions, and provided feedback on the manuscripts. My co-authors contributed by providing feedback on the manuscripts and through the insightful discussions we had on the technical aspects of the papers. In particular, Prof. Ng is an expert in the area of wireless communications and optimization techniques. He helped me in gaining a better understanding of the system models of wireless networks and provided me with feedback and comments on our joint papers. Prof. Yu was a postdoctoral fellow on the Institute of Digital Communications (IDC) and now is a research assistant professor at the Hong Kong University of Science and Technology. He is an expert on IRS and optimization techniques and he helped me validate the proposed IRS optimization frameworks and provided feedback and suggestions on our joint papers. Prof. Jamali was a postdoctoral fellow at IDC and is now a professor at the Technical University of Darmstadt. He is an expert in IRS and system modeling and he helped me validate the proposed IRS schemes and provided feedback and suggestions on our joint papers. Dr. Sun was a Ph.D. student at IDC until the year 2020 and we had discussions on how to model UAV and IRS communication systems.

Appendices B-F are based on the following published research papers.

Appendix B:

- D. Xu, Y. Sun, D. W. K. Ng, and R. Schober, "Multiuser MISO UAV communications in uncertain environments with no-fly zones: robust trajectory and resource allocation design," *IEEE Trans. Commun.*, vol. 68, no. 5, pp. 3153-3172, May 2020.

Appendix C:

- D. Xu, X. Yu, Y. Sun, D. W. K. Ng, and R. Schober, "Resource allocation for IRS-assisted full-duplex cognitive radio systems," *IEEE Trans. Commun.*, vol. 68, no. 12, pp. 7376-7394, Dec. 2020.

Appendix D:

- D. Xu, V. Jamali, X. Yu, D. W. K. Ng, and R. Schober, "Optimal resource allocation design for large IRS-assisted SWIPT systems: A scalable optimization framework," *IEEE Trans. Commun.*, vol. 70, no. 2, pp. 1423-1441, Feb. 2022.

Appendix E:

- D. Xu, X. Yu, Y. Sun, D. W. K. Ng, and R. Schober, "Resource allocation for secure IRS-assisted multiuser MISO systems," in *Proc. IEEE Global Commun. Conf. Wkshps.*, Waikoloa, HI, USA, Dec. 2019, pp. 1-6.

Appendix F:

- D. Xu, X. Yu, D. W. K. Ng, and R. Schober, "Resource allocation for active IRS-assisted multiuser communication systems," in *Proc. Asilomar Conf. on Signals, Systems, and Computers*, Pacific Grove, CA, USA, Oct. 2021, pp. 113-119.

A complete list of the publications of the author, including those which have not been used in this dissertation are listed in Appendix A.

Inhaltsverzeichnis

Abbildungsverzeichnis

Kapitel 1

Introduction

Over the past decades, the wireless communication industry has witnessed significant advances. By exploiting key technologies such as orthogonal frequency-division multiplexing (OFDM), multiple-input multiple-output (MIMO), and turbo codes, the fourth generation (4G) wireless communication networks achieved a data rate of 1 Gbit/s for mobile users, which has promoted many innovative mobile applications [1]. Yet, due to the tremendously increased numbers of devices and the corresponding immense traffic demand, a more powerful and more comprehensive successor for the 4G network was needed. This has hastened the wireless communication industry to standardize and deploy worldwide the fifth generation (5G) wireless communication networks starting from 2020. According to the Cisco annual internet report [2], the number of global mobile devices will grow up to 13.1 billion by 2023. As a result, future wireless networks are expected to serve a gigantic number of conventional communication users. In addition to a large number of users, future wireless networks are also supposed to provide enhanced mobile broadband (eMBB) and ultra-reliable low latency communications (URLLC) [3]. On the other hand, future wireless networks are also envisaged to support various Internet-of-Things (IoT) applications with high reliability such as smart homes, vehicle autopiloting, and environmental monitoring [4]. For example, by setting up a wireless sensor network in a farm or a forest, the required information for implementing an irrigation system or monitoring fire disasters can be collected. However, the traditional techniques adopted in the current wireless networks, including 5G, cannot meet these enhanced requirements. Furthermore, in addition to serving various types of mobile devices, future wireless networks are envisioned to provide real-time on-demand communication services, e.g., emergency and disaster responses [5]. For instance, it is desired to establish temporal communication links to serve disaster-stricken civilians after the terrestrial infrastructure of cellular systems has been destroyed by an earthquakes. However, traditional wireless communication systems are not capable of supporting such applications.

These new requirements have spurred both academia and industry to seek new promising techniques to enhance the performance of future wireless networks in a power- and spectral-efficient manner. One promising solution in that regard is to migrate to higher frequency bands which have not been exploited for communication previously, e.g., millimeter-wave (mmWave) [6, 7] and terahertz (THz) frequencies [8], to increase the available spectrum for wireless communications. On the other hand, researchers and system designers also explore new means to utilize the spectrum intelligently. In particular, noticing that most of the allocated spectrum is used in an inefficient manner, cognitive radio (CR) techniques have been proposed to reuse the licensed frequency bands in unlicensed secondary systems as long as the performance of the primary systems is not impaired [9]. Moreover, by deploying dual-functional radar and communication (DFRC) base stations (BSs), integrated sensing and communication (ISAC) facilitates the spectral coexistence of radar and wireless communication systems, which dramatically improves spectral efficiency [10–12]. Also, by integrating a large number of antenna elements at the transceivers, massive MIMO techniques allow us to substantially boost both spectral and power efficiency in wireless communication systems. Benefiting from advanced self-interference (SI) cancellation techniques, full-duplex (FD) wireless communication has become a practical option which potentially doubles the spectral efficiency of conventional half-duplex wireless networks [13]. Besides, supported by advanced successive interference cancellation (SIC) techniques, rate-splitting multiple access (RSMA) and non-orthogonal multiple access (NOMA) [14] have been developed to accommodate multiple users in a given time-frequency resource in a more spectral-efficient manner compared to conventional orthogonal multiple access techniques [15].

Although the above-mentioned technologies have significant advantages, their limitations should not be overlooked. Specifically, the effectiveness of the aforementioned technologies crucially depends on the radio propagation environments. Yet, as the wireless channel is fundamentally random and largely uncontrollable, the expected performance gains induced by the aforementioned technologies may not be achievable in practical wireless communication systems. For example, if the BS and the user to be served are far from each other or the line-of-sight (LoS) link is unavailable due to blockage, the received signal power can be too low, leading to poor performance. Alternatively, in a radio propagation environment with few scatterers, the channel between the BS and the user, in general, has a low rank, which degrades the diversity and multiplexing gains and thus, restricts the number of supported users. To overcome these limitations, very recently, two revolutionary techniques, namely, unmanned aerial vehicles (UAVs) and intelligent reflecting surfaces (IRSs) have been introduced in wireless communication research. In particular, as high-mobility flying

drones, UAVs can be integrated into existing cellular networks to establish temporal LoS-dominant links to provide on-demand high data rate communication services for ground users. A detailed discussion of UAV communication is provided in Section 1.1. On the other hand, consisting of a set of passive elements that can be adjusted individually to change the phase of an incident electromagnetic (EM) wave, IRSs can be smartly programmed to customize favorable radio propagation environments. A detailed discussion of IRS-assisted communication is provided in Section 1.2.

The rest of this introductory section is organized as follows. Section 1.1 introduces some basic concepts and applications of UAV communication systems. In Section 1.2, some fundamentals and use cases and applications of IRS-assisted communication systems are presented. Finally, in Section 1.3, we provide an overview of the contributions of this thesis.

1.1 UAV Communication Systems

In this section, we introduce the main characteristics of UAVs and discuss the opportunities and challenges of UAV communications. Then, we review some application scenarios of UAV communication systems.

1.1.1 Characteristics of UAVs

UAVs, also known as drones, are small aircrafts operated by ground-based controllers or equipped with various degrees of smart algorithm-granted autonomy. In terms of wing configuration, there are two main categories of UAVs, namely, fixed-wing and rotary-wing UAVs. Typical fixed-wing UAVs have greater payloads, higher maximum velocity, and longer endurance, while runways or launchers are required for takeoff and landing [16]. In contrast, rotary-wing UAVs usually have smaller payloads and lower flying speed and are similar to helicopters who are able to take off and land vertically and hover at desired locations. Thanks to the development of UAV miniaturization and modular technologies and the constantly reducing cost, interest in utilizing UAVs in commercial and civilian applications has skyrocketed in recent years [17]. Thus, it is not surprising that UAVs have also been proposed as a promising means to enhance system performance and extend service coverage of wireless networks, cf. Fig. 1.1. Compared to traditional terrestrial cellular systems, UAV-assisted communication systems provide completely new design opportunities but also face new challenges.

- **High Mobility:** In conventional wireless systems, the communication infrastructure such as BSs, relays, and access points, are usually deployed at fixed locations. In contrast, due to their flying capability, UAVs can be exploited to

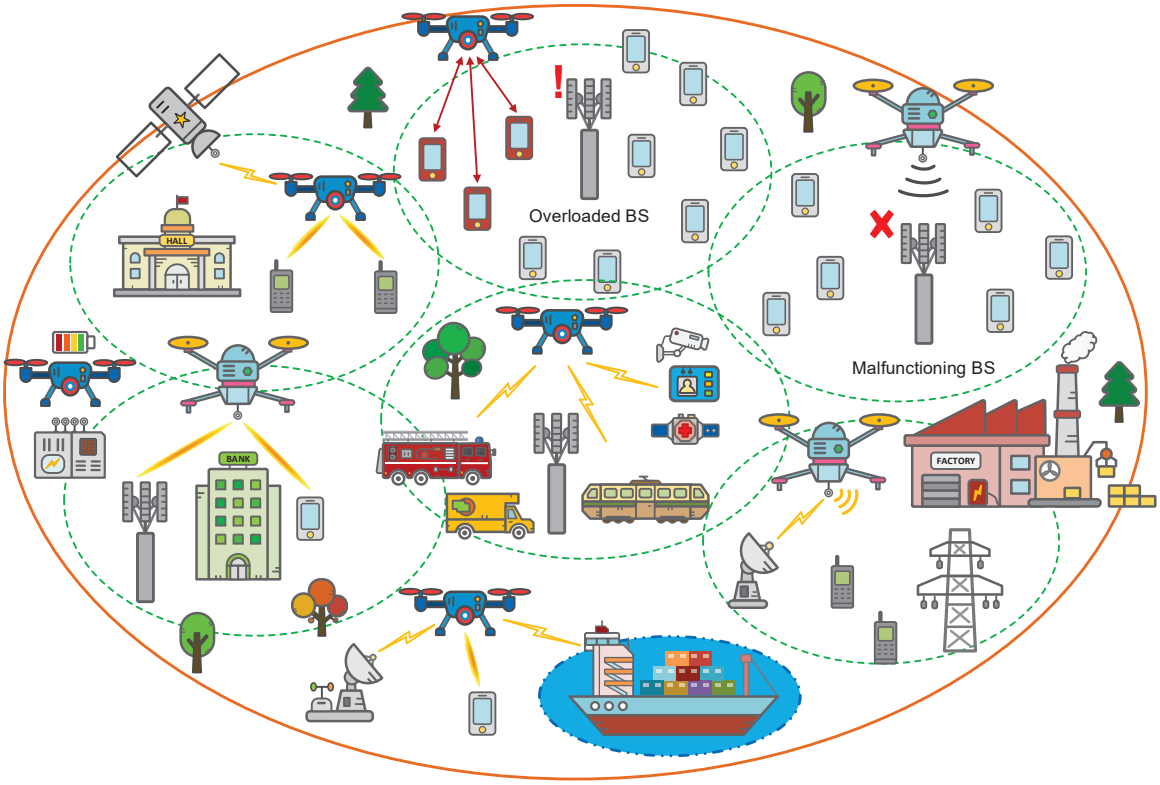

Abbildung 1.1: Illustration of UAVs supported wireless network. UAVs can be integrated into satellite, marine, and cellular communication systems to enhance system performance. Thanks to their characteristics, UAVs are also promising enablers for smart factories, auto-pilot driving, and real-time information collecting.

quickly establish temporal communication links [18,19]. In particular, given the real-time locations of the ground users, the three-dimensional (3D) trajectory of the UAV can be optimized to reduce the distance-dependent path loss, which facilitates power-efficient communications. For instance, an individual UAV can be assigned to one moving user to provide customized real-time tracking and communication service. For rotary-wing UAVs, they can hover at pre-designed positions and act as static aerial BSs to continuously serve ground users within an area. Yet, the high mobility of the UAVs also imposes several new challenges for UAV communications design [20]. In fact, the maximum speed of rotary-wing UAVs is usually more than 20 m/s while fixed-wing UAVs can fly at up to 70 m/s. As a result, the velocity of the UAV has to be carefully controlled to avoid safety issues, e.g., UAV collisions and crashes. Moreover, due to security and confidentiality concerns, system designers may also have to take into account geometrical constraints such as no-fly zones (NFZs) when planning the UAV trajectory.

- **High Altitude:** Different from traditional terrestrial BSs and users, UAVs can adjust their altitude based on the application scenario. As a result, UAV communications extend the conventional two-dimensional (2D) network topology structure to a 3D structure, which facilitates 3D coverage for wireless networks [21]. For example, by deploying UAVs at appropriate height, temporal links can be established to provide emergency communication services for users on the top floors of high-rise buildings or in mountains [22]. Moreover, since there are usually few blocking objects around the UAVs, the probability of having LoS links between the UAV and ground users is much higher compared to conventional terrestrial cellular systems. In fact, the LoS-dominant air-ground links are a mixed blessing for wireless networks. On the one hand, compared to conventional terrestrial links, LoS-dominant air-ground links suffer from less channel variation in both the time domain and the frequency domain, which facilitates high-quality and reliable communications between the UAV and ground users. On the other hand, this also requires more efficient interference management to avoid severe air-ground interference to co-existing terrestrial wireless networks. Moreover, as flying equipments, UAVs are easier to identify and detect compared to conventional terrestrial communication infrastructures. As a result, UAV-mounted transceivers are more vulnerable to jamming attacks and eavesdropping, which makes security a main concern for the design of UAV communication systems [23].

- **Simple Modular Structure:** As flying vehicle platforms, UAVs can conveniently carry various functional modules to accomplish different kinds of tasks. For instance, by installing cameras and image processing modules, UAVs can be deployed as image collection nodes [16]. Moreover, powered by an onboard battery module, UAVs can be flexibly deployed in target areas regardless of whether the power grid is available or not. Yet, this also prevents UAVs from providing sustainable communication services in practice. First, due to the limited capacity of the onboard battery, UAVs have to regularly return to ground bases to replace or recharge their batteries. Second, a large amount of power is actually consumed by the aerodynamic module needed to keep the UAV aloft and adjust the real-time position of the UAV. In fact, this aerodynamic power consumption is a function of the UAV velocity and is usually on the order of hundreds or thousands of watts, cf. Fig. 1.2. This is significantly larger than the communication power consumption [24]. As a result, it is necessary to carefully design the UAV velocity and trajectory to facilitate power-efficient UAV communications.

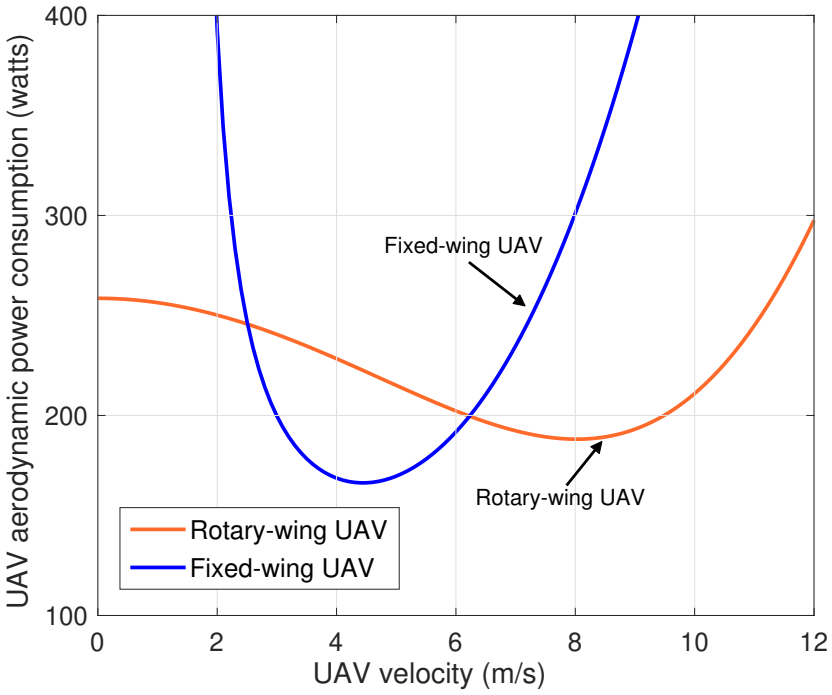

Abbildung 1.2: The aerodynamic power consumption watts) versus flight velocity for two types of UAVs. The aerodynamic power consumption models of the fixed-wing and the rotary-wing and the corresponding simulation parameters were choose based on [24] and [25], respectively.

1.1.2 Application Scenarios of UAV Communications

UAVs can be integrated into conventional terrestrial wireless networks to provide on-demand communication services from the sky. In general, UAVs can be utilized as static aerial communication platforms or as flying communication platforms [26]. Some potential application scenarios of UAV communication systems are illustrated in Fig. 1.3. In particular, acting as relays, UAVs can establish LoS-dominant air-ground channels and assist data transmission between terrestrial BSs and users. Moreover, equipped with data collection modules, UAVs can fly along the optimized trajectory and gather desired information from sensor networks in an efficient manner. Furthermore, in case a terrestrial BS is temporally malfunctioning or the cellular system is crowded with users, UAVs can be deployed at a desired position and act as aerial BSs to provide communication service in the target area. Besides, several UAVs may cooperate with each other to further enhance system performance and extend coverage.

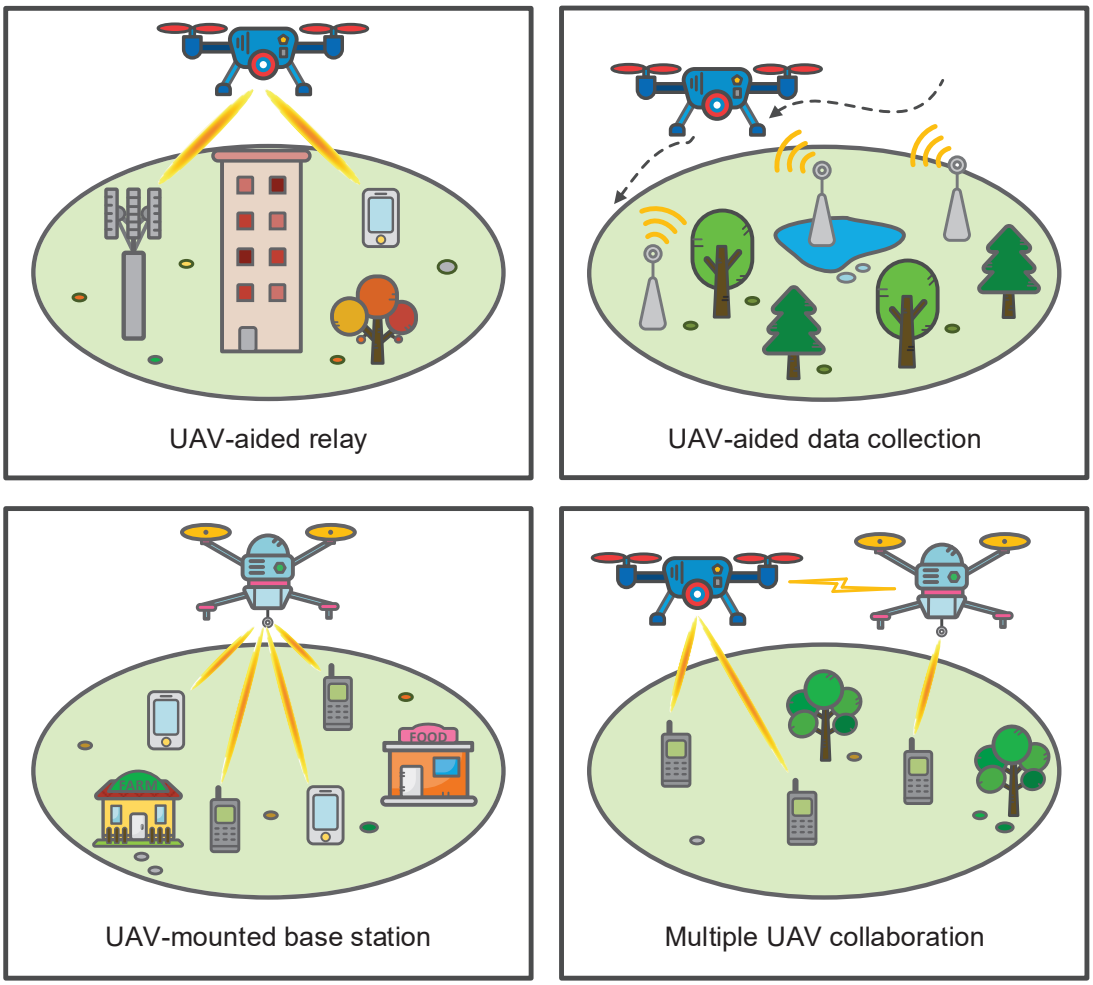

Abbildung 1.3: Illustration of some application scenarios of UAV communications.

1.2 IRS-Assisted Communication Systems

In this section, we introduce the fundamentals of IRSs and discuss the opportunities and difficulties when integrating IRSs into conventional communication systems. Then, we also briefly review some of the application scenarios of IRS-assisted communication systems.

1.2.1 IRS Characteristics

Thanks to significant advancements in radio frequency (RF) micro-electro-mechanical systems, programmable metasurfaces, i.e., IRSs, have recently attracted considerable research attention in wireless communications [27]. Specifically, a typical IRS is a rectangular metasurface comprising a group of sub-wavelength elements where each element is capable of varying the phase of impinging EM waves [28]. As a result,

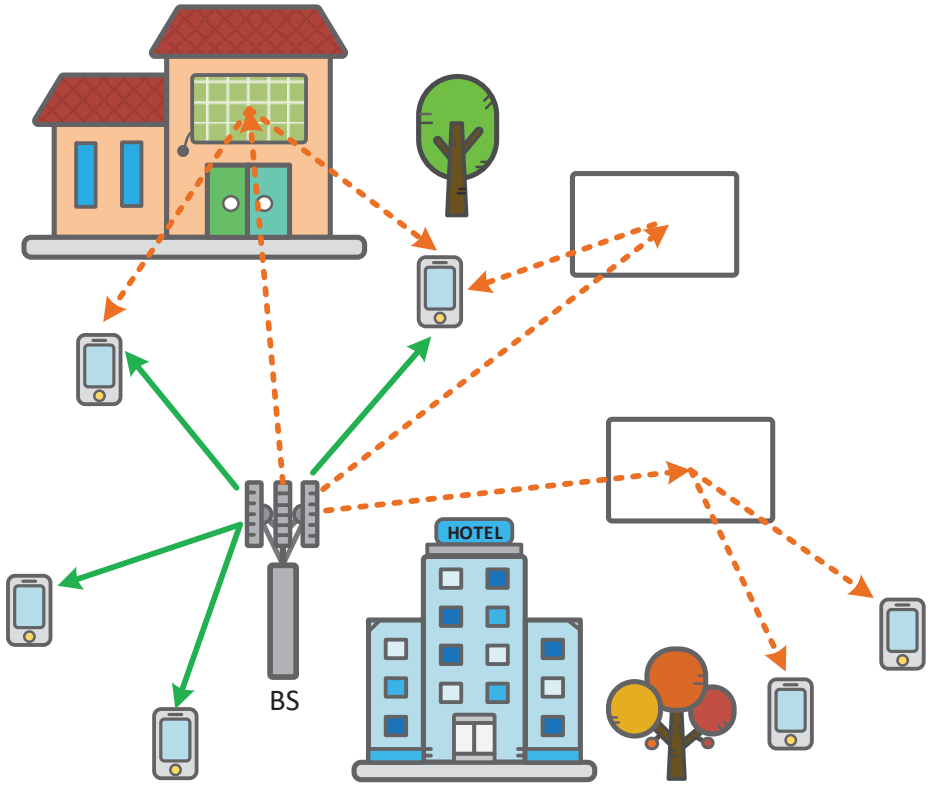

Abbildung 1.4: Illustration of an IRS-assisted multiuser wireless network where the direct links and reflecting links between the BS and user devices are denoted by green-colored solid-line arrows and orange-colored dashed-line arrows, respectively.

by intelligently coordinating their reflecting elements, we can favorably reconfigure adverse radio propagation environments, which improves the performance of wireless communication systems. An example of an IRS-assisted wireless network is depicted in Fig. 1.4. Yet, to exploit the promising advantages of IRSs, one has to carefully tackle the new challenges induced by IRS-assisted wireless communication systems.

- **Passive Nature:** A typical IRS consists of a group of reflecting elements such as printed dipoles and phase shifters. As a result, compared to conventional active antenna arrays, IRSs are not equipped with RF chains, and only require a very low circuit power to maintain operation. According to [29], the circuit power required to support one IRS element is roughly 2 mW. Hence, IRSs can be a promising solution to facilitate power-efficient communication in future wireless networks. Yet, due to the absence of RF chains, the channel estimation approaches developed for conventional BS-supported wireless networks may not be directly applied to acquire the channel state information (CSI) of IRS-assisted links, i.e., the BS-IRS link and the IRS-user link. As a compromise, new channel estimation approaches such as discrete Fourier transform (DFT)-based

algorithms have been developed to acquire the CSI of the cascaded channel of the BS-IRS-user link [30].

- **Programmability:** IRS elements can be tuned to change the properties of an incident EM wave and reflect it in a desired direction. Hence, operating the IRS elements with different phase-shift configurations allows us to customize desirable wireless channels to realize various design objectives such as signal enhancement, interference suppression, and coverage extension. In fact, to fully unlock the potential of IRSs, the reflection configurations of all IRS elements have to be properly designed via optimization. Yet, this introduces new design challenges for wireless communication systems. First, to enhance the desired signal power while mitigating interference, a large number of phase-shift coefficients have to be jointly optimized at the IRS, which potentially leads to a heavy computation burden for practical IRS systems [31]. As a result, it is necessary to develop scalable optimization frameworks and computationally-efficient optimization algorithms for IRS-assisted communication systems. Second, the operation of the IRSs makes them part of the wireless channel, and thus, the phase-shift matrix of the IRS is intrinsically multiplied with other optimization variables such as the active beamforming vectors or the transmit power of the BS. To circumvent this obstacle, advanced optimization algorithms that can effectively tackle the resulting variable coupling are needed. Third, due to the passive nature of IRSs, perfect CSI of the IRS-assisted cascaded channels is challenging to obtain [32]. As a result, to facilitate reliable communications, it is necessary to take into account the impact of channel estimation errors when designing practical IRS-assisted systems.

- **Simple Structure:** Usually integrated as thin planar surfaces, IRSs are adjustable in size and lightweight and can be conveniently installed on interior walls, building facades, and vehicles. As a result, IRSs can be smoothly and flexibly integrated into existing wireless communication systems [33]. Yet, to employ IRSs in a cost-efficient and effective manner, system designers have to exploit prior knowledge regarding the radio propagation environment when designing an IRS deployment strategy.

- **FD Mode:** IRSs naturally operate in an FD manner, and benefiting from their passivity, they do not introduce any SI and avoid circuit noise amplification. As a result, they can be handily amalgamated into existing FD wireless communication systems [34]. However, both the location and the reflection coefficient matrix

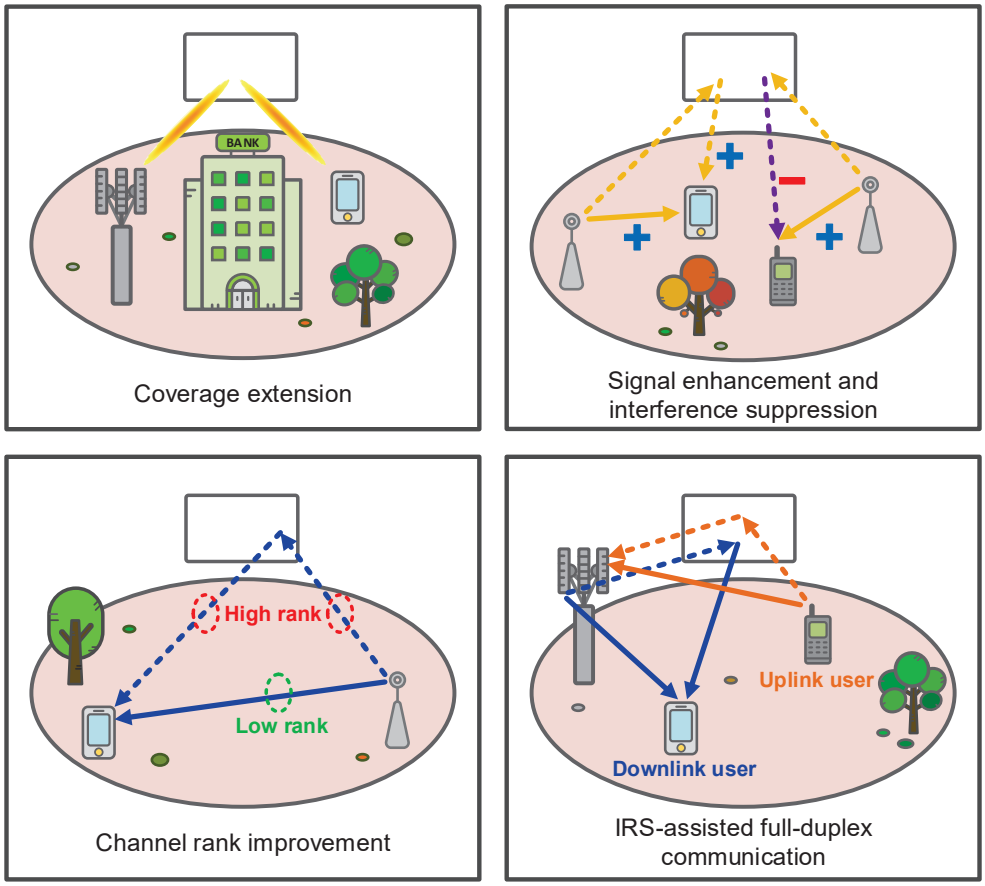

Abbildung 1.5: Illustration of some basic applications of IRSs in wireless communication systems.

of IRSs have to be carefully designed to mitigate the severe SI and co-channel interference caused by the other components of FD wireless networks.

1.2.2 Application Scenarios of IRSs in Wireless Communications

Considering the above-mentioned properties, IRSs can be widely and densely deployed in wireless communication systems to improve spectral- and power-efficiency in an economic manner [35]. In Fig. 1.5, we show some basic applications of IRSs in wireless communication systems. Specifically, in case the direct link between the BS and a user suffers from severe attenuation due to blockage, an IRS can be exploited to establish an additional reflected link, which assists in the information transmission and extends service coverage. Moreover, by smartly adjusting the reflection coefficient matrix of the IRS, we can amalgamate the signals in the reflected link and the direct link in an additive or subtractive manner such that the intended signal power strength is enhanced or interference is mitigated at the users, respectively [36]. Furthermore,

compared to the direct link, the extra IRS-induced link usually has a higher rank [34, 37], which can be exploited to improve the diversity gain. Besides, due to their programmability and FD nature, IRSs are an enabler for future FD wireless networks.

1.3 Review of Contributions

In this section, we review the contributions of this thesis. In particular, we adopt the following format for reviewing every contribution. (1) We first discuss some background for the main focus topic of the contribution. This includes some key aspects of resource allocation design and relevant examples as well as an overview of the relevant works in the literature. (2) Then, we discuss and highlight different aspects of the contribution and compare them with existing works.

1.3.1 Resource Allocation Design for UAV Communication Systems

Compared to conventional wireless communication systems, the design of UAV-assisted communication systems offers more degrees of freedom (DoFs) and meanwhile has to overcome more obstacles. In particular, to achieve the desired system design target, the position or the trajectory of the UAV has to be jointly optimized with the other resources available in wireless networks. Moreover, different from conventional fixed terrestrial infrastructures, one has to properly design the UAV propulsion-related parameters to provide satisfactory communication services in a power-efficient manner. Besides, geometrical constraints should also be considered when applying UAVs in wireless networks. In the following, we list several key aspects of resource allocation in UAV communication systems and review some related works in the literature.

1.3.1.1 Background

UAV Position/Trajectory Design: In wireless networks, the UAV can act as a static aerial BS or a mobile BS. As a result, depending on the application scenario, one can either optimize the hovering position or the trajectory of the UAV. Note that since fixed-wing UAVs are incapable of hovering, hovering position design is applicable only for rotary-wing UAVs. As for rotary-wing UAVs, the UAV hovering position is usually optimized to achieve specific design objectives, e.g., minimizing the UAV time of operation or minimizing the required number of UAVs. For instance, the authors of [38] studied the efficient deployment of UAVs to maximize the coverage of UAV-assisted wireless networks. Alternatively, the hovering positions of the UAVs can be jointly optimized with the power policy to facilitate power-efficient communications.

For instance, the authors of [22] considered a UAV aerial BS and jointly optimized its location and beamforming vectors for minimization of the total transmit power for multiuser communication. However, when the design objective also involves the UAV's aerodynamic power, UAV hovering is not a power-efficient choice. This is due to the fact that for rotary-wing UAVs, hovering is in general not the most power-saving status, cf. Fig. 1.2. As a result, rather than hovering at the desired position, a rotary-wing UAV would circle around that position at a speed that maximizes the UAV service duration for a given onboard energy, cf. [39, 40]. Inspired by this observation, the authors of [41] assumed that the UAV flies cyclically around the desired hovering position and studied the most power-efficient UAV circling radius and user partitioning strategy for a UAV-aided cellular system.

On the other hand, since the UAV trajectory design usually involves a continuous time horizon, it is challenging to directly tackle such a problem. To overcome this difficulty, a discrete path planning approach is commonly adopted in the literature [42]. Specifically, for a given UAV operation time horizon T, the UAV trajectory is discretized into N distinct waypoints, where each waypoint corresponds to a sufficiently small time slot with duration T/N. Moreover, as discussed in Section 1.1.1, the high altitude of the UAV facilitates LoS-dominant air-ground channels. In fact, the probability of having an LoS channel depends on the flight height and the elevation angle of the UAV. Many works in the literature assumed that the altitude of the UAV is sufficiently high to have a purely LoS air-ground channel [39, 43, 44]. Other works adopted a Rician fading channel model for the air-ground channel [40, 45]. Depending on which kind of air-ground channel model is adopted, there are in general two different UAV trajectory optimization frameworks, i.e., offline trajectory design and online trajectory design. In particular, since for pure LoS channels, the distance-dependent path loss is the only relevant effect, the air-ground channel gain is known in advance for given locations of the UAV and ground users. As a result, the UAV trajectory can be designed in an offline manner. In [43], by adopting the pure LoS air-ground channel model, the authors jointly optimized the user scheduling, user association, UAV trajectory, and transmit power offline to maximize the energy efficiency of a multi-UAV enabled wireless communication system. On the other hand, for the Rician fading channel model, offline UAV trajectory design is not feasible as non-causal knowledge of the channel coefficient would be required which is usually unavailable in practice. As a compromise, a waypoint-by-waypoint online trajectory optimization framework is required. In particular, the online framework updates the CSI of the whole system at each waypoint and then, optimizes the position of the next waypoint by assuming the channel remains unchanged during duration T/N. Employing this approach, the authors of [40] developed the jointly optimal UAV trajectory and transmit power and

subcarrier allocation policy for maximization of the sum throughput of a UAV communication system. Similarly, in [45], an online optimization algorithm that jointly optimized the trajectory and beamforming policy of the UAV is developed to facilitate power-efficient UAV communications.

Although UAVs enjoy 3D mobility, many existing works focused on optimizing the 2D UAV trajectory and assumed that the UAV flies horizontally at a constant altitude [39,43–45]. The reason behind this choice is two-fold. First, for safety concerns, most countries have released civil UAV operational rules to strictly constrain the altitudes of UAVs. Second, the path loss of the air-ground link is proportional to the flight height of the UAV. Hence, the minimum altitude is preferable to reduce the path loss. Assuming that the UAV flies at the minimum safety height, which avoids all terrain obstacles within the service area, the authors of [46] investigated the optimal trajectory to maximize the amount of energy transferred to a number of ground energy harvesting (EH) receivers. Besides, by employing a fly-and-hover protocol, i.e., flexibly switching rotary-wing UAVs between hovering mode and flying mode, the UAV can provide timely and high-quality customized services such as UAV-assisted wireless power transfer and UAV-enabled target sensing [47].

Aerodynamic Constraints: The mobility and maneuverability of the UAV introduce additional constraints for resource allocation design in UAV-assisted communication systems. Recall that the UAV aerodynamic power consumption is in general much larger than the communication-related power consumption. As a result, given the limited capacity of the onboard battery, $P_{\max}$, the UAV power constraint should include the aerodynamic power P_{aero} and the communication-related power P_{com}, i.e.,

$$P_{\text{tot}} = P_{\text{aero}} + P_{\text{com}} \leq P_{\max}, \tag{1.1}$$

Depending on the type of UAV, the aerodynamic power consumption model can be different. In particular, for fixed-wing UAVs performing horizontal flight under quasi-static equilibrium conditions, the aerodynamic power consumption model is given by [24]

$$P_{\text{aero}}^{\text{f}}(v) = c_1 v^3 + \frac{c_2}{v}, \tag{1.2}$$

where c_1 and c_2 are two parameters that are related to the specific features of the UAV. As for rotary-wing UAVs, the aerodynamic power consumption model is given by [25]

$$P_{\text{aero}}^{\text{r}}(v) = \frac{\sqrt{2}Wc_3^2}{\sqrt{v^2 + \sqrt{v^4 + 4c_3^4}}} + c_4 V_{\text{T}}^3 \left[1 + c_5 \left(\frac{v}{V_{\text{T}}}\right)^2\right] + c_6 v^3, \tag{1.3}$$

where W is a parameter whose value is determined by the thrust-to-weight ratio of the UAV [25] and V_{T} represents the speed of the rotor tip. Constants c_3, c_4, c_5, and c_6 are rotary-wing UAV related parameters [25]. Compared to the aerodynamic power model of fixed-wing UAVs in (1.2), the aerodynamic power consumption model of rotary-wing UAVs is more complicated which leads to an additional obstacle for the resource allocation design of rotary-wing UAV-assisted communication systems. By employing a series of mathematical transformations, the authors of [45] obtain the optimal UAV speed policy that maximizes the service duration of a rotary-wing UAV. Exploiting the first-order Taylor approximation, the authors of [39] replaced the aerodynamic power consumption model in (1.3) with a more tractable model and showed that the approximated version of (1.3) is accurate when the value of v is large.

In addition to the aforementioned UAV power constraint, the high mobility of the UAV also incurs kinetic constraints for UAV trajectory design. First, there are limitations for the maximum and minimum UAV speeds, i.e.,

$$V_{\min} \leq v \leq V_{\max}. \tag{1.4}$$

In particular, the maximum UAV speed is related to the UAV's maximum output power and should be strictly controlled according to civil UAV operational rules. On the other hand, for rotary-wing UAVs, the minimum UAV speed $V_{\min}$ can be zero which corresponds to the hovering mode. For fixed-wing UAVs, the value of $V_{\min}$ has to be positive. Moreover, the UAV's maximum acceleration is determined by its engine performance. As a result, the UAV is not able to arbitrarily vary its speed between two adjacent waypoints, which induces the following kinetic constraint:

$$\Big|v[n+1] - v[n]\Big| \leq a_{\max}\frac{T}{N}, \tag{1.5}$$

where n is the time slot index and $a_{\max} > 0$ is the UAV's maximum acceleration. Taking into account the above constraints, the authors of [24] studied the joint UAV speed and acceleration design to maximize the energy efficiency of a fixed-wing UAV-assisted wireless communication system. Assuming that the UAV is in a quasi-static equilibrium state, the authors of [40] investigated the jointly optimal UAV speed, transmit power, and subcarrier allocation design that maximized the sum spectral efficiency of a rotary-wing UAV-enabled cellular system.

Geometrical Constraints: In practice, for government buildings, military facilities, and civil aviation airports, NFZs are commonly imposed on UAVs for safety or security reasons. As the flight height of the UAV is usually fixed, most of the existing works focus on 2D NFZs [45, 48, 49]. Depending on how the NFZs are modeled, there are in

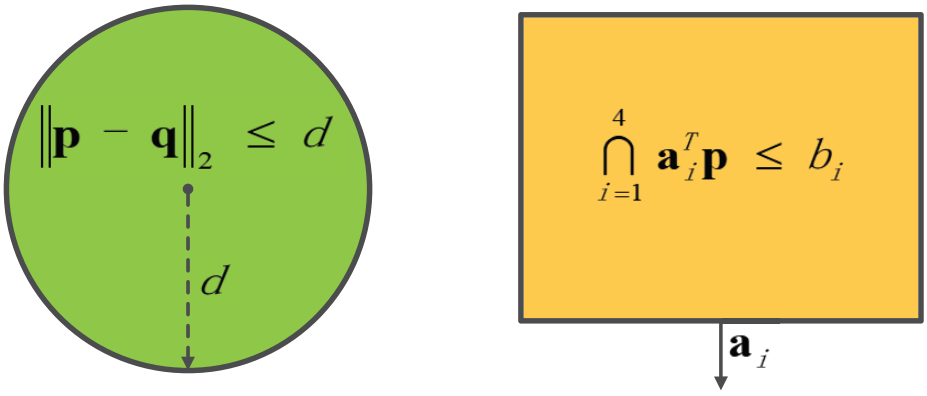

Abbildung 1.6: Illustration of a circle NFZ and a rectangular NFZ.

general two types of 2D NFZ-induced constraints, cf. Fig. 1.6. In particular, the NFZ can be modeled as a circle which is given by

$$\mathcal{P} = \left\{ \mathbf{p} \in \mathbb{R}^2 \;\middle|\; \|\mathbf{p} - \mathbf{q}\|_2 \leq d \right\}, \tag{1.6}$$

where $\|\cdot\|_2$ denotes the l_2-norm of its argument. Vectors $\mathbf{p} \in \mathbb{R}^2$ and $\mathbf{q} \in \mathbb{R}^2$ denote the UAV 2D position and the origin of the 2D NFZ, respectively. Besides, d is the radius of the circle NFZ. On the other hand, an M-sided polygon NFZ can be represented as the intersection of M half-spaces, which is given by

$$\mathcal{P} = \left\{ \mathbf{p} \in \mathbb{R}^2 \;\middle|\; \bigcap_{i=1}^{M} \mathbf{a}_i^T \mathbf{p} \leq b_i \right\}, \tag{1.7}$$

where $(\cdot)^T$ denote the transpose of its argument. Moreover, each half-space is defined by a linear inequality $\mathbf{a}_i^T \mathbf{p} \leq b_i$. As a result, for any waypoint, the UAV is outside the NFZ if its 2D position $\mathbf{r}$ satisfies the following constraint:

$$\mathbf{r} \notin \mathcal{P}. \tag{1.8}$$

We note that compared to polygon NFZs, circle NFZs are easier to incorporate when designing the UAV trajectory.

In addition to the NFZ-induced constraint, it is necessary to take into account other geometrical constraints, e.g., the initial and final positions of the UAV, to facilitate the application of UAVs in wireless communication systems. In particular, the UAVs are usually launched at pre-determined locations such as UAV bases and control centers. Moreover, after completing their mission, UAVs are required to return to specific regions for maintenance or recharging. As a result, we have

$$\mathbf{r}[0] \in \mathcal{D}_{\text{ini}}, \;\; \mathbf{r}[N] \in \mathcal{D}_{\text{fin}}, \tag{1.9}$$

where $\mathcal{D}_{\text{ini}} \subseteq \mathbb{R}^2$ and $\mathcal{D}_{\text{fin}} \subseteq \mathbb{R}^2$ denote the required launching and takeoff region for UAV trajectory design, respectively.

Besides, when multiple UAVs collaborate with each other, it is necessary to delineate a safe region around each UAV to avoid UAV collision. In particular, the safe region can be modeled as a circle whose center is the current position of the UAV with the pre-determined safe distance being the radius, which leads to

$$\left\|\mathbf{r}[n] - \mathbf{r}^{'}[n]\right\|_2 \geq D_{\text{safe}}, \tag{1.10}$$

where $\mathbf{r}[n]$ and $\mathbf{r}^{'}[n]$ denote the positions of two different UAVs in time slot n and D_{safe} is a pre-defined UAV safe distance. Taking into account this constraint, the authors of [50] studied collision-free optimal trajectory design for a multi-UAV enabled wireless network.

1.3.1.2 Author's Contributions

In this part, we clarify the motivation of our work in [45] and explain the novel aspects of the considered UAV communication system model and the developed resource allocation schemes. Below, we summarize our main contributions:

- **Uniform Linear/Planar Array UAVs:** In the literature, most existing works adopted a single-antenna UAV to serve multiple single-antenna devices orthogonally in the frequency domain or in the time domain [39,40,43,44]. However, the performance of the aforementioned air-ground communication systems can be significantly improved if the UAV-mounted transceivers are equipped with multiple antennas. To this end, we proposed to employ a uniform linear array (ULA), cf. [22], or a more general structure, a uniform planar array (UPA), cf. [45], at the UAV to meet the QoS requirements of multiple single-antenna ground devices in a spectral- and power-efficient manner. Our works [22] and [45] are the first two papers that modeled multi-antenna UAV systems and investigated the corresponding optimal transmit beamforming vector design.

- **UAV Communications in Uncertain Environments:** Although the works in [40, 44, 48, 49] have revealed significant performance gains when exploiting UAVs in wireless communication systems, the developed resource allocation schemes may not achieve the expected gains in practical UAV-assisted communication systems. In particular, the designs developed in [40,44,48,49] are based on several idealistic assumptions, e.g., perfectly stable flight of the UAV and perfect CSI of the whole system. First, in practice, due to the unavoidable wind gusts, it is challenging for the UAV to maintain stability and preclude unfavorable body

jittering during the flight. According to the measurement results in [21], the jittering angles of UAVs can be as large as 10 degrees, which cannot be neglected for practical UAV communications. Impaired by jittering, it is challenging for the UAV onboard sensors to precisely measure the angle-of-departure (AoD) of the air-ground links. As a result, if left unattended, the resulting jittering-induced AoD variance can significantly degrade the beamforming gain introduced by the UPA at the UAV. To capture this effect, in [45], we propose a bounded AoD uncertainty model which constrains the maximum AoD estimation error by a deterministic value. Second, when operating a UAV in strong wind gusts, the UAV ground speed, i.e., the horizontal speed of the UAV with respect to the ground, is actually the sum of the horizontal wind speed and the UAV air speed. As a result, even if the UAV's air speed is appropriately controlled, we cannot prevent the UAV from violating the corresponding operation constraint. Moreover, when encountering high horizontal wind speeds, the UAV may deviate from the intended trajectory, causing a collision or crashing accident. Because of the random nature of the wind, it is challenging to estimate the precise wind speed in each time slot. As a compromise, we make the conservative assumption that the wind gusts always exist during the considered time horizon and adopt a bounded wind speed uncertainty model to restrict the maximum wind speed. Third, although global positioning system (GPS) modules are commonly installed at the ground user devices, the real-time user location information may not be perfectly known because of the limited positioning accuracy of practical GPS modules. As a result, we also model the 2D user location uncertainty in [45]. Our work [45] was the first paper that considered a practical UAV communication system in an uncertain environment accounting for jittering-induced AoD uncertainty, the randomness of wind speed, and user location estimation errors and, further, developed a corresponding robust UAV trajectory design algorithm.

- **Polygon NFZs:** Considering the fact that NFZs are commonly imposed in practical UAV systems, it is necessary to take into account corresponding geometrical constraints for UAV trajectory design. Most existing works adopted a circle NFZ model as it introduces a convex constraint for resource allocation optimization [48, 49]. However, as shown in [51], practical NFZs are usually delineated as polygons. As a result, in our work [45], we considered a general and practical case where multiple polygon NFZs coexist in the region to be served. In particular, we model each polygon NFZ in a similar way as in (1.7). With the help of a binary indicator function, we first represented the condition that the UAV does not violate one NFZ by a Boolean operator 'or' function. Then, for

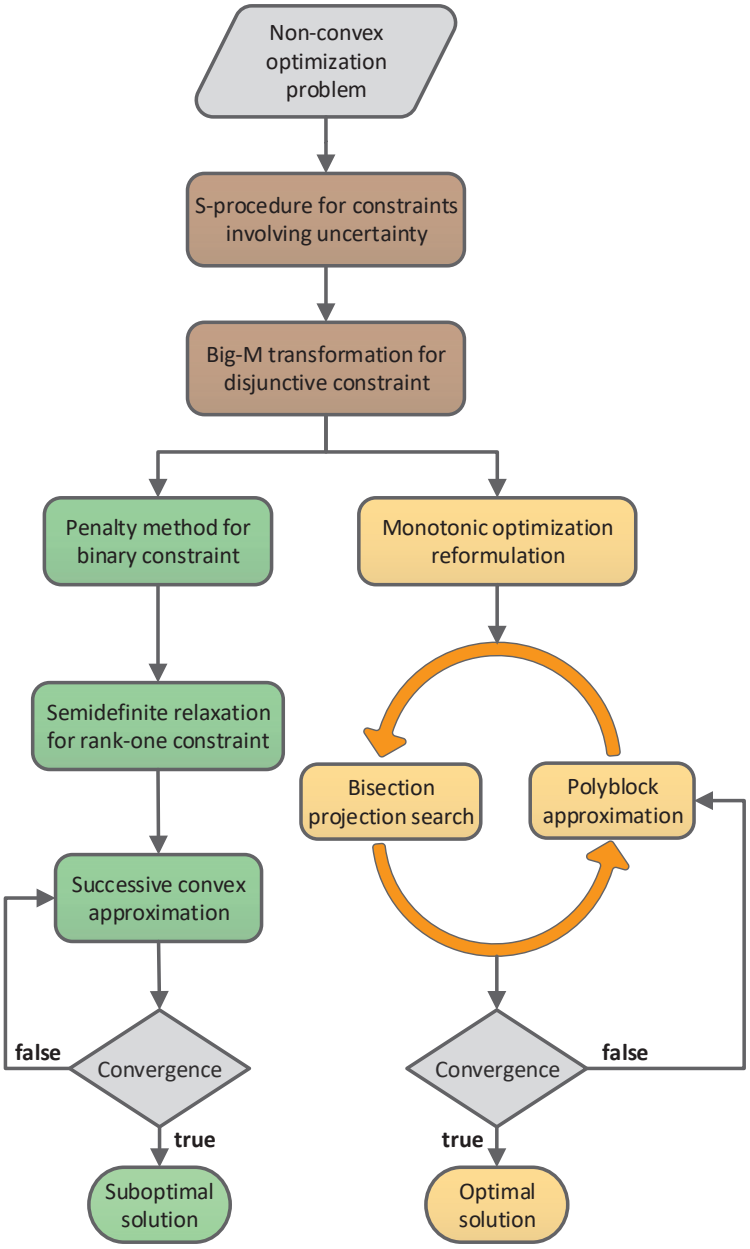

Abbildung 1.7: Illustration of key steps for obtaining the globally optimal solution and locally optimal solution of the optimization problem formulated in [45].

multiple coexisting NFZs, we derive a disjunctive programming constraint. The UAV does not intrude any NFZ if this disjunctive constraint is satisfied. Since the disjunctive programming constraint imposes an obstacle for solving the formulated resource allocation optimization problem, we transformed the original problem equivalently into a mixed-integer programming problem by employing the Big-M transformation [52]. Our work [45] is the first paper in the UAV communication literature that adopted the polygon NFZ model for UAV trajectory

design and, further, proposed a corresponding optimization technique for the resulting challenging problem.

- **Optimal Solution:** In [45], we studied the joint robust UAV trajectory and beamforming vector design to facilitate power-efficient UAV communications, i.e., to minimize the summation of the UAV aerodynamic power and the transmit power. Since the AoDs of the air-ground links vary with the UAV's real-time location, it is arduous to offline design the UAV 2-D horizontal track and downlink beamforming strategy for a sequence of time slots. Hence, we exploited monotonic optimization theory and developed an online optimization framework that yielded the optimal trajectory and beamformers of the UAV in each time slot. A detailed review of monotonic optimization will be presented in Section 2.2.3. The proposed monotonic optimization-based algorithm enables the performance evaluation of any suboptimal schemes but also entails a high computational complexity that grows exponentially with the number of optimization variables. To facilitate real-time online UAV design, we also developed a successive convex approximation (SCA)-based low-complexity suboptimal algorithm. The SCA approach will be introduced in detail in Section 2.2.1. To summarize the resource allocation schemes developed in [45], in Fig. 1.7, we provide a flow chart that contains the main steps of the proposed monotonic optimization-based and SCA-based algorithms.

1.3.2 Resource Allocation Design for IRS-Assisted Communications

The novel and attractive features of IRSs make them a promising enabler for future wireless networks. The key to unleashing the full potential of IRSs is to jointly design their phase shifts and the other components of the wireless communication system. To this end, one has to carefully model the properties of IRSs. In the literature, various IRS models have been proposed to account for the different properties of IRSs, which induce different constraints for the design of IRS-assisted wireless systems. Moreover, system designers have to carefully take into account the IRS deployment problem to provide high-quality communication in a cost- and power-efficient manner. Furthermore, since perfect CSI of the IRS-assisted cascaded channels is challenging to obtain, it is necessary to take into account channel estimation errors and develop robust resource allocation algorithms to facilitate reliable communications in practical IRS-assisted systems. Besides, other issues such as discrete IRS phase shifts should also be considered for practical IRS-assisted communication systems. In the following,

we list several key aspects of resource allocation optimization design for IRS-assisted communications and briefly review some related works in the literature.

1.3.2.1 Background

IRS Model-Induced Constraints: Depending on the adopted IRS models, system designers have to consider different constraints when investigating IRS design. In the following, we introduce several commonly adopted theoretical IRS models and discuss the corresponding challenges for IRS design.

- **Independent Diffusive Scatterer (IDS)-Based Model:** The IDS-based IRS model has been widely adopted in many works that investigated the resource allocation algorithm design for IRS-assisted communication systems [53–58]. For instance, adopting an IDS-based IRS model, the authors of [53] investigated the joint active and passive beamforming design and revealed a significant performance improvement with IRSs in multiuser communication systems. In particular, this model assumes that each IRS element acts as a diffusive scatterer and is able to independently vary the incident signal by adding an additional phase shift. Accordingly, the impact of the IRS can be modeled by a diagonal matrix, where the entries of the main diagonal represent the reflection coefficients of the IRS elements. Considering the passive nature of IRSs, the magnitude of the reflection coefficient of each IRS element cannot exceed one, leading to a unit-modulus constraint for the reflection coefficients. The corresponding unit-modulus constraint of an IRS comprising M elements can be modeled as

$$\mathbf{\Psi} = \text{diag}\left(e^{j\theta_1}, \cdots, e^{j\theta_m}, \cdots, e^{j\theta_M}\right), \tag{1.11}$$

  where θ_m is the phase shift of the m-th reflecting element of the IRS. We note that this unit-modulus constraint defines a multi-dimensional complex circle manifold which makes the resulting optimization problem intractable. In general, it is challenging to develop a systematic approach that can solve such an optimization problem optimally. In the literature, the globally optimal solution was shown to be accessible only for some special cases. For instance, the authors of [59] developed an argument division-based branch-and-bound (BnB) algorithm and revealed the performance ceiling of an IRS-enabled single-user system. The computational complexity of such algorithms is prohibitively high for practical IRS systems, which has motivated researchers to develop computationally-efficient algorithms by sacrificing part of the performance gain. In particular, some works proposed to first transform the original optimization problem with (1.11) into an equivalent semidefinite programming problem with a rank-one constraint and

then, tackle it by employing SDR, cf. [53–55]. Unfortunately, this approach cannot ensure a rank-one solution for the equivalent optimization problem. As a result, Gaussian randomization is further applied to produce a unit-rank solution. However, this may cause an infeasibility issue as the resulting solution is not guaranteed to satisfy the QoS constraint. To circumvent this difficulty, some works proposed to employ the manifold optimization approach to directly handle the unit-modulus constraint problem [56]. Alternatively, the unit modulus constraint can be replaced by an equivalent rank-constraint, and then, can be further recast as a difference of convex functions (DC) constraint. Inspired by this observation, some works propose to employ the SCA approach to obtain a suboptimal solution to such a problem. For example, the authors of [60] proposed to rewrite the rank-one constraint as the difference of two matrix norm functions and convexified the resulting constraint by constructing a first-order Taylor approximation-based surrogate function for SCA.

- **Impedance-Network (INW)-Based Model:** The IDS model is based on the assumption that each IRS element can be separately controlled and there is no connection between the IRS elements. As a result, the available DoFs of an IDS-based IRS are determined by the number of IRS elements. Inspired by this, the authors of [61] proposed to connect all IRS elements via an impedance network, which introduces additional DoFs for IRS design. This novel IRS architecture, referred to as the INW-based IRS model, allows us to simultaneously adjust the phases and the magnitudes of incident signals. In particular, the INW model introduces the following constraints on the IRS matrix design

$$\mathbf{\Psi} = \mathbf{\Psi}^T, \;\; \mathbf{\Psi}^H\mathbf{\Psi} = \mathbf{I}_M, \tag{1.12}$$

where $(\cdot)^H$ denotes the conjugate transpose of its argument and $\mathbf{I}_M$ refers to the identity matrix of dimension M. Equation (1.12) indicates that $\mathbf{\Psi}$ is a complex symmetric unitary matrix. Compared to the IDS-based model, although the INW-based model introduces more DoFs that can be exploited to improve system performance, it also has several drawbacks. First, the IDS-based model can be regarded as a single connected reconfigurable impedance network, which is a special case of the fully connected INW-based model. As a result, the INW-based model requires more reconfigurable impedance components to establish the connections between the IRS elements, which increases the deployment cost and the complexity of the hardware implementation. Second, compared to the IDS model-induced constraint in (1.11), the constraint in (1.12) is even more challenging for IRS design. In particular, it is difficult to transform the complex

symmetric unitary matrix constraint into a more tractable form. As a result, there is only a limited number of works that adopted this model for investigating IRS system design. The work in [61] was the first paper that paved the way for INW-based IRS design. In particular, the authors of [61] considered a special case where an IRS-assisted system serves only one user and developed a quasi-Newton-based algorithm that maximized the received signal power at the user. Considering the fact that the constraint in (1.12) can be mapped to a complex Stiefel manifold in Riemannian space, one may exploit manifold optimization theory to develop an efficient resource allocation optimization algorithm for a multiuser system.

- **Physics-Based Model:** Although the IDS- and INW-based IRS models account for the phase shift and passive nature of the IRS, they do not take into account the physical characteristics of IRSs, such as the EM wave angle of arrival (AoA) and AoD and the size of the IRS elements. Thus, the IDS and INW models cannot exploit these essential and practical properties for the design of IRS-assisted systems effectively. This motivates the development of a physics-based IRS model, which accurately captures the unique EM environment in practical IRS systems, cf. [37, 62]. This physics-based IRS model is based on the generalized radar cross-section matrix $\mathbf{G}$, whose entries can be expressed as follows

$$g(\phi_{\mathrm{t}}, \phi_{\mathrm{r}}). \tag{1.13}$$

  Here, $g(\phi_{\mathrm{t}}, \phi_{\mathrm{r}})$ is the response function for a plane wave impinging from a direction characterized by AoA ϕ_{t} to a reflected direction characterized by AoD ϕ_{r} for a given reflection pattern of the IRS. In fact, for a practical radio propagation environment, there are usually a finite number of scatterers. As a result, only limited numbers of AoAs and AoDs can be exploited by the IRS to receive a signal from the intended transmitter or reflect a signal to the destination. Inspired by this observation, the authors of [37] proposed a two-stage optimization framework that sequentially designs a physics-based IRS in an offline stage and an online stage. Specifically, the IRS is partitioned into several tiles and for each configuration of the phase shifts of a tile, the resulting impact on the wireless channel is modeled taking into account the incident and reflection angles. As a result, a set of different transmission modes is constructed offline, where each transmission mode effectively corresponds to a given configuration of the phase shifts. Then, in the online stage, the transmission mode selection policy is jointly designed with the other wireless resources to achieve the desired design objective [63]. In [37], the authors provided initial results for exploiting the two-stage

optimization framework for resource allocation optimization in an IRS-assisted multiuser communication system. Furthermore, employing the two-stage optimization framework, the authors of [64] investigated the optimal phase-shift codebook design to maximize the received power in an intended direction.

- **Active IRS:** Although the above IRS models have been widely adopted in the literature to study IRS design, their passivity constitutes a bottleneck for significant performance enhancement of conventional communication systems. In practice, due to the double path loss effect, there is usually a significant path loss gap between the IRS-induced reflected link and the unobstructed direct link [37]. This issue, if left unattended, can severely degrade the performance gain achieved by deploying passive IRSs in conventional communication systems. Considering the fact that passive IRSs enable a square-law beamforming gain [53], one promising way to compensate for the severe large-scale fading is to substantially increase the number of passive IRS elements. Yet, employing such a large passive IRS in a wireless network not only results in considerable signaling overhead for CSI acquisition but also significantly complicates IRS optimization. To overcome these difficulties, the authors of [65] proposed to amend conventional passive IRSs by adding additional reflection-type amplifiers. This novel IRS architecture, referred to as active IRSs, can simultaneously adjust the phase and the magnitude of the reflected signals at the expense of consuming extra power for amplification. In particular, by exploiting an external power supply, active IRSs can effectively reduce the double path loss-induced performance degradation of passive IRSs without significantly increasing the computational burden and signaling overhead. Active IRSs can be modeled by the product of an amplification coefficient matrix $\mathbf{A}$ and a phase-shift matrix $\mathbf{\Theta}$. For a given limited available power, P_{IRS}, the amplification power of the active IRS has to satisfy the following constraint

$$P_s(\mathbf{A}, \mathbf{\Theta}) + P_n(\mathbf{A}, \mathbf{\Theta}) \leq P_{\text{IRS}}. \tag{1.14}$$

Here, $P_s(\mathbf{A}, \mathbf{\Theta})$ denotes the amplification power for the desired signals. Moreover, $P_n(\mathbf{A}, \mathbf{\Theta})$ denotes the variance of the amplified dynamic noise that is generated by the power amplification [65]. The amplification power constraint in (1.14) involves two optimization variables $\mathbf{A}$ and $\mathbf{\Theta}$, which further aggravates the variables coupling issue for IRS design. To circumvent this difficulty, the authors of [66] developed a block coordinate descent (BCD)-based algorithm that maximizes the spectral efficiency of active IRS-assisted multiuser systems.

IRS Deployment: In practice, depending on the application scenario, there are different IRS deployment policies. Specifically, given a total number of IRS elements, one can either adopt a centralized deployment strategy, i.e., constructing a large IRS at a desired location, or alternatively, one can divide the IRS elements into several groups and deploy several small IRSs in a distributed manner in the wireless network. For instance, the work in [60] showed that a uniform allocation with the same number of reflecting elements deployed at several small IRSs is favorable for performance enhancement of IRS-assisted wireless networks with uniformly distributed users. The authors of [67] investigated the deployment strategy in an IRS-assisted network comprising two users and unveiled that centralized deployment outperforms distributed deployment when the rates of the two users are different. On the other hand, due to the double path loss effect, it is usually advantageous to deploy the IRSs in close vicinity of either the BS or the user. In particular, the authors of [53] proposed to deploy the IRS close to a set of users to provide communication services for these users in a power-efficient manner. In [68], the authors studied the optimal IRS deployment design for maximization of the sum rate for different multiple access schemes. Furthermore, since the IRSs reflect all incident signals, system designers have to carefully choose the location of the IRS to avoid severe inter-cell interference or information leakage. For instance, the authors of [69] investigated different network geometries and compared the corresponding secrecy rates for an IRS-assisted multiuser communication system. Besides, the IRSs should be deployed by exploiting prior knowledge of the radio propagation environment and taking into account additional practical factors such as deployment cost and space constraints. In Fig. 1.8, we show some typical IRS deployment scenarios in wireless communication systems.

Robust IRS Design: As we mentioned in Section 1.2.1, the passivity of the IRS makes it difficult to obtain the perfect CSI of the cascaded channel of the BS-IRS-user link. To facilitate reliable communication in practical systems, the resource allocation algorithms should be robust against channel estimation errors. In the literature, CSI uncertainty is characterized by adopting either a bounded model or a statistical model. In particular, the bounded CSI error model constructs an uncertainty region with a known bound, which contains all possible CSI errors. This introduces an intractable semi-infinite constraint in the problem formulation. Such a constraint is usually recast into a more tractable linear matrix inequality (LMI) constraint and then, is efficiently tackled by employing the S-procedure. A detailed description of the S-procedure can be found in [45, 57], cf. Appendices B and C. For instance, the authors of [70] adopted a CSI error model with a deterministic bound for the cascaded reflected channels and developed a penalty-based algorithm for minimization of the total transmit power of an IRS-assisted wireless network. Similarly, in [71], the

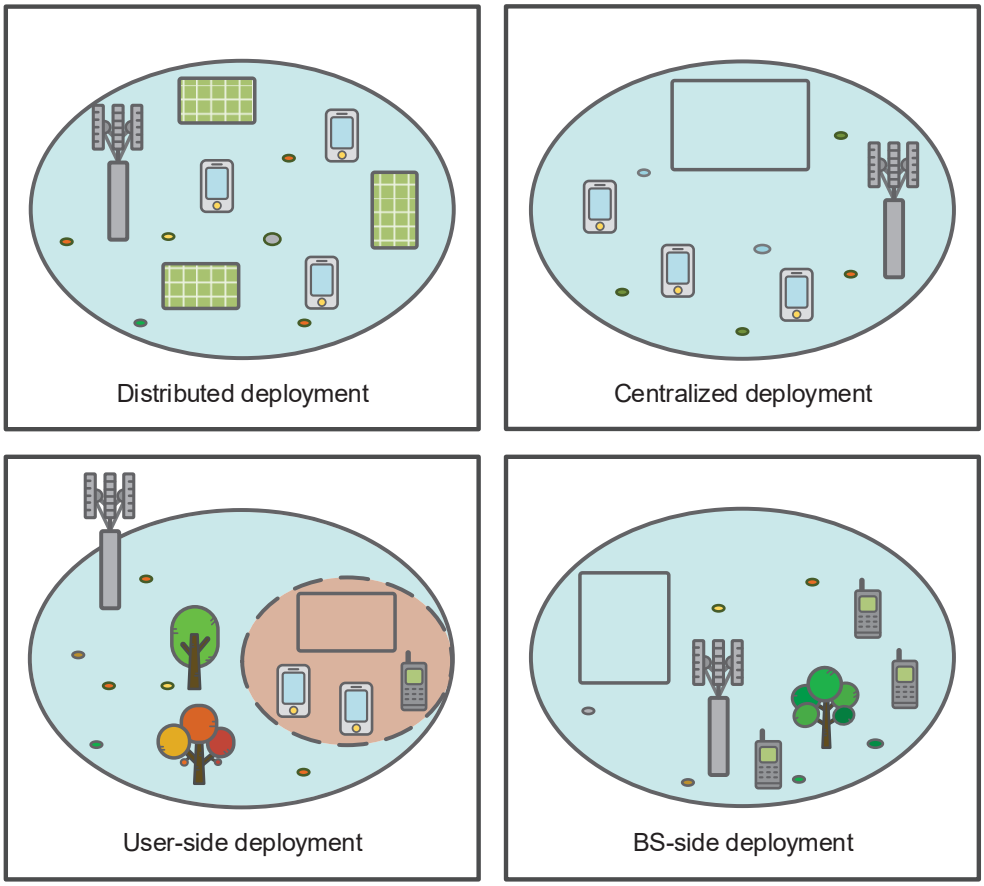

Abbildung 1.8: Illustration of some typical IRS deployment scenarios in wireless communication systems.

authors modeled the IRS-assisted channels by a norm-bounded CSI uncertainty region and proposed a computationally-efficient algorithm for maximization of the sum rate of an IRS-aided multiuser cellular system. On the other hand, for the statistical CSI uncertainty model, the channel estimation error is assumed to follow a circularly symmetric complex Gaussian distribution with zero mean and known variance, resulting in a probabilistic chance constraint for optimization. Such a constraint can be tackled by either leveraging a Bernstein-type inequality to obtain an approximated convex version of the original constraint [72] or deriving a tractable inverse cumulative distribution function [73].

IRS Impairments: As a component in practical communication systems, IRSs inevitably suffer from hardware impairments. In the literature, many works [53–56, 67, 68, 71] on IRS design assumed that the phase-shift set of the IRS elements, $\mathcal{F}$, is continuous, e.g., $\mathcal{F} = [0,\ 2\pi]$, which is an over-idealized assumption for practical IRSs. In fact, the cardinality of the phase shift set is determined by the number of electronic

devices (e.g., phase shifters or positive-intrinsic-negative diodes) integrated into one single IRS element. As a result, an IRS with a large number of possible phase shifts not only leads to a complicated integrated circuit design but also consumes a large space. To overcome these difficulties, some works considered the practical case where each IRS element has only a small set of possible discrete phase shifts to choose from [74–76]. In particular, the impact of having only two phase shifts for each IRS element on the performance of an IRS-assisted NOMA system was studied in [75]. Assuming a finite phase shift set for the IRS, the authors of [76] developed a BnB-based optimal scheme that maximized the minimum signal-to-interference-plus-noise (SINR) among the users of an IoT network.

1.3.2.2 Author's Contributions

In this part, we explain our four contributions [57, 63, 77, 78] on resource allocation algorithm design for IRS-assisted communication systems, see Appendices C, D, E, and F. In particular, for each work, we list several aspects to clarify the motivation and introduce the novel aspects of the system model, problem formulation, and solution. Furthermore, to illustrate the algorithm design in each work, we show a flow chart that summarizes the key transformations and optimization methods of the developed resource allocation schemes. In the following, we sequentially discuss our main contributions in [57, 63, 77, 78].

Contributions of [57]:

- **IRS-Enabled Interference Suppression in CR Networks:** Underlay CR has emerged as an efficient means to ameliorate spectrum utilization in wireless networks. Yet, due to co-existing transmissions of the primary and secondary networks in the same frequency band, incumbent users may suffer from severe interference originating from the unlicensed network. To appropriately manage the interference leakage of the secondary network, we proposed to exploit IRSs to create beneficial wireless channel conditions for CR networks. Specifically, to facilitate reliable communications for the primary users, we modeled the secondary network-induced interference and suppressed this interference below a maximum tolerable threshold by smartly designing the IRS phase shifts. Considering the fact that the primary users may not interact with the secondary BS, we assumed that the secondary BS can only acquire imperfect CSI of the primary users and took into account the corresponding CSI uncertainty for resource allocation design. Our work [57] was one of the earliest papers that exploited IRSs in wireless networks to simultaneously mitigate or suppress detrimental interference and promote favorable signal power levels.

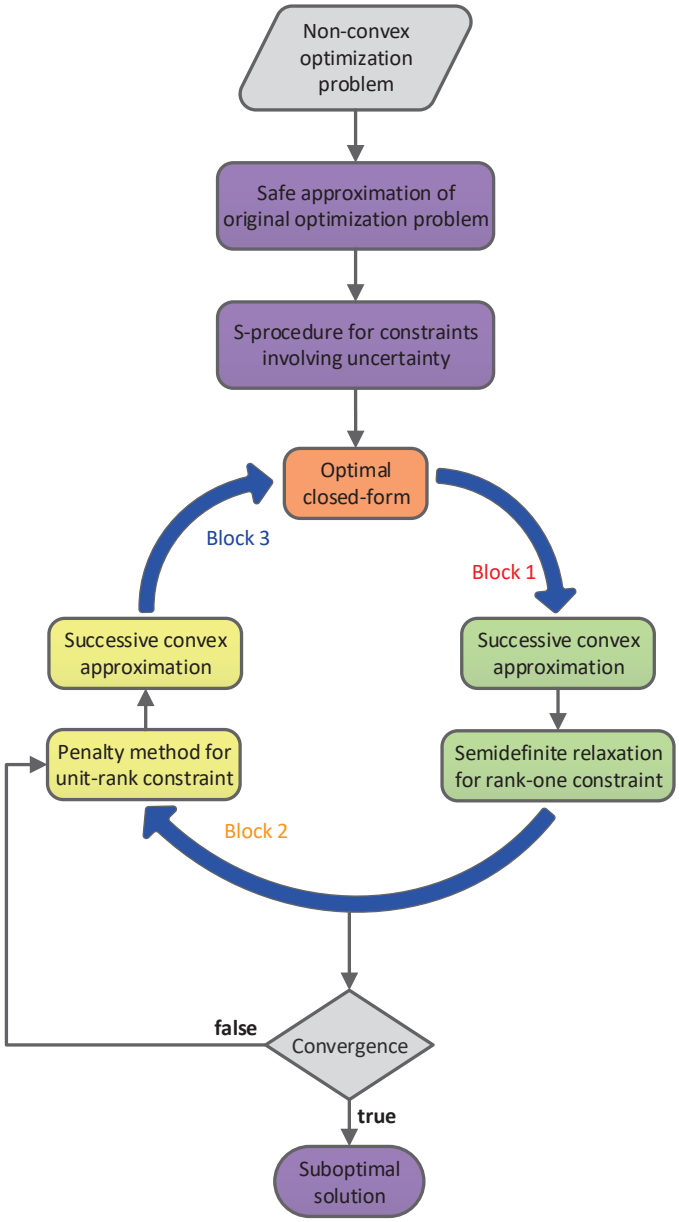

Abbildung 1.9: Illustration of the optimization framework proposed in [57].

- **IRS-Assisted FD Communications:** As FD programmable devices, IRSs are excellent boosters to existing FD networks to promote spectral efficiency and inhibit severe interference. In [57], we considered an IRS-assisted FD CR network, where the IRS was deployed to assist an FD BS in serving a group of half-duplex single-antenna downlink and uplink user devices in the same time-frequency domain. In particular, we modeled the residual SI at the secondary FD BS and revealed that the IRS-induced higher-order reflections of the SI were negligible compared to the SI itself. This first unveiled the fact that by carefully choosing the location of the IRS and employing advanced SI cancellation techniques, the deployment of the IRS would not aggravate the SI in conventional

FD networks. Moreover, our simulation results showed that by jointly optimizing the IRS elements with the other available resources, we could effectively mitigate the co-channel interference and significantly increase spectral efficiency compared to a baseline scheme without IRS. Our work [57] was the first paper that exploited the FD nature of IRSs to facilitate high-quality FD communications and developed a corresponding optimization framework for IRS-assisted FD communications.

- **Upper Bound for Semi-Infinite Constraint:** In practice, it is challenging for the unlicensed FD BS to acquire the perfect CSI of the incumbent users in the primary network. To capture the effect of this on FD CR network design, we adopted a bounded CSI uncertainty model for the primary users, which imposed a semi-infinite constraint on the resource allocation optimization problem. Due to the coupling between the beamforming vectors and the IRS reflection matrix and the product of uncertainty terms, it was difficult to directly transform this constraint into a tractable form, e.g., an LMI constraint. To circumvent this difficulty, we exploited the Minkowski inequality to derive a tractable upper bound for the interference term in the semi-infinite constraint. As a result, we obtained an approximated version of the original optimization problem, and then, by efficiently solving this substitute, we obtained a high-quality suboptimal solution to the original optimization problem. Via computer simulations, we showed that the proposed upper bound for the semi-infinite constraint was tight.

- **Computational-Efficient BCD-Based Algorithm:** In [57], the robust resource allocation design was formulated as a non-convex optimization problem taking into account the maximum power allowance of the FD BS and the maximum interference leakage tolerance of the primary users. Due to the IRS-induced unit-modulus constraint, the coupled optimization variables, and the product of the uncertainty terms, it was very arduous to obtain the optimal solution in polynomial time. Given the above considerations, we developed a computationally-efficient BCD-based optimization framework for the considered IRS-aided FD CR system. In particular, we partitioned the original optimization problem into three subproblems and efficiently tackled them in an alternating manner. We clarified that the proposed BCD-based algorithm produced a high-quality solution with guaranteed convergence and confirmed this via simulations. In Fig. 1.9, we show the key elements and transformations of the proposed BCD-based algorithm.

Contributions of [63]:

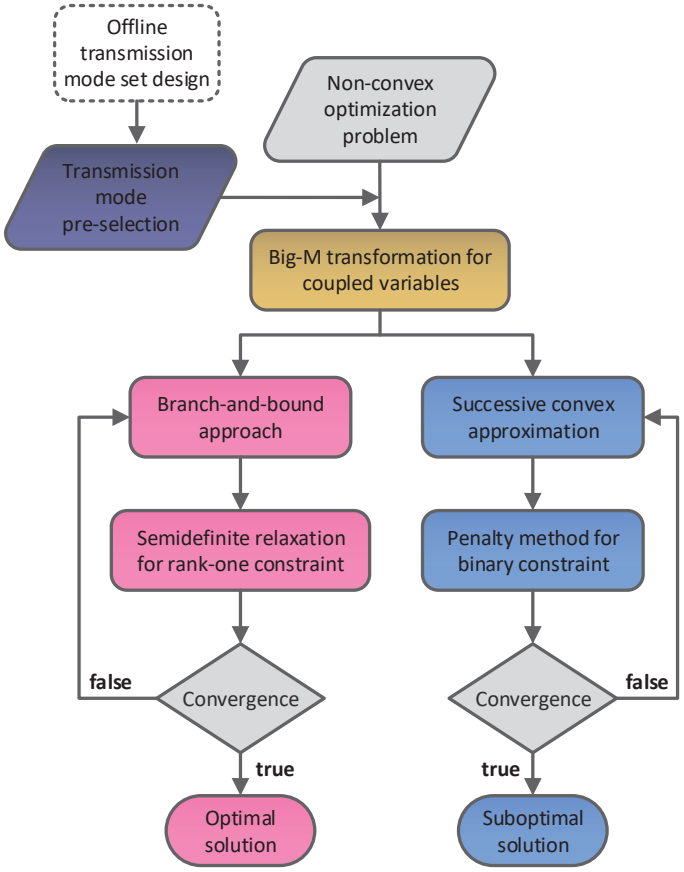

Abbildung 1.10: Flow chart of the optimal and suboptimal resource allocation optimization algorithms developed in [63].

- **Practical Large IRS-Assisted Simultaneous Wireless Information and Power Transfer (SWIPT) Systems:** In practice, the IRS usually comprises thousands of phase-shift elements [29, 79]. Yet, most existing works in the literature proposed to optimize the phase shift of each individual IRS element, and thus, the complexity of this element-wise optimization framework was proportional to the number of elements [53–55, 67, 68, 71]. Hence, for practically large IRSs, such an optimization framework may lead to a significant computational burden which hampers real-time IRS design. To overcome this difficulty, we employed a novel scalable optimization framework developed in [37] to design a large IRS-assisted SWIPT system, cf. Appendix D. Moreover, unlike many existing works, which assumed an over-simplified linear energy harvesting model [80, 81], in our work [63], we adopted a realistic sigmoidal function-based energy harvesting model for energy harvesting receivers.

- **Transmission Mode Pre-Selection Criterion Design:** In [63], we adopted a scalable two-stage optimization framework to design the considered system in two consecutive offline and online stages. Given a transmission mode set

generated in the offline stage, we developed two new transmission mode preselection criteria to remove less efficient transmission modes. Simulation results showed that compared to the trial criterion developed in [37], our two new criteria respectively taking into account user fairness and exploiting concrete features of SWIPT systems achieved a better performance.

- **Optimal Solution:** After excluding less efficient transmission modes from the set, we jointly optimized the downlink beamforming and IRS transmission mode selection strategy to minimize the total transmit power at the BS. The resource allocation algorithm design was formulated as a non-convex combinatorial optimization problem taking into account the QoS constraints of both the information decoding receivers and the energy harvesting receivers. To establish a performance upper bound, we developed an enumeration-based optimal scheme by exploiting BnB theory. In particular, we derived upper and lower bounds for the original optimization problem, formulated a node partition rule, and developed a problem branching strategy for the considered problem. The BnB-based algorithm produced the globally optimal solution to the original optimization problem in a finite number of iterations.

- **Suboptimal Solution:** Due to high complexity of the BnB-based algorithm, we capitalized on the penalty method and SCA to develop a low-complexity algorithm at the expense of an acceptable loss in performance. This algorithm asymptotically converged to a local minimum value of the considered problem within a few iterations which makes it attractive for application in practical IRS systems. Simulation results confirmed the close-to-optimal performance of the suboptimal scheme. The flow chart that contains the key steps of the proposed optimal and suboptimal schemes is shown in Fig. 1.10.

Contributions of [77]:

- **IRS-Enabled Secure Communications in Multiuser Systems:** Considering the random nature of wireless channels, traditional security provisioning techniques such as physical layer security may not ensure secure communications, especially in an unfavorable radio propagation environment. To overcome this difficulty, in [77], we proposed to exploit the IRS for physical layer security provisioning in an IRS-assisted communication system. Unlike the works in [69, 82] that focused on IRS-assisted single-user systems, our work in [77] was the first to consider a more general multiuser system and developed a corresponding algorithm that maximized the system sum secrecy rate.

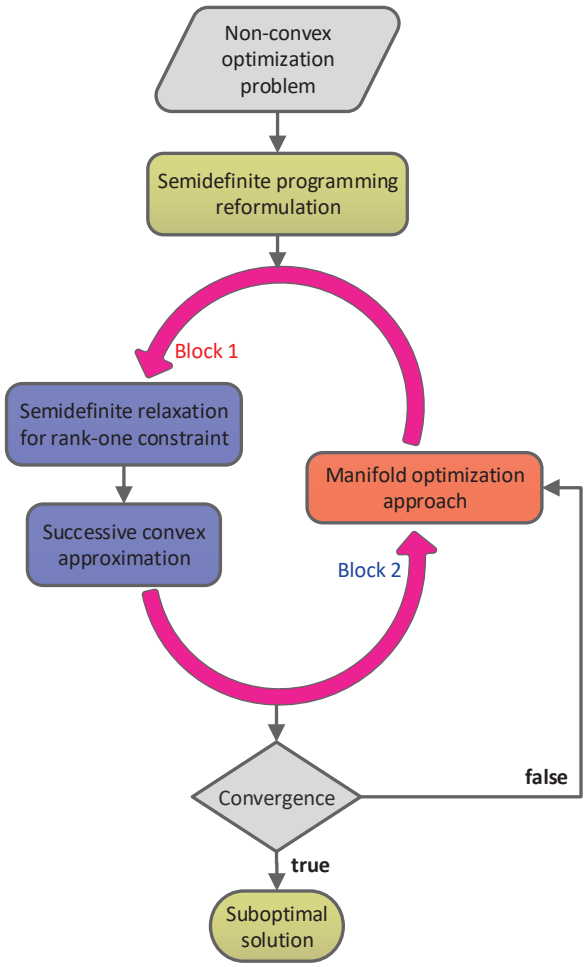

Abbildung 1.11: The flow chart of the resource allocation optimization algorithm developed in [77].

- **Artificial Noise-Enhanced Physical Layer Security:** Although the IRS can be exploited to customize favorable wireless channels, it is still possible that the system sum secrecy rate is low, especially when the eavesdropper has sufficient computational resources to exclude all multiuser interference from the received mixed signal stream. To overcome this shortcoming, in [77], we proposed to utilize artificial noise (AN) at the BS to intentionally demote the quality of the eavesdropper's channel. To this end, we jointly designed the downlink beamformers, the AN covariance matrix, and the reflection matrix at the IRS. Although employing AN did not introduce additional non-convex constraints, it indeed increased the number of the optimization variables and exacerbated the coupling of variables in the optimization problem. This prompted us to attach great importance to computational complexity when designing the optimization algorithm.

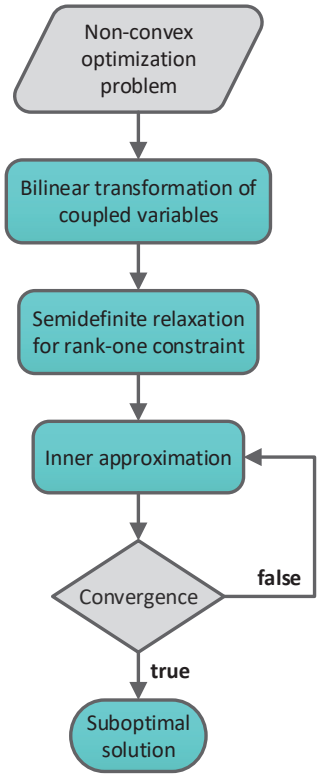

Abbildung 1.12: Flow chart of the resource allocation optimization algorithm proposed in [78].

- **Computationally-Efficient Algorithm:** Due to the unit-modulus constraint and the coupling between the IRS phase-shift pattern and other optimization variables, it was difficult to find the maximum value of the considered optimization problem. As a compromise, we developed a low-complexity suboptimal algorithm that divided the original feasible set into two disjoint subsets and efficiently solved the resulting two subproblems in an alternating manner. In particular, given fixed IRS phase-shift coefficients, we obtained the locally optimal solution of the subproblem involving the other optimization variables by employing SCA and SDR. Then, the phase-shift matrix was updated via the manifold optimization approach for given fixed beamforming vectors and the AN pattern. The overall algorithm was assured to yield a stationary point of the considered optimization problem. Our work [77] was one of the earliest papers that exploited manifold optimization theory to directly tackle the IRS-induced unit-modulus constraint. The flow chart of the developed algorithm is illustrated in Fig. 1.11.

Contributions of [78]:

- **Active IRS-Assisted Green Communications:** Due to the double path loss effect, conventional passive IRS may not be able to provide the desired per-

formance gains for wireless networks. To tackle this obstacle, we proposed to deploy a more powerful IRS, i.e., an active IRS, in a multiuser wireless network and investigated the joint BS beamforming vector and IRS reflection coefficient design to provide satisfactory communication services for multiple users in a power-efficient manner. Simulation results showed that although active IRSs required an extra power supply, they did further boost the energy efficiency of the considered system compared to a conventional passive IRSs. Moreover, we also revealed that active IRSs could effectively mitigate the double path loss effect and facilitate IRS-assisted green communications. Our work [78] was one of the earliest papers that proposed to employ active IRSs to enhance the performance of wireless networks and developed a corresponding efficient resource allocation algorithm.

- **Bilinear Transformation-based Low-Complexity Algorithm:** Different from passive IRSs that can merely adjust the phase of the impinging signals, active IRSs introduce extra DoFs by varying the magnitude of the impinging signals. This is realized by jointly designing the amplification factor and the phase-shift coefficient of the active IRSs subject to an additional maximum amplification power constraint. Yet, the multiplicative form of the IRS reflection matrix exacerbates the coupling issue for joint BS and IRS design. In the literature, such variable coupling is usually tackled by employing BCD, i.e., separating the coupled optimization variables into different optimization blocks and solving one block at a time. Yet, such straightforward algorithms compromise the joint optimality of the considered problems. Moreover, rather than developing a stand-alone BCD algorithm, other advanced optimization tools have to be exploited to avoid infeasible solutions. Given the above considerations, in [78], we proposed to exploit a novel bilinear transformation (BT) for efficient algorithm design. In particular, the BT intrinsically sidestepped the variable coupling by regarding the product term of the IRS optimization variables as a new entirety, leading to an equality constraint. Then, this equality constraint was transformed equivalently into two more tractable constraints, i.e., a DC constraint and a positive semidefinite constraint, which could be efficiently tackled by existing approaches such as SCA. By applying the proposed BT-based algorithm, we could find local minima of the considered optimization problem. The flow chart of the developed BT-based algorithm is illustrated in Fig. 1.12.

Kapitel 2

Fundamentals of Mathematical Optimization

In this chapter, we provide some basic information about mathematical optimization theory that we believe can help the readers to better understand our contributions in Appendices B-F. In particular, in Section 2.1, we review some basic concepts and definitions of mathematical optimization, concentrating on the particular role of convex optimization. Yet, in most cases, wireless network design intrinsically results in a non-convex optimization problem. As a result, in Section 2.2, we introduce some optimization techniques that we utilized to tackle the different types of non-convex optimization problems formulated in our works [45, 57, 63, 77, 78], cf. Appendices B-F. We note that, in both sections, we provide only the level of detail that is needed for the scope of this thesis. A comprehensive overview of mathematical optimization can be found in [83].

2.1 Convex Optimization Problems

As a subfield of mathematical optimization, convex optimization, i.e., aiming to minimize a convex function over a convex set, has found numerous applications in a wide range of disciplines such as engineering and economics. Due to their favorable properties (cf. Section 2.1.3), convex optimization problems can be efficiently and optimally solved by employing well-tested algorithms such as the interior-point algorithm [83] or subgradient projection algorithm [84]. Moreover, some standard convex program solvers such as CVX [85] and YALMIP [86] are widely adopted in the resource allocation and system design literature to efficiently solve convex optimization problems. As a result, it is a great advantage if an optimization problem can be formulated or recognized as a convex problem. Therefore, in the following, we review some fundamental aspects of convex optimization.

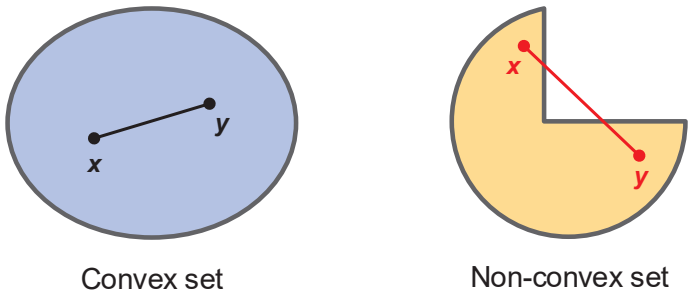

Abbildung 2.1: Illustration of a convex set and a non-convex set. The red-colored and greed-colored curves represent a non-convex function and a convex function, respectively.

2.1.1 Convex Sets

Definition 2.1 (Convex set [83]). *A set $\mathcal{S}$ is convex if, given any two points in $\mathcal{S}$, the line segment that connects the two points also lies in $\mathcal{S}$, i.e., if for any x, $y \in \mathcal{S}$ and $0 \leq \alpha \leq 1$, we have*

$$\alpha x + (1 - \alpha)y \in \mathcal{S}. \tag{2.1}$$

In Fig. 2.1, we show simple examples of convex and non-convex sets in $\mathbb{R}^2$. Note that circles, ellipsoids, Euclidean balls, hypercubes, polygons having interior angles less than 180 degrees, and non-negative orthants are all convex sets. Also, the intersection of an arbitrary number of convex sets is again a convex set. On the other hand, rings or sets of integers are non-convex sets [87].

2.1.2 Convex Functions

Definition 2.2 (Convex Function [83]). *A function $f : \mathcal{X} \to \mathbb{R}$ is convex if its domain $\mathcal{X}$ is a convex set and for any x, $y \in \mathcal{X}$ and $0 \leq \alpha \leq 1$, we have*

$$f(\alpha x + (1 - \alpha)y) \leq \alpha f(x) + (1 - \alpha)f(y). \tag{2.2}$$

This inequality can be interpreted as follows: The line segment that connects the two points $\big(x, f(x)\big)$ and $\big(y, f(y)\big)$ lies above the graph of f, cf. Fig. 2.2. Clearly, all linear and affine functions are convex functions [83]. Throughout this thesis, we denote the sets of non-negative real numbers and positive real numbers by $\mathbb{R}_+$ and $\mathbb{R}_{++}$, respectively. In the following, we provide some examples of convex functions that appear in our works in Appendices B-F.

- **Power function:** For $p \geq 1$ or $p \leq 0$, x^p is convex on $\mathbb{R}_+$ while for $0 \leq p \leq 1$, $-x^p$ is convex on $\mathbb{R}_+$.
- **Exponential function:** For any $a \in \mathbb{R}$, e^{ax} is convex on $\mathbb{R}$.

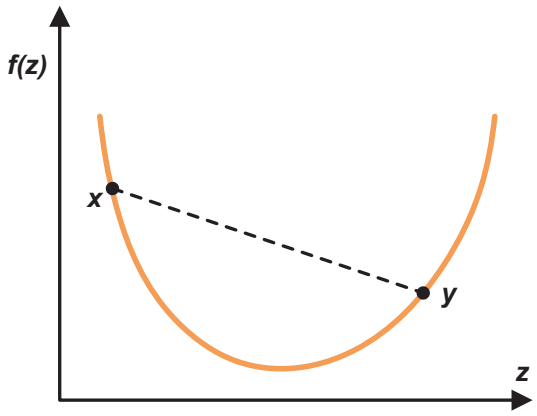

Abbildung 2.2: Illustration of the graph of a convex function. The line that connects any two different points on the graph is always above the graph itself.

- **Logarithmic function:** $-\log(x)$ is convex on $\mathbb{R}_{++}$.
- **Norms:** Every norm on $\mathbb{R}^n$ is convex.
- **Max function:** $f(\mathbf{x}) = \max(x_1, \cdots, x_n)$ is convex on $\mathbb{R}^n$.

Moreover, the non-negative weighted sums of convex functions, the point-wise maximum and supremum of convex functions, and the perspective of a convex function are again convex functions. Besides, if a function f is convex, then $-f$ is a concave function [83].

2.1.3 Convex Optimization

A convex optimization problem in standard form is given by [83]

$$\begin{aligned} \underset{\mathbf{x}}{\text{minimize}} \quad & f(\mathbf{x}) \\ \text{subject to} \quad & g_i(\mathbf{x}) \leq 0, \ i = 1, \cdots, m, \\ & h_i(\mathbf{x}) = 0, \ i = 1, \cdots, p, \end{aligned} \tag{2.3}$$

where

- $\mathbf{x} \in \mathbb{R}^n$ is the variable to be optimized;
- the objective function $f(\mathbf{x}) : \mathbb{R}^n \to \mathbb{R}$ is a convex function;
- the inequality constraint functions $g_i(\mathbf{x}) : \mathbb{R}^n \to \mathbb{R}$, $i = 1, \cdots, m$, are convex functions;
- the equality constraint functions $h_i(\mathbf{x}) : \mathbb{R}^n \to \mathbb{R}$, $i = 1, \cdots, p$, are affine functions.

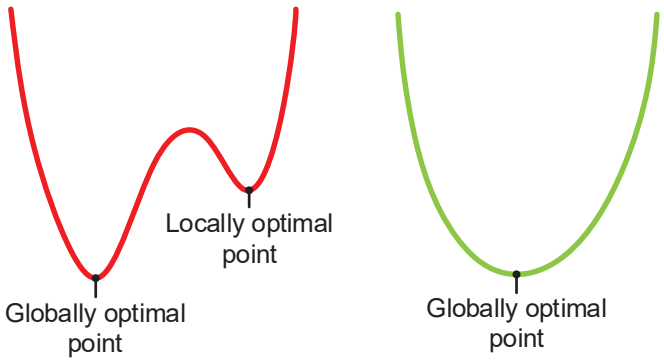

Abbildung 2.3: Illustration of the globally optimal points of convex (green curve) and non-convex (red curve) functions.

In addition, the feasible set of (2.3) is also convex. In other words, we solve a convex optimization problem by minimizing a convex objective function over a convex feasible region. Note that one fundamental property of convex optimization problems is that any locally optimal point is also the globally optimal point, cf. Fig. 2.3.

Next, we briefly introduce some special classes of convex optimization problems, cf. Fig. 2.4, that appear in our works in Appendices B-F.

- **Linear programming problems:** If the objective and constraint functions are all affine functions, the corresponding problem is called a linear programming (LP) problem. A standard LP problem is given as follows

$$\begin{aligned} \underset{\mathbf{x}\in\mathbb{R}^n}{\text{minimize}} \quad & \mathbf{c}^T\mathbf{x} + d \\ \text{subject to} \quad & \mathbf{A}\mathbf{x} \leq \mathbf{b}, \end{aligned} \tag{2.4}$$

  where $\mathbf{c} \in \mathbb{R}^n$, $\mathbf{A} \in \mathbb{R}^{m\times n}$, and $\mathbf{b} \in \mathbb{R}^m$. Besides, constant $d \in \mathbb{R}$ is usually omitted as it has no impact on the solution. In the literature, communication resource allocation algorithm designs such as bandwidth allocation [88] and time slot assignment [89] are usually formulated as LP problems.

- **Quadratic programming problems:** A convex optimization problem is referred to as a quadratic programming (QP) problem if its objective function is quadratic and the constraints are affine or quadratic functions. A standard QP problem is given by [90]

$$\begin{aligned} \underset{\mathbf{x}\in\mathbb{R}^n}{\text{minimize}} \quad & \frac{1}{2}\mathbf{x}^T\mathbf{S}\mathbf{x} + \mathbf{c}^T\mathbf{x} + d \\ \text{subject to} \quad & \mathbf{A}\mathbf{x} \leq \mathbf{b}, \end{aligned} \tag{2.5}$$

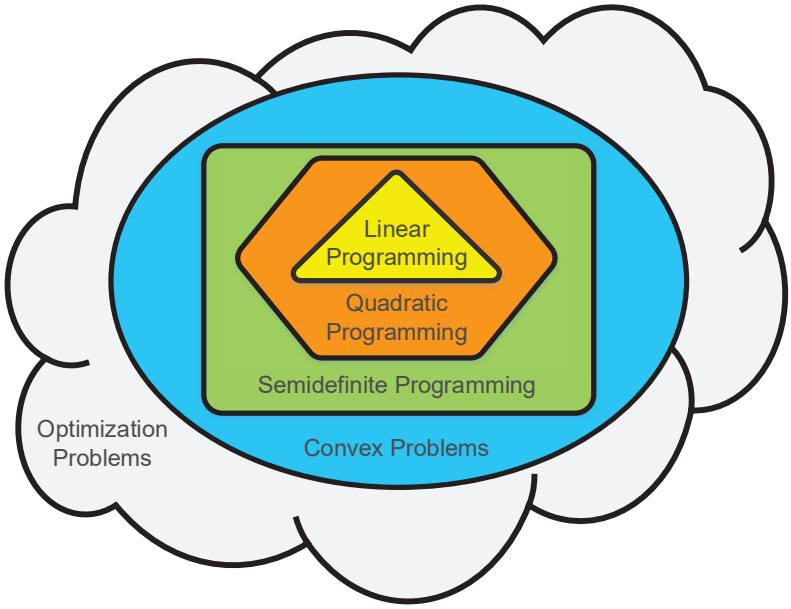

Abbildung 2.4: Illustration of the hierarchy of convex optimization problems.

where $\mathbf{S}$ is an n-dimensional real-valued positive semidefinite matrix. QP is commonly adopted when designing power allocation policies [91, 92] in cellular systems and for UAV trajectory planning in UAV-assisted communication systems [93, 94].

- **Semidefinite programming problems:** A standard semidefinite programming (SDP) problem contains a matrix non-negativity constraint on the variable and a set of linear inequalities, and is given as follows [95]

$$\begin{aligned} \underset{\mathbf{X}}{\text{minimize}} \quad & \text{Tr}(\mathbf{PX}) \\ \text{subject to} \quad & \text{Tr}(\mathbf{QX}) \leq r, \quad \mathbf{X} \succeq \mathbf{0}, \end{aligned} \tag{2.6}$$

where $\mathbf{X} \succeq \mathbf{0}$ indicates matrix $\mathbf{X}$ is an n-dimensional real-valued positive semidefinite matrix. Matrices $\mathbf{P}$ and $\mathbf{Q}$ are also n-dimensional real-valued positive semidefinite matrices and $r \in \mathbb{R}_+$. SDP can be used to obtain optimal beamforming policies in wireless networks [96, 97] or tackle IRS phase-shift design problems in IRS-assisted communication systems [98, 99].

To facilitate efficient optimization algorithm design, the above optimization problems are sometimes transformed into equivalent versions by introducing slack variables [83] or employing epigraph reformulations [87].

2.2 Non-Convex Optimization Techniques

In this section, we explain the basic ideas behind some of the optimization techniques that are adopted in our works in Appendices B-F. In particular, in Sections 2.2.1 and 2.2.2, we introduce SCA and BCD methods, respectively, which can be utilized to tackle non-convex optimization problems efficiently and yield high-quality suboptimal solutions. To obtain a performance benchmark for these suboptimal methods, in Sections 2.2.3 and 2.2.4, we discuss monotonic optimization and BnB approaches, which allow us to directly solve non-convex optimization problems and find the globally optimal solution at the cost of a large amount of computational resources. Note that there is always a complexity-optimality trade-off in resource allocation algorithm design, and we can manipulate this trade-off to satisfy the requirements of different application scenarios.

2.2.1 Successive Convex Approximation Method

When designing wireless networks, system designers always prefer to formulate the resource allocation algorithm design as a convex optimization problem since, in this case, the optimal resource allocation policy can be quickly found. Yet, as more advanced technologies are introduced in wireless communication systems and different wireless resources are to be jointly allocated, system designers are faced with more complicated system models and non-convex resource allocation optimization problems become unavoidable. In most cases, the non-convexity originates from a non-convex objective function or a few non-convex constraints while the remaining functions in the optimization problem are still convex. This observation inspired the development of the SCA method. The basic idea behind the SCA method can be explained as follows: Approximate the involved non-convex functions by tractable convex functions and iteratively solve a sequence of approximated versions of the original problem until convergence. We assume an optimization problem with a non-convex objective function, which is given as follows

$$\begin{aligned} \underset{x\in\mathbb{R}}{\text{minimize}} \quad & f(x) \\ \text{subject to} \quad & g(x) \leq c. \end{aligned} \tag{2.7}$$

Instead of directly solving the above non-convex problem, we construct a surrogate function, e.g., a global overestimator, for the objective function in (2.7) as follows

$$\overline{f}(x) \triangleq f'(x^{(j)})(x - x^{(j)}) \geq f(x), \tag{2.8}$$

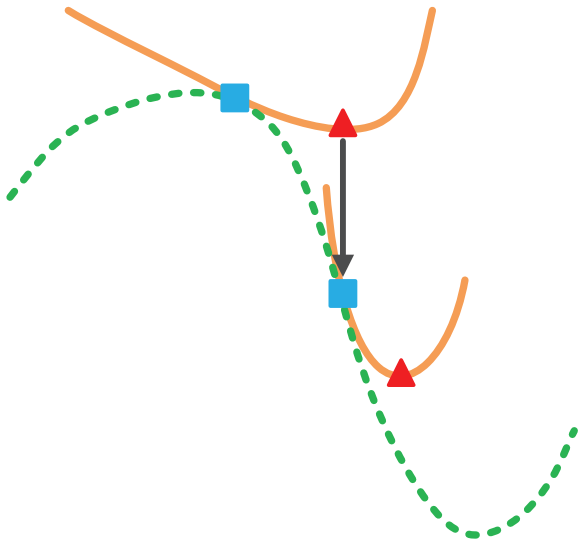

Abbildung 2.5: Illustration of the basic idea behind the SCA algorithm for a minimization problem. The green-colored dashed line and the orange-colored solid line denote the original objective function $f(x)$ and the corresponding overestimators $\overline{f}(x)$, respectively. The blue-colored rectangles and the red-colored triangles denote the feasible points of $f(x)$ and the optimal point of $\overline{f}(x)$, respectively.

where $x^{(j)}$ is a given feasible point and j is the iteration index. Then, in the j-th iteration of the SCA algorithm, an upper bound of the minimization problem in (2.7) can be obtained by solving the following optimization problem

$$\begin{aligned} \underset{x\in\mathbb{R}}{\text{minimize}} \quad & \overline{f}(x) \\ \text{subject to} \quad & g(x) \leq c. \end{aligned} \tag{2.9}$$

By employing the SCA algorithm, the upper bound for (2.7) is gradually tightened. It has been proved in [100] that SCA methods are assured to provide a locally optimal solution to the original problem in (2.7). In Fig. 2.5, we illustrate the basic idea behind the SCA method. In our works [45] and [63], we develop SCA-based algorithms to find locally optimal solutions to the considered optimization problems, cf. Appendices B and D.

2.2.2 Block Coordinate Descent Method

To effectively improve the performance of wireless networks, system designers have to jointly design the available communication resources such as power and bandwidth. Yet, in some wireless communication systems, e.g., IRS-assisted communication systems, the optimization variables such as the IRS phase-shift matrix and the BS beam-

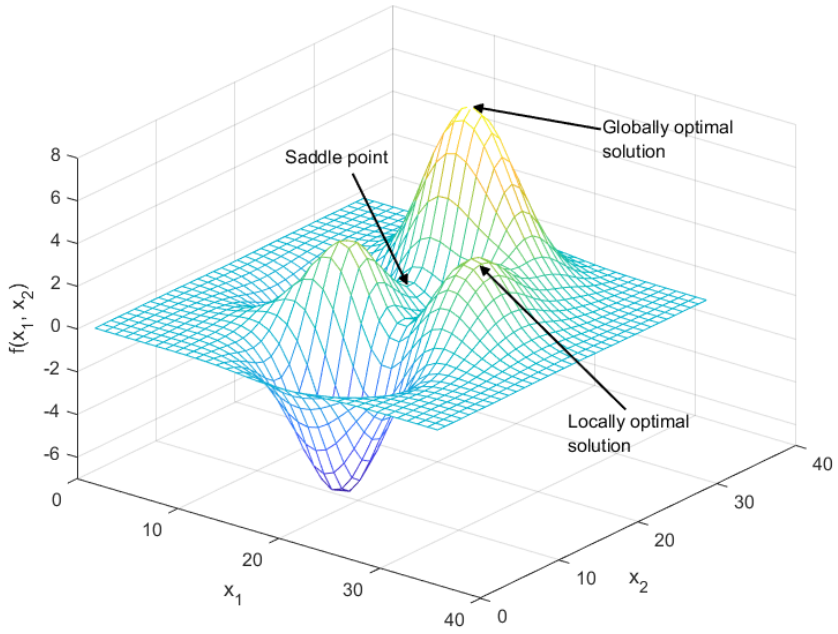

Abbildung 2.6: Illustration of the globally optimal solution, locally optimal solution, and saddle point of a maximization problem to which the BCD-based algorithm potentially converges.

forming vectors appear as a product term in the problem formulation [101]. This inevitably causes a coupling issue for efficient resource allocation algorithm design, which is challenging to handle. An optimization problem containing two coupled optimization variables, x_1 and x_2, is given by

$$\begin{aligned} \underset{x_1,x_2\in\mathbb{R}}{\text{minimize}} \quad & f(x_1,x_2) \\ \text{subject to} \quad & g(x_1,x_2) \leq c. \end{aligned} \tag{2.10}$$

In fact, the joint optimization of the coupled variables x_1 and x_2 results in an intrinsically challenging non-convex problem. To circumvent this difficulty, a widely adopted method is BCD. In particular, instead of directly solving the original optimization problem, the BCD approach divides the coupled optimization variables into disjoint blocks where each block is associated with one subproblem. Then, each subproblem is solved alternately. Hence, the optimization problem in (2.10) can be tackled by solving the following two subproblems in an alternating manner

subproblem 1:

$$\begin{aligned} \underset{x_1 \in \mathbb{R}}{\text{minimize}} \quad & f(x_1|x_2^{(i)}) \\ \text{subject to} \quad & g(x_1|x_2^{(i)}) \leq c. \end{aligned} \tag{2.11}$$

subproblem 2:

$$\begin{aligned} \underset{x_2 \in \mathbb{R}}{\text{minimize}} \quad & f(x_2|x_1^{(i)}) \\ \text{subject to} \quad & g(x_2|x_1^{(i)}) \leq c. \end{aligned} \tag{2.12}$$

where $x_1^{(i)}$ and $x_2^{(i)}$ represent the feasible solutions in the i-th iteration of the BCD algorithm. In particular, in the i-th iteration, we solve for x_1 or x_2 with the other variable fixed. According to [102], the BCD algorithm is guaranteed to converge to a stationary point of the original optimization problem. However, since the BCD method destroys the joint optimality of the original optimization problem, the resulting stationary points can be the globally optimal solution, locally optimal solutions, or saddle points. In Fig. 2.6, we consider a maximization problem involving two coupled optimization variables and show the aforementioned points that can be obtained by employing the BCD algorithm. In fact, both the optimization order of the blocks and the initial points have an impact on the value to which the BCD algorithm converges. In our works [57] and [77], we develop BCD algorithms to find suboptimal solutions to the considered optimization problems, cf. Appendices C and E.

2.2.3 Monotonic Optimization Approach

Although many resource allocation optimization problems have a non-convex nature, they do preserve monotonicity, i.e., the objective function is monotonically increasing or decreasing with respect to the optimization variables over the feasible set [103]. Hence, one can exploit this property to iteratively reduce an upper bound on the objective function until the optimum is obtained. A standard form monotonic optimization problem is given as follows [104]

$$\begin{aligned} \underset{\mathbf{x} \in \mathbb{R}_+^n}{\text{maximize}} \quad & f(\mathbf{x}) \\ \text{subject to} \quad & \mathbf{x} \in \mathcal{G}, \end{aligned} \tag{2.13}$$

where $f(\mathbf{x}) : \mathbb{R}_+^n \to \mathbb{R}$ is an increasing function of $\mathbf{x}$. More mathematical preliminaries on monotonic optimization can be found in Appendix B. Moreover, $\mathbf{x}$ belongs to a normal set $\mathcal{G}$, i.e., for any $\mathbf{x} \in \mathcal{G}$ the set $[\mathbf{0}, \mathbf{x}] \subseteq \mathcal{G}$. The above monotonic optimization problem can be optimally solved by employing advanced monotonic optimization

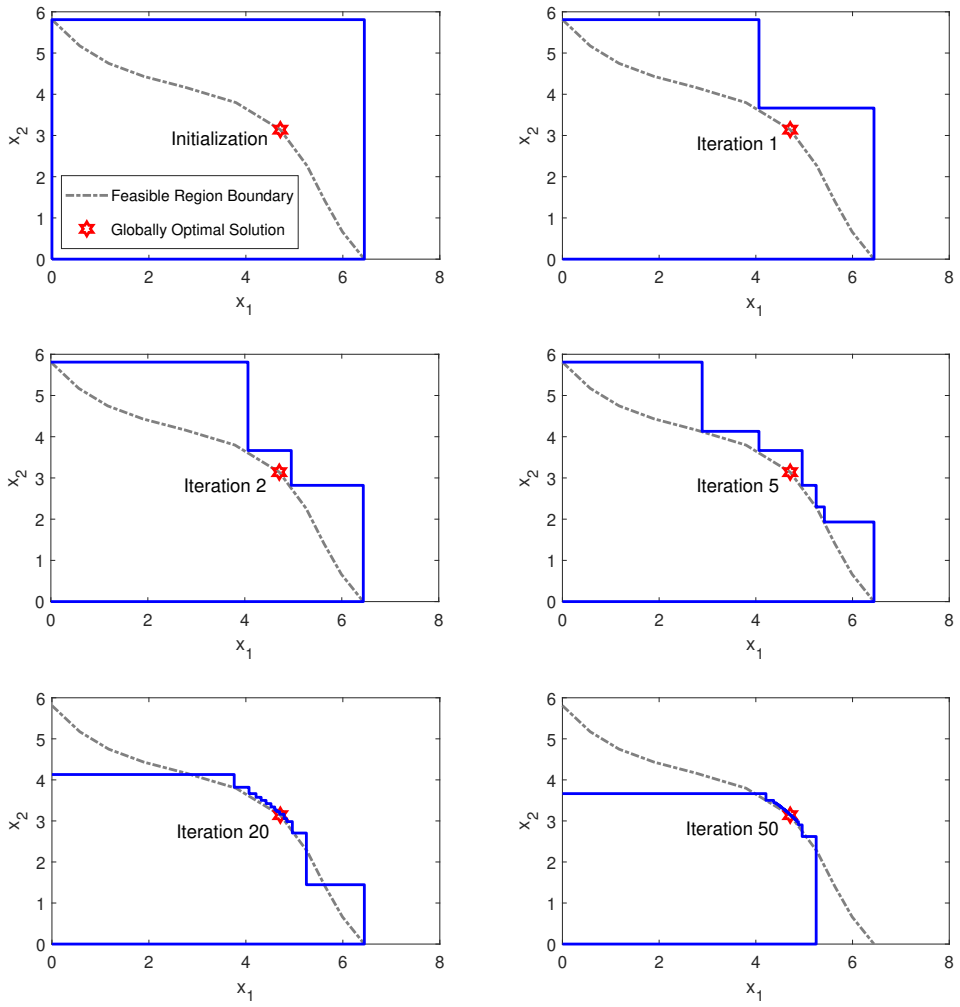

Abbildung 2.7: Illustration of a few snapshots of the polyblock outer approximation algorithm to produce the optimum of a monotonic optimization problem involving two optimization variables x_1 and x_2. The blue-colored polyblock encloses the feasible set of the monotonic optimization problem and the dashed line denotes the boundary of the feasible set. The red-colored star denotes the globally optimal solution to the considered problem.

algorithms, e.g., the two-layer polyblock outer approximation algorithm [104, 105]. In particular, a polyblock $\mathcal{P}$ that contains the feasible set $\mathcal{G}$ is constructed and an upper bound of the objective function can be calculated based on the vertex of $\mathcal{P}$. Then, in the outer layer of the algorithm, the block $\mathcal{P}$ is successively pruned by removing a cone from the non-negative orthant over iterations. Since it is difficult to characterize the whole feasible set $\mathcal{G}$, a bisection projection search is implemented in the inner layer of the algorithm to find the projection of a vertex on the upper bounda-

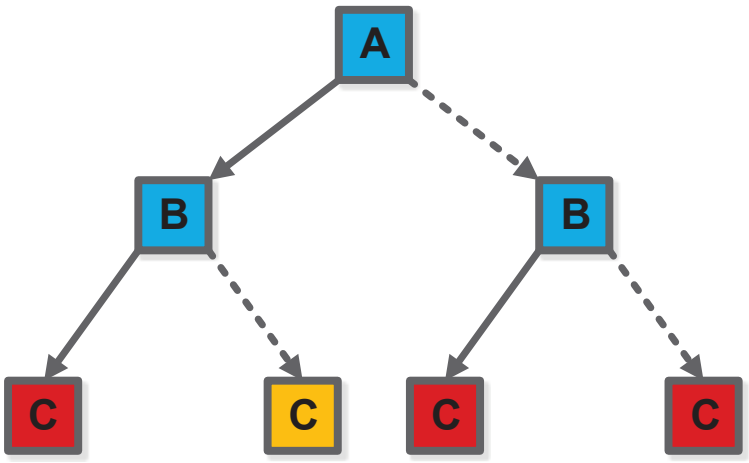

Abbildung 2.8: Illustration of a BnB-based tree structure for solving a BIP problem involving two binary optimization variables. The solid-line arrows and dashed-line arrows denote the two cases where the optimization variable is set to 0 and 1, respectively. The yellow-colored and red-colored nodes denote the optimal and non-optimal solutions to the BIP problem, respectively.

ry of the feasible set. We terminate the two-layer algorithm if the gap between the vertex of the current $\mathcal{P}$ and its projection on the upper boundary of $\mathcal{G}$ is smaller than a pre-defined threshold. It has been proved in [104] that this two-layer iterative algorithm always terminates at the optimum of the considered problem. Yet, the computational complexity of such an algorithm increases exponentially with the number of optimization variables. In the literature, monotonic optimization has been shown to be a promising means for revealing a performance upper bound for UAV-assisted communication systems [40] and NOMA systems [68]. An example of the polyblock outer approximation algorithm is given in Fig. 2.7. Note that although the feasible region of the considered two-variable optimization problem is a non-convex set, the polyblock outer approximation algorithm finds the optimum after sequentially shrinking the polyblock for roughly 50 times. A monotonic optimization-based algorithm is developed in our contribution [45] to determine a performance upper bound of the considered system, cf. Appendix B.

2.2.4 Branch-and-Bound Approach

In the literature, some resource allocation designs such as user scheduling and subcarrier assignment involve integer optimization variables [92], leading to non-convex

binary integer programming (BIP) problems. In particular, a BIP problem involves a discrete feasible set and is given as follows

$$\begin{aligned} \underset{\mathbf{x}}{\text{minimize}} \quad & f(\mathbf{x}) \\ \text{subject to} \quad & \mathbf{x} \in \{0,1\}^n . \end{aligned} \tag{2.14}$$

The binary feasible set makes the optimization problem intrinsically non-convex. To tackle such a difficulty, some works proposed to directly relax the discrete feasible set into a continuous set, i.e., replacing $\{0,1\}^n$ by $[0,\ 1]^n$. Yet, by doing this, the resulting solution is likely to be an infeasible solution to the original optimization problem [106]. Alternatively, one may transform the binary constraint into the following equivalent constraints

$$0 \leq x_i \leq 1,\ i = 1, \cdots, n, \tag{2.15}$$

$$\sum_{i=1}^{n} x_i - x_i^2 \leq 0. \tag{2.16}$$

However, the inequality constraint in (2.16) is a non-convex DC constraint, which is still an obstacle for optimal resource allocation algorithm design. Given the above considerations, the BnB approach has emerged as an effective means to find the optimum of the optimization problem in (2.14). The essential idea behind BnB algorithms is to implement a tree expansion by repeatedly employing three steps, i.e., partitioning, branching, and bounding, until the optimal solution is acquired [107]. Initially, we map the feasible set of the original problem onto the root node of the search tree. For a given partitioning rule, we split each node into two subnodes, where each subnode represents a subset of the feasible set of the original problem. Accordingly, we formulate two subproblems and optimize each subproblem over a given feasible set associated with a subnode. Then, we compute the objective function value of each subproblem and construct both an upper bound and a lower bound for the original optimization problem. A subnode is removed from the tree if its objective function value is larger than the upper bound (for minimization problems) or smaller than the lower bound (for maximization problems). As the search tree continues to expand, the original feasible set is progressively divided into more subsets. In each iteration, we check the objective function values of each subproblem associated with a subnode and update the current bounds. The above procedure is repeated until there is a negligible difference between the upper bound and the lower bound. It has been proved in [108] that as long as the number of optimization variables is finite, the BnB algorithm is assured to converge to the optimal value of the considered optimization problem in

a limited number of iterations. In Fig. 2.8, we illustrate a three-tier search tree of a BnB algorithm developed for a BIP problem involving 2 binary optimization variables. In fact, to find the optimal values of n binary optimization variables, we need to construct an $(n+1)$-tier search tree comprising at most 2^n subnodes in the last tier. A BnB algorithm is proposed in our contribution [63] to solve the considered optimization problem optimally in a limited number of iterations, cf. Appendix D.

Kapitel 3

Conclusions and Future Research Directions

3.1 Conclusions

UAV and IRS are both promising enablers for future high-data rate communication systems. Although their operational mechanisms are completely different, they both provide additional DoFs for resource allocation design, which can be utilized to create favorable wireless links to enhance system performance. Because of their ability to modify the wireless channels, both techniques can be exploited to provide customized services for dedicated users, which is a new key element for wireless network design. In this dissertation, we investigated the resource allocation algorithm design for UAV communication systems and IRS-assisted communication systems. In particular, in Chapter 1, we provided a general overview of our contributions in the larger context of resource allocation design for UAV- and IRS-assisted system. In Chapter 2, fundamental convex optimization concepts and key optimization tools required to understand the author's contributions were discussed. Our contribution focused on UAV communications in uncertain environments, IRS-assisted FD CR networks, large IRS-assisted SWIPT systems, secure passive IRS-assisted systems, and active IRS-assisted systems, and are reprinted in Appendices B, C, D, E, and F, respectively. In the following, we summarize the main takeaways from our contributions and the key findings of this dissertation.

UAV Communications in Uncertain Environments: In our contribution [45], Appendix B, we proposed to employ a rotary-wing UAV-based flying BS to provide reliable communication services for a set of ground user devices in an uncertain environment with practical polygon NFZs. To this end, we modeled the UAV body jittering, user location estimation error, randomness of wind gusts, and polygon NFZs. Then, we jointly optimized the 2-D velocity and beamforming policy for minimization of the total UAV power consumption while meeting the QoS constraints of the

ground devices. The performance cap of the considered system was revealed by a monotonic optimization-based optimal algorithm while an SCA-based low-complexity algorithm was developed to facilitate the real-time online design of the UAV system. Our simulations results showed that: 1) for both the optimal and suboptimal schemes, the UAV consumes significantly less power compared to that for non-robust schemes and two low-complexity benchmark schemes; 2) the body jittering and the imperfect knowledge of the user location has to be carefully considered to facilitate reliable communications for practical UAV systems; 3) by exploiting the available information on the wind speed, we can control the UAV to fly along the desired trajectory in a power-efficient manner; 4) in the presence of NFZs and under strong wind conditions, it is of utmost importance to develop robust resource allocation algorithms for the safe operation of UAVs.

IRS-Assisted FD CR Networks: In our contribution [57], Appendix C, we proposed to deploy an IRS in an FD CR network and exploited the programmablity of the IRS to combat the severe interference in the considered system. To this end, we jointly optimized the downlink and uplink beamforming policy at the FD BS, the IRS reflection coefficients, and the transmit power of the uplink users for maximization of the spectral efficiency of the secondary network. To tackle the variable coupling in the formulated problem, we divided the original feasible set into three disjoint subsets where each subset was associated with a subproblem. Exploiting BCD optimization theory, we efficiently solved the three subproblems in an alternating manner. The proposed BCD-based algorithm produced an efficient suboptimal solution to the considered problem. Via simulations, we showed that: 1) the proposed scheme significantly outperforms four considered baseline schemes in terms of system spectral efficiency; 2) to achieve the performance gains introduced by IRSs, system designers have to take into account the CSI uncertainty of the PUs for robust IRS-assisted FD CR system design; 3) by jointly designing the IRS with the other components of FD CR networks, the severe interference in FD CR systems can be effectively suppressed.

Large IRS-Assisted SWIPT Systems: In our contribution [63], Appendix D, we considered a SWIPT system assisted by a practically large IRS and adopted a realistic sigmoidal function-based EH model and a physics-based IRS model. To facilitate efficient real-time design for the considered system, we adopted a novel scalable two-stage design framework consisting of an offline pre-design stage and an online optimization stage. Specifically, for a given transmission mode set generated offline, we developed two novel transmission mode pre-selection criteria to wisely exclude unfavorable candidates from the set. Subsequently, we designed the optimal transmission mode selection and beamforming policy for the considered system via online optimization to minimize the total transmit power. The performance upper bound of

the considered system was revealed by a BnB-based enumeration algorithm. We also developed an SCA-based iterative algorithm to tackle the formulated combinatorial optimization problem in polynomial time. Our simulation results showed that: 1) the proposed schemes significantly reduce the required transmit power consumption compared to three baseline schemes with simpler implementation; 2) the low-complexity SCA-based algorithm achieves a near-optimal performance with a low computational complexity; 3) the scalable optimization framework and the developed algorithms enable us to flexibly manipulate the tradeoff between complexity and performance as needed for different IRS application scenarios.

Secure Passive IRS-Assisted Systems: In our contribution [77], Appendix E, we proposed to exploit IRSs and AN to improve the physical layer security of a multiuser MISO system. In particular, we jointly optimized the active beamforming vectors, the AN covariance matrix, and the IRS passive beamforming matrix for maximization of the system sum secrecy rate. Capitalizing on SCA and manifold optimization methods, we developed a polynomial time alternating optimization algorithm and determined a high-quality solution to the formulated non-convex problem. Our simulation results revealed that: 1) the proposed scheme can substantially improve the system secrecy performance compared to two baseline schemes with partially fixed resource allocation policies; 2) the location of the IRS has to be carefully chosen to reduce the detrimental double path loss effect.

Active IRS-Assisted Systems: In our contribution [78], Appendix F, we proposed to exploit the active IRS in a multiuser communication system to effectively compensate for the double path loss effect-induced performance loss. To this end, we jointly designed the BS beamformers and the IRS reflection coefficients to facilitate green communications in the considered system. To tackle the non-convex optimization problem complicated by coupled optimization variables, we resorted to a novel bilinear transformation to preserve joint optimality and developed an efficient algorithm that is guaranteed to converge to a locally optimal solution to the considered problem. Simulation results showed that: 1) the proposed scheme can significantly lower the required transmit power compared to two baseline schemes; 2) active IRSs outperform conventional passive IRSs in terms of energy efficiency and are promising means to extenuate the disadvantageous double fading effect when employing IRSs in wireless networks.

3.2 Topics for Future Research

In the following, we discuss potential directions for future research that are related to the contribution chapters of this dissertation.

- **UAV Communications:** For UAV communications, the following future research directions are attractive.
  - *Optimization Framework for Swarm UAV Systems:* Due to the high mobility and low cost, a large number of UAVs can be deployed in conventional wireless networks and collaborate with each other to accomplish sophisticated and demanding tasks. To this end, various types of constraints have to be taken into account for swarm UAV system design [109]. First, kinetic constraints and power constraints should be imposed on the UAV trajectory design to facilitate power-efficient UAV communications. Second, geometrical constraints such as NFZs or safe regions should be incorporated in the corresponding design problem to ensure secure and safe communications. Third, to provide ubiquitous and sustainable communication services, system designers may also have to account for other practical issues such as UAV charging and maintenance. As a result, more efficient and comprehensive optimization frameworks are needed to support real-time swarm UAV communications.
  - *Deep Learning-Based UAV Communication Systems:* In the literature on UAV communications, most works adopted a remote control UAV or a UAV with a pre-designed trajectory. However, these mechanisms either require a human operator or may not be adaptive to the quickly varying radio propagation environment. To fully exploit the high maneuverability of the UAV, one can employ deep learning theory to develop an adaptive optimization framework to support autonomous UAVs [110]. In particular, based on field measurement data, a decision-making optimization framework can be established by training artificial neural networks. How to apply deep learning techniques to achieve fully autonomous UAV-enabled adaptive communications is an attractive topic for future research.
- **IRS-Assisted Communications:** For IRS-assisted communications, the following future research topics are of interest.
  - *Resource Allocation Algorithm Design for INW-Based IRS Systems:* Compared to IDS-based or active IRS models, the INW-based IRS model provides additional DoFs for IRS design which can further enhance system performance without consuming additional amplification power [61]. Yet, due to the INW model-induced intractable constraints, the corresponding resource allocation algorithm design for a multiuser communication system is still an open problem. Developing the optimal algorithm to reveal

a performance benchmark for the INW-based IRS model or suboptimal algorithms to facilitate efficient design for practical INW-based IRS-assisted systems are interesting research directions.

– *Frequency-Dependent Response Model for IRSs:* Most of the works in the literature assumed that the IRS response is identical for EM waves having different frequencies. This assumption is in general valid for the sub-6 GHz frequency band. Yet, for future wireless networks where the carrier frequency can be in the mmWave or terahertz frequency ranges, this assumption may no longer be valid, cf. [27]. Hence, to effectively release the full potential of IRSs in future wireless networks, it is necessary to exploit data acquired in field measurements and develop a new IRS model to capture the impact of the frequency of the impinging waves on the IRS phase responses.

– *Optimization Framework Design for Multifunctional IRSs:* Due to the development of advanced meta-materials, meta-surface elements become gradually empowered with more functionalities such as wave absorption, refraction, and beam separation [111]. Moreover, due to the sub-wavelength size and the low cost of meta-surface elements, the designers can integrate different kinds of meta-surface elements into one single IRS to satisfy the requirements of different application scenarios. Yet, for such multifunctional IRSs, it is necessary to modify the existing design frameworks to support the development of more flexible resource allocation algorithms taking into account additional design dimensions such as different operational modes and the number of elements. This is an attractive research direction to facilitate the application of more powerful IRSs in future wireless networks.

Anhang A

Author's Publication List

During his doctoral program, the author has published the following papers as first author. Publications which are used as part of this dissertation are marked by "∗".

- **Journal Publications:**

  [1] ∗ **D. Xu**, V. Jamali, X. Yu, D. W. K. Ng, and R. Schober, "Optimal resource allocation design for large IRS-assisted SWIPT systems: A scalable optimization framework," *IEEE Trans. Commun.*, vol. 70, no. 2, pp. 1423-1441, Feb. 2022. [Google scholar citations: 10]

  [2] ∗ **D. Xu**, X. Yu, Y. Sun, D. W. K. Ng, and R. Schober, "Resource allocation for IRS-assisted full-duplex cognitive radio systems," *IEEE Trans. Commun.*, vol. 68, no. 12, pp. 7376-7394, Dec. 2020. [Google scholar citations: 117]

  [3] ∗ **D. Xu**, Y. Sun, D. W. K. Ng, and R. Schober, "Multiuser MISO UAV communications in uncertain environments with no-fly zones: robust trajectory and resource allocation design," *IEEE Trans. Commun.*, vol. 68, no. 5, pp. 3153-3172, May 2020. [Google scholar citations: 78]

- **Conference Publications:**

  [1] ∗ **D. Xu**, X. Yu, D. W. K. Ng, and R. Schober, "Resource allocation for active IRS-assisted multiuser communication systems," in *Proc. Asilomar Conf. on Signals, Systems, and Computers*, Pacific Grove, CA, USA, Oct. 2021, pp. 113-119. [Google scholar citations: 10]

  [2] **D. Xu**, X. Yu, V. Jamali, D. W. K. Ng, and R. Schober, "Resource allocation for large IRS-assisted SWIPT systems with non-linear energy harvesting model," in *Proc. IEEE Wireless Commun. Netw. Conf. (WCNC)*, Nanjing, China, Mar. 2021, pp. 1-7. [Google scholar citations: 22]

[3] **D. Xu**, X. Yu, and R. Schober, "Resource allocation for intelligent reflecting surface-assisted cognitive radio networks," in *Proc. IEEE Int. Workshop Signal Process. Adv. Wireless Commun. (SPAWC)*, Atlanta, GA, USA, May 2020, pp. 1-5. [Google scholar citations: 30]

[4] $*$ **D. Xu**, X. Yu, Y. Sun, D. W. K. Ng, and R. Schober, "Resource allocation for secure IRS-assisted multiuser MISO systems," in *Proc. IEEE Global Commun. Conf. Wkshps.*, Waikoloa, HI, USA, Dec. 2019, pp. 1-6. [Google scholar citations: 119]

[5] **D. Xu**, Y. Sun, D. W. K. Ng, and R. Schober, "Robust resource allocation for UAV systems with UAV jittering and user location uncertainty," in *Proc. IEEE Global Commun. Conf. Wkshps.*, Abu Dhabi, United Arab Emirates, Dec. 2018, pp. 1-6. [Google scholar citations: 22]

During his doctoral program, the author has contributed to the following papers.

- **Journal Publications:**

  [**1**] Z. Ding, **D. Xu**, R. Schober, and H. V. Poor, "Hybrid NOMA offloading in multi-user MEC networks," *IEEE Trans. Wireless Commun.*, vol. 21, no. 7, pp. 5377-5391, Jul. 2022.

  [**2**] X. Yu, V. Jamali, **D. Xu**, D. W. K. Ng, and R. Schober, "Smart and reconfigurable wireless communications: From IRS modeling to algorithm design," *IEEE Wirel. Commun.*, vol. 2, no. 6, pp. 118-125, Dec. 2021.

  [**3**] X. Yu, **D. Xu**, D. W. K. Ng, and R. Schober, "IRS-assisted green communication systems: Provable convergence and robust optimization," *IEEE Trans. Commun.*, vol. 69, no. 9, pp. 6313-6329, Sept. 2021.

  [**4**] X. Yu, **D. Xu**, Y. Sun, D. W. K. Ng, and R. Schober, "Robust and secure wireless communications via intelligent reflecting surfaces," *IEEE J. Sel. Areas Commun., Special Issue on Wireless Networks Empowered by Reconfigurable Intelligent Surfaces*, vol. 38, no. 11, pp. 2637-2652, Nov. 2020.

  [**5**] Y. Sun, **D. Xu**, D. W. K. Ng, L. Dai, and R. Schober, "Optimal 3D-trajectory design and resource allocation for solar-powered UAV communication systems," *IEEE Trans. Commun.*, vol. 67, no. 6, pp. 4281-4298, Jun. 2019. [Received **2022 IEEE Communications Society Stephen O. Rice Prize**]

- **Conference Publications:**

  [**1**] X. Yu, **D. Xu**, D. W. K. Ng, and R. Schober, "Power-efficient resource allocation for multiuser MISO systems via intelligent reflecting surfaces," in *Proc. IEEE Global Commun. Conf. (GLOBECOM)*, Taiwan, Dec. 2020, pp. 1-6.

  [**2**] X. Yu, **D. Xu**, and R. Schober, "Optimal beamforming for MISO communications via intelligent reflecting surfaces," in *Proc. IEEE Int. Workshop Signal Process. Adv. Wireless Commun. (SPAWC)*, Atlanta, GA, USA, May 2020, pp. 1-5.

  [**3**] X. Yu, **D. Xu**, and R. Schober, "Enabling secure wireless communications via intelligent reflecting surfaces," in *Proc. IEEE Global Commun. Conf. (GLOBECOM)*, Waikoloa, HI, USA, Dec. 2019, pp. 1-6. [Received **2019 IEEE Communications Society GLOBECOM Best Paper Award**]

[**4**] X. Yu, **D. Xu**, and R. Schober, "MISO wireless communication systems via intelligent reflecting surfaces," in *Proc. IEEE/CIC Int. Conf. Commun. China (ICCC)*, Changchun, China, Aug. 2019, pp. 735-740.

[**5**] Y. Sun, D. W. K. Ng, **D. Xu**, L. Dai, and R. Schober, "Resource allocation for solar powered UAV communication systems," in *Proc. IEEE Int. Workshop Signal Process. Adv. Wireless Commun. (SPAWC)*, Kalamata, Greece, Jun. 2018, pp. 1-5.

Anhang B

Publication 1

[J1] **D. Xu**, Y. Sun, D. W. K. Ng, and R. Schober, "Multiuser MISO UAV communications in uncertain environments with no-fly zones: robust trajectory and resource allocation design," *IEEE Trans. Commun.*, vol. 68, no. 5, pp. 3153-3172, May 2020.[1]

[1]© 2020 IEEE. Reprinted, with permission, from D. Xu, Y. Sun, D. W. K. Ng, and R. Schober, "Multiuser MISO UAV communications in uncertain environments with no-fly zones: robust trajectory and resource allocation design," *IEEE Trans. Commun.*, May 2020.

Multiuser MISO UAV Communications in Uncertain Environments With No-Fly Zones: Robust Trajectory and Resource Allocation Design

Dongfang Xu, *Student Member, IEEE*, Yan Sun, *Member, IEEE*, Derrick Wing Kwan Ng, *Senior Member, IEEE*, and Robert Schober, *Fellow, IEEE*

***Abstract*— In this paper, we investigate robust resource allocation algorithm design for multiuser downlink multiple-input single-output (MISO) unmanned aerial vehicle (UAV) communication systems, where we account for the various uncertainties that are unavoidable in such systems and, if left unattended, may severely degrade system performance. We jointly optimize the two-dimensional (2-D) trajectory and the transmit beamforming vector of the UAV for minimization of the total power consumption. The algorithm design is formulated as a non-convex optimization problem taking into account the imperfect knowledge of the angle of departure (AoD) caused by UAV jittering, user location uncertainty, wind speed uncertainty, and polygonal no-fly zones (NFZs). Despite the non-convexity of the optimization problem, we solve it optimally by employing monotonic optimization theory and semidefinite programming relaxation which yields the optimal 2-D trajectory and beamforming policy. Since the developed optimal resource allocation algorithm entails a high computational complexity, we also propose a suboptimal iterative low-complexity scheme based on successive convex approximation to strike a balance between optimality and computational complexity. Our simulation results reveal not only the significant power savings enabled by the proposed algorithms compared to two baseline schemes, but also confirm their robustness with respect to UAV jittering, wind speed uncertainty, and user location uncertainty. Moreover, our results unveil that the joint presence of wind speed uncertainty and NFZs has a considerable impact on the UAV trajectory. Nevertheless, by counteracting the wind speed uncertainty with the proposed robust design, we can simultaneously minimize the total UAV power consumption and ensure a secure trajectory that does not trespass any NFZ.**

***Index Terms*— Robust trajectory design, multi-antenna UAV, UAV communication systems, no-fly zones, aerodynamic power consumption, disjunctive programming, monotonic optimization.**

I. Introduction

UNMANNED aerial vehicle (UAV) based wireless communication systems have received considerable attention as a promising approach for offering real-time high data-rate communication services [1]– [8]. Compared to conventional cellular systems relying on a fixed terrestrial infrastructure, UAV-assisted communication systems can provide on-demand connectivity by flexibly deploying UAV-mounted wireless transceivers over a target area. For instance, in the case of natural disasters and major accidents, UAVs can be employed as aerial base stations to establish temporary communication links in a timely and cost-effective manner. Moreover, due to their high mobility and maneuverability, UAVs can adapt their trajectories based on the actual environment and terrain which improves system performance [4]. As a result, UAV-assisted communication systems have drawn significant attention from both academia and industry. For instance, the authors of [5] studied suboptimal UAV trajectory design for maximization of the energy-efficiency of UAV communication systems. The authors of [6] proposed a suboptimal joint trajectory, power allocation, and user scheduling algorithm for maximization of the minimum user throughput in multi-UAV systems. Secure UAV communications was investigated in [7] where the trajectory of a UAV and its transmit power were jointly optimized to maximize the system secrecy rate. The authors of [8] proposed a solar-powered UAV communication system and studied the jointly optimal resource allocation and UAV trajectory design for maximization of the system sum throughput. In fact, the throughput of UAV communication systems can be further improved by equipping multiple antennas at the wireless transceivers [9]. In particular, the authors of [10] studied suboptimal beamforming design and UAV positioning for maximization of the system sum throughput of wireless

Manuscript received October 30, 2019; revised January 15, 2020; accepted January 20, 2020. Date of publication January 29, 2020; date of current version May 15, 2020. Dongfang Xu is supported by the Chinese Scholarship Council (CSC). D. W. K. Ng is supported by funding from the UNSW Digital Grid Futures Institute, UNSW, Sydney, under a cross-disciplinary fund scheme and by the Australian Research Council's Discovery Project (DP190101363). This article was presented in part at the IEEE Globecom 2018 Workshop [1]. The associate editor coordinating the review of this article and approving it for publication was M. J. Hossain. *(Corresponding author: Dongfang Xu.)*

Dongfang Xu and Robert Schober are with the Institute for Digital Communications, Friedrich-Alexander-University Erlangen-Nürnberg (FAU), 91054 Erlangen, Germany (e-mail: dongfang.xu@fau.de; robert.schober@fau.de).

Yan Sun is with Huawei Technologies Co., Ltd., Shanghai 518129, China (e-mail: sunyan49@huawei.com).

Derrick Wing Kwan Ng is with the School of Electrical Engineering and Telecommunications, University of New South Wales, Sydney, NSW 2052, Australia (e-mail: w.k.ng@unsw.edu.au).

Color versions of one or more of the figures in this article are available online at http://ieeexplore.ieee.org.

Digital Object Identifier 10.1109/TCOMM.2020.2970043

UAV relay networks. In [11], the authors studied the jointly suboptimal beamforming and power allocation design for maximization of the achievable rate of a UAV-enabled relaying system. However, the designs in [5]– [8], [10], [11] assume a perfectly stable flight and perfect knowledge of the locations of the users which are overly idealistic assumptions for practical UAV-based communication systems. In practice, the stability of the UAV is impaired by unavoidable body jittering during the flight [12], [13], and in general, perfect knowledge of the user locations cannot be acquired due to the limited accuracy of positioning modules [14]. Since their design is based on idealistic assumptions, the existing resource allocation schemes cannot provide reliable high data-rate communication services in the presence of UAV jittering and user location uncertainty.

In practical UAV communication systems, UAV-mounted transceivers flying in the sky commonly encounter strong wind which leads to non-negligible body jittering [15]. It is reported in [16] that the jittering angles of UAVs can assume values of up to 10 degrees. As a result, the estimation of the angles of departure (AoDs) between the UAV and the ground users becomes inaccurate which leads to increased AoD estimation errors [17]. In fact, the impact of AoD estimation errors cannot be neglected in UAV-based communication systems, especially for multiple-input single-output (MISO) communication systems. In particular, the gain introduced by multiple antennas cannot be fully exploited in the presence of AoD estimation errors. Moreover, as the communication links between the UAV and the ground users are typically line-of-sight (LoS) dominated [18], accurate AoD knowledge is essential for performing efficient beamforming at the UAVs. However, in the presence of AoD estimation errors, UAVs cannot perform accurate beamforming which can degrade the system performance significantly. Moreover, wind also affects the UAV ground speed and alters the planned trajectory, which may cause serious safety issues such as speeding or crashing of UAVs [19]. Therefore, taking into account the impact of wind is of utmost importance for the design of practical UAV communication systems. In addition, the impact of the weather conditions and electromagnetic interference may cause large user location estimation errors [14]. The additional path loss resulting from user location uncertainty may impair the communication links between the UAV and the ground users. Furthermore, the schemes in [5]– [8], [10], [11] do not consider any geometrical constraints on the UAV trajectory, which may be imposed in practical UAV-based communication systems. For example, flying UAVs above areas such as military bases, government agencies, strategic facilities, and civil aviation airports is strictly prohibited [20], [21]. As a result, for security reasons, no-fly zones (NFZs) are commonly imposed on UAVs, which makes the trajectory design for UAV-assisted communications more challenging [22]. To tackle this issue, some initial efforts have been made in the literature [20], [23]. In particular, the authors of [20] proposed a decision-making algorithm based on Dubins path theory to prevent UAVs from cruising over NFZs. The authors in [23] investigated the resource allocation design for UAV-enabled communication systems and proposed an iterative algorithm to maximize the system sum throughput by jointly optimizing the subcarrier allocation policy and the UAV trajectory taking into account NFZs. However, these works assumed cylindrical NFZs which is not always justified. According to [24], practical NFZs can be modeled as polygons, and cylindrical NFZs are only a subcase of polygonal NFZs. Hence, the algorithms developed in [20] and [23] cannot ensure accurate trajectory design for realistic UAV communication systems. Indeed, UAV resource allocation and trajectory optimization taking into account polygonal NFZs results in a disjunctive programming problem [25] which complicates the algorithm design. Furthermore, most of the existing trajectory design and resource allocation algorithms for UAV-assisted communication systems are based on suboptimal solutions of the respective optimization problems [5]– [7], [23], and the performance gap between these algorithms and the optimal solutions is not known. To the best of the authors' knowledge, the optimal joint trajectory and resource allocation algorithm design for multiuser UAV communication systems in the presence of AoD estimation errors, user location uncertainty, wind speed uncertainty, and polygonal NFZs has not been investigated in the literature, yet.

In this paper, we address the aforementioned issues. To this end, the joint trajectory and resource allocation algorithm design for multiuser downlink UAV communication systems is formulated as a non-convex optimization problem for minimization of the total UAV power consumption in each time slot. The problem formulation takes into account the imperfect knowledge of the AoD caused by UAV jittering, wind speed uncertainty, user location uncertainty, polygonal NFZs, and the quality-of-service (QoS) requirements of the users. Although the considered optimization problem is non-convex and difficult to tackle, we solve it optimally by employing monotonic optimization theory [26] and semidefinite programming (SDP) relaxation [27] to obtain the optimal 2-D trajectory and the optimal beamformer. Due to its high computational complexity, the optimal scheme mostly serves as a performance benchmark for low-complexity suboptimal schemes. Therefore, we also develop a low-complexity suboptimal iterative algorithm based on successive convex approximation (SCA) [28], which is shown to achieve a close-to-optimal performance. Our simulation results not only reveal the dramatic power savings enabled by the proposed resource allocation algorithms compared to two baseline schemes but also confirm their robustness with respect to UAV jittering, wind speed uncertainty, and user location uncertainty. Moreover, our results show that the impact of NFZs and wind speed uncertainty on the power consumption of the UAV can be efficiently mitigated by the proposed robust design.

The remainder of this paper is organized as follows. In Section II, we introduce the considered MISO UAV communication system model and formulate the proposed optimization problem. The optimal and suboptimal joint 2-D trajectory and beamforming algorithm designs are provided in Sections III and IV, respectively. In Section V, simulation results are presented, and Section VI concludes the paper.

Notations: In this paper, matrices and vectors are denoted by boldface capital and lower case letters, respectively. $\mathbb{R}^{N\times M}$ and $\mathbb{C}^{N\times M}$ denote the sets of all $N \times M$ real-valued and complex-valued matrices, respectively. $\mathbb{H}^N$ denotes the set of

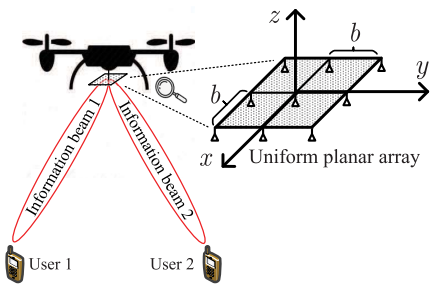

Fig. 1. A multiuser unmanned aerial vehicle (UAV) communication system with one UAV and $K = 2$ users. The UAV is equipped with a 3×3 uniform planar array.

all $N \times N$ Hermitian matrices. $\mathbf{I}_N$ denotes the N-dimensional identity matrix. $|\cdot|$ and $||\cdot||$ represent the absolute value of a complex scalar and the Euclidean norm of a vector, respectively. arcsin and arccos denote the inverse sine and cosine functions, respectively. $\wedge$ and $\vee$ denote the Boolean operations "AND" and "OR", respectively. $\mathbf{x}^T$ and $\mathbf{x}^H$ denote the transpose and conjugate transpose of vector $\mathbf{x}$, respectively. The inequality $\mathbf{x} \leq \mathbf{y}$ of two vectors $\mathbf{x}$, $\mathbf{y} \in \mathbb{R}^N$ holds if $x_i \leq y_i$ for $i = 1, \cdots, N$. $\mathrm{diag}(a_1, \cdots, a_n)$ returns a diagonal matrix with diagonal entries $a_1, \cdots, a_n$. $[\mathbf{A}]_{i,i}$ denotes the (i,i)-entry of matrix $\mathbf{A}$. $\mathrm{Rank}(\mathbf{A})$ and $\mathrm{Tr}(\mathbf{A})$ are the rank and the trace of square matrix $\mathbf{A}$, respectively. $\mathbf{A} \succeq \mathbf{0}$ means matrix $\mathbf{A}$ is positive semidefinite. $\mathbf{A} \otimes \mathbf{B}$ denotes the Kronecker product of two matrices $\mathbf{A}$ and $\mathbf{B}$. $\mathcal{E}\{\cdot\}$ denotes statistical expectation. $x \sim \mathcal{CN}(\mu, \sigma^2)$ indicates that random variable x is circularly symmetric complex Gaussian distributed with mean μ and variance σ^2. $\triangleq$ means "defined as". $\nabla_{\mathbf{x}} f(\mathbf{x})$ denotes the gradient vector of function $f(\mathbf{x})$ with respect to $\mathbf{x}$.

II. System Model and Problem Formulation

In this section, we first discuss the communication system, UAV jittering, wind speed uncertainty, user location uncertainty, polygonal NFZ, and aerodynamic power consumption models. Subsequently, we formulate the proposed optimization problem.

A. Multiuser UAV Communication System

The considered multiuser UAV communication system model comprises one rotary-wing UAV-mounted transmitter and K single-antenna users, indexed $\mathcal{K} \triangleq \{1, \cdots, K\}$, cf. Figure 1. The UAV-mounted transmitter is equipped with $M = M_x M_y$ antennas composing an $M_x \times M_y$ uniform planar array (UPA) [29]. For convenience, we define the set of all antenna elements as $\mathcal{M} \triangleq \{1, \cdots, M\}$. In order to guarantee flight safety, we assume that the UAV flies at a fixed flight altitude[1] H_0 which is higher than the tallest obstacles in the service area [5]– [7]. Moreover, we define $\mathbf{v}_u[n] \triangleq (v_u^x[n], v_u^y[n])$ as the 2-D horizontal velocity of the UAV in time slot n. To facilitate the UAV trajectory algorithm design, we employ the discrete path planning approach [30]. In particular, we discretize the UAV trajectory during the operation time horizon T into N_{T} distinct waypoints, i.e., time horizon T is divided into N_{T} sufficiently small time slots of equal duration $\delta_{\mathrm{T}} = T/N_{\mathrm{T}}$.

In scheduling time slot n, the UAV transmits K independent signals simultaneously to the K users. Specifically, the transmit signal to user k is given by $\mathbf{x}_k[n] = \mathbf{w}_k[n] s_k[n]$, where $s_k[n] \in \mathbb{C}$ and $\mathbf{w}_k[n] \in \mathbb{C}^{M \times 1}$ represent the information symbol for user k and the corresponding beamforming vector in time slot n, respectively. Without loss of generality, we assume $\mathcal{E}\{|s_k[n]|^2\} = 1$.

In this paper, we assume that the air-to-ground communication links between the UAV and the ground users are LoS channels.[2] In particular, the channel vector between the UAV and user k in time slot n is given by [31]

$$\mathbf{h}_k[n] = \sqrt{\varrho}\, \|\mathbf{r}_0[n] - \mathbf{r}_k\|^{-1} \mathbf{a}_k[n], \tag{1}$$

where $\varrho = (\frac{c}{4\pi f_c})^2$ is a constant with c being the speed of light and f_c being the center frequency of the information carrier. $\mathbf{r}_0[n] = (x_0[n],\ y_0[n],\ H_0)$ and $\mathbf{r}_k = (x_k,\ y_k,\ 0)$ denote the 3-D Cartesian coordinates of the UAV in time slot n and user k, respectively. Moreover, $\sqrt{\varrho}\, \|\mathbf{r}_0[n] - \mathbf{r}_k\|^{-1}$ and $\mathbf{a}_k[n] \in \mathbb{C}^{M \times 1}$ are the average channel power gain and the antenna array response (AAR) between the UAV and user k in time slot n, respectively. In particular, the AAR vector is given by [32],

$$\begin{aligned}\mathbf{a}_k[n] = &\big(1, \cdots, e^{-j\frac{2\pi b f_c}{c}\sin\theta_k[n](m_x-1)\cos\varphi_k[n]}, \cdots,\\ &e^{-j\frac{2\pi b f_c}{c}\sin\theta_k[n](M_x-1)\cos\varphi_k[n]}\big)\\ &\otimes \big(1, \cdots, e^{-j\frac{2\pi b f_c}{c}\sin\theta_k[n](m_y-1)\sin\varphi_k[n]}, \cdots,\\ &e^{-j\frac{2\pi b f_c}{c}\sin\theta_k[n](M_y-1)\sin\varphi_k[n]}\big)\\ \triangleq\ &\mathbf{a}\big(\theta_k[n], \varphi_k[n]\big),\end{aligned} \tag{2}$$

where b is the distance between the antenna elements of the UPA, and m_x and m_y index the rows and columns of the UPA, respectively. $\theta_k[n]$ and $\varphi_k[n]$ are the vertical and horizontal AoD of the path between the UAV and user k in time slot n, respectively. The AoDs $\theta_k[n]$ and $\varphi_k[n]$ are functions of the locations of user k and the UAV and are given by

$$\theta_k[n] = \arcsin\frac{H_0}{\|\mathbf{r}_0[n] - \mathbf{r}_k\|} \text{ and } \varphi_k[n] = \arccos\frac{y_0[n] - y_k}{\|\mathbf{r}_0'[n] - \mathbf{r}_k'\|}, \tag{3}$$

respectively. Here, $\mathbf{r}_0'[n] = (x_0[n],\ y_0[n])^T$ contains the horizontal coordinates of the UAV in time slot n, and $\mathbf{r}_k' = (x_k,\ y_k)^T$ contains the horizontal coordinates of user k.

[1] In this paper, we focus on 2-D trajectory optimization and assume that the flight altitude is chosen sufficiently large such that a LoS between the UAV and the ground users is guaranteed. This assumption would not be valid for three dimensional (3-D) trajectory optimization which would lead to an even more challenging design problem. 3-D trajectory optimization in the presence of uncertainty is an interesting topic for future work.

[2] We note that according to field measurements [33], for a UAV with a flight altitude of 100 meters and a cell with a radius of 600 meters, the air-to-ground links between the UAV and the ground users are guaranteed to be LoS channels in rural areas. Besides, depending on the type of terrain and the size of the cells, the flight altitude of the UAV can be adjusted such that the LoS probability of the air-to-ground channel approaches one [34].

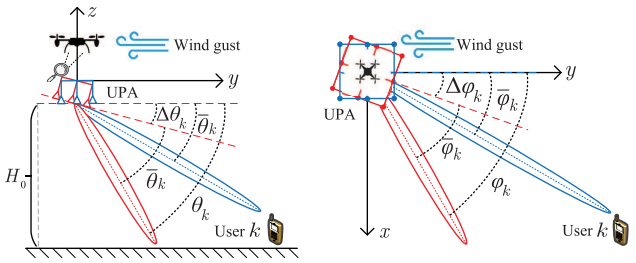

Fig. 2. LoS channel model for the link between an antenna element and user k. The blue beam points to user k, whereas the red beam shows the actual beam direction caused by jittering. The left and right hand side figures illustrate the estimated AoDs $\overline{\theta}_k$ and $\overline{\varphi}_k$, the actual AoDs θ_k and φ_k, and the AoD uncertainty $\Delta\theta_k$ and $\Delta\varphi_k$ in the vertical and horizontal planes, respectively.

The received signal at user k in time slot n is given by

$$d_k[n]=\underbrace{\mathbf{h}_k^H[n]\mathbf{w}_k[n]s_k[n]}_{\text{desired signal}}+\underbrace{\sum_{r\in\mathcal{K}\setminus\{k\}}\mathbf{h}_k^H[n]\mathbf{w}_r[n]s_r[n]}_{\text{multiuser interference}}+n_k[n], \tag{4}$$

where $n_k[n]\sim\mathcal{CN}(0,\sigma_{n_k}^2)$ denotes the additive complex white Gaussian noise (AWGN) at user k in time slot n. Considering (2) and (4), the received signal-to-interference-plus-noise ratio (SINR) of user k in time slot n is given by

$$\Gamma_k[n]=\frac{\frac{\varrho}{\left\|\mathbf{r}_0'[n]-\mathbf{r}_k'\right\|^2+H_0^2}\left|\mathbf{a}_k^H[n]\mathbf{w}_k[n]\right|^2}{\frac{\varrho}{\left\|\mathbf{r}_0'[n]-\mathbf{r}_k'\right\|^2+H_0^2}\sum\limits_{r\in\mathcal{K}\setminus\{k\}}\left|\mathbf{a}_k^H[n]\mathbf{w}_r[n]\right|^2+\sigma_{n_k}^2}. \tag{5}$$

B. UAV Jittering Model

In practice, the stability of the UAV is impacted by the random nature of wind gusts. In particular, in the presence of wind, UAVs suffer from unavoidable body jittering, leading to jittering angles [35]. Impaired by the jittering angles, the onboard sensors of the UAV are unable to accurately measure the AoD between the UAV and the users. Hence, AoD estimation errors occur which leads to imperfect AoD knowledge at the UAV. To capture this effect, we adopt a deterministic model for the resulting AoD uncertainty [9]. Specifically, the AoDs between the UAV and user k in time slot n, i.e., $\theta_k[n]$ and $\varphi_k[n]$, are modeled as:

$$\theta_k[n]=\overline{\theta}_k[n]+\Delta\theta_k[n],\ \varphi_k[n]=\overline{\varphi}_k[n]+\Delta\varphi_k[n],\forall k, \tag{6}$$

$$\Omega_k=\left\{(\theta_k[n],\varphi_k[n])\ \middle|\ e_1(\Delta\theta_k[n])^2+e_2(\Delta\varphi_k[n])^2\leq\alpha^2\right\}, \tag{7}$$

where $(\overline{\theta}_k[n],\overline{\varphi}_k[n])$ and $(\Delta\theta_k[n],\Delta\varphi_k[n])$ represent the estimated AoD between the UAV and user k and the unknown AoD error, respectively, cf. Figure 2. Moreover, $e_1\geq 0$ and $e_2\geq 0$ are parameters for modelling the uncertainty of the horizontal and vertical AoDs, respectively, and continuous set Ω_k contains all possible AoD uncertainties with bounded maximum variation α.

Considering (6), we rewrite the AAR vector as

$$\begin{aligned}\mathbf{a}_k[n]=&\Big(1,\cdots,e^{-\overline{b}\sin\left(\overline{\theta}_k[n]+\Delta\theta_k[n]\right)(m_x-1)\cos\left(\overline{\varphi}_k[n]+\Delta\varphi_k[n]\right)},\\&\cdots,e^{-\overline{b}\sin\left(\overline{\theta}_k[n]+\Delta\theta_k[n]\right)(M_x-1)\cos\left(\overline{\varphi}_k[n]+\Delta\varphi_k[n]\right)}\Big)\\&\otimes\Big(1,\cdots,e^{-\overline{b}\sin\left(\overline{\theta}_k[n]+\Delta\theta_k[n]\right)(m_y-1)\sin\left(\overline{\varphi}_k[n]+\Delta\varphi_k[n]\right)},\\&\cdots,e^{-\overline{b}\sin\left(\overline{\theta}_k[n]+\Delta\theta_k[n]\right)(M_y-1)\sin\left(\overline{\varphi}_k[n]+\Delta\varphi_k[n]\right)}\Big),\end{aligned} \tag{8}$$

where $\overline{b}=\frac{j2\pi bf_c}{c}$. We note that $\mathbf{a}_k[n]$ is a nonlinear function with respect to $\Delta\theta_k[n]$ and $\Delta\varphi_k[n]$, which complicates the robust resource allocation algorithm design. To tackle this issue and since $\Delta\theta_k[n]$ and $\Delta\varphi_k[n]$ are generally small, we approximate $\mathbf{a}_k[n]$ by applying the first order Taylor series expansion. In particular, for given $\overline{\theta}_k[n]$ and $\overline{\varphi}_k[n]$, we have

$$\begin{aligned}\mathbf{a}_k[n]\approx\overline{\mathbf{a}}_k[n]&+\frac{\partial\mathbf{a}_k[n]}{\partial\theta_k[n]}\Big|_{\theta_k[n]=\overline{\theta}_k[n],\varphi_k[n]=\overline{\varphi}_k[n]}\Delta\theta_k[n]\\&+\frac{\partial\mathbf{a}_k[n]}{\partial\varphi_k[n]}\Big|_{\theta_k[n]=\overline{\theta}_k[n],\varphi_k[n]=\overline{\varphi}_k[n]}\Delta\varphi_k[n],\end{aligned} \tag{9}$$

where $\overline{\mathbf{a}}_k[n]\in\mathbb{C}^{M\times 1}$ denotes the AAR estimate of user k given by

$$\overline{\mathbf{a}}_k[n]=\mathbf{a}\big(\theta_k[n],\varphi_k[n]\big)\big|_{\theta_k[n]=\overline{\theta}_k[n],\varphi_k[n]=\overline{\varphi}_k[n]}. \tag{10}$$

For notational convenience, we rewrite the AAR between the UAV and user k in time slot n as

$$\mathbf{a}_k[n]=\overline{\mathbf{a}}_k[n]+\mathbf{D}_k[n]\mathbf{u}_k[n], \tag{11}$$

where $\mathbf{u}_k[n]\triangleq\left[\Delta\theta_k[n],\Delta\varphi_k[n]\right]^T\in\mathbb{R}^2$ and $\mathbf{D}_k[n]\triangleq\left(\frac{\partial\mathbf{a}_k[n]}{\partial\theta_k[n]},\frac{\partial\mathbf{a}_k[n]}{\partial\varphi_k[n]}\right)\in\mathbb{C}^{M\times 2}$. Besides, the AoD set Ω_k can be rewritten as

$$\Omega_k=\left\{(\theta_k[n],\varphi_k[n])\ \middle|\ \mathbf{u}_k^T[n]\mathbf{E}\mathbf{u}_k[n]\leq\alpha^2\right\},\ \forall k, \tag{12}$$

where $\mathbf{E}=\begin{pmatrix}e_1&0\\0&e_2\end{pmatrix}\succeq\mathbf{0}$.

Remark 1: We note that the linearized AAR model in (11) is employed since $\Delta\theta_k[n]$ and $\Delta\varphi_k[n]$ are small in practice and to facilitate resource allocation design. In our simulations, we adopt the nonlinear AAR model in (2) to evaluate the proposed resource allocation algorithm.

C. Wind Speed Model

In practice, the UAV trajectory is influenced by wind [20]. In particular, the UAV ground speed[3] is affected by horizontal wind [36]. Without a careful design, the UAV is unable to operate along the desired trajectory. According to [36], the UAV ground speed in time slot n is given by the vector sum of the 2-D horizontal UAV air speed, $\mathbf{v}_u[n]$, and the horizontal wind speed, $\mathbf{v}_w[n]$, i.e., $\mathbf{v}_u[n]+\mathbf{v}_w[n]$. However, in practice, it is difficult to accurately estimate the instantaneous wind speed in each time slot due to the limited estimation accuracy of wind sensors and the randomness of wind [37]. To capture

[3]Ground speed is the horizontal speed of an aircraft relative to the ground [36].

this effect, we adopt a deterministic model for the resulting wind speed uncertainty [9]. The horizontal wind speed $\mathbf{v}_w[n]$ in time slot n is modeled as [38]:

$$\mathbf{v}_w[n] = \overline{\mathbf{v}}_w[n] + \Delta\mathbf{v}_w[n], \tag{13}$$

$$\mathbf{v}_w[n] \in \Xi \triangleq \left\{\mathbf{v}_w[n] \in \mathbb{R}^2 \mid \|\Delta\mathbf{v}_w[n]\| \leq \Delta V_w^{\max}\right\}, \tag{14}$$

where $\overline{\mathbf{v}}_w[n]$ and $\Delta\mathbf{v}_w[n]$ are the wind speed estimate and the wind speed uncertainty in time slot n, respectively. Moreover, continuous set Ξ contains all possible wind speed uncertainties with bounded maximum wind speed uncertainty magnitude $\Delta V_w^{\max}$.

D. User Location Model

In this paper, we assume that user devices are equipped with global positioning system (GPS) modules to obtain information regarding their own locations [39]. However, in general, the user location information is imperfect due to the limited positioning accuracy of practical GPS modules, satellite shadowing, and atmospheric impairments.[4] The resulting user location uncertainty should be taken into account for resource allocation algorithm design. In particular, since we assume that all users are on the ground, their z coordinates are set to 0. Moreover, we assume that all users are stationary. Then, the horizontal coordinates of user k are given by $x_k = \overline{x}_k + \Delta x_k$ and $y_k = \overline{y}_k + \Delta y_k$, where $\overline{x}_k$ and $\overline{y}_k$ are the user location estimates available at the UAV, and Δx_k and Δy_k denote the corresponding user location estimation errors. On the other hand, exploiting onboard multi-sensor systems and advanced positioning strategies, the positioning accuracy of UAVs can be improved to centimeter level [40]. As a result, we assume that the UAV perfectly knows its own location in each time slot. In particular, the estimated horizontal coordinates and the horizontal location estimation error of user k are defined as $\overline{\mathbf{r}}'_k = (\overline{x}_k,\ \overline{y}_k)^T$ and $\Delta\mathbf{r}'_k = (\Delta x_k,\ \Delta y_k)^T$, respectively. Then, the distance between the UAV and user k can be rewritten as

$$\|\mathbf{r}_0[n] - \mathbf{r}_k\| = \sqrt{\left\|\mathbf{r}'_0[n] - (\overline{\mathbf{r}}'_k + \Delta\mathbf{r}'_k)\right\|^2 + H_0^2}. \tag{15}$$

Furthermore, we define set Ψ_k collecting the possible location uncertainties of user k as follows:

$$\Psi_k \triangleq \left\{\mathbf{r}'_k \in \mathbb{R}^2 \mid (\Delta\mathbf{r}'_k)^T\Delta\mathbf{r}'_k \leq D_k^2\right\},\ \forall k \in \mathcal{K}, \tag{16}$$

where D_k is the bounded magnitude radius of the uncertainty region, whose value depends on the positioning accuracy.

E. No-Fly Zone Model

In this paper, we take NFZs into account for trajectory design [23]. In particular, we assume that there are J polygonal NFZs within the UAV service area, and the j-th NFZ is a polygon with S_j sides. Then, we model the polygonal NFZs by applying analytic geometry theory. Specifically, each polygonal NFZ is represented by the intersection of a finite number of half-spaces, and each half-space is defined as the solution of a set of affine inequalities, i.e.,

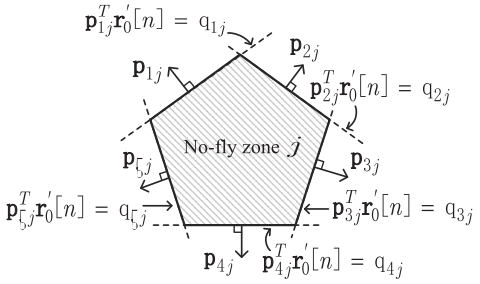

Fig. 3. A pentagonal no-fly zone composed of the intersection of five halfspaces.

$$\mathcal{D}_{ij} = \left\{\mathbf{d} \in \mathbb{R}^2 \mid \mathbf{p}_{ij}^T\mathbf{d} < q_{ij}, i \in \mathcal{S}_j, j \in \mathcal{J}\right\}, \tag{17}$$

where $\mathbf{d}$ are the 2-D coordinates of a horizontal plane with normal vector $\mathbf{p}_{ij} \in \mathbb{R}^2$ and offset $q_{ij} \in \mathbb{R}$, cf. Figure 3. Moreover, $\mathcal{S}_j \triangleq \{1, \cdots, S_j\}$ and $\mathcal{J} \triangleq \{1, \cdots, J\}$ denote the set of the sides of polygonal NFZ j and the set of polygonal NFZs, respectively. Besides, $\mathbf{p}_{ij}$ and q_{ij} can be determined in advance since the location and the size of the NFZs are set by regulation and known to the public.

As a result, the UAV does not violate NFZ j in time slot n if $\mathbf{r}'_0[n] \notin \mathcal{D}_{ij}$, $\forall i \in \mathcal{S}_j$. In other words, $\mathbf{r}'_0[n]$ has to satisfy at least one of the following S_j inequalities:

$$\mathbf{p}_{ij}^T\mathbf{r}'_0[n] \geq q_{ij}, \forall i \in \mathcal{S}_j. \tag{18}$$

To facilitate the trajectory design, we define an indicator function as follows [41]

$$Y_{ij}(\mathbf{r}'_0[n]) = \begin{cases} 1, & \mathbf{p}_{ij}^T\mathbf{r}'_0[n] \geq q_{ij} \\ 0, & \mathbf{p}_{ij}^T\mathbf{r}'_0[n] < q_{ij},\ \forall i,\ \forall j. \end{cases} \tag{19}$$

Therefore, the UAV does not trespass any NFZ in time slot n, if the following equality holds

$$\bigwedge_{j\in\mathcal{J}} \bigvee_{i\in\mathcal{S}_j} Y_{ij}(\mathbf{r}'_0[n]) = 1,\ \forall j. \tag{20}$$

In particular, the UAV is not in NFZ j if for any $i \in \mathcal{S}_j$, function $Y_{ij}(\mathbf{r}'_0[n])$ is equal to 1. Moreover, the UAV is able to bypass all NFZs, if $\bigvee_{i\in\mathcal{S}_j} Y_{ij}(\mathbf{r}'_0[n])$ is equal to 1 for all $j \in \mathcal{J}$.

F. Aerodynamic Power Consumption

We assume that the cruising speed is constant during each time slot [42]. According to the classic aerodynamic theory for rotary-wing UAVs [43], the aerodynamic power consumption of level flight in time slot n can be modeled as [44]

$$P_{\text{aero}}[n] = P_{\text{induced}}[n] + P_{\text{profile}}[n] + P_{\text{parasite}}[n], \tag{21}$$

where $P_{\text{induced}}[n]$, $P_{\text{profile}}[n]$, and $P_{\text{parasite}}[n]$ denote the induced power, profile power, and parasite power,[5] respec-

[4]The positioning errors of fourth-generation long-term evolution (4G LTE) network devices are typically in the range between 10 and 50 meters, depending on the adopted positioning protocol [39].

[5]The induced power generates thrust by propeling air downwards. The profile power overcomes the rotational drag encountered by rotating the propeller blades. The parasite power resists the body drag [43], [45].

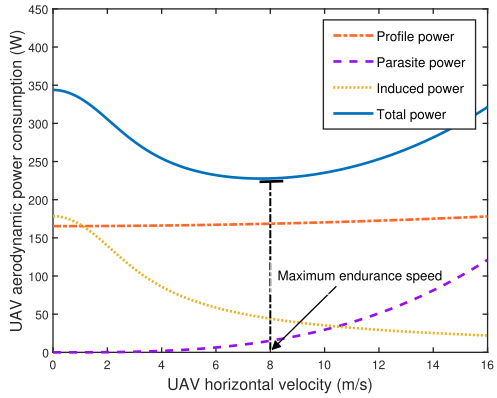

Fig. 4. UAV aerodynamic power consumption (Watt) versus horizontal velocity (m/s).

tively, and are given by [44, Eq. (7.9)]:

$$P_{\text{induced}}[n] = \frac{\sqrt{2}W_u c_1^2}{\sqrt{\|\mathbf{v}_u[n]\|^2 + \sqrt{\|\mathbf{v}_u[n]\|^4 + 4c_1^4}}}, \quad (22)$$

$$P_{\text{profile}}[n] = c_2\, V_{\text{T}}^3\Big[1 + c_3\Big(\frac{\|\mathbf{v}_u[n]\|}{V_{\text{T}}}\Big)^2\Big], \quad (23)$$

$$P_{\text{parasite}}[n] = c_4\, \|\mathbf{v}_u[n]\|^3, \quad (24)$$

respectively. W_u is defined as $W_u = k_i k_r m_u g_0$, where k_i, k_r, m_u, and g_0 denote the induced-power factor [44], the thrust-to-weight factor [45], the mass of the UAV, and the gravitational acceleration, respectively. V_{T} denotes the rotor tip speed and c_1, c_2, c_3, and c_4 are UAV aerodynamic power consumption parameters [44].

The aerodynamic power consumption of the UAV is a function of the horizontal velocity, cf. Figure 4. For Figure 4, we adopted the same parameter values as for the simulation results in Section V, see Table I. From Figure 4, we observe that, for rotary-wing UAVs, hovering is generally not the most power-conserving state. The optimal UAV speed that minimizes the total aerodynamic power consumption of the UAV is referred to as the maximum endurance speed, see Figure 4.

Remark 2: According to the theory of aerodynamics of UAVs [19], wind has a two-fold impact on the UAV aerodynamic power consumption. On the one hand, wind impacts the UAV aerodynamic power consumption by affecting the UAV ground speed. For UAV trajectory design in the presence of wind, the UAV has to adjust its air speed in each time slot such that the ground speed ensures a safe and power-efficient operation. As a result, the UAV aerodynamic power consumption may significantly change due to the wind-induced changes of UAV air speed, cf. Figure 10. On the other hand, wind also influences the air density around the rotor blades which leads to variations in the aerodynamic power consumption [19]. Yet, these power variations are relative small for moderate wind speeds and the corresponding model seems intractable for UAV trajectory and resource allocation algorithm design [46], [47]. Hence, to obtain a tractable optimization problem, in this paper, we assume that wind only affects the ground speed. This approach is in line with existing literature, cf. [36], [46], [48]. A more refined model capturing all wind-induced effects on the UAV aerodynamic power consumption is an interesting topic for future work.

G. Optimization Problem Formulation

In practice, the endurance of the UAVs is restricted by the limited onboard battery capacity [49]. Hence, a power-efficient resource allocation is of utmost importance for UAV-assisted communication systems. Therefore, in this paper, we adopt the minimization of the total power consumption as design objective. Moreover, since the AoDs in (3) depend on the UAV location, designing the UAV trajectory and beamforming policy jointly for all N_{T} time slots is intractable. Therefore, in this paper, we develop a greedy policy and optimize the trajectory and beamformers of the UAV for minimization of the total power consumption in each time slot. Since the displacement of the UAV in each time slot is relatively small, we assume that the AoDs remain unchanged during one time slot. Hence, the UAV trajectory and the beamforming policy in time slot n are designed based on the AoDs at the end of time slot $n-1$. This procedure is repeated for time slots $n = 1, \cdots, N_{\text{T}}$, and the whole UAV trajectory is obtained by combining the respective time slot trajectories. The optimal trajectory and the beamforming vector in time slot n are obtained by solving the following optimization problem[6]:

$$\begin{aligned}
&\underset{\mathbf{w}_k, \mathbf{r}_0', \mathbf{v}_u}{\text{minimize}} \quad \eta \sum_{k\in\mathcal{K}} \mathbf{w}_k^H \mathbf{w}_k + P_{\text{aero}} + M \cdot P_{\text{circ}} \qquad (25)\\
&\text{s.t. C1:} \left[\sum_{k\in\mathcal{K}} \mathbf{w}_k \mathbf{w}_k^H\right]_{i,i} \le P_i, \ \forall i,\\
&\quad \text{C2:} \min_{\substack{\mathbf{r}_k' \in \Psi_k,\\ \mathbf{u}_k \in \Omega_k}} \frac{\frac{\varrho}{\|\mathbf{r}_0' - \mathbf{r}_k'\|_2^2 + H_0^2} \left|\mathbf{a}_k^H \mathbf{w}_k\right|^2}{\frac{\varrho}{\|\mathbf{r}_0' - \mathbf{r}_k'\|_2^2 + H_0^2} \sum_{r\in\mathcal{K}\setminus\{k\}} \left|\mathbf{a}_k^H \mathbf{w}_r\right|^2 + \sigma_{n_k}^2}\\
&\qquad \ge \Gamma_{\text{req}_k}, \forall k,\\
&\quad \text{C3:} \|\mathbf{v}_u - \mathbf{v}_u[n-1]\| \le a_{\max}\delta_T,\\
&\quad \text{C4:} \min_{\mathbf{v}_w \in \Xi} \|\mathbf{v}_u + \mathbf{v}_w\|\, \delta_T \ge \|\mathbf{r}_0' - \mathbf{r}_0'[n-1]\|,\\
&\quad \text{C5:} \ \|\mathbf{v}_u\| \le V_u^{\max}, \text{C6:} \max_{\mathbf{v}_w \in \Xi} \|\mathbf{v}_u + \mathbf{v}_w\| \le V_g^{\max},\\
&\quad \text{C7:} \bigwedge_{j\in\mathcal{J}} \bigvee_{i\in\mathcal{S}_j} Y_{ij}(\mathbf{r}_0') = 1, \quad \text{C8:} \ \|\mathbf{r}_0'\|_2 \le R_{\text{p}},
\end{aligned}$$

where $\eta > 1$ and P_{circ} denote the power amplifier efficiency and the circuit power consumption of the radio frequency (RF) chain of one antenna element, respectively. Constraint C1 limits the transmit power of the i-th antenna element P_i, whose value is determined by the analog RF front-end. Γ_{req_k} in constraint C2 is the minimum SINR required by user k and ensures that the QoS requirements of the users are met.[7] Constraint C3 restricts the change of the UAV speed from one

[6]Since the optimization problem in (25) is solved for each time slot, for convenience, we drop time slot index n for the optimization variables.

[7]Constraint C2 is equivalent to a per time slot throughput constraint. We note that a constraint on the accumulated throughput can be satisfied by selecting an appropriate throughput constraint for each time slot and solving the considered optimization problem for each time slot.

TABLE I
SYSTEM PARAMETERS ADOPTED IN SIMULATIONS

f_c	Carrier center frequency	2.4 GHz	B_w	Bandwidth	200 kHz
K	Number of users	6	M	Number of antennas at the UAV	9
m_u	Mass of the UAV	4.5 kg	g_0	The gravitational acceleration	9.8 $\mathrm{m/s^2}$
T	Time horizon	10 minutes	δ_{T}	Duration of each time slot	0.02 s
b	Antenna element separation	0.0625 m	$\sigma^2_{n_k}$	AWGN variance	-110 dBm
P_{circ}	UAV circuit power	300 mW	P_i	UAV per-antenna power allowance	2.5 W
H_0	UAV fixed flight altitude	100 m	$a_{\max}$	UAV maximum acceleration	2 $\mathrm{m/s^2}$
$V_u^{\max}$	Maximum UAV speed	15 m/s	$V_g^{\max}$	Maximum ground speed	18 m/s
η	Power amplifier efficiency	5	$\overline{\mathbf{v}}_w$	Mean wind speed	3 m/s
e_1	UAV horizontal AoD uncertainty	1	e_2	UAV vertical AoD uncertainty	1
c_1	UAV aerodynamic coefficient	2.804 $\sqrt{\mathrm{m/kg}}$	c_2	UAV aerodynamic coefficient	2.2×10^{-4} [44]
c_3	UAV aerodynamic coefficient	3 [44]	c_4	UAV aerodynamic coefficient	0.0296 Ns/m [36]
Γ_{req_k}	Minimum required SINR at user k	14 dB	D_k	User location uncertainty radius	20 meters
ρ_k	Maximum AoD uncertainty	0.1	ρ_w	Maximum wind speed uncertainty	0.2
ϵ_{POA}	Error tolerance for **Algorithms 1**	0.01	ϵ_{POA}	Error tolerance for **Algorithms 2**	0.01
ϵ_{SCA}	Error tolerance for **Algorithms 3**	0.01	G	Penalty factor	10^5
χ	Penalty factor	10^5	V_{T}	Rotor tip speed	100 (m/s)
k_i	Induced-power factor	1.1 [44, Table A.4]	k_r	Thrust-to-weight ratio	1 [45]

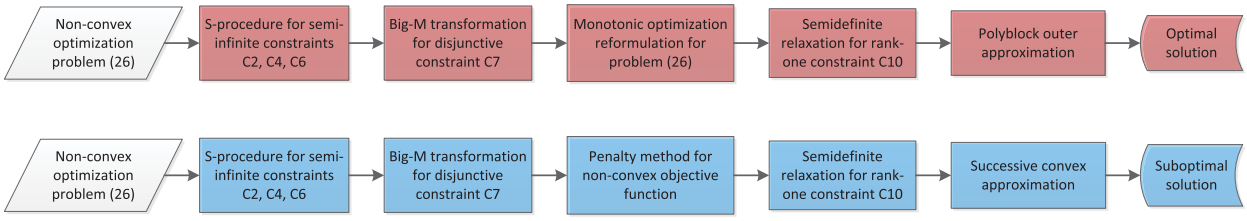

Fig. 5. Illustration of the key steps of the proposed algorithms. The red boxes and the blue boxes represent the key steps of the proposed optimal and suboptimal schemes, respectively. The parallelogram shaped boxes, the square shaped boxes, and the curved shaped boxes indicate the considered optimization problem, the key operations used for solving the considered optimization problem, and the obtained solutions, respectively.

time slot to the next, where $a_{\max}$ denotes the maximum acceleration of the UAV which is limited by its engines. Constraint C4 restricts the maximum displacement of the UAV in each time slot in the presence of wind speed uncertainty. Constraint C5 constrains the maximum UAV horizontal velocity $V_u^{\max}$. $V_g^{\max}$ in constraint C6 limits the maximum UAV speed for safety reasons. Constraint C7 ensures that the UAV does not pass through an NFZ. R_{p} in constraint C8 denotes the radius of the circular service area. Since $M \cdot P_{\mathrm{circ}}$ is constant for a given number of antenna elements, we omit it when solving (25) in the following.

We note that problem (25) is a non-convex optimization problem involving disjunctive programming [25] and semi-infinite programming [50]. Such non-convex problems are in general intractable. In particular, the non-convex objective function, the semi-infinite constraints C2, C4, and C6, and the disjunctive constraint C7 are the main obstacles for solving the considered trajectory and resource allocation optimization problem. Yet, despite these challenges, we will develop an algorithm for finding the optimal solution of (25) by exploiting the unique properties of the problem in the next section.

Remark 3: In this paper, we assume that the flight direction of the UAV in each time slot can be estimated by the sensors equipped at the UAV [40]. We note that small estimation errors for the flight direction of the UAV can be incorporated into the AoD uncertainty model and handled by the proposed robust trajectory design and resource allocation algorithms.

Remark 4: We note that, in uncertain environments, the proposed time slot-by-time slot algorithm design for joint UAV trajectory design and resource allocation may be preferable compared to a joint design across all time slots. In particular, in practice, the location of the users and the wind speed may vary over time. As a result, algorithms assuming the system parameters are fixed for the entire flight duration may not be able to satisfy the QoS requirement of moving users or may lead to violations of safety regulations due to outdated user location and wind speed information. In contrast, the proposed algorithms do not suffer from the aforementioned limitations since the system parameters can be adapted in each time slot.

Remark 5: In practice, UAVs are controlled and operated by ground UAV control stations [51]. In this paper, we assume that the UAV control station constantly acquires wind information from nearby weather stations and collects location information of the UAV and ground users via feedback channels. Moreover, at the beginning of each time slot, the instantaneous CSI of the channels between the UAV and the ground users is acquired via handshaking and is transmitted to the UAV control station via feedback channels. The per time slot UAV trajectory and beamforming policy is computed at the UAV control station. Then, the obtained solution is informed to the UAV via a control channel.

III. OPTIMAL SOLUTION OF THE OPTIMIZATION PROBLEM

In this section, we develop an algorithm that finds a globally optimal solution for optimization problem (25). In particular, we first transform the semi-infinite constraints in (25) into

linear matrix inequalities (LMIs). Then, we recast the disjunctive programming constraint into a mixed integer linear programming constraint. Subsequently, we solve the optimization problem optimally by employing monotonic optimization theory and SDP relaxation. The key steps for finding the optimal solution of the considered optimization problem are illustrated in Figure 5, top part (red boxes).

A. Transformation of the Semi-Infinite Constraints

For the sake of notational simplicity, we define $\mathbf{W}_k = \mathbf{w}_k\mathbf{w}_k^H$, $\mathbf{A}_k = \mathbf{a}_k\mathbf{a}_k^H$, $\forall k$, and rewrite (25) in equivalent form as

$$\begin{aligned}
&\underset{\mathbf{W}_k\in\mathbb{H}^{N_\mathrm{T}},\mathbf{r}_0',\mathbf{v}_u}{\text{minimize}} \quad \eta\sum_{k\in\mathcal{K}}\mathrm{Tr}(\mathbf{W}_k)+P_{\text{aero}}\\
&\text{s.t. C1:}\left[\sum_{k\in\mathcal{K}}\mathrm{Tr}(\mathbf{W}_k)\right]_{i,i}\le P_i,\ \forall i,\\
&\quad\text{C2:}\min_{\substack{\mathbf{r}_k'\in\Psi_k,\\ \mathbf{u}_k\in\Omega_k}}\frac{\frac{\varrho}{\left\|\mathbf{r}_0'-\mathbf{r}_k'\right\|^2+H_0^2}\mathrm{Tr}(\mathbf{W}_k\mathbf{A}_k)}{\sum_{r\in\mathcal{K}\setminus\{k\}}\frac{\varrho}{\left\|\mathbf{r}_0'-\mathbf{r}_k'\right\|^2+H_0^2}\mathrm{Tr}(\mathbf{W}_r\mathbf{A}_k)+\sigma_{n_k}^2}\\
&\qquad\ge\Gamma_{\mathrm{req}_k},\\
&\quad\text{C3-C8, C9:}\mathbf{W}_k\succeq\mathbf{0},\ \forall k,\text{C10:}\mathrm{Rank}(\mathbf{W}_k)\le 1,\ \forall k,
\end{aligned}\tag{26}$$

where $\mathbf{W}_k\succeq\mathbf{0}$, $\mathbf{W}_k\in\mathbb{H}^{N_\mathrm{T}}$, and $\mathrm{Rank}(\mathbf{W}_k)\le 1$ in constraints C9 and C10 are imposed to ensure that $\mathbf{W}_k=\mathbf{w}_k\mathbf{w}_k^H$ holds after optimization. Moreover, constraints C2, C4, and C6 are intractable semi-infinite constraints, as variables $\mathbf{r}_k'$, $\mathbf{u}_k$, and $\mathbf{v}_w$ are continuous in sets Ψ_k, Ω_k, and Ξ, respectively. To obtain a tractable optimization problem, we transform constraints C2, C4, and C6 into LMIs. Specifically, constraint C2 is very challenging to handle, since the left hand side term is a non-convex fractional term which contains continuous variables $\mathbf{r}_k'$ and $\mathbf{u}_k$. To facilitate the transformation of the semi-infinite constraints, we first rewrite constraint C2 as

$$\begin{aligned}
\text{C2:}\min_{\substack{\mathbf{r}_k'\in\Psi_k,\\ \mathbf{u}_k\in\Omega_k}}&\frac{\mathrm{Tr}(\mathbf{W}_k\mathbf{A}_k)}{\sum_{r\in\mathcal{K}\setminus\{k\}}\mathrm{Tr}(\mathbf{W}_r\mathbf{A}_k)+\frac{\left\|\mathbf{r}_0'-\mathbf{r}_k'\right\|^2+H_0^2}{\varrho}\sigma_{n_k}^2}\\
&\ge\Gamma_{\mathrm{req}_k},\quad\forall k.
\end{aligned}\tag{27}$$

Then, we define a slack variable $\tau_k\in\mathbb{R}$ to decouple variables $\mathbf{r}_k'$ and $\mathbf{u}_k$ and rewrite C2 equivalently in terms of two constraints C2a and C2b [52], [53] as follows:

$$\text{C2a:}\min_{\mathbf{u}_k\in\Omega_k}\mathrm{Tr}(\mathbf{W}_k\mathbf{A}_k)-\Gamma_{\mathrm{req}_k}\sum_{r\in\mathcal{K}\setminus\{k\}}\mathrm{Tr}(\mathbf{W}_r\mathbf{A}_k)\ge\tau_k,\ \forall k,\tag{28}$$

$$\text{C2b:}\ \tau_k\ge\max_{\mathbf{r}_k'\in\Psi_k}\Gamma_{\mathrm{req}_k}\frac{\sigma_{n_k}^2(\left\|\mathbf{r}_0'-\mathbf{r}_k'\right\|^2+H_0^2)}{\varrho},\forall k.\tag{29}$$

The two continuous variables $\mathbf{r}_k'$ and $\mathbf{u}_k$ are decoupled now. Next, we take the square of both sides of the inequality in constraint C4 and define a slack variable $\zeta\in\mathbb{R}$. Then, constraint C4 can be equivalently rewritten as

$$\text{C4a:}\ \zeta\ge\frac{1}{\delta_T^2}\left\|\mathbf{r}_0'-\mathbf{r}_0'[n-1]\right\|^2,\tag{30}$$

$$\text{C4b:}\ \left\|\mathbf{v}_u+\mathbf{v}_w\right\|^2\ge\zeta,\ \forall\mathbf{v}_w\in\Xi.\tag{31}$$

Similarly, we can rewrite constraint C6 as:

$$\text{C6}:\left\|\mathbf{v}_u+\mathbf{v}_w\right\|^2\le(V_g^{\max})^2,\ \forall\mathbf{v}_w\in\Xi.\tag{32}$$

Now, we introduce a lemma for transforming constraints C2a, C2b, C4b, and C6 into LMIs.

Lemma 1 (S-Procedure [54]:) Let a function $f_m(\mathbf{x})$, $m\in\{1,2\}$, $\mathbf{x}\in\mathbb{C}^{N\times 1}$, be defined as

$$f_m(\mathbf{x})=\mathbf{x}^H\mathbf{B}_m\mathbf{x}+2\mathrm{Re}\left\{\mathbf{b}_m^H\mathbf{x}\right\}+b_m,\tag{33}$$

where $\mathbf{B}_m\in\mathbb{H}^N$, $\mathbf{b}_m\in\mathbb{C}^{N\times 1}$, and $\mathrm{b}_m\in\mathbb{R}^{1\times 1}$. Then, the implication $f_1(\mathbf{x})\le 0\Rightarrow f_2(\mathbf{x})\le 0$ holds if and only if there exists a $\delta\ge 0$ such that

$$\delta\begin{bmatrix}\mathbf{B}_1 & \mathbf{b}_1\\ \mathbf{b}_1^H & b_1\end{bmatrix}-\begin{bmatrix}\mathbf{B}_2 & \mathbf{b}_2\\ \mathbf{b}_2^H & b_2\end{bmatrix}\succeq\mathbf{0},\tag{34}$$

provided that there exists a point $\widehat{\mathbf{x}}$ such that $f_m(\widehat{\mathbf{x}})<0$.

Using Lemma 1, the following implication can be obtained: $\mathbf{u}_k^T\mathbf{E}\mathbf{u}_k-\alpha^2\le 0\Rightarrow$ C2a holds if and only if there exist $\vartheta_k\ge 0$ such that

$$\begin{aligned}
\overline{\text{C2}}\text{a:}\ &\mathbf{S}_{\overline{\text{C2a}}_k}(\mathbf{W}_k,\tau_k,\vartheta_k)\\
&=\begin{bmatrix}\vartheta_k\mathbf{E} & \mathbf{0}\\ \mathbf{0} & -\vartheta_k\alpha^2-\tau_k\end{bmatrix}\\
&\quad+\mathbf{U}_k^H\begin{bmatrix}\mathbf{W}_k-\Gamma_{\mathrm{req}_k}\sum_{r\in\mathcal{K}\setminus\{k\}}\mathbf{W}_r\end{bmatrix}\mathbf{U}_k\succeq\mathbf{0},\quad\forall k,
\end{aligned}\tag{35}$$

holds, where $\mathbf{U}_k=\begin{bmatrix}\mathbf{D}_k & \overline{\mathbf{a}}_k\end{bmatrix}$. Similarly, we apply Lemma 1 to C2b, C4b, and C6 and obtain the respective equivalent constraints which are shown at the top of this page, where β_k, γ_k, $\iota\ge 0$. We note that constraints $\overline{\text{C2}}$b, $\overline{\text{C4}}$b, and $\overline{\text{C6}}$ are still non-convex, due to the quadratic terms $\left\|\mathbf{r}_0'\right\|^2$ and $\left\|\mathbf{v}_u\right\|^2$. For handling $\overline{\text{C2}}$b, $\overline{\text{C4}}$b, and $\overline{\text{C6}}$, we define slack variables $\varpi_k\in\mathbb{R}$, $\varepsilon\in\mathbb{R}$, and $\mu\in\mathbb{R}$ and rewrite constraints $\overline{\text{C2}}$b, $\overline{\text{C4}}$b, and $\overline{\text{C6}}$ which are shown on the top of this page, respectively. We note that constraints $\overline{\text{C2}}$c, $\overline{\text{C4}}$c, $\overline{\text{C4}}$d, and $\overline{\text{C6}}$a are convex constraints, and constraints $\overline{\text{C2}}$d and $\overline{\text{C6}}$b are monotonically increasing in ϖ_k and μ, respectively. For convenience, we define set $\mathcal{A}$ to collect optimization variables τ_k, ϑ_k, β_k, γ_k, and ι.

B. Transformation of the Disjunctive Constraint

The disjunctive programming in constraint C7 is an obstacle to solving problem (26). To overcome this obstacle, we define auxiliary binary optimization variable $l_{ij}\in\{0,1\}$ and introduce the following theorem.

Theorem 1: The disjunctive programming in constraint C7 is equivalent to the following mixed integer linear programming [55]:

$$\mathbf{p}_{ij}^T\mathbf{r}_0'-q_{ij}+Gl_{ij}\ge 0,\ \forall i,\ \forall j,\tag{43}$$

if binary variable l_{ij} satisfies inequality $\sum_{i\in\mathcal{S}_j} l_{ij} \le S_j - 1$, and G is a sufficiently large constant.

Proof: Please refer to Appendix A. ■

Based on Theorem 1, we can rewrite constraint C7 as mixed integer linear constraints:

$$\text{C7a:}\mathbf{p}_{ij}^T\mathbf{r}_0' - q_{ij} + Gl_{ij} \ge 0,\ \forall i,\ \forall j, \tag{44}$$

$$\text{C7b:}\sum_{i\in\mathcal{S}_j} l_{ij} \le S_j - 1,\ \forall j, \text{C7c: } l_{ij} \in \{0,1\},\ \forall i,\ \forall j. \tag{45}$$

We note that constraint C7c is a binary constraint which is difficult to handle. Hence, we further rewrite C7c in the equivalent form as:

$$\text{C7d:}\sum_{j\in\mathcal{J}}\sum_{i\in\mathcal{S}_j}(l_{ij} - l_{ij}^2) \le 0, \text{C7e:} 0 \le l_{ij} \le 1,\ \forall i,\ \forall j. \tag{46}$$

Now, the optimization variable l_{ij} is a continuous variable between zero and one. Yet, we note that constraint C7d is a non-convex and non-monotonic function. To tackle this problem, we define a slack variable $t \in \mathbb{R}$ and rewrite constraint C7d as:

$$\text{C7f:}\sum_{j\in\mathcal{J}}\sum_{i\in\mathcal{S}_j} l_{ij}^2 + t \ge \overline{S}, \text{C7g:}\sum_{j\in\mathcal{J}}\sum_{i\in\mathcal{S}_j} l_{ij} + t \le \overline{S}, \tag{47}$$

where $\overline{S}$ is a constant and defined as $\overline{S} \triangleq \sum_{j\in\mathcal{J}} S_j$. We note that constraint C7f is monotonically increasing in t and constraint C7g is a convex constraint.

C. Mathematical Preliminaries for Monotonic Optimization

In this subsection, we introduce some mathematical preliminaries [26], [56] required for monotonic optimization and the derivation of the corresponding algorithm in the next two subsections.

Definition 1 (Increasing Function): A function $f\colon \mathbb{R}_+^n \to \mathbb{R}$ is increasing if $f(x) \le f(y)$ when $0 \le x \le y$.

Definition 2 (Normal Set): A set $\mathcal{G} \in \mathbb{R}_+^n$ is normal if for any point $\mathbf{x} \in \mathcal{G}$, all other points $\mathbf{x}'$ such that $\mathbf{0} \le \mathbf{x}' \le \mathbf{x}$ are also in set $\mathcal{G}$.

Proposition 1 [56]: The union and the intersection of normal sets are still normal sets.

Definition 3 (Conormal Set): A set $\mathcal{H} \in \mathbb{R}_+^n$ is conormal if $\mathbf{x} \in \mathcal{H}$ and $\mathbf{x}' \ge \mathbf{x}$ implies $\mathbf{x}' \in \mathcal{H}$.

Definition 4 (Polyblock): A set $\mathcal{P} \in \mathbb{R}_+^n$ is called a polyblock if it is the union of a finite number of boxes $[\mathbf{0}, \mathbf{x}]$.

Proposition 2 [56]: Any polyblock is closed and normal. The intersection of a finite number of polyblocks is a polyblock.

Proposition 3 [56]: If vector variable $\mathbf{x}$ belongs to a polyblock $\mathcal{P}$, and $f(\mathbf{x})\colon \mathbb{R}_+^n \to \mathbb{R}$ is an increasing function of $\mathbf{x}$, then the maximum of $f(\mathbf{x})$ over polyblock $\mathcal{P}$ must occur at one vertex of $\mathcal{P}$.

Definition 5 (Projection): Given any vector variable $\mathbf{x} \in \mathbb{R}_+^n$ and any nonempty normal set $\mathcal{G} \in \mathbb{R}_+^n$, $\pi_{\mathcal{G}}(\mathbf{x})$ is a projection of $\mathbf{x}$ on $\mathcal{G}$ if $\pi_{\mathcal{G}}(\mathbf{x}) = \lambda\mathbf{x}$ with $\lambda = \max\{\eta \mid \eta\mathbf{x} \in \mathcal{G}\}$.

Definition 6 (Upper Boundary): A point $\mathbf{y} \in \mathbb{R}_+^n$ is an upper boundary point of a closed normal set $\mathcal{G}$ if $\mathcal{G} \cap \{x \in \mathbb{R}_+^n \mid \mathbf{x} > \mathbf{y}\} = \emptyset$.

D. Monotonic Optimization Framework

In this subsection, we develop an optimal algorithm for UAV trajectory and resource allocation design based on monotonic optimization theory [26].The proposed algorithm exploits the monotonicity of the formulated problem and provides a systematic approach to finding the globally optimal solution within a finite number of iterations. The performance achieved

$$\overline{\text{C2}}\text{b: } \mathbf{S}_{\overline{\text{C2b}}_k}(\mathbf{r}_0', \tau_k, \beta_k) = \begin{bmatrix} (\beta_k - 1)\mathbf{I}_2 & \mathbf{r}_0' - \overline{\mathbf{r}}_k' \\ (\mathbf{r}_0' - \overline{\mathbf{r}}_k')^T & -\beta_k D_k^2 - \|\mathbf{r}_0'\|^2 + 2(\overline{\mathbf{r}}_k')^T\mathbf{r}_0' - \|\overline{\mathbf{r}}_k'\|^2 - H_0^2 + \dfrac{\varrho\tau_k}{\Gamma_{\text{req}_k}\sigma_{n_k}^2} \end{bmatrix} \succeq \mathbf{0},\ \forall k, \tag{36}$$

$$\overline{\text{C4}}\text{b: } \mathbf{S}_{\overline{\text{C4b}}_k}(\mathbf{v}_u, \zeta_k, \gamma_k) = \begin{bmatrix} (\gamma_k + 1)\mathbf{I}_2 & \mathbf{v}_u + \overline{\mathbf{v}}_w \\ (\mathbf{v}_u + \overline{\mathbf{v}}_w)^T & -\gamma_k(\Delta V_w^{\max})^2 + \|\mathbf{v}_u\|^2 + 2\mathbf{v}_u^T\overline{\mathbf{v}}_w + \|\overline{\mathbf{v}}_w\|^2 - \zeta_k \end{bmatrix} \succeq \mathbf{0},\ \forall k, \tag{37}$$

$$\overline{\text{C6}}\text{: } \mathbf{S}_{\overline{\text{C6}}}(\mathbf{v}_u, \iota) = \begin{bmatrix} (\iota - 1)\mathbf{I}_2 & -\mathbf{v}_u - \overline{\mathbf{v}}_w \\ -(\mathbf{v}_u + \overline{\mathbf{v}}_w)^T & -\iota(\Delta V_w^{\max})^2 - \|\mathbf{v}_u\|^2 - 2\mathbf{v}_u^T\overline{\mathbf{v}}_w - \|\overline{\mathbf{v}}_w\|^2 + (V_g^{\max})^2 \end{bmatrix} \succeq \mathbf{0}, \tag{38}$$

$$\overline{\text{C2}}\text{c: } \mathbf{S}_{\overline{\text{C2c}}_k}(\mathbf{r}_0', \tau_k, \beta_k, \varpi_k) = \begin{bmatrix} (\beta_k - 1)\mathbf{I}_2 & \mathbf{r}_0' - \overline{\mathbf{r}}_k' \\ (\mathbf{r}_0' - \overline{\mathbf{r}}_k')^T & -\beta_k D_k^2 - R_{\text{p}}^2 + \varpi_k + 2(\overline{\mathbf{r}}_k')^T\mathbf{r}_0' - \|\overline{\mathbf{r}}_k'\|^2 - H_0^2 + \dfrac{\varrho\tau_k}{\Gamma_{\text{req}_k}\sigma_{n_k}^2} \end{bmatrix} \succeq \mathbf{0},\ \forall k, \tag{39}$$

$$\overline{\text{C4}}\text{c: } \mathbf{S}_{\overline{\text{C3c}}_k}(\mathbf{v}_u, \zeta_k, \gamma_k, \varepsilon) = \begin{bmatrix} (\gamma_k + 1)\mathbf{I}_2 & \mathbf{v}_u + \overline{\mathbf{v}}_w \\ (\mathbf{v}_u + \overline{\mathbf{v}}_w)^T & -\gamma_k(\Delta V_w^{\max})^2 + \varepsilon + 2\mathbf{v}_u^T\overline{\mathbf{v}}_w + \|\overline{\mathbf{v}}_w\|^2 - \zeta_k \end{bmatrix} \succeq \mathbf{0},\ \forall k, \tag{40}$$

$$\overline{\text{C6}}\text{a: } \mathbf{S}_{\widehat{\text{C6a}}}(\mathbf{v}_u, \iota, \mu) = \begin{bmatrix} (\iota - 1)\mathbf{I}_2 & -\mathbf{v}_u - \overline{\mathbf{v}}_w \\ -(\mathbf{v}_u + \overline{\mathbf{v}}_w)^T & -\iota(\Delta V_w^{\max})^2 - (V_u^{\max})^2 + \mu - 2\mathbf{v}_u^T\overline{\mathbf{v}}_w - \|\overline{\mathbf{v}}_w\|^2 + (V_g^{\max})^2 \end{bmatrix} \succeq \mathbf{0}, \tag{41}$$

$$\overline{\text{C2}}\text{d: } R_{\text{p}}^2 \le \varpi_k + (\mathbf{r}_0')^T\mathbf{r}_0',\ \forall k, \quad \overline{\text{C4}}\text{d: } \varepsilon \ge \mathbf{v}_u^T\mathbf{v}_u, \quad \overline{\text{C6}}\text{b: } (V_u^{\max})^2 \le \mu + \mathbf{v}_u^T\mathbf{v}_u, \tag{42}$$

by the optimal algorithm can serve as a performance upper bound for any low-complexity suboptimal algorithm. To facilitate the application of monotonic optimization, we transform (26) into the canonical form of a monotonic optimization problem [26]. First, to transform the objective function into the maximization of a monotonically increasing function, we define an auxiliary variable $z \in \mathbb{R}$ representing the difference between the actual total UAV power consumption and the maximum total UAV power consumption. In particular, z satisfies the following constraint:

$$\text{C11: } z \le \widehat{P} - \Big(\sum_{k\in\mathcal{K}} \mathrm{Tr}(\mathbf{W}_k) + \sqrt{2}W_u c_1^2 \widehat{u} + c_2\, V_{\mathrm{T}}^3\Big[1 + c_3\Big(\frac{\|\mathbf{v}_u\|}{V_{\mathrm{T}}}\Big)^2\Big] + c_4 \|\mathbf{v}_u\|^3\Big), \quad (48)$$

where $\widehat{u} \in \mathbb{R}$ is a slack variable which meets the following constraint

$$\text{C12: } \widehat{u} \ge \frac{1}{\sqrt{\|\mathbf{v}_u\|^2 + \sqrt{\|\mathbf{v}_u\|^4 + 4c_1^4}}}. \quad (49)$$

Moreover, $\widehat{P}$ is an upper bound on the total UAV power consumption and is defined as $\widehat{P} \triangleq \sum_{i\in\mathcal{M}} P_i + W_u c_1 + c_2\, V_{\mathrm{T}}^3\Big[1 + c_3\Big(\frac{V_u^{\max}}{V_{\mathrm{T}}}\Big)^2\Big] + c_4 (V_u^{\max})^3$, where $V_u^{\max}$ is the maximum UAV speed. As C11 and C12 are monotonically increasing functions in z and $\widehat{u}$, respectively, (26) can be equivalently rewritten as the following monotonic optimization problem:

$$\underset{\substack{\mathbf{W}_k, \mathbf{r}_0', \mathbf{v}_u, l_{ij},\\ \mathcal{A}, \varpi_k, \varepsilon, \mu, t, z, \widehat{u}}}{\text{maximize}} \; z - \widehat{P} \text{ s.t.} (\varpi_k, \varepsilon, \mu, t, z, \widehat{u}) \in \mathcal{F}, \quad (50)$$

where set $\mathcal{F} = \mathcal{G} \cap \mathcal{H}$ is the intersection of normal set $\mathcal{G}$ and conormal set $\mathcal{H}$ [26], and $\mathcal{G}$ and $\mathcal{H}$ are given by

$$\mathcal{G} \triangleq \{(t, z) \mid (t, z) \in \mathcal{U}\}, \quad (51)$$

$$\mathcal{H} \triangleq \{(\varpi_k, \varepsilon, \mu, t, \widehat{u}) \mid (\varpi_k, \varepsilon, \mu, t, \widehat{u}) \in \mathcal{V}\}, \quad (52)$$

where feasible set $\mathcal{U}$ is spanned by constraints C1, $\overline{\text{C2}}$a, $\overline{\text{C2}}$c, C3, C4a, $\overline{\text{C4}}$c, C5, $\overline{\text{C6}}$a, C7a, C7b, C7e, C7g, C8-C10, and C11, and feasible set $\mathcal{V}$ is spanned by constraints $\overline{\text{C2}}$d, $\overline{\text{C4}}$d, $\overline{\text{C6}}$b, C7f, and C12. Since $\widehat{P}$ is a constant and does not affect the optimal solution of the considered problem, we omit it in the following for notational simplicity. We note that problem (50) is in the canonical form of a monotonic optimization problem.

E. Optimal Algorithm Design

In this section, we design an iterative algorithm based on polyblock outer approximation [26] to solve the considered problem. Due to the monotonicity of the objective function, the optimal solution of (50) is on the upper boundary of feasible set $\mathcal{F}$. In general, the upper boundary of feasible set $\mathcal{F}$ is not known in advance. Hence, we approach the boundary by iteratively pruning a polyblock $\mathcal{P}$, simultaneously ensuring $\mathcal{P}$ always contains feasible set $\mathcal{F}$. In particular, in time slot n, based on vertex $\boldsymbol{\nu}^{(1)}$, we initially construct a polyblock $\mathcal{P}^{(1)}$ that includes feasible set $\mathcal{F}$. Moreover, the vertex $\boldsymbol{\nu}^{(1)}$ is defined as $\boldsymbol{\nu}^{(1)} \triangleq (\varpi_k^{(1)}, \varepsilon^{(1)}, \mu^{(1)}, t^{(1)}, z^{(1)}, \widehat{u}^{(1)})$ and the vertex set of $\mathcal{P}^{(1)}$ is denoted as $\mathcal{T}^{(1)} = \{\boldsymbol{\nu}^{(1)}\}$. Based on vertex $\boldsymbol{\nu}^{(1)}$, we generate $K+5$ new vertices in the vertex set $\widehat{\mathcal{T}}^{(1)} = \{\widehat{\boldsymbol{\nu}}_1^{(1)}, \cdots, \widehat{\boldsymbol{\nu}}_Q^{(1)}\}$. Specifically, we calculate $\widehat{\boldsymbol{\nu}}_i^{(1)} = \boldsymbol{\nu}^{(1)} - (\nu_i^{(1)} - \pi_i(\boldsymbol{\nu}^{(1)}))\mathbf{e}_i$, $\forall i \in \{1, \cdots, K+5\}$, where $\nu_i^{(1)}$ and $\pi_i(\boldsymbol{\nu}^{(1)})$ are the i-th elements of $\boldsymbol{\nu}^{(1)}$ and $\boldsymbol{\pi}(\boldsymbol{\nu}^{(1)})$ in time slot n, respectively. Moreover, $\boldsymbol{\pi}(\boldsymbol{\nu}^{(1)}) \in \mathbb{R}^{K+5}$ denotes the projection of $\boldsymbol{\nu}^{(1)}$ onto set $\mathcal{G}$, and $\mathbf{e}_i$ is a unit vector with the i-th element equal to 1. Then, we shrink $\mathcal{P}^{(1)}$ by replacing $\boldsymbol{\nu}^{(1)}$ by $K+5$ new vertices in $\widehat{\mathcal{T}}^{(1)}$ and obtain a new polyblock $\mathcal{P}^{(2)}$ which still satisfies $\mathcal{P}^{(2)} \supset \mathcal{F}$. The vertex set of $\mathcal{P}^{(2)}$ is updated by setting $\mathcal{T}^{(2)} = (\mathcal{T}^{(1)} \setminus \{\boldsymbol{\nu}^{(1)}\}) \cup \widehat{\mathcal{T}}^{(1)}$. Subsequently, for each vertex in set $\mathcal{T}^{(2)} \cap \mathcal{H}$, we calculate the projections onto the upper boundary of $\mathcal{G}$. Then, the vertex whose projection maximizes the objective function of problem (50) is chosen as the optimal vertex $\boldsymbol{\nu}^{(2)}$ in $\mathcal{T}^{(2)} \cap \mathcal{H}$, i.e., $\boldsymbol{\nu}^{(2)} = \underset{\boldsymbol{\nu}\in\mathcal{T}^{(2)}\cap\mathcal{H}}{\arg\max} \{z\}$. The aforementioned procedure is applied repeatedly to shrink $\mathcal{P}^{(2)}$ based on vertex $\boldsymbol{\nu}^{(2)}$. As a result, a smaller polyblock is constructed in each iteration, leading to $\mathcal{P}^{(1)} \supset \mathcal{P}^{(2)} \supset \cdots \supset \mathcal{F}$. The algorithm

---

$$\begin{aligned}
&\text{Find } \{\mathbf{W}_k, \mathbf{r}_0', \mathbf{v}_u, l_{ij}, \mathcal{A}\}\\
&\text{s.t. } \overline{\text{C2}}\text{c:}\mathbf{S}_{\overline{\text{C2}}\text{c}_k}(\mathbf{r}_0', \tau_k, \beta_k, \varpi_k) = \begin{bmatrix} (\beta_k - 1)\mathbf{I}_2 & \mathbf{r}_0' - \overline{\mathbf{r}}_k' \\ (\mathbf{r}_0' - \overline{\mathbf{r}}_k')^T & -\beta_k D_k^2 - R_{\mathrm{p}}^2 + \widehat{\lambda}(\varpi_k)^{(m)} + 2(\overline{\mathbf{r}}_k')^T \mathbf{r}_0' + \|\mathbf{r}_0'\|^2 - H_0^2 + \frac{\varrho\tau_k}{\Gamma_{\mathrm{req}_k}\sigma_{n_k}^2} \end{bmatrix} \succeq \mathbf{0},\\
&\overline{\text{C4}}\text{c:}\mathbf{S}_{\overline{\text{C4}}\text{c}_k}(\mathbf{v}_u, \zeta_k, \gamma_k, \varepsilon) = \begin{bmatrix} (\gamma_k + 1)\mathbf{I}_2 & \mathbf{v}_u + \overline{\mathbf{v}}_w \\ (\mathbf{v}_u + \overline{\mathbf{v}}_w)^T & -\gamma_k (V_w^{\max})^2 + \widehat{\lambda}(\varepsilon)^{(m)} + 2\mathbf{v}_u^T \overline{\mathbf{v}}_w + \|\overline{\mathbf{v}}_w\|^2 - \zeta_k \end{bmatrix} \succeq \mathbf{0}, \ \forall k,\\
&\overline{\text{C6}}\text{a:}\mathbf{S}_{\overline{\text{C6}}\text{a}}(\mathbf{v}_u, \iota, \mu) = \begin{bmatrix} (\iota - 1)\mathbf{I}_2 & -\mathbf{v}_u - \overline{\mathbf{v}}_w \\ -(\mathbf{v}_u + \overline{\mathbf{v}}_w)^T & -\iota (V_w^{\max})^2 - (V_w^{\max})^2 + \widehat{\lambda}(\mu)^{(m)} - 2\mathbf{v}_u^T \overline{\mathbf{v}}_w - \|\overline{\mathbf{v}}_w\|^2 + (V_g^{\max})^2 \end{bmatrix} \succeq \mathbf{0},\\
&\text{C7g:} \sum_{j\in\mathcal{J}} \sum_{i\in\mathcal{S}_j} l_{ij} + \widehat{\lambda}(t)^{(m)} \le \overline{S},\\
&\text{C11:} \widehat{\lambda}(z)^{(m)} + \sum_{k\in\mathcal{K}} \mathrm{Tr}(\mathbf{W}_k) + \sqrt{2}W_u c_1^2 \widehat{\lambda}(\widehat{u})^{(m)} + c_2\, V_{\mathrm{T}}^3\Big[1 + c_3\Big(\frac{\|\mathbf{v}_u\|}{V_{\mathrm{T}}}\Big)^2\Big] + c_4 \|\mathbf{v}_u\|^3 \le \widehat{P},\\
&\text{C1}, \overline{\text{C2}}\text{a}, \text{C3}, \text{C4a}, \text{C5}, \text{C7a}, \text{C7b}, \text{C7e}, \text{C8-C10}.
\end{aligned} \quad (53)$$

Algorithm 1 Optimal Polyblock Approximation Based Algorithm

1: Set the initial UAV location $\mathbf{r}_0'[0] = (0,0)$ and initial UAV speed $\mathbf{v}_u[0] = (0,0)$. Initialize polyblock $\mathcal{P}^{(1)}[n]$ with vertex set $\mathcal{T}^{(1)}[n] = \{\boldsymbol{\nu}^{(1)}[n]\}$ and vertex $\boldsymbol{\nu}^{(1)}[n] = \big(\varpi_k^{(1)}[n], \varepsilon^{(1)}[n], \mu^{(1)}[n], t^{(1)}[n], z^{(1)}[n], \widehat{u}^{(1)}[n]\big)$ as follows: $(\varpi_k[n])^{(1)} = 4R_{\mathrm{p}}^2$, $(\varepsilon[n])^{(1)} = (V_u^{\max})^2$, $(\mu[n])^{(1)} = (V_u^{\max})^2$, $(t[n])^{(1)} = \overline{S}$, $(z[n])^{(1)} = \widehat{P}$, and $(\widehat{u}[n])^{(1)} = 1/(\sqrt{2}c_1)$, $\forall k \in \mathcal{K}$. Set the error tolerance $0 \leq \varepsilon_{\mathrm{POA}} \ll 1$ and the maximum number of iterations M_{POA}.
2: Set time slot index $n = 1$ and iteration index $m = 1$.
3: **repeat**
4: Calculate the AoDs via (3) based on the current location information of the UAV $\mathbf{r}_0'[n-1]$
5: **repeat**
6: Calculate the projection of vertex $\boldsymbol{\nu}^{(m)}[n]$ onto set $\mathcal{G}[n]$, i.e., $\boldsymbol{\pi}(\boldsymbol{\nu}^{(m)}[n])$, with **Algorithm 2**.
7: Generate $K+5$ new vertices $\widehat{\mathcal{T}}^{(m)}[n] = \Big\{\widehat{\boldsymbol{\nu}}_1^{(m)}[n], \cdots, \widehat{\boldsymbol{\nu}}_{K+5}^{(m)}[n]\Big\}$, where $\widehat{\boldsymbol{\nu}}_i^{(m)}[n] = \boldsymbol{\nu}^{(m)}[n] - \big(\nu_i^{(1)}[n] - \pi_i(\boldsymbol{\nu}^{(m)}[n])\big)\mathbf{e}_i$, $\forall i \in \{1, \cdots, K+5\}$.
8: Construct a smaller polyblock $\mathcal{P}^{(m+1)}[n]$ with new vertex set $\mathcal{T}^{(m+1)}[n] = \big(\mathcal{T}^{(m)}[n] - \boldsymbol{\nu}^{(m)}[n]\big) \cup \widehat{\mathcal{T}}^{(m)}[n]$.
9: Find $\boldsymbol{\nu}^{(m+1)}[n]$ as that vertex of $\mathcal{T}^{(m+1)}[n] \cap \mathcal{H}[n]$ whose projection maximizes the objective function of the problem, i.e., $\boldsymbol{\nu}^{(m+1)}[n] = \underset{\boldsymbol{\nu}[n] \in \mathcal{T}^{(m+1)}[n] \cap \mathcal{H}[n]}{\arg\max} \{z[n]\}$.
10: Set $m = m + 1$.
11: **until** $\frac{\|\boldsymbol{\nu}^{(m)}[n] - \boldsymbol{\pi}(\boldsymbol{\nu}^{(m)}[n])\|}{\|\boldsymbol{\nu}^{(m)}[n]\|} \leq \epsilon_{\mathrm{POA}}$
12: Store the optimal solution $\boldsymbol{\nu}^*[n]$.
13: Set $n = n + 1$
14: **until** $n > N_{\mathrm{T}}$

terminates if $\frac{\|\boldsymbol{\nu}^{(m)} - \boldsymbol{\pi}(\boldsymbol{\nu}^{(m)})\|}{\|\boldsymbol{\nu}^{(m)}\|} \leq \epsilon_{\mathrm{POA}}$ or index $m \geq M_{\mathrm{POA}}$, where the error tolerance constant $\epsilon_{\mathrm{POA}} > 0$ specifies the accuracy of the approximation and the maximum number of iterations M_{POA} guarantees that the algorithm terminates in finite time. The proposed polyblock outer approximation algorithm is summarized in **Algorithm 1**.[8]

We note that the projection of vertex $\boldsymbol{\nu}^{(m)}$ onto the upper boundary of set $\mathcal{G}$, i.e., $\boldsymbol{\pi}(\boldsymbol{\nu}^{(m)})$, is required in each iteration of **Algorithm 1**. In particular, in the m-th iteration of the n-th time slot, the projection of the vertex $\boldsymbol{\nu}^{(m)}$ onto set $\mathcal{G}$ is given by $\boldsymbol{\pi}(\boldsymbol{\nu}^{(m)}) = \widehat{\lambda}\boldsymbol{\nu}^{(m)}$. Moreover, the projection parameter $\widehat{\lambda}$ is obtained as $\widehat{\lambda} = \max\{\widehat{\alpha} \mid \widehat{\alpha}\boldsymbol{\nu}^{(m)} \in \mathcal{G}\}$ where $\widehat{\lambda} \in [0,1]$. Hence, $\widehat{\lambda}$ can be obtained by employing the bisection search method [26]. Specifically, in the m-th iteration, for a given projection parameter $\widehat{\lambda}$ and vertex $\boldsymbol{\nu}^{(m)}$, we have $\widehat{\lambda}\boldsymbol{\nu}^{(m)} \in \mathcal{G}$ if the problem in (53) is feasible, where (53) is shown at the bottom of the previous page. We note that feasible set $\mathcal{G}$ is

[8]According to [56], the proposed polyblock outer approximation algorithm is guaranteed to converge to the globally optimal solution of the monotonic optimization problem in (50). The details of the convergence proof can be found in [56, Section 5].

Algorithm 2 Bisection Projection Search Algorithm

1: Initialize $\lambda_{\min} = 0$, $\lambda_{\max} = 1$, and set error tolerance $0 < \delta_{\mathrm{BS}} \ll 1$.
2: **repeat**
3: Let $\widehat{\lambda}[n] = (\lambda_{\min} + \lambda_{\max})/2$.
4: Check the feasibility of $\widehat{\lambda}[n]$ by solving (53), i.e., whether $\widehat{\lambda}[n]\boldsymbol{\nu}^{(m)}[n] \in \mathcal{G}[n]$. If feasible, $\lambda_{\min} = \widehat{\lambda}[n]$; else $\lambda_{\max} = \widehat{\lambda}[n]$
5: **until** $\lambda_{\max} - \lambda_{\min} < \delta_{\mathrm{BS}}$.
6: Obtain $\widehat{\lambda}[n] = \lambda_{\min}$ and the projection of vertex $\boldsymbol{\nu}^{(m)}[n]$ onto set $\mathcal{G}[n]$, i.e., $\boldsymbol{\pi}(\boldsymbol{\nu}^{(m)}[n]) = \widehat{\lambda}[n]\boldsymbol{\nu}^{(m)}[n]$. The corresponding optimization variables $(\mathbf{W}_k[n], \mathbf{r}_0'[n], \mathbf{v}_u[n], \tau[n], \zeta[n], \vartheta[n], \beta[n], \gamma[n], \iota[n], l_{ij}[n])$ are obtained by solving (53) for $\widehat{\lambda}[n] = \lambda_{\min}$.

spanned by the constraints of (53). The proposed projection bisection search algorithm is summarized in **Algorithm 2**. We note that problem (53) is non-convex due to rank-one constraint C10. To tackle this problem, we employ SDP relaxation by removing constraint C10 from the problem formulation. Then, (53) is a convex problem and can be solved efficiently by standard convex optimization solvers such as CVX [57]. In addition, the tightness of the SDP relaxation of optimization problem (53) is revealed in the following theorem.

Theorem 2: If $\Gamma_{\mathrm{req}_k} > 0$, a rank-one beamforming matrix $\mathbf{W}_k$ can always be obtained.

Proof: Problem (53) is similar to [52, Problem (46)] and the proof of Theorem 2 closely follows [52, Appendix B]. Hence, we omit the details of the proof due to space constraints. ■

The globally optimal UAV trajectory and beamforming policy of the considered system can be obtained by **Algorithm 1**. However, the computational complexity of **Algorithm 1** increases exponentially with the number of users which is prohibitive for real-time operation of UAV-based communication systems. In order to strike a balance between complexity and optimality, in the next section, we propose a suboptimal scheme which finds a locally optimal solution with low computational complexity. Nevertheless, **Algorithm 1** provides a valuable benchmark for any suboptimal design.

Remark 6: In this paper, as is commonly done in the literature [58], [59], we assume that the considered optimization problem is feasible for trajectory and resource allocation algorithm design. In practice, the feasibility of the problem depends on the channel condition and the QoS requirements of the users. If the problem is infeasible, user scheduling can be performed at the upper layers to temporarily exclude some user from being served to make the problem feasible.

IV. Suboptimal Solution of the Optimization Problem

In this section, we propose a suboptimal algorithm based on SCA to strike a balance between computational complexity and optimality, see Figure 5, bottom part (blue boxes). To start

with, we rewrite problem (26) as:

$$\begin{aligned}&\underset{\substack{\mathbf{W}_k,\mathbf{r}_0',\mathbf{v}_u,\\ l_{ij},\mathcal{A},\widehat{u},g}}{\text{minimize}} \ \eta\sum_{k\in\mathcal{K}}\text{Tr}(\mathbf{W}_k)+g\\ &\text{s.t. C1},\overline{\text{C2}}\text{a},\overline{\text{C2}}\text{b},\text{C3},\text{C4a},\overline{\text{C4}}\text{b},\text{C5},\overline{\text{C6}},\\ &\quad \text{C7a},\text{C7b},\text{C7d},\text{C7e},\text{C8-C10},\\ &\quad \text{C12:}\widehat{u}\geq\frac{1}{\sqrt{\|\mathbf{v}_u\|^2+\sqrt{\|\mathbf{v}_u\|^4+4c_1^4}}},\\ &\quad \text{C13:}g\geq\sqrt{2}W_u c_1^2\widehat{u}+c_2\ V_{\text{T}}^3\Big[1+c_3\Big(\frac{\|\mathbf{v}_u\|}{V_{\text{T}}}\Big)^2\Big]+c_4\|\mathbf{v}_u\|^3,\end{aligned}\tag{54}$$

where $g\in\mathbb{R}$ is an auxiliary variable. We note that (54) is a non-convex problem due to non-convex constraints $\overline{\text{C2}}$b, $\overline{\text{C4}}$b, $\overline{\text{C6}}$, C7d, C10, and C12. Specifically, constraints $\overline{\text{C2}}$b, $\overline{\text{C4}}$b, and $\overline{\text{C6}}$ are non-convex due to the quadratic terms $\|\mathbf{r}_0'\|^2$ and $\|\mathbf{v}_u\|^2$. For handling this, we construct a global underestimator [60] of $\|\mathbf{r}_0'\|^2$ at point $(x_0^{(m)},y_0^{(m)})$ to approximate $\|\mathbf{r}_0'\|^2$. In particular, we rewrite constraint $\overline{\text{C2}}$b as $\widetilde{\text{C2}}$b which is shown at the bottom of this page in (55), where $\widetilde{c}_1$ is a linear function of (x_0,y_0) defined as:

$$\widetilde{c}_1\triangleq 2x_0x_0^{(m)}+2y_0y_0^{(m)}-(x_0^{(m)})^2-(y_0^{(m)})^2.\tag{58}$$

Similarly, for point $\big((v_u^x)^{(m)},(v_u^y)^{(m)}\big)$, constraints $\overline{\text{C4}}$b and $\overline{\text{C6}}$ can be rewritten as $\widetilde{\text{C4}}$b and $\widetilde{\text{C6}}$ which are shown at the bottom of this page in (56) and (57), respectively, where $\widetilde{c}_2$ is a global underestimator of $\|\mathbf{v}_u\|^2$ at point $\big((v_u^x)^{(m)},(v_u^y)^{(m)}\big)$ defined as:

$$\widetilde{c}_2\triangleq 2(v_u^x)^{(m)}v_u^x+2(v_u^y)^{(m)}v_u^y-\big[(v_u^x)^{(m)}\big]^2-\big[(v_u^y)^{(m)}\big]^2.\tag{59}$$

We note that constraints $\widetilde{\text{C2}}$b, $\widetilde{\text{C4}}$b, and $\widetilde{\text{C6}}$ are convex. However, non-convex constraint C7d in problem (54) is still an obstacle for the design of a computationally efficient algorithm. To resolve this issue, we introduce the following theorem:

Theorem 3: The optimization problem in (54) can be equivalently recast as follows

$$\begin{aligned}&\underset{\substack{\mathbf{W}_k,\mathbf{r}_0',\mathbf{v}_u,\\ l_{ij},\mathcal{A},\widehat{u},g}}{\text{minimize}} \ \sum_{k\in\mathcal{K}}\text{Tr}(\mathbf{W}_k)+g+\chi\sum_{j\in\mathcal{J}}\sum_{i\in S_j}\big(l_{ij}-l_{ij}^2\big)\\ &\text{s.t. C1},\overline{\text{C2}}\text{a},\widetilde{\text{C2}}\text{b},\text{C3},\text{C4a},\widetilde{\text{C4}}\text{b},\text{C5},\widetilde{\text{C6}},\\ &\quad \text{C7a},\text{C7b},\text{C7e},\text{C8-C10},\text{C12},\text{C13},\end{aligned}\tag{60}$$

if χ is a sufficiently large constant that penalizes the objective function for any l_{ij} not equal to 0 or 1.

Proof: Please refer to Appendix B. ■

The remaining non-convexity of problem (60) is due to the objective function and constraints C10 and C12. In particular, to tackle the non-convexity of constraint C12, we rewrite it in equivalent form as follows:

$$\text{C12a:}\widehat{u}\geq\frac{1}{\widetilde{\alpha}},\ \text{C12b:}(\widetilde{\alpha})^2\leq\widetilde{\beta}+\sqrt{\widetilde{\gamma}},\tag{61}$$

$$\text{C12c:}\widetilde{\beta}\leq\|\mathbf{v}_u\|^2,\ \text{C12d:}\widetilde{\gamma}\leq(\widetilde{\beta})^2+4c_1^4,\tag{62}$$

$$\text{C12e:}\widetilde{\alpha},\widetilde{\beta},\widetilde{\gamma}\geq 0,\tag{63}$$

where $\widetilde{\alpha},\widetilde{\beta}$, and $\widetilde{\gamma}\in\mathbb{R}$ are auxiliary optimization variables. We note that constraints C12c and C12d are still non-convex. However, the objective function and the constraint functions in C12c and C12d are differences of convex functions. Hence, problem (60) is a difference of convex programming problem [60]. We can obtain a locally optimal solution by employing SCA [28]. In particular, considering the objective function, for any point $l_{ij}^{(m)}$, we have

$$l_{ij}^2\geq 2l_{ij}l_{ij}^{(m)}-(l_{ij}^{(m)})^2,\tag{64}$$

where the right hand side of (64) is a global underestimator of l_{ij}^2. Similarly, we can construct global underestimators for constraints C12c and C12d as follows:

$$\begin{aligned}\widetilde{\text{C12}}\text{c:}\ &\widetilde{\beta}2[(v_u^x)^{(m)}v_u^x+(v_u^y)^{(m)}v_u^y]\\ &-\big[(v_u^x)^{(m)}\big]^2-\big[(v_u^y)^{(m)}\big]^2\leq 0,\end{aligned}\tag{65}$$

$$\widetilde{\text{C12}}\text{d:}\ \widetilde{\gamma}-2\widetilde{\beta}^{(m)}\widetilde{\beta}+(\widetilde{\beta}^{(m)})^2\leq 4c_1^4.\tag{66}$$

To simplify the notation, we further define $\widetilde{\Upsilon}$, $\widetilde{\Lambda}$, $\widetilde{\Upsilon}^{(m)}$, and $\widetilde{\Lambda}^{(m)}$ to collect $\{\mathbf{v}_u,\mathbf{r}_0',l_{ij},\widetilde{\beta},\kappa\}$, $\{\mathbf{W}_k,\mathcal{A},\widehat{u},g,\varsigma,\mu,\lambda\}$, $\{\mathbf{v}_u^{(m)},(\mathbf{r}_0')^{(m)},l_{ij}^{(m)},\widetilde{\beta}^{(m)},\kappa^{(m)}\}$, and $\{\mathbf{W}_k^{(m)},\mathcal{A}^{(m)},\widehat{u}^{(m)},g^{(m)},\varsigma^{(m)},\ \mu^{(m)},\lambda^{(m)}\}$, respectively. Then, we can obtain an upper bound for (60) by solving the following convex optimization problem:

$$\begin{aligned}&\underset{\substack{\mathbf{W},\mathbf{r}',\mathbf{v},\mathcal{A},\widehat{u},\\ \mathbf{g},\boldsymbol{\kappa},\boldsymbol{\varsigma},\boldsymbol{\mu},\boldsymbol{\lambda}}}{\text{minimize}} \ \sum_{k\in\mathcal{K}}\text{Tr}(\mathbf{W}_k)+g\\ &\qquad+\chi\sum_{j\in\mathcal{J}}\sum_{i\in S_j}\big(l_{ij}-2l_{ij}l_{ij}^{(m)}+(l_{ij}^{(m)})^2\big)\\ &\text{s.t. C1},\overline{\text{C2}}\text{a},\widetilde{\text{C2}}\text{b},\text{C3},\text{C4a},\widetilde{\text{C4}}\text{b},\text{C5},\widetilde{\text{C6}},\text{C7a},\text{C7b},\\ &\quad \text{C7e},\text{C8-C10},\text{C12a},\text{C12b},\widetilde{\text{C12}}\text{c},\widetilde{\text{C12}}\text{d},\text{C12e}.\end{aligned}\tag{67}$$

In problem (67), the remaining non-convex constraint is rank-one constraint C10. Similar to the optimal algorithm, we apply SDP relaxation to problem (67) by removing constraint C10, and the tightness of the SDP relaxation can be proved similar to Theorem 2. Then, we employ the iterative algorithm summarized in **Algorithm 3** to tighten the obtained

$$\widetilde{\text{C2}}\text{b:}\mathbf{S}_{\widetilde{\text{C2b}}_k}(\mathbf{r}_0',\tau_k,\beta_k)=\begin{bmatrix}(\beta_k-1)\mathbf{I}_2 & \mathbf{r}_0'-\overline{\mathbf{r}}_k'\\ (\mathbf{r}_0'-\overline{\mathbf{r}}_k')^T & -\beta_kD_k^2-\widetilde{c}_1+2(\overline{\mathbf{r}}_k')^T\mathbf{r}_0'-\|\overline{\mathbf{r}}_k'\|^2-H_0^2+\dfrac{\varrho\tau_k}{\Gamma_{\text{req}_k}\sigma_{n_k}^2}\end{bmatrix}\succeq\mathbf{0},\ \forall k,\tag{55}$$

$$\widetilde{\text{C4}}\text{b:}\mathbf{S}_{\widetilde{\text{C4b}}_k}(\mathbf{v}_u,\zeta_k,\gamma_k)=\begin{bmatrix}(\gamma_k+1)\mathbf{I}_2 & \mathbf{v}_u+\overline{\mathbf{v}}_w\\ (\mathbf{v}_u+\overline{\mathbf{v}}_w)^T & -\gamma_k(V_w^{\max})^2+\widetilde{c}_2+2\mathbf{v}_u^T\overline{\mathbf{v}}_w+\|\overline{\mathbf{v}}_w\|^2-\zeta_k\end{bmatrix}\succeq\mathbf{0},\ \forall k,\tag{56}$$

$$\widetilde{\text{C6}}\text{:}\mathbf{S}_{\widetilde{\text{C6}}}(\mathbf{v}_u,\iota)=\begin{bmatrix}(\iota-1)\mathbf{I}_2 & -\mathbf{v}_u-\overline{\mathbf{v}}_w\\ -(\mathbf{v}_u+\overline{\mathbf{v}}_w)^T & -\iota(V_w^{\max})^2-\widetilde{c}_2-2\mathbf{v}_u^T\overline{\mathbf{v}}_w-\|\overline{\mathbf{v}}_w\|^2+(V_g^{\max})^2\end{bmatrix}\succeq\mathbf{0},\tag{57}$$

Algorithm 3 Suboptimal Successive Convex Approximation Based Algorithm

1: Set the initial UAV location $\mathbf{r}_0'[0] = (0, 0)$ and UAV speed $\mathbf{v}_u[0] = (0, 0)$. Set the initial point $\widetilde{\Upsilon}^{(1)}$ and error tolerance ϵ_{SCA}.
2: Set time slot $n = 1$ and iteration index $m = 1$
3: **repeat**
4: Calculate the AoDs via (3) based on the current location information of the UAV $\mathbf{r}_0'[n-1]$
5: **repeat**
6: For given $\widetilde{\Upsilon}^{(m)}[n]$, solve the convex problem in (67) and store the intermediate solution $\widetilde{\Upsilon}[n]$ and $\widetilde{\Lambda}[n]$
7: Set $m = m + 1$ and $\widetilde{\Upsilon}^{(m)}[n] = \widetilde{\Upsilon}[n]$
8: **until** $\frac{\|\widetilde{\Upsilon}^{(m)}[n] - \widetilde{\Upsilon}^{(m-1)}[n]\|}{\|\widetilde{\Upsilon}^{(m-1)}[n]\|} \leq \epsilon_{\mathrm{SCA}}$
9: Store the UAV trajectory and resource allocation policy $\widetilde{\Upsilon}^*[n] = \widetilde{\Upsilon}^{(m)}[n]$ and $\widetilde{\Lambda}^*[n] = \widetilde{\Lambda}^{(m)}[n]$ for time slot n
10: Set $n = n + 1$
11: **until** $n > N_{\mathrm{T}}$

upper bound. In each iteration, after dropping C10, the convex problem (67) can be solved efficiently by standard convex program solvers such as CVX [57]. The proposed suboptimal iterative algorithm converges to a locally optimal solution of (54) in polynomial time [28].

The computational complexity of the proposed suboptimal algorithm with respect to the numbers of users, K, and the total number of transmit antennas at the UAV, M, is given by[9] [59], [61]

$$\mathcal{O}\Big(\big((M+K)M^3+(M+K)^2M^2+(M+K)^3\big)T_{\mathrm{i}}\sqrt{M}\log(\epsilon_{\mathrm{SCA}})\Big) \tag{68}$$

for a given error tolerance ϵ_{SCA}, where $\mathcal{O}(\cdot)$ is the big-O notation and T_{i} is the required number of iterations. We note that algorithms with polynomial time computational complexity are considered to be fast algorithms in the literature and are desirable for real-time implementation [41, Chapter 34].

Remark 7: In this paper, to make the resource allocation design tractable, we design the beamforming vectors based on the linearized AAR model in (11). This approximation may lead to a violation of the original QoS constraint C2 for the actual nonlinear AAR model in (2). To circumvent this problem, we solve (25) for a more stringent minimum SINR requirement, i.e., $\Gamma_{\mathrm{req}_k} + \gamma$, where $\gamma > 0$ is a small positive constant, which is chosen such that C2 is fulfilled also for the nonlinear AAR model.

V. Simulation Results

In this section, the performance of the proposed resource allocation scheme is investigated via simulations. Specifically, there are K users which are uniformly and randomly distributed within a single cell of radius 600 meters. We assume that the K users are located within $D_k = 20$ meters from their respective estimated locations. Moreover, we take into account the RF chain circuit power consumption P_{circ} when calculating the total UAV power consumption. For ease of presentation, in the sequel, we define the maximum normalized estimation error of the AoD between the UAV and user k as $\rho_k = \frac{\alpha}{\sqrt{(\theta_k)^2+(\varphi_k)^2}}$, where $\rho_i = \rho_j$, $\forall i, j \in \mathcal{K}$. Similarly, we define the maximum normalized wind speed uncertainty in time slot n as $\rho_w = \frac{\Delta V_w^{\max}}{\|\overline{\mathbf{v}}_w\|}$. Unless otherwise specified, we set $\rho_k = 0.1$, $\forall k \in \mathcal{K}$, and $\rho_w = 0.2$. Besides, in order to investigate the impact of wind, we assume that the magnitude of the wind speed estimate $|\overline{\mathbf{v}}_w|$ is 3 m/s for all time slots. To evaluate the performance, we employ the nonlinear AAR model in (2). We choose $\gamma = 0.3$ dB for all results shown, which ensures that the desired SINR Γ_{req_k} is achieved for the proposed schemes in all considered cases. Furthermore, to study the impact of polygonal NFZs, we consider a scenario with NFZ and a scenario without NFZ. In particular, for the scenario with NFZs, we assume that there are several polygonal NFZs randomly distributed within the cell. In addition, we adopt the total UAV power consumption as the performance metric, which is calculated by $\frac{\sum_{n=1}^{N_{\mathrm{T}}}\left(\eta\sum_{k\in\mathcal{K}}\mathbf{w}_k^H\mathbf{w}_k+P_{\mathrm{aero}}\right)}{N_{\mathrm{T}}}+M\cdot P_{\mathrm{circ}}$. The adopted parameter values are listed in Table I.

We also consider two baseline schemes for comparison. For baseline scheme 1, we jointly optimize the beamformer and the 2-D positioning of the UAV for minimization of the UAV transmit power taking into account transmit power constraint C1, QoS constraint C2, and NFZ constraint C7. In this case, the UAV hovers at the obtained optimal position and employs the optimal beamforming policy. For baseline scheme 2, the UAV hovers at the initial point $(0, 0)$ and employs maximum ratio transmission (MRT) for beamforming, i.e., the beamforming vector is set as $\mathbf{w}_k = \sqrt{p_k}\mathbf{h}_k\|\mathbf{h}_k\|^{-1}$, where p_k is the power allocated to the k-th user. We optimize p_k to satisfy the QoS requirements of the users. In addition, since for most channel realizations baseline scheme 2 cannot simultaneously fulfill the per-antenna power constraint and the QoS requirements of all users, we omit constraint C1 for baseline scheme 2 to obtain feasible solutions.

A. UAV Trajectory

Figure 6 and Figure 7 depict the 2-D trajectory of the UAV in the horizontal plane for different resource allocation schemes. In Figure 6, we show the trajectories of the proposed optimal and suboptimal schemes and the baseline schemes in the absence of wind and NFZs. In particular, the proposed optimal and suboptimal schemes pursue similar aerial trajectories where the UAV first moves towards the centroid of the region spanned by the majority of the users which facilitates power efficient data transmission. Then, the UAV adopts a circling path around the centroid to reduce the aerodynamic power consumption. This is due to the fact that for rotary-wing UAVs, cruising flight generally consumes less power than hovering flight, cf. Figure 4. For baseline scheme 1, the UAV hovers at the centroid point and satisfies the QoS requirements of

[9] According to [61, Theorem. 3.12], the computational complexity of an SDP problem with m SDP constraints, where each constraint contains an $n \times n$ positive semidefinite matrix, is given by $\mathcal{O}\big(mn^3 + m^2n^2 + m^3\big)$. For the problem at hand, we have $m = M + K$ and $n = M$.

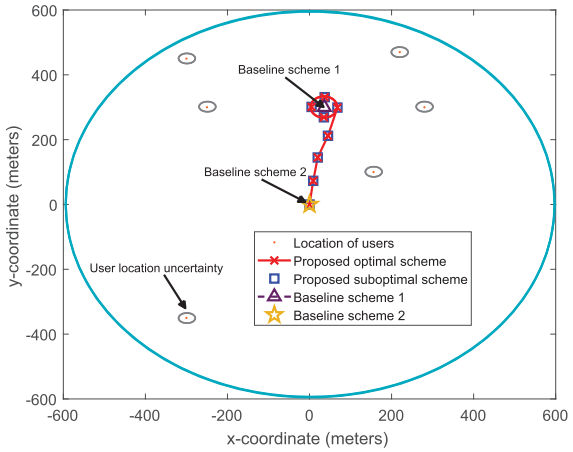

Fig. 6. Trajectory in the horizontal plane for a time horizon of $T = 10$ minutes for different resource allocation schemes in the absence of wind and NFZs.

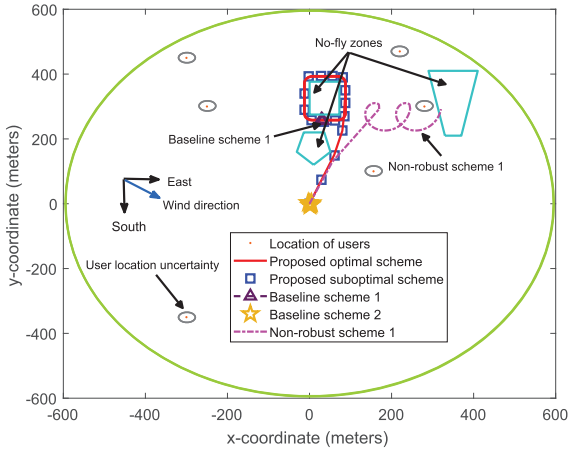

Fig. 7. Trajectory in the horizontal plane for a time horizon of $T = 10$ minutes for different resource allocation schemes in the presence of wind and three NFZs.

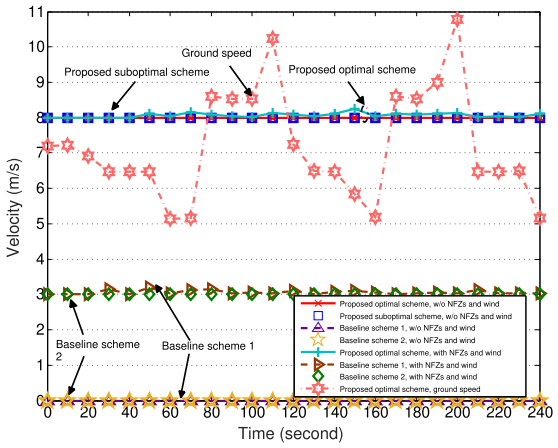

Fig. 8. 2-D velocity (m/s) versus time (s) in horizontal plane for a time horizon $T = 4$ minutes and different resource allocation schemes in the presence of wind speed uncertainty and NFZs.

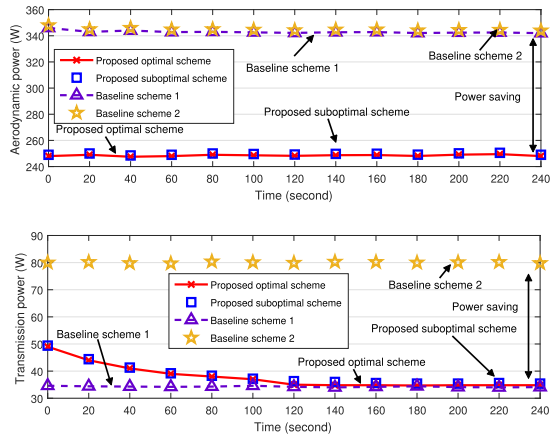

Fig. 9. Upper-half figure: UAV aerodynamic power consumption (W) versus time for different resource allocation schemes; lower-half figure: UAV transmission power consumption (W) versus time for different resource allocation schemes.

all users with an optimized beamforming policy. For baseline scheme 2, the UAV remains stationary at the initial point $(0, 0)$ during the whole time horizon.

In Figure 7, we illustrate the trajectories of the proposed optimal and suboptimal schemes and the baseline schemes in the presence of wind and three polygonal NFZs. The direction of the wind speed estimate is 110° clockwise from north. As can be seen from Figure 7, the addition of wind and three polygonal NFZs changes the trajectory of the UAV. Specifically, for the proposed optimal and suboptimal schemes, the UAV first detours to avoid flying over the pentagon shaped NFZ and then adapts its trajectory by cruising around the rectangular NFZ. In fact, in order to save transmit power, the UAV prefers to fly as close as possible to the majority of the users. Yet, due to the wind speed uncertainty, the UAV has to keep a small safe distance from the boundary of the rectangular shaped NFZ, such that the trajectory does not cross the boundary of the NFZ. For baseline scheme 1, the UAV hovers right outside the rectangular NFZ. In fact, this is a compromise between power-efficient transmission and safety requirements. Moreover, for both baseline schemes, the UAV slightly moves around the desired hovering point due to the wind speed uncertainty. Besides, we also show the trajectory of a non-robust scheme in Figure 7. In particular, for non-robust scheme 1, an optimization problem similar to (25) is formulated and solved by employing the proposed optimization algorithm without taking into account the wind and the NFZs. Compared to the trajectory of the proposed optimal scheme, for non-robust scheme 1, the actual trajectory is significantly altered. In particular, due to the wind, the ground speed varies over time and cannot be fully controlled which leads to a spiral trajectory. Furthermore, the UAV flies over the trapezoid shaped NFZ which violates the safety requirements. In other words, it is impossible to guarantee safety and reliable UAV-assisted communication if the wind speed and the NFZs are not properly taken into account for UAV trajectory design.

B. UAV Velocity, Aerodynamic Power, and Transmit Power versus Time

In Figure 8, we study the horizontal velocity of the UAV during a period of $T = 4$ minutes for different resource allocation schemes and different scenarios. As can be observed,

for the the scenario without NFZs and wind, the UAV flies at a horizontal speed of 8 m/s during the entire period for both the proposed optimal and suboptimal schemes. In fact, the UAV prefers a speed of 8 m/s rather than full speed, since there is no restriction on the total time and cruising the UAV at $|\mathbf{v}_u| = 8$ m/s minimizes the aerodynamic power consumption of the UAV, cf. Figure 4. For the baseline schemes, the UAV hovers at the desired position and the initial point during the entire time horizon, respectively, cf. Figure 6. On the other hand, for the scenario with NFZs and wind, for the proposed optimal and suboptimal schemes, the UAV again starts with a speed of 8 m/s. Then, the UAV has to slightly increases its speed to compensate the negative impact of the wind. For the baseline schemes, the UAV operates with speeds around 3 m/s to compensate the wind speed such that it remains static at the desired position. Besides, in Figure 8, we also depict the ground speed of the UAV for the proposed optimal scheme in the presence of wind and NFZs. In particular, it can be observed that the ground speed changes periodically. This is due to the fact that the UAV circles around the rectangular shaped NFZ.

In Figure 9, we show the aerodynamic and transmit power consumptions of the UAV during a period of $T = 4$ minutes for different resource allocation schemes in the presence of NFZs and wind. In particular, it can be observed that the aerodynamic power consumptions for the proposed optimal and suboptimal schemes and the baseline schemes remain unchanged over the whole considered time horizon. This is due to the fact that, for these schemes, the UAVs either fly with a uniform speed or remain hovering as a result of the respective optimization. On the other hand, the transmit power consumptions for the proposed optimal and suboptimal schemes decrease with time. This is due to the fact that the UAV first flies towards the centroid of the region spanned by the majority of the users which facilitates power efficient data transmission. Meanwhile, the UAV decreases its transmit power while approaching the centroid to maintain the minimum required SINR per user. As for baseline scheme 1, the UAV hovers at the optimal position and employs an efficient beamforming policy which entails almost the same transmit power consumption as the proposed optimal and suboptimal schemes. For baseline scheme 2, the UAV transmitter cannot fully exploit the degrees of freedom (DoFs) available for resource allocation since the beamforming vector $\mathbf{w}_k$ is partially fixed. Hence, a higher transmit power is required to the QoS constraints of the ground users.

C. Average Total UAV Power Consumption Versus Wind Speed Estimate

In Figure 10, we study the average total UAV power consumption versus wind speed estimate $|\overline{\mathbf{v}}_w|$ for different resource allocation schemes and different maximum normalized wind speed uncertainties ρ_w in the presence of three NFZs. As can be observed, when $|\overline{\mathbf{v}}_w| \leq 9$ m/s, the average total UAV power consumption of the proposed optimal and suboptimal schemes slightly increases with $|\overline{\mathbf{v}}_w|$. This is due to the fact that for wind speed estimates of less than 9 m/s, a UAV with a speed of 8 m/s, which is preferable with respect to its aerodynamic power consumption, can always adjust its air speed direction such that the desired trajectory can be followed. In contrast, when $|\overline{\mathbf{v}}_w| > 9$ m/s, for safety reason, the UAV has to decrease its speed such that the UAV ground speed will not exceed the maximum ground speed $V_g^{\max} = 18$ m/s. This leads to a substantially higher aerodynamic power consumption, cf. Figure 4. On the other hand, for the two baseline schemes, as $|\overline{\mathbf{v}}_w|$ increases, the total power consumption first dramatically decreases and then rapidly increases. In particular, when $|\overline{\mathbf{v}}_w|$ increases from 0 to 8 m/s, the UAV has to speed up to counteract the wind speed and maintain hovering at the desired position. According to Figure 4, this is beneficial for the consumed aerodynamic power. As $|\overline{\mathbf{v}}_w|$ further increases, a higher speed and thus, a higher aerodynamic power consumption is required for hovering. Furthermore, as can be observed, for wind speed estimates of less than 6 m/s, the proposed optimal and suboptimal schemes achieve substantial power savings compared to the two baseline schemes. In fact, for the proposed optimal and suboptimal schemes, trajectory design introduces extra DoFs, which provides substantial power savings over the baseline schemes with their stationary UAVs.

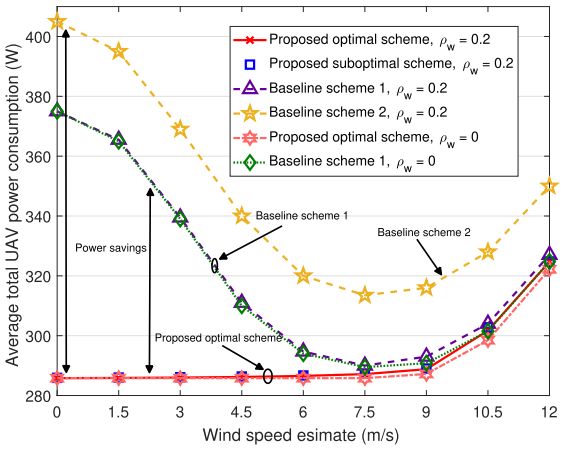

Fig. 10. Average total UAV power consumption (Watt) versus wind speed estimate $|\overline{\mathbf{v}}_w|$ for different resource allocation schemes in the presence of wind speed uncertainty and NFZs.

D. Average Total UAV Power Consumption Versus Number of Transmit Antennas

In Figure 11, we study the average total UAV power consumption versus the number of antennas equipped at the UAV, M, for different resource allocation schemes in the presence of wind speed uncertainty and three NFZs. In addition to baseline schemes 1 and 2, we consider a further baseline scheme in this subsection. In particular, for baseline scheme 3, the UAV orbits around the origin $(0, 0)$ with uniform speed and employs zero-forcing (ZF) beamforming such that multiuser interference (MUI) is avoided at the users. Specifically, based on the estimated AoD, the direction of beamforming vector $\mathbf{w}_k$ for desired user k is fixed and lies in the null space spanned by all the other users' channels. Then, we jointly

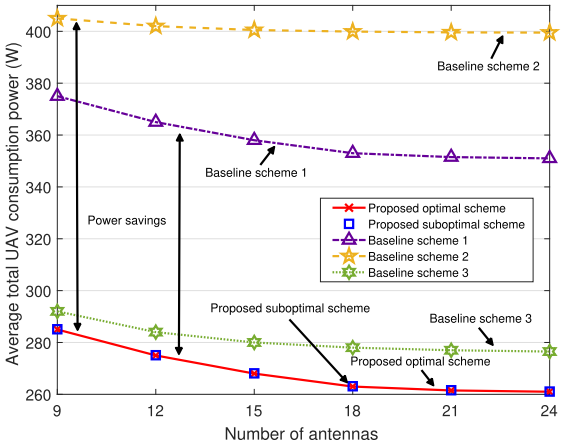

Fig. 11. Average total UAV power consumption (Watt) versus number of antennas at the UAV, M, for different resource allocation schemes in the presence of wind speed uncertainty and NFZs.

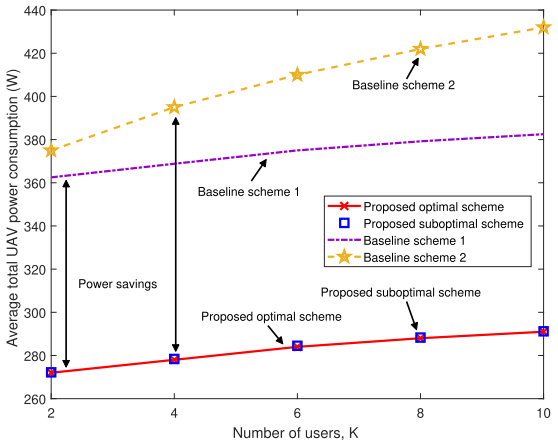

Fig. 12. Average total UAV power consumption (Watt) versus number of users, K, for $M = 12$ antennas at the UAV and different resource allocation schemes in the presence of wind speed uncertainty and NFZs.

optimize the speed of the UAV and the power allocated to $\mathbf{w}_k$ for minimization of the total UAV power consumption subject to transmit power constraint C1, QoS constraint C2, and maximum speed constraints C5 and C6 as in (25). As can be observed, for the proposed schemes and baseline schemes 1, 2, and 3, the total UAV power consumption decreases as the number of transmit antennas increases. This is due to the fact that the extra DoFs provided by the additional antennas facilitate a more precise beamforming and can efficiently mitigate MUI. In particular, a substantial performance gain can be achieved when increasing the number of antennas, as the resulting beamforming gain outweighs the additional incurred circuit power consumption. Yet, there is a diminishing return in the performance gain for larger numbers of antennas due to channel hardening. Furthermore, we can observe that the three baseline schemes consume considerably more power compared to the proposed optimal and suboptimal schemes. In particular, for baseline scheme 1, a substantial amount of power is consumed to maintain the hovering status. While for baseline scheme 2, in addition to the considerable power needed for hovering, the fixed MRT beamforming policy also leads to a higher transmit power consumption. This is because the fixed MRT beamforming vector is unable to fully exploit the extra DoFs introduced by additional transmit antennas. As a result, the total UAV power consumption decreases only slightly as the number of transmit antennas increases. For baseline scheme 3, the total power consumption is also higher compared to that of the proposed optimal and suboptimal schemes. This is due to the fact that the UAV transmitter cannot fully exploit the available DoFs since the ZF beamforming vector is partially fixed which negatively affects the required transmit power.

E. Average Total UAV Power Consumption Versus Number of Users

In Figure 12, we investigate the average total UAV power consumption versus the number of users for different resource allocation schemes in the presence of wind and NFZs. As can be observed, the average total UAV power consumption for

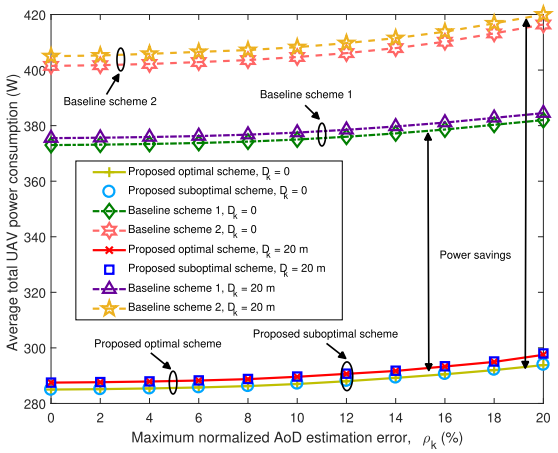

Fig. 13. Average total UAV power consumption (Watt) versus maximum normalized AoD estimation error, ρ_k, for different resource allocation schemes in the presence of wind speed uncertainty and NFZs.

the proposed schemes and the baseline schemes increases with the number of users. This is because, if the number of users is higher, the UAV-mounted transmitter has to dedicate more DoFs to MUI mitigation which decreases the flexibility in trajectory and beamforming design leading to a performance degradation. Moreover, it can be observed that the proposed suboptimal scheme closely approaches the performance of the optimal scheme for all considered numbers of users. The two baseline schemes cause a substantially higher power consumption compared to the proposed schemes. This is due to the fact that the baseline schemes cannot fully exploit the DoFs introduced by the mobility of the UAV. For baseline scheme 2, in addition to the considerable power needed for hovering, the fixed MRT beamforming policy leads to a substantial increase in transmit power.

F. Average Total UAV Power Consumption Versus Maximum Normalized AoD Estimation Error

In Figure 13, we study the average total UAV power consumption versus the maximum normalized AoD estimation error, ρ_k, for different resource allocation schemes and

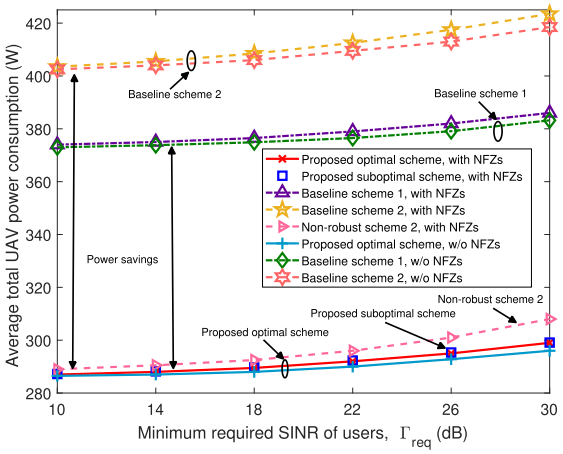

Fig. 14. Average total UAV power consumption (Watt) versus the minimum required SINR of the users, Γ_{req_k}, for different resource allocation schemes in the presence of wind speed uncertainty and NFZs.

different user location uncertainties in the presence of wind speed uncertainty and NFZs. As expected, the total UAV power consumption for all schemes increases monotonically with ρ_k. This can be explained by the fact that, as the AoD estimation error increases, the AAR uncertainty increases. As a result, it becomes more difficult for the UAV-mounted transmitter to perform accurate beamforming. Hence, the UAV-mounted transmitter is forced to transmit the information signal with a higher power to meet the QoS requirements of the users. Moreover, we observe that the total UAV power consumption for all schemes increases with increasing user location uncertainty radius D_k. In fact, for larger D_k, the UAV has to employ a less focused beamformer to cover the whole user location uncertainty area which leads to a higher transmit power for satisfying the users' QoS requirements. Furthermore, the proposed optimal and suboptimal schemes achieve considerable power savings compared to the two baseline schemes due to the joint optimization of the 2-D trajectory and the beamforming policy. In fact, the optimal trajectory and the optimal beamforming policy complement each other for efficient reduction of the total power consumption. On the one hand, the trajectory design allows the UAV to perform beamforming at the most favourable position. On the other hand, due to the precise beamforming, the UAV can follow its trajectory at the most power-efficient speed.

G. Average Total UAV Power Consumption Versus Minimum Required User SINRs

Figure 14 shows the average total UAV power consumption versus the minimum required user SINRs, Γ_{req_k}, for different resource allocation schemes. As expected, the average total UAV power consumption of all schemes is monotonically non-decreasing with respect to the minimum SINR threshold Γ_{req}. To meet a more stringent minimum required SINR, the UAV has to increase its transmit power. Moreover, compared to the scenario without NFZs, all considered schemes consume slightly more power in the presence of NFZs. In fact, for the proposed optimal and suboptimal schemes, the UAV has to circle around the NFZs, whereas for baseline scheme 1, the UAV has to adopt a suboptimal hovering position to avoid trespassing the NFZs, which leads to a higher transmit power, cf. Figure 7. Besides, we also show the average total power consumption of non-robust scheme 2 in Figure 14. In particular, for non-robust scheme 2, an optimization problem similar to (25) is formulated and solved but the estimated AoD and user locations are treated as the actual ones. Then, using the actual AoDs and user locations (which is not possible in practice, of course), we loosen the power constraint in C1 until the resulting beamforming vectors $\mathbf{w}_k$ satisfy the QoS requirements of all users. As can be observed, non-robust scheme 2 results in a higher total power consumption compared to the proposed robust scheme across the entire considered range of Γ_{req}. In fact, due to the AoD and user location uncertainties, the focused beamforming vector of non-robust scheme 2 may point into a the wrong direction, cf. Figure 2, which degrades the system performance.

VI. Conclusion

In this paper, we investigated the optimal robust trajectory and beamforming algorithm design for multiuser MISO UAV communication systems. Since UAV jittering and user location uncertainty can severely degrade the system performance while wind speed uncertainty and NFZs may lead to safety concerns, we took these aspects into account to facilitate reliable and safe communication services for ground users. In particular, we jointly optimized the 2-D trajectory and the downlink beamformer of a UAV for minimization of the total UAV power consumption. The problem formulation took into account AoD estimation errors caused by UAV jittering, user location uncertainty, wind speed uncertainty, and polygonal NFZs. Since the coupling of the AoDs and the UAV trajectory makes joint resource allocation design across multiple time slots intractable, we optimized the trajectory and the beamforming policy on a time slot by time slot basis. Despite the non-convexity of the resulting problem, we solved the problem optimally by employing monotonic optimization theory and SDP relaxation. To strike a balance between optimality and computational complexity, we also proposed a suboptimal iterative low-complexity scheme based on SCA. Our results reveal not only the significant power savings enabled by the proposed optimal and suboptimal schemes compared to two baseline and two non-robust schemes, but also confirm their robustness with respect to UAV jittering and user location uncertainty. Moreover, our results show that the UAV can fly along the desired trajectory with the minimum possible aerodynamic power consumption if the average wind speed is smaller than the maximum endurance speed of the UAV. Besides, our results unveil that a robust design is necessary to ensure safe operation of the UAV in the presence of wind speed uncertainty and NFZs.

Appendix

A. Proof of Theorem 1

We start the proof by rewriting constraint C7 as $\bigvee_{i\in\mathcal{S}_j} Y_i(\mathbf{r}_0') = 1,\ \forall j$. In particular, we first assume that equality

$\bigvee_{i\in\mathcal{S}_j} Y_i(\mathbf{r}_0') = 1,\ \forall j$, holds. Then, there exist $\mathbf{r}_0'$ satisfying at least one of the S_j inequalities $\mathbf{p}_{ij}^T\mathbf{r}_0' \geq q_{ij},\ \forall i,\ \forall j$. Moreover, since $l_{ij} \in \{0,1\}$ and $G \gg 1$, inequality $\mathbf{p}_{ij}^T\mathbf{r}_0' - q_{ij} + Gl_{ij} \geq 0,\ \forall i,\ \forall j$, holds.

On the other hand, assume that there exist $\mathbf{r}_0'$ satisfying the inequality $\mathbf{p}_{ij}^T\mathbf{r}_0' - q_{ij} + Gl_{ij} \geq 0,\ \forall i,\ \forall j$. Since the binary variable l_{ij} meets the inequality $\sum_{i\in\mathcal{S}_j} l_{ij} \leq S_j - 1,\ \forall j$, at least one l_{ij} is equal to 0. Consequently, at least one of the S_j inequalities $\mathbf{p}_{ij}^T\mathbf{r}_0' - q_{ij} + Gl_{ij} \geq 0$ must hold for $l_{ij} = 0$. As a result, $\mathbf{r}_0'$ satisfies at least one inequality $\mathbf{p}_{ij}^T\mathbf{r}_0' \geq q_{ij}\ \forall i,\ \forall j$. Hence, the logical equality $\bigvee_{i\in\mathcal{S}_j} Y_i(\mathbf{r}_0') = 1,\ \forall j$, holds and the proof of Theorem 1 is complete.

B. Proof of Theorem 3

We start the proof by exploiting the abstract Lagrangian duality [62]. In particular, we define

$$\widetilde{\mathcal{L}}(\mathbf{W}_k, g, l_{ij}, \chi) = \sum_{k\in\mathcal{K}} \mathrm{Tr}(\mathbf{W}_k) + g + \chi \sum_{j\in\mathcal{J}} \sum_{i\in S_j} \left(l_{ij} - l_{ij}^2\right). \tag{69}$$

We note that $\widetilde{\mathcal{L}}(\mathbf{W}_k, g, l_{ij}, \chi)$ is upper bounded if $\chi \geq 0$ and $\sum_{j\in\mathcal{J}} \sum_{i\in S_j} \left(l_{ij} - l_{ij}^2\right) \leq 0$. Thus, we can rewrite the optimization problem in (60) equivalently as

$$\phi^* = \underset{\substack{\mathbf{W}_k,\mathbf{r}_0',\mathbf{v}_u,\\ l_{ij},\mathcal{A},g}}{\mathrm{minimize}} \underset{\chi\geq 0}{\mathrm{maximize}} \widetilde{\mathcal{L}}(\mathbf{W}_k, g, l_{ij}, \chi), \tag{70}$$

where ϕ^* denotes the optimal value of (60). On the other hand, the dual problem of (60) is given by

$$\underset{\chi\geq 0}{\mathrm{maximize}} \underset{\substack{\mathbf{W}_k,\mathbf{r}_0',\mathbf{v}_u,\\ l_{ij},\mathcal{A},g}}{\mathrm{minimize}} \widetilde{\mathcal{L}}(\mathbf{W}_k, g, l_{ij}, \chi) = \underset{\chi\geq 0}{\mathrm{maximize}} \boldsymbol{\Upsilon}(\chi), \tag{71}$$

where $\boldsymbol{\Upsilon}(\chi)$ is defined as $\boldsymbol{\Upsilon}(\chi) \triangleq \underset{\substack{\mathbf{W}_k,\mathbf{r}_0',\mathbf{v}_u,\\ l_{ij},\mathcal{A},g}}{\mathrm{minimize}} \widetilde{\mathcal{L}}(\mathbf{W}_k, g, l_{ij}, \chi)$ for notational simplicity. Then, the primal problem (70) and the equivalent dual problem (71) meet the following inequalities:

$$\begin{aligned} &\underset{\chi\geq 0}{\mathrm{maximize}}\ \boldsymbol{\Upsilon}(\chi) \\ &= \underset{\chi\geq 0}{\mathrm{maximize}}\ \underset{\substack{\mathbf{W}_k,\mathbf{r}_0',\mathbf{v}_u,\\ l_{ij},\mathcal{A},g}}{\mathrm{minimize}}\ \widetilde{\mathcal{L}}(\mathbf{W}_k, g, l_{ij}, \chi) \\ &\overset{(a)}{\leq} \underset{\substack{\mathbf{W}_k,\mathbf{r}_0',\mathbf{v}_u,\\ l_{ij},\mathcal{A},g}}{\mathrm{minimize}}\ \underset{\chi\geq 0}{\mathrm{maximize}}\ \widetilde{\mathcal{L}}(\mathbf{W}_k, g, l_{ij}, \chi) = \phi^*, \end{aligned} \tag{72}$$

where (a) is due to the weak duality. We note that $\widetilde{\mathcal{L}}(\mathbf{W}_k, g, l_{ij}, \chi)$ is monotonically increasing in variable χ since $\sum_{j\in\mathcal{J}} \sum_{i\in S_j} \left(l_{ij} - l_{ij}^2\right) \geq 0$ for $0 \leq l_{ij} \leq 1,\ \forall i,\ \forall j$. As a result, $\boldsymbol{\Upsilon}(\chi)$ is also increasing with χ. Moreover, (72) implies that $\boldsymbol{\Upsilon}(\chi)$ is bounded from above by the optimal value of problem (60), i.e., ϕ^*. Denote the optimal solution of the dual problem in (71) by χ^* and $\Phi^* \triangleq \{\mathbf{W}_k^*, (\mathbf{r}_0')^*, \mathbf{v}_u^*, l_{ij}^*\mathcal{A}^*, g^*\}$. Then, we study the solution structure of the dual problem (71) by considering the following two cases. For the first case, we assume that $\sum_{j\in\mathcal{J}} \sum_{i\in S_j} \left(l_{ij}^* - (l_{ij}^*)^2\right) = 0$ for the dual problem in (71). As a result, Φ^* is also a feasible solution to the primal problem in (60). Consequently, by substituting Φ^* into the optimization problem in (26), we have

$$\phi^* \leq \sum_{k\in\mathcal{K}} \mathrm{Tr}(\mathbf{W}_k^*) + g^* \overset{(b)}{=} \widetilde{\mathcal{L}}(\mathbf{W}_k^*, g^*, l_{ij}^*, \chi^*) = \boldsymbol{\Upsilon}(\chi^*), \tag{73}$$

where (b) is due to the assumption of $\sum_{j\in\mathcal{J}} \sum_{i\in S_j} \left(l_{ij}^* - (l_{ij}^*)^2\right) = 0$. By combining (72) and (73), we can conclude that the gap between the equivalent primal problem (70) and the dual problem (71) is zero, i.e.,

$$\begin{aligned} &\underset{\chi\geq 0}{\mathrm{maximize}} \underset{\substack{\mathbf{W}_k,\mathbf{r}_0',\mathbf{v}_u,\\ l_{ij},\mathcal{A},g}}{\mathrm{minimize}} \widetilde{\mathcal{L}}(\mathbf{W}_k, g, l_{ij}, \chi) \\ &\qquad = \underset{\substack{\mathbf{W}_k,\mathbf{r}_0',\mathbf{v}_u,\\ l_{ij},\mathcal{A},g}}{\mathrm{minimize}} \underset{\chi\geq 0}{\mathrm{maximize}} \widetilde{\mathcal{L}}(\mathbf{W}_k, g, l_{ij}, \chi) \end{aligned} \tag{74}$$

must hold for $\sum_{j\in\mathcal{J}} \sum_{i\in S_j} \left(l_{ij} - l_{ij}^2\right) = 0$. Furthermore, the monotonicity of $\boldsymbol{\Upsilon}(\chi)$ with respect to χ implies that $\boldsymbol{\Upsilon}(\chi) = \phi^*,\ \forall \chi \geq \chi^*$, which proves the result in Theorem 3.

Next, we study the case of $\sum_{j\in\mathcal{J}} \sum_{i\in S_j} \left(l_{ij}^* - (l_{ij}^*)^2\right) > 0$ for the dual problem in (71). In this case, $\boldsymbol{\Upsilon}(\chi^*) = \underset{\chi\geq 0}{\mathrm{maximize}} \boldsymbol{\Upsilon}(\chi) \to \infty$ is unbounded from above since $\boldsymbol{\Upsilon}(\chi)$ is monotonically increasing in χ. This contradicts the inequality in (72) as the primal problem in (60) has a finite objective value. Therefore, $\sum_{j\in\mathcal{J}} \sum_{i\in S_j} \left(l_{ij}^* - (l_{ij}^*)^2\right) = 0$ holds for the optimal solution and the proof of Theorem 3 is complete.

REFERENCES

[1] D. Xu, Y. Sun, D. W. K. Ng, and R. Schober, "Robust resource allocation for UAV systems with UAV jittering and user location uncertainty," in *Proc. IEEE Global Commun. Workshop Wireless Netw. Control Unmanned Auton. Vehicles*, Dec. 2018, pp. 1–6.

[2] V. W. S. Wong, R. Schober, D. W. K. Ng, and L. C. Wang, *Key Technologies for 5G Wireless Systems*. Cambridge, U.K.: Cambridge Univ. Press, 2017.

[3] J. Zhang, E. Björnson, M. Matthaiou, D. W. K. Ng, H. Yang, and D. J. Love, "Multiple antenna technologies for beyond 5G," 2019, *arXiv:1905.01094*. [Online]. Available: https://arxiv.org/abs/1905.01094

[4] S. Hayat, E. Yanmaz, and R. Muzaffar, "Survey on unmanned aerial vehicle networks for civil applications," *IEEE Commun. Surveys Tuts.*, vol. 18, no. 4, pp. 2624–2661, 2nd Quart., 2016.

[5] Y. Zeng and R. Zhang, "Energy-efficient UAV communication with trajectory optimization," *IEEE Trans. Wireless Commun.*, vol. 16, no. 6, pp. 3747–3760, Jun. 2017.

[6] Q. Wu, Y. Zeng, and R. Zhang, "Joint trajectory and communication design for multi-UAV enabled wireless networks," *IEEE Trans. Wireless Commun.*, vol. 17, no. 3, pp. 2109–2121, Mar. 2018.

[7] G. Zhang, Q. Wu, M. Cui, and R. Zhang, "Securing UAV communications via trajectory optimization," in *Proc. IEEE Global Commun. Conf. (GLOBECOM)*, Dec. 2017, pp. 1–6.

[8] Y. Sun, D. Xu, D. W. K. Ng, L. Dai, and R. Schober, "Optimal 3D-trajectory design and resource allocation for solar-powered UAV communication systems," *IEEE Trans. Commun.*, vol. 67, no. 6, pp. 4281–4298, Jun. 2019.

[9] D. W. K. Ng, E. S. Lo, and R. Schober, "Robust beamforming for secure communication in systems with wireless information and power transfer," *IEEE Trans. Wireless Commun.*, vol. 13, no. 8, pp. 4599–4615, Aug. 2014.

[10] F. Jiang and A. L. Swindlehurst, "Optimization of UAV heading for the ground-to-air uplink," *IEEE J. Sel. Areas Commun.*, vol. 30, no. 5, pp. 993–1005, Jun. 2012.

[11] Q. Song, S. Jin, and F.-C. Zheng, "Joint power allocation and beamforming for UAV-enabled relaying systems with channel estimation errors," in *Proc. IEEE 87th Veh. Technol. Conf. (VTC Spring)*, Jun. 2018, pp. 1–5.

[12] J. Verbeke and S. Debruyne, "Vibration analysis of a UAV multirotor frame," in *Proc. ISMA Int. Conf. Noise Vib. Eng.*, Sep. 2016, pp. 2401–2409.

[13] Z. Li, M. Lao, and S. K. Phang, "Development and design methodology of an anti-vibration system on micro-UAVs," in *Proc. Int. Micro Air Vehicle Conf. Flight Competition*, Sep. 2017, pp. 223–228.

[14] W. J. Hughes Technical Center, "Global positioning system standard positioning service performance analysis report," GPS Product Team, Federal Aviation Admin., SeaTac, WA, USA, Tech. Rep. 102, Jan. 2015.

[15] H. S. Choi, S. Lee, H. Ryu, H. Shim, and C. Ha, "Dynamics and simulation of the effects of wind on UAVs and airborne wind measurement," *Trans. Jpn. Soc. Aeronaut. Space Sci.*, vol. 58, no. 4, pp. 187–192, Jun. 2015.

[16] B. Ahmed, H. R. Pota, and M. Garratt, "Flight control of a rotary wing UAV using backstepping," *Int. J. Robust Nonlinear Control*, vol. 20, no. 6, pp. 639–658, 2009.

[17] N. Sun and J. Wu, "Minimum error transmissions with imperfect channel information in high mobility systems," in *Proc. IEEE Mil. Commun. Conf. (MILCOM)*, Nov. 2013, pp. 922–927.

[18] X. Lin *et al.*, "The sky is not the limit: LTE for unmanned aerial vehicles," *IEEE Commun. Mag.*, vol. 56, no. 4, pp. 204–210, Apr. 2018.

[19] A. Birk, E. Wiggerich, H. Bülow, M. Pfingsthorn, and S. Schwertfeger, "Safety, security, and rescue missions with an unmanned aerial vehicle (UAV)," *J. Intell. Robot. Syst.*, vol. 64, no. 1, pp. 57–76, Oct. 2011.

[20] K. P. Valavanis and G. J. Vachtsevanos, *Handbook of Unmanned Aerial Vehicles*. Dordrecht, The Netherlands: Springer, 2015.

[21] P. Zhao, W. Chen, and W. Yu, "Guidance law for intercepting target with multiple no-fly zone constraints," *Aeronaut. J.*, vol. 121, no. 1244, pp. 1479–1501, Oct. 2017.

[22] T. Shima and S. Rasmussen, *UAV Cooperative Decision and Control: Challenges and Practical Approaches*. Philadelphia, PA, USA: SIAM, 2009.

[23] R. Li *et al.*, "Joint trajectory and resource allocation design for UAV communication systems," in *Proc. IEEE Globecom Workshops (GC Wkshps)*, Dec. 2018, pp. 1–6.

[24] Worldwide Aviation Database. *OpenAIP*. Accessed: May 2019. [Online]. Available: http://maps.openaip.net/

[25] E. Balas, "Disjunctive programming," in *Annals of Discrete Mathematics*, vol. 5. Amsterdam, The Netherlands: Elsevier, 1979, pp. 3–51.

[26] Y. J. A. Zhang, L. P. Qiang, and J. W. Huang, "Monotonic optimization in communication and networking systems," *Found. Trends Netw.*, vol. 7, no. 1, pp. 1–75, 2013.

[27] Y. Sun, D. W. K. Ng, J. Zhu, and R. Schober, "Multi-objective optimization for robust power efficient and secure full-duplex wireless communication systems," *IEEE Trans. Wireless Commun.*, vol. 15, no. 8, pp. 5511–5526, Aug. 2016.

[28] Q. T. Dinh and M. Diehl, "Local convergence of sequential convex programming for nonconvex optimization," in *Recent Advances in Optimization and its Applications in Engineering*. Berlin, Germany: Springer, 2010, pp. 93–102.

[29] F. Hodjat and S. Hovanessian, "Nonuniformly spaced linear and planar array antennas for sidelobe reduction," *IEEE Trans. Antennas Propag.*, vol. AP-26, no. 2, pp. 198–204, Mar. 1978.

[30] S. A. Bortoff, "Path planning for UAVs," in *Proc. IEEE Amer. Control Conf.*, Sep. 2000, vol. 1, no. 6, pp. 364–368.

[31] R. Y. Sun and D. W. Matolak, "Air-ground channel characterization for unmanned aircraft systems part II: Hilly and mountainous settings," *IEEE Trans. Veh. Technol.*, vol. 66, no. 3, pp. 1913–1925, Jun. 2017.

[32] D. Tse and P. Viswanath, *Fundamentals of Wireless Communication*. Cambridge, U.K.: Cambridge Univ. Press, 2005.

[33] A. Colpaert, E. Vinogradov, and S. Pollin, "Aerial coverage analysis of cellular systems at LTE and mmWave frequencies using 3D city models," *Sensors*, vol. 18, no. 12, pp. 4311–4327, Dec. 2018.

[34] A. Al-Hourani, S. Kandeepan, and S. Lardner, "Optimal LAP altitude for maximum coverage," *IEEE Wireless Commun. Lett.*, vol. 3, no. 6, pp. 569–572, Dec. 2014.

[35] A. Da Ronch, *Advanced UAV Aerodynamics, Flight Stability and Control*. Hoboken, NJ, USA: Wiley, 2017.

[36] Z. Liu, R. Sengupta, and A. Kurzhanskiy, "A power consumption model for multi-rotor small unmanned aircraft systems," in *Proc. Int. Conf. Unmanned Aircr. Syst. (ICUAS)*, Jun. 2017, pp. 310–315

[37] A. Cho, J. Kim, S. Lee, and C. Kee, "Wind estimation and airspeed calibration using a UAV with a single-antenna GPS receiver and pitot tube," *IEEE Trans. Aerosp. Electron. Syst.*, vol. 47, no. 1, pp. 109–117, Jan. 2011.

[38] B. Harper, J. Kepert, and J. Ginger, *Guidelines for Converting between Various Wind Averaging Periods in Tropical Cyclone Conditions*. Geneva, Switzerland: World Meteorological Organization, 2010.

[39] *An Overview LTE Positioning (White Paper)*, Spirent, Crawley, U.K., 2012.

[40] F. Zimmermann, C. Eling, L. Klingbeil, and H. Kuhlmann, "Precise positioning of UAVs-dealing with challenging RTK-GPS measurement conditions during automated UAV flights," *ISPRS Ann.*, vol. 4, pp. 95–102, Aug. 2017.

[41] T. Cormen, C. Leiserson, R. Rivest, and C. Stein, *Introduction to Algorithms*. Cambridge, MA, USA: MIT Press, 2009.

[42] P. J. Enright and B. A. Conway, "Discrete approximations to optimal trajectories using direct transcription and nonlinear programming," *J. Guid., Control, Dyn.*, vol. 15, no. 4, pp. 994–1002, Jul. 1992.

[43] W. Johnson, *Helicopter Theory*. Chelmsford, MA, USA: Courier Corporation, 2014.

[44] J. Seddon and S. Newman, *Basic Helicopter Aerodynamics*, 3rd ed. Hoboken, NJ, USA: Wiley, 2011.

[45] Y. Zeng, J. Xu, and R. Zhang, "Energy minimization for wireless communication with rotary-wing UAV," *IEEE Trans. Wireless Commun.*, vol. 18, no. 4, pp. 2329–2345, Apr. 2019.

[46] B. H. Wang, D. B. Wang, Z. A. Ali, B. T. Ting, and H. Wang, "An overview of various kinds of wind effects on unmanned aerial vehicle," *Meas. Control*, vol. 52, nos. 7–8, pp. 731–739, Sep. 2019.

[47] F. Schiano, J. Alonso-Mora, K. Rudin, P. Beardsley, R. Siegwart, and B. Sicilianok, "Towards estimation and correction of wind effects on a quadrotor UAV," in *Proc. Int. Micro Air Vehicle Conf. Competition (IMAV)*, vol. 52, May 2014, pp. 134–141.

[48] F. Cheng and J. Gulding, "Computing wind-optimal routes for flight performance benchmarking," in *Proc. 16th AIAA Aviation Technol., Integr., Oper. Conf.*, 2016, p. 1

[49] L. Gupta, R. Jain, and G. Vaszkun, "Survey of important issues in UAV communication networks," *IEEE Commun. Surveys Tuts.*, vol. 18, pp. 1123–1152, 2nd Quart., 2017.

[50] R. Hettich and K. O. Kortanek, "Semi-infinite programming: Theory, methods, and applications," *Soc. Ind. Appl. Math.*, vol. 35, no. 3, pp. 380–429, Sep. 1993.

[51] Y. Zeng, R. Zhang, and T. J. Lim, "Wireless communications with unmanned aerial vehicles: Opportunities and challenges," *IEEE Commun. Mag.*, vol. 54, no. 5, pp. 36–42, May 2016.

[52] Y. Sun, D. W. K. Ng, J. Zhu, and R. Schober, "Robust and secure resource allocation for full-duplex MISO multicarrier NOMA systems," *IEEE Trans. Commun.*, vol. 66, no. 9, pp. 4119–4137, Sep. 2018.

[53] E. Boshkovska, D. W. K. Ng, N. Zlatanov, A. Koelpin, and R. Schober, "Robust resource allocation for MIMO wireless powered communication networks based on a non-linear EH model," *IEEE Trans. Commun.*, vol. 65, no. 5, pp. 1984–1999, May 2017.

[54] S. Boyd and L. Vandenberghe, *Convex Optimization*. Cambridge, U.K.: Cambridge Univ. Press, 2004.

[55] A. Richards and J. P. How, "Aircraft trajectory planning with collision avoidance using mixed integer linear programming," in *Proc. Amer. Control Conf.*, May 2002, vol. 3, no. 3, pp. 1936–1941.

[56] H. Tuy, "Monotonic optimization: Problems and solution approaches," *SIAM J. Optim.*, vol. 11, no. 2, pp. 464–494, Jan. 2000.

[57] M. Grant and S. Boyd. (Mar. 2014). *CVX: MATLAB Software for Disciplined Convex Programming, Version 2.1*. [Online]. Available: http://cvxr.com/cvx

[58] D. Ng and R. Schober, "Cross-layer scheduling for OFDMA amplify-and-forward relay networks," *IEEE Trans. Veh. Technol.*, vol. 59, no. 3, pp. 1443–1458, Mar. 2010.

[59] D. W. K. Ng and R. Schober, "Secure and green SWIPT in distributed antenna networks with limited backhaul capacity," *IEEE Trans. Wireless Commun.*, vol. 14, no. 9, pp. 5082–5097, Sep. 2015.

[60] D. W. K. Ng, Y. Wu, and R. Schober, "Power efficient resource allocation for full-duplex radio distributed antenna networks," *IEEE Trans. Wireless Commun.*, vol. 15, no. 4, pp. 2896–2911, Apr. 2016.

[61] I. Pólik and T. Terlaky, "Interior point methods for nonlinear optimization," *Nonlinear Optimization*. Berlin, Germany: Springer, 2010, pp. 215–276.
[62] C. Goh and X. Q. Yang, *Duality in Optimization and Variational Inequalities*. London, U.K.: CRC Press, 2002.

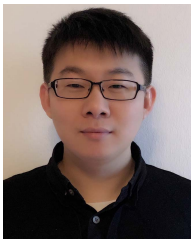

Dongfang Xu (Student Member, IEEE) received the B.S. degree in communication engineering from Shandong University, Jinan, China, in 2014, and the M.S. degree in communication and multimedia engineering from Friedrich-Alexander-University Erlangen-Nürnberg, Erlangen, Germany, in 2017, where he is currently pursuing the Ph.D. degree in electrical engineering. His research interests include convex and nonconvex optimization, unmanned aerial vehicle communications, and physical layer security.

Yan Sun (Member, IEEE) received the B.S. degree in communication engineering from the PLA Information Engineering University, Zhengzhou, China, in 2011, the M.S. degree in telecommunication engineering from Xidian University, Xi'an, China, in 2014, and the Ph.D. degree in electrical engineering from Friedrich-Alexander-University Erlangen-Nürnberg (FAU), Erlangen, Germany, in 2019.

He currently works as a Senior Research Engineer with Huawei, Shanghai, China. His research interests include convex and non-convex optimization, UAV communications, and AI-aided air-interface. He was awarded the IEEE Student Travel Grant for attending the IEEE Global Telecommunication Conference (Globecom) 2016 and IEEE International Conference on Acoustics, Speech and Signal Processing (ICASSP) 2017. He was also honoured as an Exemplary Reviewer of IEEE TRANSACTION ON COMMUNICATIONS in 2017 and 2018, the Best Reviewer of IEEE TRANSACTION ON WIRELESS COMMUNICATIONS in 2017, and an Exemplary Reviewer of IEEE COMMUNICATION LETTER in 2016 and 2017, respectively.

Derrick Wing Kwan Ng (Senior Member, IEEE) received the bachelor's degree (Hons.) and the M.Phil. degree in electronic engineering from The Hong Kong University of Science and Technology (HKUST) in 2006 and 2008, respectively, and the Ph.D. degree from The University of British Columbia (UBC) in 2012. He was a Senior Post-Doctoral Fellow at the Institute for Digital Communications, Friedrich-Alexander-University Erlangen-Nürnberg (FAU), Germany. He is currently working as a Senior Lecturer and a Scientia Fellow of the University of New South Wales, Sydney, Australia. His research interests include convex and non-convex optimization, physical layer security, wireless information and power transfer, and green (energy-efficient) wireless communications. He received the Best Paper Awards at the IEEE TCGCC Best Journal Paper Award 2018, INISCOM 2018, IEEE International Conference on Communications (ICC) 2018, IEEE International Conference on Computing, Networking and Communications (ICNC) 2016, IEEE Wireless Communications and Networking Conference (WCNC) 2012, the IEEE Global Telecommunication Conference (Globecom) 2011, and the IEEE Third International Conference on Communications and Networking in China 2008. He has been serving as an editorial assistant to the Editor-in-Chief of IEEE TRANSACTIONS ON COMMUNICATIONS since January 2012. In addition, he is listed as a Highly Cited Researcher by Clarivate Analytics in 2018 and 2019, respectively.

Robert Schober (Fellow, IEEE) received the Diploma (Univ.) and Ph.D. degrees in electrical engineering from Friedrich-Alexander University of Erlangen-Nüremberg (FAU), Germany, in 1997 and 2000, respectively.

From 2002 to 2011, he was a Professor and Canada Research Chair at The University of British Columbia (UBC), Vancouver, Canada. Since January 2012, he has been an Alexander von Humboldt Professor and the Chair for Digital Communication at FAU. His research interests fall into the broad areas of communication theory, wireless communications, and statistical signal processing. He currently serves as a member of the Editorial Board of the PROCEEDINGS OF THE IEEE and as the VP Publications for the IEEE Communication Society (ComSoc). He received several awards for his work, including the 2002 Heinz Maier- Leibnitz Award of the German Science Foundation (DFG), the 2004 Innovations Award of the Vodafone Foundation for Research in Mobile Communications, a 2006 UBC Killam Research Prize, a 2007 Wilhelm Friedrich Bessel Research Award of the Alexander von Humboldt Foundation, the 2008 Charles McDowell Award for Excellence in Research from UBC, a 2011 Alexander von Humboldt Professorship, a 2012 NSERC E.W.R. Stacie Fellowship, and a 2017 Wireless Communications Recognition Award by the IEEE Wireless Communications Technical Committee. Since 2017, he has been listed as a Highly Cited Researcher by the Web of Science. He is a fellow of the Canadian Academy of Engineering and a fellow of the Engineering Institute of Canada. From 2012 to 2015, he has served as the Editor-in-Chief for IEEE TRANSACTIONS ON COMMUNICATIONS.

Anhang C

Publication 2

[J2] **D. Xu**, X. Yu, Y. Sun, D. W. K. Ng and R. Schober, "Resource Allocation for IRS-Assisted Full-Duplex Cognitive Radio Systems," in IEEE Transactions on Communications, vol. 68, no. 12, pp. 7376-7394, Dec. 2020, doi:10.1109/TCOMM.2020.3020838.[1]

[1]© 2020 IEEE. Reprinted, with permission, from D. Xu, X. Yu, Y. Sun, D. W. K. Ng, and R. Schober, "Resource allocation for IRS-assisted full-duplex cognitive radio systems," *IEEE Trans. Commun.*, Dec. 2020.

Resource Allocation for IRS-Assisted Full-Duplex Cognitive Radio Systems

Dongfang Xu, *Student Member, IEEE*, Xianghao Yu, *Member, IEEE*, Yan Sun, *Member, IEEE*, Derrick Wing Kwan Ng, *Senior Member, IEEE*, and Robert Schober, *Fellow, IEEE*

***Abstract*— In this article, we investigate the resource allocation design for intelligent reflecting surface (IRS)-assisted full-duplex (FD) cognitive radio systems. In particular, a secondary network employs an FD base station (BS) for serving multiple half-duplex downlink (DL) and uplink (UL) users simultaneously. An IRS is deployed to enhance the performance of the secondary network while helping to mitigate the interference caused to the primary users (PUs). The DL transmit beamforming vectors and the UL receive beamforming vectors at the FD BS, the transmit power of the UL users, and the phase shift matrix at the IRS are jointly optimized for maximization of the total spectral efficiency of the secondary system. The design task is formulated as a non-convex optimization problem taking into account the imperfect knowledge of the PUs' channel state information (CSI) and their maximum interference tolerance. Since the maximum interference tolerance constraint is intractable, we apply a safe approximation to transform it into a convex constraint. To efficiently handle the resulting approximated optimization problem, which is still non-convex, we develop an iterative block coordinate descent (BCD)-based algorithm. This algorithm exploits semidefinite relaxation, a penalty method, and successive convex approximation and is guaranteed to converge to a stationary point of the approximated optimization problem. Our simulation results do not only reveal that the proposed scheme yields a substantially higher system spectral efficiency for the secondary system than several baseline schemes, but also confirm its robustness against CSI uncertainty. Besides, our results illustrate the tremendous potential of IRS for managing the various types of interference arising in FD cognitive radio networks.**

***Index Terms*— Block coordinate descent, imperfect channel state information, intelligent reflecting surface, cognitive radio, full-duplex.**

Manuscript received March 17, 2020; revised July 5, 2020; accepted August 20, 2020. Date of publication September 1, 2020; date of current version December 16, 2020. D. Xu is supported by the Chinese Scholarship Council (CSC). X. Yu is supported by the Alexander von Humboldt Foundation. D. W. K. Ng is supported by funding from the UNSW Digital Grid Futures Institute, UNSW, Sydney, under a cross-disciplinary fund scheme and by the Australian Research Council's Discovery Project (DP190101363). This article was presented in part at the 21st IEEE International Workshop on Signal Processing Advances in Wireless Communications (SPAWC), Atlanta, Georgia, USA, May 2020 [1]. The associate editor coordinating the review of this article and approving it for publication was M. Bennis. *(Corresponding author: Xianghao Yu.)*

Dongfang Xu, Xianghao Yu, Yan Sun, and Robert Schober are with the Institute for Digital Communications, Friedrich-Alexander-University Erlangen-Nürnberg (FAU), 91054 Erlangen, Germany (e-mail: dongfang.xu@fau.de; xianghao.yu@fau.de; yan.sun@fau.de; robert.schober@fau.de).

Derrick Wing Kwan Ng is with the School of Electrical Engineering and Telecommunications, University of New South Wales, Sydney, NSW 2052, Australia (e-mail: w.k.ng@unsw.edu.au).

Color versions of one or more of the figures in this article are available online at https://ieeexplore.ieee.org.

Digital Object Identifier 10.1109/TCOMM.2020.3020838

I. Introduction

RADIO spectrum is a naturally limited resource in wireless communication systems. During the last couple of decades, most of the available spectrum has been licensed and allocated to provide various high data-rate communication services. This has led to the problem of a spectrum crunch for future wireless communication systems [2]. However, according to measurements of the actual spectrum utilization, e.g. [3], [4], a large amount of the allocated spectrum is highly underutilized. To improve the utilization of the limited spectral resource, cognitive radio (CR) has been proposed to offer communication services to unlicensed secondary systems within licensed frequency bands. One promising approach to spectrum sharing is underlay CR where the secondary system is allowed to use the spectrum concurrently with the primary users (PUs) as long as the quality-of-service (QoS) of the PUs is not severely impaired. Thus, to limit the performance degradation caused to the primary network, the secondary system has to be carefully designed [4]–[6]. For example, the authors of [5] developed a joint transmit power allocation and receive beamforming design to minimize the total transmit power of the secondary transmitter, while constraining the interference to the PUs to be below a given threshold. In [6], the authors proposed a multi-objective optimization framework and developed a Pareto-optimal resource allocation algorithm to realize simultaneous wireless power and secure information transfer in CR networks. However, since the CR networks in [5], [6] employ half-duplex (HD) base stations (BSs) and the uplink (UL) and downlink (DL) transmissions are performed in orthogonal frequency bands, the radio spectral resources are still underutilized.

To boost wireless spectral efficiency, full-duplex (FD) communication has recently drawn considerable research interest [7]–[11]. In fact, by incorporating FD BSs into CR networks, the spectral efficiency can be potentially doubled compared to traditional HD CR networks. However, since in CR networks the secondary system has to share the spectrum with the primary system, the QoS of the PUs is inevitably impaired by the simultaneous UL and DL transmissions of the secondary system. In general, compared to the PUs in conventional HD CR networks, because of the larger number of concurrent transmissions, the PUs in FD CR networks suffer from more severe interference, which degrades the performance of the primary network [7], [8]. Moreover, the self-interference (SI) and co-channel interference (CCI) caused

by the simultaneous DL and UL transmissions, if left unattended, can also significantly degrade the performance of the secondary system [7]. To effectively manage the interference in FD CR networks, different resource allocation designs were developed in [9]–[11]. In [9], the sub-channel assignment, user pairing, and power allocation was jointly optimized to improve the spectral efficiency of a FD CR system. In [10], the authors investigated robust DL beamforming and UL power allocation for minimization of the maximum interference leakage to the PUs while taking into account the QoS requirements of the SUs. In [11], multi-antenna precoding and relaying strategies for cooperative FD CR systems were developed to maximize the spectral efficiency of the secondary system while taking into account a minimum required data rate for the PUs. Despite these promising results, the PUs in FD CR systems may still suffer from significant interference as the radio frequency (RF) propagation environment of wireless systems is essentially random and largely uncontrollable. In fact, in unfavorable radio propagation environments, the designs proposed in [9]–[11] cannot mitigate the interference caused to the PUs such that their QoS requirements may be violated. In this case, since the PUs have a higher priority for utilizing the spectrum, the communication in the secondary network may be strictly limited leading to a severe performance degradation of the secondary network. To overcome this problem, more effective interference management methods are urgently needed to facilitate reliable and spectrum-efficient FD CR networks.

Recently, intelligent reflecting surfaces (IRSs) have emerged as a promising solution for harnessing interference in wireless communication systems [12]–[19]. In particular, an IRS is a planar metasurface comprising a set of small passive low-cost elements, such as phase shifters and printed dipoles, which can be tuned individually to reflect the incident signals with a desired phase shift [20]. By adaptively and smartly tuning the phase shifts of the IRS elements according to the dynamic radio propagation environment, the wireless channel can be proactively manipulated, which introduces additional degrees of freedom (DoFs) for resource allocation [12]. Moreover, the reflected signals can be combined with the non-reflected signals in a constructive or destructive manner to enhance the desired signal power strength or to suppress detrimental interference, which improves the overall system performance. Besides, due to their relatively simple structure [20], IRSs can be flexibly installed on building facades and interior walls, and thus can be smoothly integrated into existing cellular communication systems [12]. Deploying IRSs may increase the complexity of resource allocation algorithm design. However, several works have shown that with an advanced but computationally-efficient resource allocation design IRS-assisted wireless systems can achieve significant performance gains compared to conventional wireless systems without IRS [13]–[15], [21], [22]. In particular, the authors of [13] considered an IRS-aided multiple-input single-output (MISO) system and studied the joint design of the beamforming at the BS and the IRS to minimize the total BS transmit power. The authors of [14] considered an IRS-enhanced single-user system and developed two computationally efficient suboptimal algorithms for maximizing the received power of the user. The authors of [15] introduced artificial noise (AN) to improve the physical layer security of an IRS-assisted multiuser communication system and jointly optimized the IRS phase shifts, DL beamformers, and AN design. The authors of [21] studied the benefits of IRSs in orthogonal frequency division multiple access systems and formulated a joint transmit power and IRS phase shift optimization problem for maximization of the system throughput. The authors of [22] investigated the joint BS beamforming and IRS phase shift design and proposed two suboptimal algorithms to guarantee physical layer security in an IRS-assisted multiple-input single-output (MISO) system. However, the authors of [13]–[15], [21], [22] considered HD systems, which cannot exploit the full potential of IRSs. In fact, since IRSs naturally operate in a FD manner [19], they can be conveniently incorporated into existing FD CR network concepts to further increase spectral efficiency. Yet, the designs proposed in [13]–[15], [21], [22] are not directly applicable to IRS-assisted FD CR networks. In particular, the simultaneous UL and DL transmissions of the secondary system, the superposition of the direct and reflected paths, and the coupling between the DL beamforming vectors, UL transmit powers, and IRS phase shifts makes the resource allocation design for IRS-assisted FD CR networks very challenging. To the best of the authors' knowledge, the design of spectrally-efficient IRS-assisted FD CR networks has not been investigated in the literature, yet.

Motivated by the above discussion, in this article, we integrate IRSs into FD CR networks and investigate the corresponding resource allocation algorithm design. In particular, as the secondary system is allowed to share the spectrum of the primary system as long as the QoS of the PUs is not severely compromised, the IRS is utilized to establish a favorable radio propagation environment. In particular, we aim to maximize the spectral efficiency of the secondary system by jointly optimizing the DL transmit beamformers, the UL transmit power, the UL receive beamformers, and the IRS phase shifts. The problem formulation takes into account the imperfect knowledge of the channel state information (CSI) of the PUs at the FD BS of the secondary system and the maximum interference leakage tolerance of the PUs. Since the maximum interference leakage tolerance constraint is intractable, we transform it into a convex constraint by applying a safe approximation. Due to the coupling between the optimization variables and the unit-modulus constraint of the IRS phase shifts, even with the safe approximation, the formulated problem is still highly non-convex and it is very challenging to obtain the optimal solution. Hence, we propose a block coordinate descent (BCD)-based iterative algorithm to obtain a suboptimal solution [23]. In particular, by applying successive convex approximation (SCA) [24] and semidefinite relaxation (SDR), the DL transmit beamforming and UL power allocation policies are obtained with the other optimization variables being fixed. Then, we derive the closed-form optimal solution for the receive beamforming vector of the secondary BS given the other optimization variables. Subsequently, we obtain the phase shift matrix of the IRS by applying a penalty method [25] and SCA. The

developed BCD algorithm is guaranteed to converge to a stationary point of the approximated optimization problem. Simulation results reveal that IRSs and the proposed algorithm can significantly enhance the performance of secondary networks while efficiently mitigating the interference to the PUs.

Notations: In this article, boldface lower case and boldface capital letters denote vectors and matrices, respectively. $\mathbb{N}$ denotes the set of nonnegative integers. $\mathbb{R}^{N\times M}$ and $\mathbb{C}^{N\times M}$ denote the space of $N\times M$ real-valued and complex-valued matrices, respectively. $\Re\{\cdot\}$ extracts the real part of a complex number. $\mathbb{H}^N$ denotes the set of all N-dimensional complex Hermitian matrices. $\mathbf{I}_N$ indicates the $N\times N$ identity matrix. $|\cdot|$ and $||\cdot||_2$ denote the absolute value of a complex scalar and the l_2-norm of a vector, respectively. $\mathbf{A}^T$, $\mathbf{A}^*$, and $\mathbf{A}^H$ stand for the transpose, the conjugate, and the conjugate transpose of matrix $\mathbf{A}$, respectively. $\mathbf{A}\succeq\mathbf{0}$ indicates that $\mathbf{A}$ is a positive semidefinite matrix. $\mathrm{Rank}(\mathbf{A})$, $\mathrm{Tr}(\mathbf{A})$, $[\mathbf{A}]_{i,i}$, and $\|\mathbf{A}\|_*$ denote the rank, the trace, the (i,i)-entry, and the trace norm of matrix $\mathbf{A}$, respectively. x_i denotes the i-th element of vector $\mathbf{x}$. $\mathrm{Diag}(\mathbf{X})$ represents a diagonal matrix whose diagonal elements are extracted from the main diagonal of matrix $\mathbf{X}$; $\mathrm{diag}(\mathbf{x})$ denotes an $N\times N$ diagonal matrix with main diagonal elements $x_1,\cdots,x_N$. $\mathcal{E}\{\cdot\}$ denotes statistical expectation. $\sim$ and $\triangleq$ stand for "distributed as" and "defined as", respectively. The distribution of a circularly symmetric complex Gaussian random variable with mean μ and variance σ^2 is denoted by $\mathcal{CN}(\mu,\sigma^2)$. The gradient vector of function $f(\mathbf{x})$ with respect to $\mathbf{x}$ is denoted by $\nabla_{\mathbf{x}}f(\mathbf{x})$. $\mathbf{x}^\dagger$ denotes the optimal value of optimization variable $\mathbf{x}$.

II. System Model

In this section, we present the IRS-assisted multiuser FD CR network model and discuss our assumptions regarding the CSI available for resource allocation.

A. IRS-Assisted Full-Duplex Cognitive Radio System Model

We consider a narrow-band IRS-assisted CR communication system[1] consisting of a primary license-holding network and a secondary unlicensed network, cf. Figure 1. In particular, the primary network comprises one primary transmitter and I PUs, while the secondary network includes one secondary FD BS, J UL users, and K DL users. The primary transmitter, the I PUs, and the $K+J$ secondary users are single-antenna HD devices. The secondary FD BS is equipped with $N_{\mathrm{T}}>1$ antennas,[2] indexed by $\mathcal{N}\triangleq\{1,\cdots,N_{\mathrm{T}}\}$, and simultaneously performs DL transmission and UL reception in the same frequency band.[3] Due to the spectrum sharing, the QoS of the primary network is impaired by interference leakage from the secondary network. To effectively suppress the interference and improve the system performance of the secondary network, an IRS is deployed. In particular, the IRS comprises M phase shifters, indexed by $\mathcal{M}\triangleq\{1,\cdots,M\}$, and is programmable and reconfigurable via an IRS controller. For notational simplicity, we define sets $\mathcal{I}=\{1,\cdots,I\}$, $\mathcal{J}=\{1,\cdots,J\}$, and $\mathcal{K}=\{1,\cdots,K\}$ for the indices of the PUs, secondary UL users, and secondary DL users, respectively.

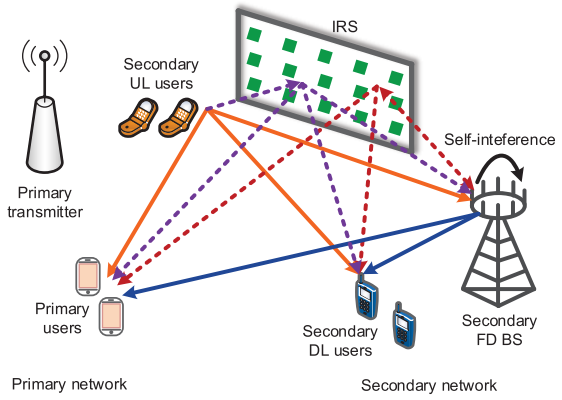

Fig. 1. CR system comprising a secondary FD base station, $J=2$ secondary UL users, and $K=2$ secondary DL users sharing the spectrum with $I=2$ PUs. The IRS is deployed to enhance the system performance of the secondary network and to mitigate the interference to the PUs. The direct paths and reflected paths are denoted by solid arrows and dashed arrows, respectively. The signals of the primary transmitter are not shown for clarity.

In a given time slot, the secondary FD BS transmits signal $\sum_{k\in\mathcal{K}}\mathbf{w}_k d_k^{\mathrm{DL}}$ to the K DL users, where $d_k^{\mathrm{DL}}\in\mathbb{C}$ and $\mathbf{w}_k\in\mathbb{C}^{N_{\mathrm{T}}\times 1}$ denote the information symbol for secondary DL user k and the corresponding beamformer, respectively. Without loss of generality, we assume $\mathcal{E}\{|d_k^{\mathrm{DL}}|^2\}=1$, $\forall k\in\mathcal{K}$. The received signals at PU i, the secondary FD BS, and secondary DL user k are given by, respectively,[4]

$$
\begin{aligned}
y_i^{\mathrm{P}} &= \underbrace{\left(f_{\mathrm{D},i}^{\mathrm{P}}+\left(\mathbf{f}_{\mathrm{R},i}^{\mathrm{P}}\right)^H\mathbf{\Psi}\mathbf{f}^{\mathrm{P-I}}\right)\sum_{n\in\mathcal{I}}\sqrt{p_n^{\mathrm{P}}}d_n^{\mathrm{P}}}_{\text{Signal from the primary transmitter}}\\
&\quad+\underbrace{\sum_{j\in\mathcal{J}}\sqrt{p_j}e_{i,j}d_j^{\mathrm{UL}}+\sum_{j\in\mathcal{J}}\sqrt{p_j}\mathbf{l}_{\mathrm{R},i}^H\mathbf{\Psi}\mathbf{h}_{\mathrm{R},j}d_j^{\mathrm{UL}}}_{\text{Interference from the secondary uplink}}\\
&\quad+\underbrace{\sum_{k\in\mathcal{K}}\mathbf{l}_{\mathrm{D},i}^H\mathbf{w}_k d_k^{\mathrm{DL}}+\sum_{k\in\mathcal{K}}\mathbf{l}_{\mathrm{R},i}^H\mathbf{\Psi}\mathbf{F}\mathbf{w}_k d_k^{\mathrm{DL}}}_{\text{Interference from the secondary downlink}}+n_i^{\mathrm{P}},\qquad(1)\\
\mathbf{y}^{\mathrm{UL}} &= \underbrace{\sum_{j\in\mathcal{J}}\sqrt{p_j}\mathbf{h}_{\mathrm{D},j}d_j^{\mathrm{UL}}+\sum_{j\in\mathcal{J}}\sqrt{p_j}\mathbf{F}^H\mathbf{\Psi}\mathbf{h}_{\mathrm{R},j}d_j^{\mathrm{UL}}}_{\text{Desired signal}}\\
&\quad+\underbrace{\mathbf{S}\sum_{k\in\mathcal{K}}\mathbf{w}_k d_k^{\mathrm{DL}}+\sum_{k\in\mathcal{K}}\mathbf{F}^H\mathbf{\Psi}\mathbf{F}\mathbf{w}_k d_k^{\mathrm{DL}}}_{\text{Self-interference}}
\end{aligned}
$$

[1]In this article, we consider an underlay CR network [26] where the secondary FD BS can opportunistically coexist with the primary transmitter as long as the interference leakage to the PUs is kept below a certain threshold.

[2]To facilitate reliable UL signal detection, we assume that the number of antennas equipped at the secondary FD BS is equal to or larger than the number of secondary UL users, i.e., $N_{\mathrm{T}}\geq J$.

[3]Simultaneous transmission and reception with the same antenna can be realized by employing a circulator-based FD radio transceiver, as demonstrated in [27].

[4]In this article, we assume that the secondary network is time-synchronized and frequency-synchronized with the primary network.

$$+\underbrace{\left(\mathbf{f}^{\mathrm{UL}}+\mathbf{F}^{H}\mathbf{\Psi}\mathbf{f}^{\mathrm{P-I}}\right)\sum_{n\in\mathcal{I}}\sqrt{p_n^{\mathrm{P}}}d_n^{\mathrm{P}}}_{\text{Interference from the primary transmitter}}+\mathbf{n}^{\mathrm{UL}}, \tag{2}$$

$$y_k^{\mathrm{DL}}=\underbrace{\mathbf{g}_{\mathrm{D},k}^{H}\mathbf{w}_k d_k^{\mathrm{DL}}+\mathbf{g}_{\mathrm{R},k}^{H}\mathbf{\Psi}\mathbf{F}\mathbf{w}_k d_k^{\mathrm{DL}}}_{\text{desired signal}}$$
$$+\underbrace{\sum_{r\in\mathcal{K}\setminus\{k\}}\mathbf{g}_{\mathrm{D},k}^{H}\mathbf{w}_r d_r^{\mathrm{DL}}+\sum_{r\in\mathcal{K}\setminus\{k\}}\mathbf{g}_{\mathrm{R},k}^{H}\mathbf{\Psi}\mathbf{F}\mathbf{w}_r d_r^{\mathrm{DL}}}_{\text{Multiuser interference}}$$
$$+\underbrace{\sum_{j\in\mathcal{J}}\sqrt{p_j}q_{j,k}d_j^{\mathrm{UL}}+\sum_{j\in\mathcal{J}}\sqrt{p_j}\mathbf{g}_{\mathrm{R},k}^{H}\mathbf{\Psi}\mathbf{h}_{\mathrm{R},j}d_j^{\mathrm{UL}}}_{\text{Co-channel interference}}$$
$$+\underbrace{\left(f_{\mathrm{D},k}^{\mathrm{DL}}+\mathbf{g}_{\mathrm{R},k}^{H}\mathbf{\Psi}\mathbf{f}^{\mathrm{P-I}}\right)\sum_{n\in\mathcal{I}}\sqrt{p_n^{\mathrm{P}}}d_n^{\mathrm{P}}}_{\text{Interference from the primary transmitter}}+n_k^{\mathrm{DL}}. \tag{3}$$

Here, $f_{\mathrm{D},i}^{\mathrm{P}}\in\mathbb{C}$ and $\mathbf{f}_{\mathrm{R},i}^{\mathrm{P}}\in\mathbb{C}^{M\times 1}$ denote the channel between the primary transmitter and PU i and the channel vector between the IRS and PU i, respectively. Diagonal matrix $\mathbf{\Psi}=\mathrm{diag}\left(e^{j\psi_1},\cdots,e^{j\psi_M}\right)$ represents the phase shift matrix of the IRS [13], where $\psi_m\in[-\pi,\pi]$, $\forall m\in\mathcal{M}$, is the phase shift introduced by the m-th IRS element. The channel between the primary transmitter and the IRS is denoted by $\mathbf{f}^{\mathrm{P-I}}\in\mathbb{C}^{M\times 1}$. $p_n^{\mathrm{P}}\in\mathbb{R}$ and $d_n^{\mathrm{P}}\in\mathbb{C}$ denote the transmit power for PU n, $\forall n\in\mathcal{I}$, and the corresponding data symbol, respectively. $\mathbf{l}_{\mathrm{D},i}\in\mathbb{C}^{N_{\mathrm{T}}\times 1}$ and $\mathbf{l}_{\mathrm{R},i}\in\mathbb{C}^{M\times 1}$ denote the channel vector between the secondary BS and PU i and the channel vector between the IRS and PU i, respectively.[5] Matrix $\mathbf{F}\in\mathbb{C}^{M\times N_{\mathrm{T}}}$ models the channel between the secondary FD BS and the IRS. Variables $d_j^{\mathrm{UL}}\in\mathbb{C}$ and $p_j\in\mathbb{R}$ are the data symbol and the corresponding power transmitted by secondary UL user j to the secondary FD BS, respectively. We assume $\mathcal{E}\{|d_j^{\mathrm{UL}}|^2\}=1$ without loss of generality. The channel gain between secondary UL user j and PU i is denoted by $e_{i,j}$. $\mathbf{h}_{\mathrm{D},j}\in\mathbb{C}^{N_{\mathrm{T}}\times 1}$ and $\mathbf{h}_{\mathrm{R},j}\in\mathbb{C}^{M\times 1}$ denote the channel vector between the secondary BS and secondary UL user j and the channel vector between the IRS and secondary UL user j, respectively. $\mathbf{S}\sum_{k\in\mathcal{K}}\mathbf{w}_k d_k^{\mathrm{DL}}$ in (2) represents the SI resulting from the DL transmission with $\mathbf{S}\in\mathbb{C}^{N_{\mathrm{T}}\times N_{\mathrm{T}}}$ denoting the SI channel matrix of the secondary FD BS. The term $\sum_{k\in\mathcal{K}}\mathbf{F}^{H}\mathbf{\Psi}\mathbf{F}\mathbf{w}_k d_k^{\mathrm{DL}}$ in (2) denotes the SI introduced by the reflection of the DL transmit signal by the IRS. $\mathbf{f}^{\mathrm{UL}}\in\mathbb{C}^{N_{\mathrm{T}}\times 1}$ denotes the channel between the primary transmitter and the secondary BS. $\mathbf{g}_{\mathrm{D},k}\in\mathbb{C}^{N_{\mathrm{T}}\times 1}$ and $\mathbf{g}_{\mathrm{R},k}\in\mathbb{C}^{M\times 1}$ denote the channel vector between the secondary BS and DL user k and the channel vector between the IRS and DL user k, respectively. The channel gain between secondary UL user j and secondary DL user k is denoted by $q_{j,k}$. $f_{\mathrm{D},k}^{\mathrm{DL}}$ denotes the channel between the primary transmitter and secondary DL user k. $\mathbf{n}^{\mathrm{UL}}\sim\mathcal{CN}(\mathbf{0},\sigma_{n_{\mathrm{U}}}^2\mathbf{I}_{N_{\mathrm{T}}})$ and $n_k^{\mathrm{DL}}\sim\mathcal{CN}(0,\sigma_{n_k}^2)$ denote the equivalent additive white Gaussian noises (AWGNs) at the secondary FD BS and secondary DL user k, which capture the combined effect of thermal noise and signal processing noise [29]. n_i^{P} includes the joint effects of thermal noise and signal processing noise at PU i.

Remark 1: In the following, for resource allocation design, we model the interference from the primary transmitter to the secondary BS and to secondary user k, i.e., $(\mathbf{f}^{\mathrm{UL}}+\mathbf{F}^{H}\mathbf{\Psi}\mathbf{f}^{\mathrm{P-I}})\sum_{n\in\mathcal{I}}\sqrt{p_n^{\mathrm{P}}}d_n^{\mathrm{P}}$ and $(f_{\mathrm{D},k}^{\mathrm{DL}}+\mathbf{g}_{\mathrm{R},k}^{H}\mathbf{\Psi}\mathbf{f}^{\mathrm{P-I}})\sum_{n\in\mathcal{I}}\sqrt{p_n^{\mathrm{P}}}d_n^{\mathrm{P}}$, as additional AWGNs $\mathbf{z}^{\mathrm{UL}}\sim\mathcal{CN}(0,\sigma_{z_0}^2\mathbf{I}_{N_{\mathrm{T}}})$ and $z_k^{\mathrm{DL}}\sim\mathcal{CN}(0,\sigma_{z_k}^2)$, $\forall k\in\mathcal{K}$, respectively. This is due to the fact that, as can be seen from (2) and (3), the signals originating from the primary transmitter may affect the IRS phase shift matrix design. To accurately capture this effect for resource allocation algorithm design, both the transmit power of the primary transmitter and the CSI between the primary transmitter and the secondary network have to be known. However, learning the power allocation policy and the CSI of the primary network would significantly increase the signalling overhead for the secondary network. As a result, resource allocation design taking into account the exact structure of the interference from the primary transmitter may not be feasible in practice. For notational simplicity, in the following, we include variances $\sigma_{z_0}^2$ and $\sigma_{z_k}^2$ in the variances of $\mathbf{n}^{\mathrm{UL}}$ and n_k^{DL}, respectively. We note that the interference from the primary transmitter is approximated as additional AWGN for resource allocation design only. For evaluation of the performance of the proposed resource allocation scheme, the actual system defined by (1)-(3) is simulated.

B. Channel State Information

In this article, we assume that both the primary network and the secondary network are time division duplex systems with slowly time-varying channels. During the channel estimation phase of the secondary network, the secondary FD BS can reliably estimate all links of the secondary network with the assistance of the SUs and the IRS [30]. As a result, we assume that the perfect CSI of the secondary network is available at the secondary FD BS for resource allocation. However, this assumption may not be valid for the channels between the secondary network and the PUs. In practice, the PUs can not be expected to directly interact with the secondary FD BS. Moreover, the PUs may be idle for a long period of time due to bursty data transmission. As a result, the CSI of the PUs can be obtained only occasionally at the secondary FD BS when the PUs are active in the primary network, which leads to outdated PU CSI at the FD BS. In this article, we develop a worst-case optimization framework to capture the impact of imperfect PU CSI on resource allocation design [31]. Specifically, the CSI of the link between the FD BS and PU i, i.e., $\mathbf{l}_{\mathrm{D},i}$, the CSI of the link between the IRS and PU i, i.e., $\mathbf{l}_{\mathrm{R},i}$, and the CSI of the link between PU i and secondary UL user j are modeled as:

$$\mathbf{l}_{\mathrm{D},i}=\overline{\mathbf{l}}_{\mathrm{D},i}+\Delta\mathbf{l}_{\mathrm{D},i}\text{ and }\Omega_{\mathrm{D},i}\triangleq\left\{\mathbf{l}_{\mathrm{D},i}|\Delta\mathbf{l}_{\mathrm{D},i}^{H}\Delta\mathbf{l}_{\mathrm{D},i}\leq\varepsilon_{\mathrm{D},i}^2\right\}, \tag{4}$$

[5]The delays between the signal propagating through the direct path and the reflected path via the IRS are typically much shorter than the symbol duration. For instance, for a cell with a radius of 50 m as considered in our simulations, cf. Figure 2, the maximum round-trip delay is 0.33 μs, which is significantly shorter than the 70 μs symbol duration in the Long-Term Evolution (LTE) standard [28]. Thus, we neglect the impact of intersymbol interference in this article.

$$\mathbf{l}_{\mathrm{R},i} = \overline{\mathbf{l}}_{\mathrm{R},i} + \Delta\mathbf{l}_{\mathrm{R},i} \text{ and } \Omega_{\mathrm{R},i} \triangleq \left\{\mathbf{l}_{\mathrm{R},i} | \Delta\mathbf{l}_{\mathrm{R},i}^H \Delta\mathbf{l}_{\mathrm{R},i} \leq \varepsilon_{\mathrm{R},i}^2\right\}, \tag{5}$$

$$e_{i,j} = \overline{e}_{i,j} + \Delta e_{i,j} \text{ and } \Omega_{i,j} \triangleq \left\{e_{i,j} | \Delta e_{i,j}^H \Delta e_{i,j} \leq \varepsilon_{i,j}^2\right\}, \tag{6}$$

respectively, where $\overline{\mathbf{l}}_{\mathrm{D},i}$, $\overline{\mathbf{l}}_{\mathrm{R},i}$, and $\overline{e}_{i,j}$ are the CSI estimates and $\Delta\mathbf{l}_{\mathrm{D},i}$, $\Delta\mathbf{l}_{\mathrm{R},i}$, and $\Delta e_{i,j}$ are the corresponding unknown estimation errors, respectively. We denote the channel uncertainty regions[6] by continuous sets $\Omega_{\mathrm{D},i}$, $\Omega_{\mathrm{R},i}$, and $\Omega_{i,j}$ with radii $\varepsilon_{\mathrm{D},i}$, $\varepsilon_{\mathrm{R},i}$, and $\varepsilon_{i,j}$, respectively.

III. Resource Allocation Problem Formulation

In this section, after introducing the adopted performance metrics, we formulate the proposed resource allocation optimization problem.

A. Performance Metrics

The achievable spectral efficiency (bits/s/Hz) of secondary DL user k is given by $R_k^{\mathrm{DL}} = \log_2(1+\Gamma_k^{\mathrm{DL}})$, where Γ_k^{DL} is the receive signal-to-noise-plus-interference ratio (SINR) of secondary DL user k and given by (7), where (7) is shown at the bottom of the page. On the other hand, the spectral efficiency (bits/s/Hz) of secondary UL user j is given by $R_j^{\mathrm{UL}} = \log_2(1+\Gamma_j^{\mathrm{UL}})$, where Γ_j^{UL} is the receive SINR of secondary UL user j and given by (8), where (8) is shown at the bottom of the page. Here, $\mathbf{v}_j \in \mathbb{C}^{N_{\mathrm{T}}\times 1}$ is the receive beamforming vector for decoding the message of secondary UL user j at the secondary FD BS. We note that due to the limited dynamic range of the receiver, the SI cannot be suppressed completely even if perfect CSI of the SI channel is available at the secondary FD BS [33]. Thus, similar to [33], [34], we model the residual SI after cancellation at each receive antenna as an independent Gaussian distortion noise with zero mean and a variance proportional to the power received at that antenna. In particular, according to [33, Eq. (4)], the term D_j^{SI} in (8) is given by (9), where (9) is shown at the bottom of the page. Here, constant η, $0 < \eta \ll 1$, captures the impact of the residual interference after SI cancellation at the secondary FD BS [35]. We note that due to the propagation attenuation between the FD BS and the IRS, the reflected interference in (9) is negligible[7] compared to self-interference. As a result, we can approximate (9) as follows

$$D_j^{\mathrm{SI}} \approx \mathrm{Tr}\Big(\eta\mathbf{v}_j\mathbf{v}_j^H \mathrm{Diag}\big(\sum_{k\in\mathcal{K}} \mathbf{S}\mathbf{w}_k\mathbf{w}_k^H\mathbf{S}^H\big)\Big). \tag{10}$$

B. Optimization Problem Formulation

In this article, we optimize $\mathbf{w}_k$, $\mathbf{v}_j$, p_j, and $\mathbf{\Psi}$ to maximize the system spectral efficiency of the secondary network while limiting the interference caused by the secondary network to the PUs. The corresponding optimization problem is formulated as follows

$$\begin{aligned}
&\underset{\mathbf{w}_k,\mathbf{v}_j,p_j,\mathbf{\Psi}}{\text{maximize}}\ F\big(\mathbf{w}_k,\mathbf{v}_j,p_j,\mathbf{\Psi}\big)\\
&\text{s.t. C1: } \sum_{k\in\mathcal{K}} \|\mathbf{w}_k\|^2 \leq P_{\max}^{\mathrm{DL}},\\
&\quad \text{C2: } 0 \leq p_j \leq p_{j,\max}, \quad \forall j,\\
&\quad \text{C3: } \left|[\mathbf{\Psi}]_{m,m}\right| = 1, \quad \forall m,\\
&\quad \text{C4: } \max_{\substack{\mathbf{l}_{\mathrm{D},i}\in\Omega_{\mathrm{D},i}\\ \mathbf{l}_{\mathrm{R},i}\in\Omega_{\mathrm{R},i}\\ e_{i,j}\in\Omega_{i,j}}} \sum_{k\in\mathcal{K}} \left|\mathbf{l}_{\mathrm{D},i}^H\mathbf{w}_k + \mathbf{l}_{\mathrm{R},i}^H\mathbf{\Psi}\mathbf{F}\mathbf{w}_k\right|^2\\
&\qquad\qquad + \sum_{j\in\mathcal{J}} p_j \left|e_{i,j} + \mathbf{l}_{\mathrm{R},i}^H\mathbf{\Psi}\mathbf{h}_{\mathrm{R},j}\right|^2 \leq p_{\mathrm{tol}_i}, \quad \forall i,
\end{aligned} \tag{11}$$

where $F\big(\mathbf{w}_k,\mathbf{v}_j,p_j,\mathbf{\Psi}\big)$ is defined as $F\big(\mathbf{w}_k,\mathbf{v}_j,p_j,\mathbf{\Psi}\big) \triangleq \sum_{j\in\mathcal{J}} \omega_j^{\mathrm{UL}} \log_2\left(1+\Gamma_j^{\mathrm{UL}}\right) + \sum_{k\in\mathcal{K}} \omega_k^{\mathrm{DL}} \log_2(1+\Gamma_k^{\mathrm{DL}})$. Here, $\omega_j^{\mathrm{UL}} \geq 0$ and $\omega_k^{\mathrm{DL}} \geq 0$ denote predefined weights for secondary UL user j and DL user k, which can be used to prioritize the UL and DL users. $P_{\max}^{\mathrm{DL}} > 0$ and $p_{j,\max} > 0$ in constraints C1 and C2 limit the maximum transmit powers of the secondary FD BS and secondary UL user j, respectively. Constraint C3 guarantees that the diagonal phase shift matrix $\mathbf{\Psi}$ has M unit modulus components on its main diagonal. C4 constrains the maximum tolerable interference leakage.

[6] In this article, we assume the radius of the channel uncertainty region is known. Yet, we note that the channel estimation error itself is a random variable which lies in the given channel uncertainty region. In practice, the CSI estimates and the channel uncertainty regions can be determined by applying existing channel estimation schemes for IRS-assisted wireless systems, see, e.g., [30], [32].

[7] For a CR network where the IRS is 100 m away from the FD BS and a path loss exponent of 2, the term $\mathbf{F}^H\mathbf{\Psi}\mathbf{F}\mathbf{w}_k\mathbf{w}_k^H\mathbf{F}^H\mathbf{\Psi}^H\mathbf{F} + \mathbf{F}^H\mathbf{\Psi}\mathbf{F}\mathbf{w}_k\mathbf{w}_k^H\mathbf{S}^H + \mathbf{S}\mathbf{w}_k\mathbf{w}_k^H\mathbf{F}^H\mathbf{\Psi}^H\mathbf{F}$ is attenuated by approximately a factor of 10^{-8} compared to the term $\mathbf{S}\mathbf{w}_k\mathbf{w}_k^H\mathbf{S}^H$.

$$\Gamma_k^{\mathrm{DL}} = \frac{\left|\mathbf{g}_{\mathrm{D},k}^H\mathbf{w}_k + \mathbf{g}_{\mathrm{R},k}^H\mathbf{\Psi}\mathbf{F}\mathbf{w}_k\right|^2}{\sum\limits_{r\in\mathcal{K}\setminus\{k\}} \left|\mathbf{g}_{\mathrm{D},k}^H\mathbf{w}_r + \mathbf{g}_{\mathrm{R},k}^H\mathbf{\Psi}\mathbf{F}\mathbf{w}_r\right|^2 + \sum\limits_{j\in\mathcal{J}} p_j \left|q_{j,k} + \mathbf{g}_{\mathrm{R},k}^H\mathbf{\Psi}\mathbf{h}_{\mathrm{R},j}\right|^2 + \sigma_{\mathrm{n}_k}^2}. \tag{7}$$

$$\Gamma_j^{\mathrm{UL}} = \frac{p_j \left|\mathbf{v}_j^H\mathbf{h}_{\mathrm{D},j} + \mathbf{v}_j^H\mathbf{F}^H\mathbf{\Psi}\mathbf{h}_{\mathrm{R},j}\right|^2}{\sum\limits_{t\in\mathcal{J}\setminus\{j\}} p_t \left|\mathbf{v}_j^H\mathbf{h}_{\mathrm{D},t} + \mathbf{v}_j^H\mathbf{F}^H\mathbf{\Psi}\mathbf{h}_{\mathrm{R},t}\right|^2 + D_j^{\mathrm{SI}} + \sigma_{\mathrm{U}}^2 \|\mathbf{v}_j\|^2}. \tag{8}$$

$$D_j^{\mathrm{SI}} = \mathrm{Tr}\Big(\eta\mathbf{v}_j\mathbf{v}_j^H \mathrm{Diag}\big(\sum_{k\in\mathcal{K}} \underbrace{\mathbf{S}\mathbf{w}_k\mathbf{w}_k^H\mathbf{S}^H}_{\text{self-interference}} + \underbrace{\mathbf{F}^H\mathbf{\Psi}\mathbf{F}\mathbf{w}_k\mathbf{w}_k^H\mathbf{F}^H\mathbf{\Psi}^H\mathbf{F} + \mathbf{F}^H\mathbf{\Psi}\mathbf{F}\mathbf{w}_k\mathbf{w}_k^H\mathbf{S}^H + \mathbf{S}\mathbf{w}_k\mathbf{w}_k^H\mathbf{F}^H\mathbf{\Psi}^H\mathbf{F}}_{\text{reflected interference}}\big)\Big). \tag{9}$$

In particular, despite the imperfection of the CSI, the secondary network is required to ensure that the interference leakage to PU i does not exceed the maximum interference tolerance p_{tol_i}.

We note that problem (11) is a highly non-convex optimization problem. In particular, the coupling of the optimization variables, the non-convexity of the objective function, the unit-modulus constraint C3, and the semi-infinite constraint C4 are the main obstacles for solving the considered resource allocation problem efficiently. To the best of the authors' knowledge, the globally optimal solution of this problem is in general intractable. In the next section, we develop a suboptimal BCD-based iterative algorithm to solve problem (11) with polynomial time complexity.

IV. Solution of the Optimization Problem

In this section, we first employ a safe approximation to convert constraint C4 to a set of convex constraints. Then, we propose a BCD-based algorithm to tackle the approximated problem, which is still highly non-convex. In fact, BCD is a widely applicable approach that divides coupled optimization variables into several blocks and solves the optimization problem for one block at a time while fixing the variables in the other blocks [23]. In particular, we divide the optimization variables into three blocks: $\{\mathbf{w}_k, p_j\}$, $\{\mathbf{v}_j\}$, and $\{\mathbf{\Psi}\}$. By employing SCA and SDR, we obtain the transmit beamforming vector $\mathbf{w}_k$ and transmit power p_j. Then, we derive a closed-form solution for receive beamforming vector $\mathbf{v}_j$. Subsequently, we solve for $\mathbf{\Psi}$ by applying a penalty method and SCA.

A. Transformation of the Semi-Infinite Constraints

In the literature, semi-infinite constraints are commonly transformed into tractable linear matrix inequality (LMI) constraints [31]. However, due to the coupling between the optimization variables and the coupling between the signals of the direct and reflect paths, it is challenging to transform constraint C4 into an LMI that is jointly convex with respect to $\mathbf{w}_k$ and $\mathbf{\Psi}$. To facilitate robust resource allocation algorithm design, we first apply inequality $|a+b+c|^2 \le 3|a|^2+3|b|^2+3|c|^2$, where a, b, and c are complex numbers, to the left hand side of constraint C4 to obtain a tractable upper bound.[8] In particular, a subset of the set defined by constraint C4 is given by

$$\begin{aligned}\overline{\mathrm{C4}}\text{:}\ \max_{\substack{\mathbf{l}_{\mathrm{D},i}\in\Omega_{\mathrm{D},i}\\ \mathbf{l}_{\mathrm{R},i}\in\Omega_{\mathrm{R},i}\\ e_{i,j}\in\Omega_{i,j}}} &\sum_{k\in\mathcal{K}}\Big(\left|\Delta\mathbf{l}_{\mathrm{D},i}^H\mathbf{w}_k\right|^2+\left|\bar{\mathbf{l}}_{\mathrm{D},i}^H\mathbf{w}_k+\bar{\mathbf{l}}_{\mathrm{R},i}^H\mathbf{\Psi}\mathbf{F}\mathbf{w}_k\right|^2\\ &+\left|\Delta\mathbf{l}_{\mathrm{R},i}^H\mathbf{\Psi}\mathbf{F}\mathbf{w}_k\right|^2\Big)\\ &+\sum_{j\in\mathcal{J}}p_j\Big(\left|\overline{e}_{i,j}+\bar{\mathbf{l}}_{\mathrm{R},i}^H\mathbf{\Psi}\mathbf{h}_{\mathrm{R},j}\right|^2\\ &+|\Delta e_{i,j}|^2+\left|\Delta\mathbf{l}_{\mathrm{R},i}^H\mathbf{\Psi}\mathbf{h}_{\mathrm{R},j}\right|^2\Big)\le\frac{p_{\mathrm{tol}_i}}{3},\quad\forall i.\end{aligned}\tag{12}$$

[8]We note that the upper bound becomes tight when a, b, and c have similar values.

In the remainder of the article, we tackle the following approximated optimization problem:

$$\begin{aligned}&\underset{\mathbf{w}_k,\mathbf{v}_j,p_j,\mathbf{\Psi}}{\text{maximize}}\ F\big(\mathbf{w}_k,\mathbf{v}_j,p_j,\mathbf{\Psi}\big)\\ &\text{s.t. C1, C2, C3, }\overline{\mathrm{C4}}.\end{aligned}\tag{13}$$

We note that any feasible solution of (13) is also a feasible solution of (11). Hence, (13) is a safe approximation of (11) [36]. Then, we define slack variables β_i, γ_i, and τ_i and rewrite constraint $\overline{\mathrm{C4}}$ equivalently as constraints $\overline{\mathrm{C4}}$a, $\overline{\mathrm{C4}}$b, $\overline{\mathrm{C4}}$c, and $\overline{\mathrm{C4}}$d which are shown at the bottom of the next page, respectively. We note that $\overline{\mathrm{C4}}$d is convex in $\mathbf{w}_k$ and $\mathbf{\Psi}$ individually while $\overline{\mathrm{C4}}$a, $\overline{\mathrm{C4}}$b, and $\overline{\mathrm{C4}}$c are still semi-infinite constraints. Next, we introduce a lemma for transforming constraints $\overline{\mathrm{C4}}$a, $\overline{\mathrm{C4}}$b, and $\overline{\mathrm{C4}}$c into LMI constraints.

Lemma 1 (S-Procedure [37]): Let a function $f_m(\mathbf{x})$, $m\in\{1,2\}$, $\mathbf{x}\in\mathbb{C}^{N\times 1}$, be defined as

$$f_m(\mathbf{x})=\mathbf{x}^H\mathbf{A}_m\mathbf{x}+2\Re\left\{\mathbf{a}_m^H\mathbf{x}\right\}+a_m,\tag{17}$$

where $\mathbf{A}_m\in\mathbb{H}^N$, $\mathbf{a}_m\in\mathbb{C}^{N\times 1}$, and $\mathrm{a}_m\in\mathbb{R}$. Then, the implication $f_1(\mathbf{x})\le 0\Rightarrow f_2(\mathbf{x})\le 0$ holds if and only if there exists a $\delta\ge 0$ such that

$$\delta\begin{bmatrix}\mathbf{A}_1 & \mathbf{a}_1\\ \mathbf{a}_1^H & a_1\end{bmatrix}-\begin{bmatrix}\mathbf{A}_2 & \mathbf{a}_2\\ \mathbf{a}_2^H & a_2\end{bmatrix}\succeq\mathbf{0},\tag{18}$$

provided that there exists a point $\widehat{\mathbf{x}}$ such that $f_m(\widehat{\mathbf{x}})<0$.

To facilitate the application of Lemma 1, we first rewrite constraint $\overline{\mathrm{C4}}$c as follows

$$\Delta\mathbf{l}_{\mathrm{R},i}^H\mathbf{\Psi}\big(\sum_{k\in\mathcal{K}}\mathbf{F}\mathbf{W}_k\mathbf{F}^H+\sum_{j\in\mathcal{J}}p_j\mathbf{H}_{\mathrm{R},j}\big)\mathbf{\Psi}^H\Delta\mathbf{l}_{\mathrm{R},i}+\tau_i\le\gamma_i,\quad\forall i,\tag{19}$$

where $\mathbf{W}_k\triangleq\mathbf{w}_k\mathbf{w}_k^H$ and $\mathbf{H}_{\mathrm{R},j}\triangleq\mathbf{h}_{\mathrm{R},j}\mathbf{h}_{\mathrm{R},j}^H$. By applying Lemma 1, the following implication can be obtained: $\Delta\mathbf{l}_{\mathrm{R},i}^H\Delta\mathbf{l}_{\mathrm{R},i}-\varepsilon_{\mathrm{R},i}^2\le 0\Rightarrow\overline{\mathrm{C4}}$c holds if and only if there exist $\delta_i\ge 0$ such that

$$\begin{aligned}&\widehat{\mathrm{C4}}\text{c: }\mathbf{S}_{\widehat{\mathrm{C4c}}_i}(\mathbf{W}_k,p_j,\mathbf{\Psi},\gamma_i,\tau_i,\delta_i)\\ &=\begin{bmatrix}\delta_i\mathbf{I}_M-\mathbf{\Psi}\mathbf{B}\mathbf{\Psi}^H & \mathbf{0}\\ \mathbf{0} & -\delta_i\varepsilon_{\mathrm{R},i}^2-\tau_i+\gamma_i\end{bmatrix}\succeq\mathbf{0},\quad\forall i,\end{aligned}\tag{20}$$

where $\mathbf{B}\triangleq\sum_{k\in\mathcal{K}}\mathbf{F}\mathbf{W}_k\mathbf{F}^H+\sum_{j\in\mathcal{J}}p_j\mathbf{H}_{\mathrm{R},j}$. To simplify the notation, we rewrite the LMI in (20) as follows

$$\begin{aligned}&\widehat{\mathrm{C4}}\text{c: }\mathbf{S}_{\widehat{\mathrm{C4c}}_i}(\mathbf{W}_k,p_j,\mathbf{\Psi},\gamma_i,\tau_i,\delta_i)\\ &=\begin{bmatrix}\delta_i\mathbf{I}_M & \mathbf{0}\\ \mathbf{0} & -\delta_i\varepsilon_{\mathrm{R},i}^2-\tau_i+\gamma_i\end{bmatrix}-\mathbf{C}^H\mathbf{\Psi}\mathbf{B}\mathbf{\Psi}^H\mathbf{C}\succeq\mathbf{0},\end{aligned}\tag{21}$$

where $\mathbf{C}=\begin{bmatrix}\mathbf{I}_M & \mathbf{0}\end{bmatrix}$. Similarly, by applying Lemma 1, we rewrite constraints $\overline{\mathrm{C4}}$a and $\overline{\mathrm{C4}}$b as follows

$$\begin{aligned}&\widehat{\mathrm{C4}}\text{a: }\mathbf{S}_{\widehat{\mathrm{C4a}}_i}(p_j,\beta_i,\iota_i)\\ &=\begin{bmatrix}\iota_i\mathbf{I}_J & \mathbf{0}\\ \mathbf{0} & -\sum_{j\in\mathcal{J}}\iota_i\epsilon_{i,j}^2-\beta_i+\frac{p_{\mathrm{tol}_i}}{3}\end{bmatrix}-\mathbf{D}_i^H\mathbf{P}\mathbf{D}_i\succeq\mathbf{0},\end{aligned}\tag{22}$$

$$\widehat{\text{C4b}}\text{: } \mathbf{S}_{\widehat{\text{C4b}}_i}(\mathbf{W}_k,\beta_i,\gamma_i,\kappa_i) = \begin{bmatrix} \kappa_i \mathbf{I}_{N_\text{T}} & \mathbf{0} \\ \mathbf{0} & -\kappa_i \varepsilon_{\text{D},i}^2 - \gamma_i + \beta_i \end{bmatrix} - \sum_{k\in\mathcal{K}} \mathbf{E}_i^H \mathbf{W}_k \mathbf{E}_i \succeq \mathbf{0}, \tag{23}$$

where $\iota_i,\ \kappa_i \geq 0$, $\mathbf{P} \triangleq \text{diag}(p_1,\cdots,p_J)$, $\mathbf{D}_i \triangleq \left[\ \mathbf{I}_J\ \mathbf{0}\ \right]$, and $\mathbf{E}_i \triangleq \left[\ \mathbf{I}_{N_\text{T}}\ \mathbf{0}\ \right]$. We note that $\widehat{\text{C4a}}$ is convex with respect to p_j and $\widehat{\text{C4b}}$ is convex with respect to $\mathbf{W}_k$. Moreover, $\widehat{\text{C4c}}$ is convex with respect to p_j and $\mathbf{W}_k$ but is still non-convex with respect to $\mathbf{\Psi}$ due to the quadratic term $\mathbf{\Psi B \Psi}^H$.

B. Optimizing $\{\mathbf{W}_k, p_j\}$ for Given $\mathbf{\Psi}$ and $\mathbf{v}_j$

For given $\mathbf{\Psi}$ and $\mathbf{v}_j$, we first rewrite the terms $\left|\mathbf{g}_{\text{D},k}^H\mathbf{w}_r + \mathbf{g}_{\text{R},k}^H\mathbf{\Psi F}\mathbf{w}_r\right|^2$ and $\left|q_{j,k} + \mathbf{g}_{\text{R},k}^H\mathbf{\Psi}\mathbf{h}_{\text{R},j}\right|^2$ in (7), the term $\left|\mathbf{h}_{\text{D},t}^H\mathbf{v}_j + \mathbf{h}_{\text{R},t}^H\mathbf{\Psi}^H\mathbf{F}\mathbf{v}_j\right|^2$ in (8), and the terms $\left|\overline{\mathbf{l}}_{\text{D},i}^H\mathbf{w}_k + \overline{\mathbf{l}}_{\text{R},i}^H\mathbf{\Psi F}\mathbf{w}_k\right|^2$ and $\left|\overline{e}_{i,j} + \overline{\mathbf{l}}_{\text{R},i}^H\mathbf{\Psi}\mathbf{h}_{\text{R},j}\right|^2$ in (16), as shown in the bottom of this page, as follows, respectively,

$$\left|\mathbf{g}_{\text{D},k}^H\mathbf{w}_k + \mathbf{g}_{\text{R},k}^H\mathbf{\Psi F}\mathbf{w}_k\right|^2 = \left|\widehat{\mathbf{g}}_k^H\mathbf{w}_k\right|^2 = \text{Tr}(\widehat{\mathbf{g}}_k\widehat{\mathbf{g}}_k^H\mathbf{W}_k), \tag{24}$$

$$\left|\mathbf{h}_{\text{D},j}^H\mathbf{v}_j + \mathbf{h}_{\text{R},j}^H\mathbf{\Psi}^H\mathbf{F}\mathbf{v}_j\right|^2 = \left|\widehat{\mathbf{h}}_j^H\mathbf{v}_j\right|^2 = \text{Tr}(\widehat{\mathbf{h}}_j\widehat{\mathbf{h}}_j^H\mathbf{v}_j\mathbf{v}_j^H), \tag{25}$$

$$\left|\overline{\mathbf{l}}_{\text{D},i}^H\mathbf{w}_k + \overline{\mathbf{l}}_{\text{R},i}^H\mathbf{\Psi F}\mathbf{w}_k\right|^2 = \left|\widehat{\mathbf{l}}_i^H\mathbf{w}_k\right|^2 = \text{Tr}(\widehat{\mathbf{l}}_i\widehat{\mathbf{l}}_i^H\mathbf{W}_k), \tag{26}$$

$$\left|q_{j,k} + \mathbf{g}_{\text{R},k}^H\mathbf{\Psi}\mathbf{h}_{\text{R},j}\right|^2 = \left|\varphi_{j,k}\right|^2, \tag{27}$$

$$\left|\overline{e}_{i,j} + \overline{\mathbf{l}}_{\text{R},i}^H\mathbf{\Psi}\mathbf{h}_{\text{R},j}\right|^2 = \left|\vartheta_{i,j}\right|^2, \tag{28}$$

where $\widehat{\mathbf{g}}_k \in \mathbb{C}^{N_\text{T}\times 1}$, $\widehat{\mathbf{h}}_j \in \mathbb{C}^{N_\text{T}\times 1}$, $\widehat{\mathbf{l}}_i \in \mathbb{C}^{N_\text{T}\times 1}$, $\varphi_{j,k} \in \mathbb{C}$, and $\vartheta_{i,j} \in \mathbb{C}$ are defined as $\widehat{\mathbf{g}}_k = \mathbf{g}_{\text{D},k} + \mathbf{F}^H\mathbf{\Psi}^H\mathbf{g}_{\text{R},k}$, $\widehat{\mathbf{h}}_j = \mathbf{h}_{\text{D},j} + \mathbf{F}^H\mathbf{\Psi}\mathbf{h}_{\text{R},j}$, $\widehat{\mathbf{l}}_i = \overline{\mathbf{l}}_{\text{D},i} + \mathbf{F}^H\mathbf{\Psi}^H\overline{\mathbf{l}}_{\text{R},i}$, $\varphi_{j,k} = q_{j,k} + \mathbf{g}_{\text{R},j}^H\mathbf{\Psi}\mathbf{h}_{\text{R},j}$, and $\vartheta_{i,j} = \overline{e}_{i,j} + \overline{\mathbf{l}}_{\text{R},i}^H\mathbf{\Psi}\mathbf{h}_{\text{R},j}$, respectively. Then, the received SINR of the k-th secondary DL user and the received SINR of the j-th secondary UL user can be rewritten as (29) and (30) which are shown at the bottom of the page, respectively. Constraint $\overline{\text{C4d}}$ can be rewritten equivalently as:

$$\widehat{\text{C4d}}\text{: } \sum_{k\in\mathcal{K}} \text{Tr}(\widehat{\mathbf{l}}_i\widehat{\mathbf{l}}_i^H\mathbf{W}_k) + \sum_{j\in\mathcal{J}} p_j \left|\vartheta_{i,j}\right|^2 \leq \tau_i, \quad \forall i. \tag{31}$$

Then, the joint DL transmit beamforming and UL power allocation design, i.e., $\{\mathbf{W}_k, p_j\}$, is formulated as follows

$$\begin{aligned} \underset{\substack{\mathbf{W}_k\in\mathbb{H}^{N_\text{T}},p_j,\\ \beta_i,\gamma_i,\tau_i,\delta_i,\iota_i,\kappa_i}}{\text{maximize}} \quad & \sum_{j\in\mathcal{J}} \omega_j^{\text{UL}} \log_2(1+\Gamma_j^{\text{UL}}) \\ & + \sum_{k\in\mathcal{K}} \omega_k^{\text{DL}} \log_2(1+\Gamma_k^{\text{DL}}) \\ \text{s.t. C1: } & \sum_{k\in\mathcal{K}} \text{Tr}(\mathbf{W}_k) \leq P_{\max}^{\text{DL}},\ \text{C2}, \widehat{\text{C4a}}, \widehat{\text{C4b}}, \widehat{\text{C4c}}, \widehat{\text{C4d}}, \\ & \text{C5: } \mathbf{W}_k \succeq \mathbf{0}, \quad \forall k, \quad \text{C6: } \text{Rank}(\mathbf{W}_k) \leq 1, \quad \forall k. \end{aligned} \tag{32}$$

$$\overline{\text{C4a}}\text{: } \max_{e_{i,j}\in\Omega_{i,j}} \sum_{j\in\mathcal{J}} p_j \left|\Delta e_{i,j}\right|^2 + \beta_i \leq \frac{p_{\text{tol}_i}}{3}, \quad \forall \text{ and } \overline{\text{C4b}}\text{: } \max_{\mathbf{l}_{\text{D},i}\in\Omega_{\text{D},i}} \sum_{k\in\mathcal{K}} \left|\Delta\mathbf{l}_{\text{D},i}^H\mathbf{w}_k\right|^2 + \gamma_i \leq \beta_i, \quad \forall i, \tag{14}$$

$$\overline{\text{C4c}}\text{: } \max_{\mathbf{l}_{\text{R},i}\in\Omega_{\text{R},i}} \sum_{k\in\mathcal{K}} \left|\Delta\mathbf{l}_{\text{R},i}^H\mathbf{\Psi F}\mathbf{w}_k\right|^2 + \sum_{j\in\mathcal{J}} p_j \left|\Delta\mathbf{l}_{\text{R},i}^H\mathbf{\Psi}\mathbf{h}_{\text{R},j}\right|^2 + \tau_i \leq \gamma_i, \quad \forall i, \tag{15}$$

$$\overline{\text{C4d}}\text{: } \sum_{k\in\mathcal{K}} \left|\overline{\mathbf{l}}_{\text{D},i}^H\mathbf{w}_k + \overline{\mathbf{l}}_{\text{R},i}^H\mathbf{\Psi F}\mathbf{w}_k\right|^2 + \sum_{j\in\mathcal{J}} p_j \left|\overline{e}_{i,j} + \overline{\mathbf{l}}_{\text{R},i}^H\mathbf{\Psi}\mathbf{h}_{\text{R},j}\right|^2 \leq \tau_i, \quad \forall i. \tag{16}$$

$$\Gamma_k^{\text{DL}} = \frac{\text{Tr}(\widehat{\mathbf{g}}_k\widehat{\mathbf{g}}_k^H\mathbf{W}_k)}{\sum\limits_{r\in\mathcal{K}\setminus\{k\}} \text{Tr}(\widehat{\mathbf{g}}_k\widehat{\mathbf{g}}_k^H\mathbf{W}_r) + \sum\limits_{j\in\mathcal{J}} p_j \left|\varphi_{j,k}\right|^2 + \sigma_{\text{n}_k}^2} \text{ and} \tag{29}$$

$$\Gamma_j^{\text{UL}} = \frac{p_j \text{Tr}(\widehat{\mathbf{h}}_j\widehat{\mathbf{h}}_j^H\mathbf{v}_j\mathbf{v}_j^H)}{\sum\limits_{t\in\mathcal{J}\setminus\{j\}} p_t \text{Tr}(\widehat{\mathbf{h}}_t\widehat{\mathbf{h}}_t^H\mathbf{v}_j\mathbf{v}_j^H) + \text{Tr}\big(\eta\mathbf{v}_j\mathbf{v}_j^H \text{Diag}\big(\sum\limits_{k\in\mathcal{K}} \mathbf{S}\mathbf{W}_k\mathbf{S}^H\big)\big) + \sigma_{\text{U}}^2 \left\|\mathbf{v}_j\right\|^2}, \tag{30}$$

$$f_1 = -\sum_{k\in\mathcal{K}} \omega_k^{\text{DL}} \log_2 \left(\sum_{r\in\mathcal{K}} \text{Tr}(\widehat{\mathbf{g}}_k\widehat{\mathbf{g}}_k^H\mathbf{W}_r) + \sum_{j\in\mathcal{J}} p_j \left|\varphi_{j,k}\right|^2 + \sigma_{\text{n}_k}^2 \right), \tag{33}$$

$$f_2 = -\sum_{j\in\mathcal{J}} \omega_j^{\text{UL}} \log_2 \left(\sum_{t\in\mathcal{J}} p_t \text{Tr}(\widehat{\mathbf{h}}_t\widehat{\mathbf{h}}_t^H\mathbf{v}_j\mathbf{v}_j^H) + \sigma_{\text{U}}^2 \left\|\mathbf{v}_j\right\|^2 + \text{Tr}\big(\eta\mathbf{v}_j\mathbf{v}_j^H \text{Diag}\big(\sum_{k\in\mathcal{K}} \mathbf{S}\mathbf{W}_k\mathbf{S}^H\big)\big) \right), \tag{34}$$

$$g_1 = -\sum_{k\in\mathcal{K}} \omega_k^{\text{DL}} \log_2 \left(\sum_{r\in\mathcal{K}\setminus\{k\}} \text{Tr}(\widehat{\mathbf{g}}_k\widehat{\mathbf{g}}_k^H\mathbf{W}_r) + \sum_{j\in\mathcal{J}} p_j \left|\varphi_{j,k}\right|^2 + \sigma_{\text{n}_k}^2 \right), \tag{35}$$

$$g_2 = -\sum_{j\in\mathcal{J}} \omega_j^{\text{UL}} \log_2 \left(\sum_{t\in\mathcal{J}\setminus\{j\}} p_t \text{Tr}(\widehat{\mathbf{h}}_t\widehat{\mathbf{h}}_t^H\mathbf{v}_j\mathbf{v}_j^H) + \sigma_{\text{U}}^2 \left\|\mathbf{v}_j\right\|^2 + \text{Tr}\big(\eta\mathbf{v}_j\mathbf{v}_j^H \text{Diag}\big(\sum_{k\in\mathcal{K}} \mathbf{S}\mathbf{W}_k\mathbf{S}^H\big)\big) \right). \tag{36}$$

Here, constraints C5, C6, and $\mathbf{W}_k \in \mathbb{H}^{N_{\mathrm{T}}}$ are imposed to ensure that $\mathbf{W}_k = \mathbf{w}_k\mathbf{w}_k^H$ holds after optimization. The non-convexity of (32) originates from the objective function and the rank constraint C6. Next, we aim to obtain a sub-optimal solution of (32) iteratively by applying SCA. For notational simplicity, we define f_1, f_2, g_1, and g_2 which are shown at the bottom of the previous page, respectively. Note that the negative objective function in (32) can be expressed as $f_1 + f_2 - g_1 - g_2$.

Then, in the n-th iteration of the SCA, for a given feasible[9] point $(\mathbf{W}_k^n, p_j^n)$, we construct a global underestimator of $g_1(\mathbf{W}_k, p_j)$ as follows

$$\begin{aligned} g_1(\mathbf{W}_k, p_j) &\geq g_1(\mathbf{W}_k^n, p_j^n) + \sum_{j\in\mathcal{J}} \nabla_{p_j} g_1(\mathbf{W}_k^n, p_j^n)(p_j - p_j^n) \\ &\quad + \sum_{k\in\mathcal{K}} \mathrm{Tr}\Big(\big(\nabla_{\mathbf{W}_k} g_1(\mathbf{W}_k^n, p_j^n)\big)^H (\mathbf{W}_k - \mathbf{W}_k^n) \Big) \\ &\triangleq \widehat{g}_1(\mathbf{W}_k, p_j, \mathbf{W}_k^n, p_j^n), \end{aligned} \tag{37}$$

where

$$\nabla_{\mathbf{W}_k} g_1 = \sum_{t\in\mathcal{K}\setminus\{k\}} \frac{-\frac{\omega_k^{\mathrm{DL}}}{\ln 2}\widehat{\mathbf{g}}_k\widehat{\mathbf{g}}_k^H}{\sum\limits_{r\in\mathcal{K}\setminus\{t\}} \mathrm{Tr}(\widehat{\mathbf{g}}_k\widehat{\mathbf{g}}_k^H\mathbf{W}_r) + \sum\limits_{j\in\mathcal{J}} p_j \left|\varphi_{j,k}\right|^2 + \sigma_{\mathrm{n}_k}^2}, \tag{38}$$

and

$$\nabla_{p_j} g_1 = \sum_{k\in\mathcal{K}} \frac{-\frac{\omega_k^{\mathrm{DL}}}{\ln 2}\left|\varphi_{j,k}\right|^2}{\sum\limits_{r\in\mathcal{K}\setminus\{k\}} \mathrm{Tr}(\widehat{\mathbf{g}}_k\widehat{\mathbf{g}}_k^H\mathbf{W}_r) + \sum\limits_{j\in\mathcal{J}} p_j \left|\varphi_{j,k}\right|^2 + \sigma_{\mathrm{n}_k}^2}. \tag{39}$$

Similarly, for a given feasible point $(\mathbf{W}_k^n, p_j^n)$, the global underestimator of $g_2(\mathbf{W}_k, p_j)$ is given by

$$\begin{aligned} g_2(\mathbf{W}_k, p_j) &\geq g_2(\mathbf{W}_k^n, p_j^n) \\ &\quad + \sum_{k\in\mathcal{K}} \mathrm{Tr}\Big(\big(\nabla_{\mathbf{W}_k} g_2(\mathbf{W}_k^n, p_j^n)\big)^H (\mathbf{W}_k - \mathbf{W}_k^n) \Big) \\ &\quad + \sum_{j\in\mathcal{J}} \nabla_{p_j} g_2(\mathbf{W}_k^n, p_j^n)(p_j - p_j^n) \\ &\triangleq \widehat{g}_2(\mathbf{W}_k, p_j, \mathbf{W}_k^n, p_j^n), \end{aligned} \tag{40}$$

where $\nabla_{\mathbf{W}_k} g_2$ and $\nabla_{p_j} g_2$ are shown at the bottom of the page, respectively.

[9]The superscript n denotes the SCA iteration index.

Algorithm 1 Successive Convex Approximation Algorithm for Obtaining $\mathbf{W}_k^\dagger$ and $p_j^\dagger$

1: Set initial point $\mathbf{W}_k^1$ and p_j^1, iteration index $n = 1$, and error tolerance $0 \leq \varepsilon_{\mathrm{SCA}} \ll 1$.
2: **repeat**
3: Solve (43) for given $\mathbf{W}_k^n$ and p_j^n and store the intermediate solution $\mathbf{W}_k$ and p_j
4: Set $n = n + 1$, $\mathbf{W}_k^n = \mathbf{W}_k$, and $p_j^n = p_j$
5: **until** $\frac{\left|\widehat{F}(\mathbf{W}_k^n, p_j^n) - \widehat{F}(\mathbf{W}_k^{n-1}, p_j^{n-1})\right|}{\left|\widehat{F}(\mathbf{W}_k^n, p_j^n)\right|} \leq \varepsilon_{\mathrm{SCA}}$
6: $\mathbf{W}_k^\dagger = \mathbf{W}_k^n$ and $p_j^\dagger = p_j^n$

Then, for a given feasible point $(\mathbf{W}_k^n, p_j^n)$ in the n-th iteration, a lower bound of the maximization problem in (32) can be obtained by solving the following optimization problem

$$\begin{aligned} &\underset{\substack{\mathbf{W}_k, p_j, \beta_i, \gamma_i, \\ \tau_i, \delta_i, \iota_i, \kappa_i}}{\text{minimize}} \ \widehat{F}(\mathbf{W}_k, p_j) \\ &\text{s.t. C1, C2, } \widehat{\text{C4a}}, \widehat{\text{C4b}}, \widehat{\text{C4c}}, \widehat{\text{C4d}}, \text{C5, C6,} \end{aligned} \tag{43}$$

where $\widehat{F}(\mathbf{W}_k, p_j)$ is defined as $\widehat{F}(\mathbf{W}_k, p_j) \triangleq f_1 + f_2 - \widehat{g}_1(\mathbf{W}_k, p_j, \mathbf{W}_k^n, p_j^n) - \widehat{g}_2(\mathbf{W}_k, p_j, \mathbf{W}_k^n, p_j^n)$. We note that the remaining non-convexity of problem (43) stems from rank-one constraint C6. Hence, we adopt SDR and remove constraint C6. The relaxed version of problem (43) can now be optimally solved by standard convex solvers such as CVX [38]. Next, we verify the tightness of SDR in the following theorem.

Theorem 1: If $P_{\max}^{\mathrm{DL}} > 0$, an optimal beamforming matrix $\mathbf{W}_k$ satisfying $\mathrm{Rank}(\mathbf{W}_k) \leq 1$ can always be obtained.

Proof: Please refer to Appendix A. ■

Then, we tighten the upper bound of (32) by solving (43) iteratively. The SCA algorithm for obtaining the optimal $\mathbf{w}_k^\dagger$ and $p_j^\dagger$ of (32) is summarized in **Algorithm 1**. We note that **Algorithm 1** is guaranteed to converge to a locally optimal solution of (32) [24].

C. Optimizing $\mathbf{v}_j$ for Given $\mathbf{\Psi}$, $\mathbf{W}_k$, and p_j

For given $\mathbf{\Psi}$, $\mathbf{W}_k$, and p_j, the UL spectral efficiency is maximized if for each UL user j, the receive beamforming vector $\mathbf{v}_j$ maximizes the corresponding receive SINR Γ_j^{UL}. In particular, we can obtain the optimal receive beamforming vector $\mathbf{v}_j$ by solving the following optimization problem [39]:

$$\underset{\mathbf{v}_j}{\text{maximize}} \ \frac{p_j\mathbf{v}_j^H\widehat{\mathbf{h}}_j\widehat{\mathbf{h}}_j^H\mathbf{v}_j}{\mathbf{v}_j^H\mathbf{R}_{\mathrm{I}_j}\mathbf{v}_j}, \tag{44}$$

$$\nabla_{\mathbf{W}_k} g_2 = -\frac{\omega_j^{\mathrm{UL}}}{\ln 2} \sum_{j\in\mathcal{J}} \frac{\eta\mathbf{v}_j\mathbf{v}_j^H\mathrm{Diag}(\mathbf{S}\mathbf{S}^H)}{\sum\limits_{t\in\mathcal{J}\setminus\{j\}} p_t\mathrm{Tr}(\widehat{\mathbf{h}}_t\widehat{\mathbf{h}}_t^H\mathbf{v}_j\mathbf{v}_j^H) + \mathrm{Tr}\big(\eta\mathbf{v}_j\mathbf{v}_j^H\mathrm{Diag}\big(\sum\limits_{k\in\mathcal{K}}\mathbf{S}\mathbf{W}_k\mathbf{S}^H\big)\big) + \sigma_{\mathrm{U}}^2\left\|\mathbf{v}_j\right\|^2}, \tag{41}$$

$$\nabla_{p_j} g_2 = -\frac{\omega_j^{\mathrm{UL}}}{\ln 2} \sum_{r\in\mathcal{J}\setminus\{j\}} \frac{\mathrm{Tr}(\widehat{\mathbf{h}}_r\widehat{\mathbf{h}}_r^H\mathbf{v}_j\mathbf{v}_j^H)}{\sum\limits_{t\in\mathcal{J}\setminus\{r\}} p_t\mathrm{Tr}(\widehat{\mathbf{h}}_t\widehat{\mathbf{h}}_t^H\mathbf{v}_r\mathbf{v}_r^H) + \mathrm{Tr}\big(\eta\mathbf{v}_j\mathbf{v}_j^H\mathrm{Diag}\big(\sum\limits_{k\in\mathcal{K}}\mathbf{S}\mathbf{W}_k\mathbf{S}^H\big)\big) + \sigma_{\mathrm{U}}^2\left\|\mathbf{v}_r\right\|^2}. \tag{42}$$

where $\widehat{\mathbf{h}}_j$ was defined in (25) and $\mathbf{R}_{\mathrm{I}_j} \in \mathbb{C}^{N_\mathrm{T}\times N_\mathrm{T}}$ is defined as follows

$$\begin{aligned}\mathbf{R}_{\mathrm{I}_j} = &\sum_{t\in\mathcal{J}\setminus\{j\}} p_t\big(\mathbf{h}_{\mathrm{D},t}\mathbf{h}_{\mathrm{D},t}^H + \mathbf{F}^H\boldsymbol{\Psi}\mathbf{h}_{\mathrm{R},t}\mathbf{h}_{\mathrm{D},t}^H \\ &+ \mathbf{h}_{\mathrm{D},t}\mathbf{h}_{\mathrm{R},t}^H\boldsymbol{\Psi}^H\mathbf{F} + \mathbf{F}^H\boldsymbol{\Psi}\mathbf{h}_{\mathrm{R},t}\mathbf{h}_{\mathrm{R},t}^H\boldsymbol{\Psi}^H\mathbf{F}\big) \\ &+ \eta\mathrm{Diag}\big(\sum_{k\in\mathcal{K}}\mathbf{S}\mathbf{W}_k\mathbf{S}^H\big) + \sigma_\mathrm{U}^2\mathbf{I}_{N_\mathrm{T}}. \end{aligned} \tag{45}$$

Moreover, the optimization problem in (44) can be recast as the following equivalent convex optimization problem [39]

$$\begin{aligned}&\underset{\mathbf{v}_j}{\text{minimize}}\ \mathbf{v}_j^H\mathbf{R}_{\mathrm{I}_j}\mathbf{v}_j \\ &\text{s.t. C7: } \sqrt{p_j}\mathbf{v}_j^H\widehat{\mathbf{h}}_j = 1. \end{aligned} \tag{46}$$

The optimal solution of (46) is given by [39]

$$\mathbf{v}_j^\dagger = \varrho_j\sqrt{p_j}\mathbf{R}_{\mathrm{I}_j}^{-1}\widehat{\mathbf{h}}_j, \tag{47}$$

where ϱ_j is a scalar to adjust $\mathbf{v}_j^\dagger$ such that equality constraint C7 is satisfied. We note that for the original problem in (44), ϱ_j can be omitted as it has no effect on the value of the objective function.

D. Optimizing $\boldsymbol{\Psi}$ for Given $\mathbf{W}_k$, p_j, and $\mathbf{v}_j$

For given $\mathbf{W}_k$, p_j, and $\mathbf{v}_j$, the optimization problem for the IRS phase shift design is given by

$$\begin{aligned}&\underset{\substack{\boldsymbol{\Psi},\beta_i,\gamma_i,\tau_i,\\ \delta_i,\iota_i,\kappa_i}}{\text{maximize}} \sum_{j\in\mathcal{J}}\omega_j^{\mathrm{UL}}\log_2(1+\Gamma_j^{\mathrm{UL}}) + \sum_{k\in\mathcal{K}}\omega_k^{\mathrm{DL}}\log_2(1+\Gamma_k^{\mathrm{DL}}) \\ &\text{s.t. C3, } \widehat{\text{C4}}\text{a, } \widehat{\text{C4}}\text{b, } \widehat{\text{C4}}\text{c, } \widehat{\text{C4}}\text{d.} \end{aligned} \tag{48}$$

We note that both the objective function and constraints C3 and $\widehat{\text{C4}}$c are non-convex functions which makes the IRS design very challenging. Next, we first tackle the non-convex objective function in (48). In particular, we rewrite the quadratic term $\left|\mathbf{g}_{\mathrm{D},k}^H\mathbf{w}_r + \mathbf{g}_{\mathrm{R},k}^H\boldsymbol{\Psi}\mathbf{F}\mathbf{w}_r\right|^2$ in (7) as follows:

$$\begin{aligned}&\left|\mathbf{g}_{\mathrm{D},k}^H\mathbf{w}_r + \mathbf{g}_{\mathrm{R},k}^H\boldsymbol{\Psi}\mathbf{F}\mathbf{w}_r\right|^2 \\ &= \mathbf{g}_{\mathrm{D},k}^H\mathbf{W}_r\mathbf{g}_{\mathrm{D},k} + 2\Re\left\{\mathbf{g}_{\mathrm{D},k}^H\mathbf{W}_r\mathbf{F}^H\boldsymbol{\Psi}^H\mathbf{g}_{\mathrm{R},k}\right\} \\ &\quad + \mathbf{g}_{\mathrm{R},k}^H\boldsymbol{\Psi}\mathbf{F}\mathbf{W}_r\mathbf{F}^H\boldsymbol{\Psi}^H\mathbf{g}_{\mathrm{R},k} \\ &= \mathbf{g}_{\mathrm{D},k}^H\mathbf{W}_r\mathbf{g}_{\mathrm{D},k} + 2\Re\left\{\mathbf{g}_{\mathrm{D},k}^H\mathbf{W}_r\mathbf{F}^H\mathrm{diag}(\mathbf{g}_{\mathrm{R},k})\boldsymbol{\theta}\right\} \\ &\quad + \boldsymbol{\theta}^H\mathrm{diag}(\mathbf{g}_{\mathrm{R},k}^H)\mathbf{F}\mathbf{W}_r\mathbf{F}^H\mathrm{diag}(\mathbf{g}_{\mathrm{R},k})\boldsymbol{\theta} \\ &= \mathrm{Tr}\Big(\begin{bmatrix}\boldsymbol{\theta}^H & \rho^*\end{bmatrix}\begin{bmatrix}\mathrm{diag}(\mathbf{g}_{\mathrm{R},k}^H)\mathbf{F} \\ \mathbf{g}_{\mathrm{D},k}^H\end{bmatrix} \\ &\qquad \times\mathbf{W}_r\begin{bmatrix}\mathbf{F}^H\mathrm{diag}(\mathbf{g}_{\mathrm{R},k}) & \mathbf{g}_{\mathrm{D},k}\end{bmatrix}\begin{bmatrix}\boldsymbol{\theta} \\ \rho\end{bmatrix}\Big) \\ &= \mathrm{Tr}(\widetilde{\boldsymbol{\theta}}^H\mathbf{G}_k\mathbf{W}_r\mathbf{G}_k^H\widetilde{\boldsymbol{\theta}}) = \mathrm{Tr}(\boldsymbol{\Theta}\mathbf{G}_k\mathbf{W}_r\mathbf{G}_k^H), \end{aligned} \tag{49}$$

where optimization variables $\boldsymbol{\theta} \in \mathbb{C}^{M\times 1}$, $\widetilde{\boldsymbol{\theta}} \in \mathbb{C}^{(M+1)\times 1}$, and $\boldsymbol{\Theta} \in \mathbb{C}^{(M+1)\times(M+1)}$ are defined as $\boldsymbol{\theta} = [e^{j\psi_1},\cdots,e^{j\psi_M}]^H$, $\widetilde{\boldsymbol{\theta}} = [\boldsymbol{\theta}^T\ \rho]^T$, and $\boldsymbol{\Theta} = \widetilde{\boldsymbol{\theta}}\widetilde{\boldsymbol{\theta}}^H$, respectively. Moreover, $\rho \in \mathbb{C}$ is a dummy variable with $|\rho|^2 = 1$. Besides, $\mathbf{G}_k \in \mathbb{C}^{(M+1)\times N_\mathrm{T}}$ is defined as $\mathbf{G}_k = \left[\left(\mathrm{diag}(\mathbf{g}_{\mathrm{R},k}^H)\mathbf{F}\right)^T\ \ \mathbf{g}_{\mathrm{D},k}^*\right]^T$.

Similarly, we rewrite the term $\left|q_{j,k} + \mathbf{g}_{\mathrm{R},k}^H\boldsymbol{\Psi}\mathbf{h}_{\mathrm{R},j}\right|^2$ in (7), the term $\left|\mathbf{h}_{\mathrm{D},t}^H\mathbf{v}_j + \mathbf{h}_{\mathrm{R},t}^H\boldsymbol{\Psi}\mathbf{F}\mathbf{v}_j\right|^2$ in (8), and the terms $\left|\bar{\mathbf{l}}_{\mathrm{D},i}^H\mathbf{w}_k + \bar{\mathbf{l}}_{\mathrm{R},i}^H\boldsymbol{\Psi}\mathbf{F}\mathbf{w}_k\right|^2$ and $\left|\overline{e}_{i,j} + \bar{\mathbf{l}}_{\mathrm{R},i}^H\boldsymbol{\Psi}\mathbf{h}_{\mathrm{R},j}\right|^2$ in (16) as follows, respectively,

$$\left|q_{j,k} + \mathbf{g}_{\mathrm{R},k}^H\boldsymbol{\Psi}\mathbf{h}_{\mathrm{R},j}\right|^2 = \mathrm{Tr}(\boldsymbol{\Theta}\mathbf{Q}_{j,k}), \tag{50}$$

$$\left|\mathbf{h}_{\mathrm{D},t}^H\mathbf{v}_j + \mathbf{h}_{\mathrm{R},t}^H\boldsymbol{\Psi}^H\mathbf{F}\mathbf{v}_j\right|^2 = \mathrm{Tr}(\boldsymbol{\Theta}^T\mathbf{H}_t\mathbf{v}_j\mathbf{v}_j^H\mathbf{H}_t^H), \tag{51}$$

$$\left|\bar{\mathbf{l}}_{\mathrm{D},i}^H\mathbf{w}_k + \bar{\mathbf{l}}_{\mathrm{R},i}^H\boldsymbol{\Psi}\mathbf{F}\mathbf{w}_k\right|^2 = \mathrm{Tr}(\boldsymbol{\Theta}\mathbf{L}_i\mathbf{W}_k\mathbf{L}_i^H), \tag{52}$$

$$\left|\overline{e}_{i,j} + \bar{\mathbf{l}}_{\mathrm{R},i}^H\boldsymbol{\Psi}\mathbf{h}_{\mathrm{R},j}\right|^2 = \mathrm{Tr}(\boldsymbol{\Theta}\mathbf{P}_{i,j}), \tag{53}$$

where $\mathbf{H}_t \in \mathbb{C}^{(M+1)\times N_\mathrm{T}}$ and $\mathbf{L}_i \in \mathbb{C}^{(M+1)\times N_\mathrm{T}}$ are defined as $\mathbf{H}_t = \left[\left(\mathrm{diag}(\mathbf{h}_{\mathrm{R},t}^H)\mathbf{F}\right)^T\ \ \mathbf{h}_{\mathrm{D},t}^*\right]^T$ and $\mathbf{L}_i = \left[\left(\mathrm{diag}(\bar{\mathbf{l}}_{\mathrm{R},i}^H)\mathbf{F}\right)^T\ \ \bar{\mathbf{l}}_{\mathrm{D},i}^*\right]^T$, respectively. Moreover, $\mathbf{Q}_{j,k} \in \mathbb{C}^{(M+1)\times(M+1)}$ and $\mathbf{P}_{i,j} \in \mathbb{C}^{(M+1)\times(M+1)}$ are defined as

$$\begin{aligned}&\mathbf{Q}_{j,k} \\ &= \begin{bmatrix}\mathrm{diag}(\mathbf{g}_{\mathrm{R},k}^H)\mathbf{H}_{\mathrm{R},j}\mathrm{diag}(\mathbf{g}_{\mathrm{R},k}) & q_{j,k}^*\mathrm{diag}(\mathbf{g}_{\mathrm{R},k}^H)\mathbf{h}_{\mathrm{R},j} \\ \mathbf{h}_{\mathrm{R},j}^H\mathrm{diag}(\mathbf{g}_{\mathrm{R},k})q_{j,k} & |q_{j,k}|^2\end{bmatrix}, \end{aligned} \tag{54}$$

$$\begin{aligned}&\mathbf{P}_{i,j} \\ &= \begin{bmatrix}\mathrm{diag}(\bar{\mathbf{l}}_{\mathrm{R},i}^H)\mathbf{H}_{\mathrm{R},j}\mathrm{diag}(\bar{\mathbf{l}}_{\mathrm{R},i}) & \overline{e}_{i,j}^*\mathrm{diag}(\bar{\mathbf{l}}_{\mathrm{R},i}^H)\mathbf{h}_{\mathrm{R},j} \\ \mathbf{h}_{\mathrm{R},j}^H\mathrm{diag}(\bar{\mathbf{l}}_{\mathrm{R},i})\overline{e}_{i,j} & |\overline{e}_{i,j}|^2\end{bmatrix}, \end{aligned} \tag{55}$$

respectively.

Then, we rewrite constraint $\widehat{\text{C4}}$d equivalently as

$$\widetilde{\text{C4}}\text{d: } \sum_{k\in\mathcal{K}}\mathrm{Tr}(\boldsymbol{\Theta}\mathbf{L}_i\mathbf{W}_k\mathbf{L}_i^H) + \sum_{j\in\mathcal{J}}\mathrm{Tr}(\boldsymbol{\Theta}\mathbf{P}_{i,j}) \le \tau_i, \quad \forall i. \tag{56}$$

We note that $\widetilde{\text{C4}}$d is a convex constraint with respect to $\boldsymbol{\Theta}$. Moreover, the receive SINR of secondary DL user k and the receive SINR of secondary UL user j can be equivalently rewritten as (57) and (58), where (57) and (58) are shown at the bottom of the next page, respectively. For notational simplicity, we define $\widetilde{f}_1$, $\widetilde{f}_2$, $\widetilde{g}_1$, and $\widetilde{g}_2$ which are shown at the bottom of the next page, respectively. Note that the negative objective function in (48) can be expressed as $\widetilde{f}_1+\widetilde{f}_2-\widetilde{g}_1-\widetilde{g}_2$.

Next, by employing singular value decomposition, we transform constraint $\widehat{\text{C4}}$c into a convex constraint. Specifically, for given $\mathbf{W}_k$ and p_j, we recast matrix $\mathbf{B}$ as $\mathbf{B} = \sum_s\widetilde{\sigma}_s\widetilde{\mathbf{u}}_s\widetilde{\mathbf{v}}_s^H$, where $\widetilde{\sigma}_s$ are the singular values of $\mathbf{B}$, and $\widetilde{\mathbf{u}}_d$ and $\widetilde{\mathbf{v}}_d$ are the corresponding left and right singular vectors of $\mathbf{B}$, respectively. Then, we rewrite the term $\mathbf{C}^H\boldsymbol{\Psi}\mathbf{B}\boldsymbol{\Psi}^H\mathbf{C}$ in constraint $\widehat{\text{C4}}$c as follows

$$\begin{aligned}\mathbf{C}^H\boldsymbol{\Psi}\mathbf{B}\boldsymbol{\Psi}^H\mathbf{C} &= \sum_s\widetilde{\sigma}_s\mathbf{C}^H\mathrm{diag}(\widetilde{\mathbf{u}}_s)\boldsymbol{\theta}\boldsymbol{\theta}^H\mathrm{diag}(\widetilde{\mathbf{v}}_s^H)\mathbf{C} \\ &= \sum_s\widetilde{\sigma}_s\widetilde{\mathbf{D}}_s\boldsymbol{\Theta}\widetilde{\mathbf{E}}_s, \end{aligned} \tag{63}$$

where $\widetilde{\mathbf{D}}_s$, $\widetilde{\mathbf{E}}_s \in \mathbb{C}^{(M+1)\times(M+1)}$ are defined as $\widetilde{\mathbf{D}}_s = \left[\mathbf{C}^H\mathrm{diag}(\widetilde{\mathbf{u}}_s)\ \mathbf{0}\right]$ and $\widetilde{\mathbf{E}}_s = \begin{bmatrix}\mathrm{diag}(\widetilde{\mathbf{v}}_s)\mathbf{C} \\ \mathbf{0}\end{bmatrix}$, respectively. Hence, we can rewrite constraint $\widehat{\text{C4}}$c equivalently as

$$\begin{aligned}&\widetilde{\text{C4}}\text{c: } \mathbf{S}_{\overline{\text{C4c}}_i}(\boldsymbol{\Theta},\tau_i,\delta_i) \\ &= \begin{bmatrix}\delta_i\mathbf{I}_M & \mathbf{0} \\ \mathbf{0} & -\delta_i\varepsilon_{\mathrm{R},i}^2 - \tau_i + \gamma_i\end{bmatrix} - \sum_s\widetilde{\sigma}_s\widetilde{\mathbf{D}}_s\boldsymbol{\Theta}\widetilde{\mathbf{E}}_s \succeq \mathbf{0}. \end{aligned} \tag{64}$$

Now, constraint $\widetilde{\text{C4c}}$ is a convex function with respect to $\boldsymbol{\Theta}$.

Therefore, for given $\mathbf{W}_k$, p_j, and $\mathbf{v}_j$, we can obtain $\boldsymbol{\Theta}$ by solving the following optimization problem

$$\begin{aligned}\underset{\substack{\boldsymbol{\Theta}\in\mathbb{H}^{M+1},\beta_i,\gamma_i,\\ \tau_i,\delta_i,\iota_i,\kappa_i}}{\text{minimize}} \quad & \widetilde{f}_1+\widetilde{f}_2-\widetilde{g}_1-\widetilde{g}_2\\ \text{s.t. } \widetilde{\text{C3}}\text{: } & \text{Diag}(\boldsymbol{\Theta})=\mathbf{I}_{M+1},\ \widetilde{\text{C4a}},\widetilde{\text{C4b}}.\widetilde{\text{C4c}},\widetilde{\text{C4d}},\\ \text{C8: } & \boldsymbol{\Theta}\succeq\mathbf{0},\quad \text{C9: } \text{Rank}(\boldsymbol{\Theta})=1,\end{aligned}\tag{65}$$

where $\boldsymbol{\Theta}\succeq\mathbf{0}$ and constraints C8 and C9 are imposed to ensure $\boldsymbol{\Theta}=\widetilde{\boldsymbol{\theta}}\widetilde{\boldsymbol{\theta}}^H$ holds after optimization. We note that the rank-one constraint C9 is an obstacle to solving problem (65). In the literature, SDR is commonly adopted to tackle the rank-one constraint [40]. Yet, applying SDR to (65) may not result in a rank-one matrix $\boldsymbol{\Theta}$. Moreover, some approximation methods such as Gaussian randomization cannot guarantee the convergence of the overall BCD algorithm [40]. To tackle this obstacle, we first transform the combinatorial constraint C9 equivalently into the following difference of convex (d.c.) functions constraint [41]:

$$\widetilde{\text{C9}}\text{: } \|\boldsymbol{\Theta}\|_*-\|\boldsymbol{\Theta}\|_2\le 0,\tag{66}$$

where $\|\boldsymbol{\Theta}\|_2$ denotes the spectral norm, i.e., $\|\boldsymbol{\Theta}\|_2=\sigma_1(\boldsymbol{\Theta})$, where $\sigma_i(\boldsymbol{\Theta})$ denotes the i-th largest singular value of matrix $\boldsymbol{\Theta}$. We note that for any $\boldsymbol{\Theta}\in\mathbb{H}^{M+1}$ and $\boldsymbol{\Theta}\succeq\mathbf{0}$, we have $\|\boldsymbol{\Theta}\|_*=\sum_i\sigma_i(\boldsymbol{\Theta})\ge\|\boldsymbol{\Theta}\|_2=\max_i\sigma_i(\boldsymbol{\Theta})$ and the equality holds if and only if $\boldsymbol{\Theta}$ is a rank-one matrix. Yet, the resulting constraint $\widetilde{\text{C9}}$ is still non-convex. To circumvent this obstacle, we adopt a penalty approach [25] and recast (65) as follows:

$$\begin{aligned}\underset{\substack{\boldsymbol{\Theta}\in\mathbb{H}^{M+1},\beta_i,\gamma_i,\\ \tau_i,\delta_i,\iota_i,\kappa_i}}{\text{minimize}} \quad & \widetilde{f}_1+\widetilde{f}_2-\widetilde{g}_1-\widetilde{g}_2+\chi\big(\|\boldsymbol{\Theta}\|_*-\|\boldsymbol{\Theta}\|_2\big)\\ \text{s.t. } & \widetilde{\text{C3}},\widetilde{\text{C4a}},\widetilde{\text{C4b}},\widetilde{\text{C4c}},\widetilde{\text{C4d}},\text{C8},\end{aligned}\tag{67}$$

where $\chi\gg 0$ is a constant which penalizes the objective function for any matrix $\boldsymbol{\Theta}$ whose rank is larger than one. Then, we use a sequence of χ_q to approach infinity and reveal that problem (67) is equivalent to problem (65) in the following theorem [25].

Theorem 2: Denote the optimal solution of problem (67) as $\boldsymbol{\Theta}_q$ with penalty factor χ_q. When χ_q is sufficiently large, i.e., $\chi_q\to\infty$, every limit point $\overline{\boldsymbol{\Theta}}$ of the sequence $\{\boldsymbol{\Theta}_q\}$ is an optimal solution of problem (65).

Proof: Please refer to Appendix B. ■

The optimization problem in (67) is still an intractable problem due to the non-convexity of the objective function. Yet, we note that $\widetilde{f}_1$, $\widetilde{f}_2$, $\widetilde{g}_1$, $\widetilde{g}_2$, $\|\boldsymbol{\Theta}\|_*$, and $\|\boldsymbol{\Theta}\|_2$ are all convex functions and the problem in (67) is in the canonical form of d.c. programming. Thus, a stationary point of (67) can be obtained by applying SCA [24]. To start with, we first construct a global underestimator of $\widetilde{g}_1$. In particular, for any feasible point $\boldsymbol{\Theta}^n$, the differentiable convex function $\widetilde{g}_1(\boldsymbol{\Theta})$ satisfies the following inequality:

$$\begin{aligned}\widetilde{g}_1(\boldsymbol{\Theta})&\ge\widetilde{g}_1(\boldsymbol{\Theta}^n)+\text{Tr}\Big(\big(\nabla_{\boldsymbol{\Theta}}\widetilde{g}_1(\boldsymbol{\Theta}^n)\big)^H(\boldsymbol{\Theta}-\boldsymbol{\Theta}^n)\Big)\\&\triangleq\overline{g}_1(\boldsymbol{\Theta},\boldsymbol{\Theta}^n),\end{aligned}\tag{68}$$

where $\nabla_{\boldsymbol{\Theta}}\widetilde{g}_1$ is shown at the bottom of the page. We note that $\overline{g}_1(\boldsymbol{\Theta},\boldsymbol{\Theta}^n)$ in (68) is a global underestimator of $\widetilde{g}_1(\boldsymbol{\Theta})$. Similarly, for feasible point $\boldsymbol{\Theta}^n$, global underestimators of $\widetilde{g}_2(\boldsymbol{\Theta})$ and $\|\boldsymbol{\Theta}\|_2$ can be constructed as follows, respectively,

$$\begin{aligned}\widetilde{g}_2(\boldsymbol{\Theta})&\ge\widetilde{g}_2(\boldsymbol{\Theta}^n)+\text{Tr}\Big(\big(\nabla_{\boldsymbol{\Theta}}\widetilde{g}_2(\boldsymbol{\Theta}^n)\big)^H(\boldsymbol{\Theta}-\boldsymbol{\Theta}^n)\Big)\\&\triangleq\overline{g}_2(\boldsymbol{\Theta},\boldsymbol{\Theta}^n),\end{aligned}\tag{69}$$

$$\Gamma_k^{\text{DL}}=\frac{\text{Tr}(\boldsymbol{\Theta}\mathbf{G}_k\mathbf{W}_k\mathbf{G}_k^H)}{\sum_{r\in\mathcal{K}\setminus\{k\}}\text{Tr}(\boldsymbol{\Theta}\mathbf{G}_k\mathbf{W}_r\mathbf{G}_k^H)+\sum_{j\in\mathcal{J}}p_j\text{Tr}(\boldsymbol{\Theta}\mathbf{Q}_{j,k})+\sigma_{\text{n}_k}^2},\tag{57}$$

$$\Gamma_j^{\text{UL}}=\frac{p_j\text{Tr}(\boldsymbol{\Theta}^T\mathbf{H}_j\mathbf{v}_j\mathbf{v}_j^H\mathbf{H}_j^H)}{\sum_{t\in\mathcal{J}\setminus\{j\}}p_t\text{Tr}(\boldsymbol{\Theta}^T\mathbf{H}_t\mathbf{v}_j\mathbf{v}_j^H\mathbf{H}_t^H)+\text{Tr}\big(\eta\mathbf{v}_j\mathbf{v}_j^H\text{Diag}\big(\sum_{k\in\mathcal{K}}\mathbf{S}\mathbf{W}_k\mathbf{S}^H\big)\big)+\sigma_{\text{U}}^2\|\mathbf{v}_j\|^2}.\tag{58}$$

$$\widetilde{f}_1=-\sum_{k\in\mathcal{K}}\omega_k^{\text{DL}}\log_2\Big(\sum_{r\in\mathcal{K}}\text{Tr}(\boldsymbol{\Theta}\mathbf{G}_k\mathbf{W}_r\mathbf{G}_k^H)+\sum_{j\in\mathcal{J}}p_j\big(\text{Tr}(\boldsymbol{\Theta}\mathbf{Q}_{j,k})\big)+\sigma_{\text{n}_k}^2\Big),\tag{59}$$

$$\widetilde{f}_2=-\sum_{j\in\mathcal{J}}\omega_j^{\text{UL}}\log_2\Big(\sum_{t\in\mathcal{J}}p_t\text{Tr}(\boldsymbol{\Theta}^T\mathbf{H}_t\mathbf{v}_j\mathbf{v}_j^H\mathbf{H}_t^H)+\text{Tr}\big(\eta\mathbf{v}_j\mathbf{v}_j^H\text{Diag}\big(\sum_{k\in\mathcal{K}}\mathbf{S}\mathbf{W}_k\mathbf{S}^H\big)\big)+\sigma_{\text{U}}^2\|\mathbf{v}_j\|^2\Big),\tag{60}$$

$$\widetilde{g}_1=-\sum_{k\in\mathcal{K}}\omega_k^{\text{DL}}\log_2\Big(\sum_{r\in\mathcal{K}\setminus\{k\}}\text{Tr}(\boldsymbol{\Theta}\mathbf{G}_k\mathbf{W}_r\mathbf{G}_k^H)+\sum_{j\in\mathcal{J}}p_j\big(\text{Tr}(\boldsymbol{\Theta}\mathbf{Q}_{j,k})\big)+\sigma_{\text{n}_k}^2\Big),\tag{61}$$

$$\widetilde{g}_2=-\sum_{j\in\mathcal{J}}\omega_j^{\text{UL}}\log_2\Big(\sum_{t\in\mathcal{J}\setminus\{j\}}p_t\text{Tr}(\boldsymbol{\Theta}^T\mathbf{H}_t\mathbf{v}_j\mathbf{v}_j^H\mathbf{H}_t^H)+\text{Tr}\big(\eta\mathbf{v}_j\mathbf{v}_j^H\text{Diag}\big(\sum_{k\in\mathcal{K}}\mathbf{S}\mathbf{W}_k\mathbf{S}^H\big)\big)+\sigma_{\text{U}}^2\|\mathbf{v}_j\|^2\Big).\tag{62}$$

$$\nabla_{\boldsymbol{\Theta}}\widetilde{g}_2=\sum_{j\in\mathcal{J}}\frac{-\frac{\omega_j^{\text{UL}}}{\ln 2}\sum_{t\in\mathcal{J}\setminus\{j\}}p_t\mathbf{H}_t\mathbf{v}_j\mathbf{v}_j^H\mathbf{H}_t^H}{\sum_{t\in\mathcal{J}\setminus\{j\}}p_t\big(\text{Tr}(\boldsymbol{\Theta}^T\mathbf{H}_t\mathbf{v}_j\mathbf{v}_j^H\mathbf{H}_t^H)\big)+\text{Tr}\big(\eta\mathbf{v}_j\mathbf{v}_j^H\text{Diag}\big(\sum_{k\in\mathcal{K}}\mathbf{S}\mathbf{W}_k\mathbf{S}^H\big)\big)+\sigma_{\text{U}}^2\|\mathbf{v}_j\|^2},\tag{70}$$

Algorithm 2 Successive Convex Approximation Algorithm for Obtaining $\mathbf{\Psi}^{\dagger}$

1: Set initial point $\mathbf{\Theta}^1$, iteration index $n = 1$, and error tolerance $0 \leq \varepsilon_{\mathrm{SCA}} \ll 1$.
2: **repeat**
3: For given $\mathbf{\Theta}^n$, obtain the intermediate solution $\mathbf{\Theta}$ by solving (72)
4: Set $n = n + 1$ and $\mathbf{\Theta}^n = \mathbf{\Theta}$
5: **until** $\frac{\left|\widetilde{F}(\mathbf{\Theta}^n) - \widetilde{F}(\mathbf{\Theta}^{n-1})\right|}{\left|\widetilde{F}(\mathbf{\Theta}^n)\right|} \leq \varepsilon_{\mathrm{SCA}}$
6: $\mathbf{\Theta}^{\dagger} = \mathbf{\Theta}^n$
7: Recover $\mathbf{\Psi}^{\dagger}$ from $\mathbf{\Theta}^{\dagger}$

Algorithm 3 Block Coordinate Descent Algorithm

1: Set initial points $(\mathbf{w}_k)^1$, $(p_j)^1$, $(\mathbf{v}_j)^1$, and $(\mathbf{\Psi})^1$, iteration index $m = 1$, and convergence tolerance $0 \leq \varepsilon_{\mathrm{BCD}} \ll 1$
2: **repeat**
3: Solve (43) for given $\mathbf{\Psi} = (\mathbf{\Psi})^m$ and $\mathbf{v}_j = (\mathbf{v}_j)^m$ by applying **Algorithm 1** and obtain $(\mathbf{w}_k)^{m+1}$ and $(p_j)^{m+1}$
4: Calculate $(\mathbf{v}_j)^{m+1}$ for given $\mathbf{\Psi} = (\mathbf{\Psi})^m$, $\mathbf{w}_k = (\mathbf{w}_k)^{m+1}$, and $p_j = (p_j)^{m+1}$ using (47)
5: Solve (72) for $\mathbf{w}_k = (\mathbf{w}_k)^{m+1}$, $p_j = (p_j)^{m+1}$, and $\mathbf{v}_j = (\mathbf{v}_j)^{m+1}$ by applying **Algorithm 2** and recover $(\mathbf{\Psi})^{m+1}$ based on $(\mathbf{\Theta})^{m+1}$
6: Set $m = m + 1$
7: **until** $\left| \frac{F\left((\mathbf{w}_k)^m, (p_j)^m, (\mathbf{v}_j)^m, (\mathbf{\Psi})^m\right)}{F\left((\mathbf{w}_k)^{m-1}, (p_j)^{m-1}, (\mathbf{v}_j)^{m-1}, (\mathbf{\Psi})^{m-1}\right)} - 1 \right| \leq \varepsilon_{\mathrm{BCD}}$, where $F(\cdot,\cdot,\cdot,\cdot)$ is defined in (11)
8: $\mathbf{w}_k^{\dagger} = (\mathbf{w}_k)^m$, $p_j^{\dagger} = (p_j)^m$, $\mathbf{v}_j^{\dagger} = (\mathbf{v}_j)^m$, $\mathbf{\Psi}^{\dagger} = (\mathbf{\Psi})^m$

where $\nabla_{\mathbf{\Theta}} \widetilde{g}_2$ is shown at the bottom of the previous page, and

$$\|\mathbf{\Theta}\|_2 \geq \|\mathbf{\Theta}^n\|_2 + \mathrm{Tr}\left(\boldsymbol{\theta}_{\max}^n (\boldsymbol{\theta}_{\max}^n)^H (\mathbf{\Theta} - \mathbf{\Theta}^n)\right) \triangleq \overline{\Theta}^n, \tag{71}$$

where $\boldsymbol{\theta}_{\max}^n$ is the eigenvector associated with the principal eigenvalue of $\mathbf{\Theta}^n$.

Therefore, for any given point $\mathbf{\Theta}^n$, an upper bound on (65) is obtained by solving the following optimization problem:

$$\begin{aligned} \underset{\substack{\mathbf{\Theta} \in \mathbb{H}^{M+1}, \beta_i, \\ \gamma_i, \tau_i, \delta_i, \iota_i, \kappa_i}}{\text{minimize}} \quad & \widetilde{F}(\mathbf{\Theta}) \triangleq \widetilde{f}_1 + \widetilde{f}_2 - \overline{g}_1 - \overline{g}_2 + \chi\left(\|\mathbf{\Theta}\|_* - \overline{\Theta}^n\right) \\ \text{s.t.} \quad & \widetilde{\text{C3}}, \widehat{\text{C4a}}, \widehat{\text{C4b}}. \widetilde{\text{C4c}}, \widetilde{\text{C4d}}, \text{C8}. \end{aligned} \tag{72}$$

Note that (72) is a convex optimization problem and the optimal solution of (72) can be obtained via CVX [38]. The proposed algorithm for solving (67) is summarized in **Algorithm 2**. We note that the function value of (67) is upper bounded by the minimum of (72). Moreover, by iteratively applying **Algorithm 2**, we can gradually tighten the upper bound and obtain a sequence of solutions $\mathbf{\Theta}$. Furthermore, the objective function of (72) is monotonically non-increasing and the developed algorithm is guaranteed to converge to a stationary point of (67) [24].

The overall BCD based algorithm is summarized in **Algorithm 3**. Recall that objective function in (43) is monotonically decreasing in each iteration of **Algorithm 1** and the receive beamforming vector $\mathbf{v}_j^{\dagger}$ admits a closed-form solution, cf. (47). We note that any limit point of the non-increasing sequence $\{(\mathbf{w}_k)^m, (p_j)^m, (\mathbf{v}_j)^m, (\mathbf{\Psi})^m\}_{m \in \mathbb{N}}$ obtained with **Algorithm 3** is a stationary point of (13). Moreover, the function value of the sequence $\{(\mathbf{w}_k)^m, (p_j)^m, (\mathbf{v}_j)^m, (\mathbf{\Psi})^m\}_{m \in \mathbb{N}}$ is guaranteed to converge to a stationary value[10] of the objective function of (13) in polynomial time [23]. We note that due to the safe approximation of constraint C4, a stationary point of (13) is a feasible suboptimal solution of the original problem in (11). Furthermore, according to [42, Theorem 3.12], the computational complexity of an SDP problem with m SDP constraints, where each constraint contains an $n \times n$ positive semidefinite matrix, is given by $\mathcal{O}\left(mn^3 + m^2n^2 + m^3\right)$. For the relaxed version of problem (43), we have $m = 3I$ and $n = N_{\mathrm{T}}$, while for problem (72), we have $m = 2I$ and $n = M + 1$. Therefore, the computational complexity of each iteration of the developed BCD algorithm is given by $\mathcal{O}\Big(\log(\frac{1}{\varepsilon_{\mathrm{SCA}}})\big(3IN_{\mathrm{T}}^3 + 9I^2N_{\mathrm{T}}^2 + 2I(M+1)^3 + 4I^2(M+1)^2 + 35I^3\big)\Big)$.

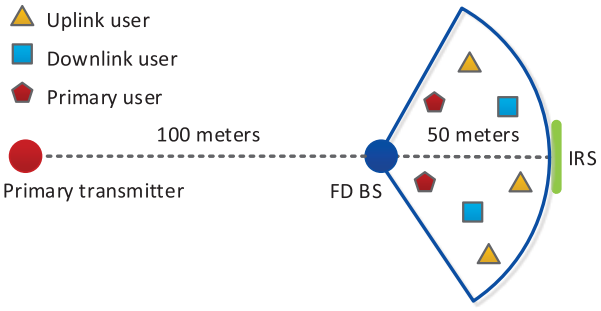

Fig. 2. Simulation setup for an IRS-assisted FD CR network which comprises $I = 2$ PUs, $K = 2$ DL users, and $J = 3$ UL users.

V. Simulation Results

In this section, we study the system performance of the proposed resource allocation scheme via simulations. The schematic system model for the simulated FD CR network is shown in Figure 2.

A. Simulation Setup

We focus on the resource allocation of one sector of the secondary network. The distance from the secondary FD BS to the IRS is 50 m.[11] Unless specified otherwise, the primary network contains $I = 2$ PUs while the secondary network comprises $K = 2$ secondary DL users and $J = 3$ secondary UL users. Both the PUs and the SUs are uniformly and randomly distributed in the considered sector. For the ease of presentation, in the sequel, the maximum normalized

[10] We note that swapping the order of steps 3, 4, and 5 would not affect the convergence of **Algorithm 3** [23]. Yet, the order of steps 3, 4, and 5 may affect the value to which **Algorithm 3** converges as a different order implies a different search direction in the feasible set.

[11] In practice, the location of the IRS can be either optimized or chosen for convenience.

estimation errors of the PU CSI are defined as $\upsilon_{\mathrm{D},i}^2 = \frac{\varepsilon_{\mathrm{D},i}^2}{\|\mathbf{l}_{\mathrm{D},i}\|^2}$, $\upsilon_{\mathrm{R},i}^2 = \frac{\varepsilon_{\mathrm{R},i}^2}{\|\mathbf{l}_{\mathrm{R},i}\|^2}$, and $\upsilon_{i,j}^2 = \frac{\varepsilon_{i,j}^2}{|e_{i,j}|^2}$, where $\upsilon_{\mathrm{D},i}^2 = \upsilon_{\mathrm{R},i}^2 = \upsilon_{i,j}^2 = \upsilon^2$, $\forall i \in \mathcal{I}$, $\forall j \in \mathcal{J}$. Moreover, the path loss model for the reflected path is given by $PL_{\mathrm{R}}^{\mathrm{S}} = C_0^2 (d_{\mathrm{BR}})^{\alpha_{\mathrm{BR}}} (d_{\mathrm{RU}})^{\alpha_{\mathrm{RU}}}$, where $C_0 = 40$ dB is a constant related to the carrier center frequency at the reference distance of 1 m. Variables $d_{\mathrm{BR}} = 50$ m and d_{RU} are the distance between the FD BS and the IRS and the distance between the IRS and the users, respectively, and $\alpha_{\mathrm{BR}} = 2.1$ and $\alpha_{\mathrm{RU}} = 2.3$ are the corresponding path loss exponents [13]. The path loss model for the direct path is given by $PL_{\mathrm{D}}^{\mathrm{S}} = C_0 (d_{\mathrm{BU}})^{\alpha_{\mathrm{BU}}}$, where $\alpha_{\mathrm{BU}} = 3.9$ is the path loss exponent.[12] The fading coefficients of the SI channel are generated as independent and identically distributed Rician random variables with Rician factor 5 dB [34]. Besides, for the channels between the secondary FD BS and all $I + J + K$ users, we model the small scale fading coefficients of the channels of the direct paths as independent and identically distributed Rayleigh random variables while the small scale fading coefficients of the channels of the reflected paths follow a Rician distribution.

Furthermore, the total transmit power of the primary transmitter is assumed to be $p^{\mathrm{P}} = \sum_{i \in \mathcal{I}} p_i^{\mathrm{P}} = 35$ dBm. Moreover, the path loss model for the reflected path between the primary transmitter and secondary DL user k is given by $PL_{\mathrm{R}_k}^{\mathrm{P}} = C_0^2 (r^{\mathrm{P}})^{\alpha_{\mathrm{PR}}} (r_k^{\mathrm{R}})^{\alpha_{\mathrm{RU}}}$, where $\alpha_{\mathrm{PR}} = 3.6$ denotes the path loss exponent of the channel between the primary transmitter and the IRS,[13] and $r^{\mathrm{P}} = 150$ m and r_k^{R} denote the distance between the primary transmitter and the IRS and the distance between the IRS and secondary DL user k, respectively. The path loss model for the reflected path between the primary transmitter and the secondary FD BS is given by $PL_{\mathrm{R}_0}^{\mathrm{P}} = C_0^2 (r^{\mathrm{P}})^{\alpha_{\mathrm{PR}}} (d_{\mathrm{BR}})^{\alpha_{\mathrm{BR}}}$. The path loss model for the direct path between the primary transmitter and secondary DL user k is given by $PL_{\mathrm{D}_k}^{\mathrm{P}} = C_0 (r_k^{\mathrm{D}})^{\alpha_{\mathrm{PU}}}$, where r_k^{D} and $\alpha_{\mathrm{PU}} = 3.9$ denote the distance between the primary transmitter and secondary DL user k and the path loss exponent of the corresponding channel. The path loss model for the direct path between the primary transmitter and the secondary FD BS is given by $PL_{\mathrm{D}_0}^{\mathrm{P}} = C_0 (r_0^{\mathrm{D}})^{\alpha_{\mathrm{PB}}}$, where $r_0^{\mathrm{R}} = 100$ m and $\alpha_{\mathrm{PB}} = 3.6$ denote the distance between the primary transmitter and the secondary FD BS and the corresponding path loss exponent, respectively.

In the following, for resource allocation algorithm design, the interference caused by the primary transmitter, i.e., $(\mathbf{f}^{\mathrm{UL}} + \mathbf{F}^H \mathbf{\Psi} \mathbf{f}^{\mathrm{P-I}}) \sum_{n \in \mathcal{I}} \sqrt{p_n^{\mathrm{P}}} d_n^{\mathrm{P}}$ and $(f_{\mathrm{D},k}^{\mathrm{DL}} + \mathbf{g}_{\mathrm{R},k}^H \mathbf{\Psi} \mathbf{f}^{\mathrm{P-I}}) \sum_{n \in \mathcal{I}} \sqrt{p_n^{\mathrm{P}}} d_n^{\mathrm{P}}$, is modelled as additional AWGN $\mathbf{z}^{\mathrm{UL}} \sim \mathcal{CN}(0, \sigma_{z_0}^2 \mathbf{I}_{N_{\mathrm{T}}})$ and $z_k^{\mathrm{DL}} \sim \mathcal{CN}(0, \sigma_{z_k}^2)$, $\forall k \in \mathcal{K}$, respectively. Variances $\sigma_{z_0}^2$ and $\sigma_{z_k}^2$, $\forall k \in \mathcal{K}$, are set as $\sigma_{z_0}^2 = p^{\mathrm{P}} \big(\frac{1}{PL_{\mathrm{R}_0}^{\mathrm{P}}} + \frac{1}{PL_{\mathrm{D}_0}^{\mathrm{P}}} \big)$ and $\sigma_{z_k}^2 = p^{\mathrm{P}} \big(\frac{1}{PL_{\mathrm{R}_k}^{\mathrm{P}}} + \frac{1}{PL_{\mathrm{D}_k}^{\mathrm{P}}} \big)$, respectively. Hence, when implementing **Algorithm 3**, the total variances of the AWGN at the secondary FD BS and at secondary DL user k are set to be $(\sigma_{z_0}^2 + \sigma_{n_{\mathrm{U}}}^2)$ and $(\sigma_{z_k}^2 + \sigma_{n_k}^2)$, $\forall k \in \mathcal{K}$, respectively. On the other hand, for performance evaluation, we apply the solution obtained with **Algorithm 3** in (2) and (3) and calculate the spectral efficiency taking into account the exact interference caused by the primary transmitter, i.e., $(\mathbf{f}^{\mathrm{UL}} + \mathbf{F}^H \mathbf{\Psi} \mathbf{f}^{\mathrm{P-I}}) \sum_{n \in \mathcal{I}} \sqrt{p_n^{\mathrm{P}}} d_n^{\mathrm{P}}$ and $(f_{\mathrm{D},k}^{\mathrm{DL}} + \mathbf{g}_{\mathrm{R},k}^H \mathbf{\Psi} \mathbf{f}^{\mathrm{P-I}}) \sum_{n \in \mathcal{I}} \sqrt{p_n^{\mathrm{P}}} d_n^{\mathrm{P}}$, respectively. Besides, for all channels involving the primary transmitter, we model the small scale fading coefficients of the channels as independent and identically distributed Rayleigh random variables. The parameter values adopted in our simulations are listed in Table I.

TABLE I
SYSTEM PARAMETERS ADOPTED IN SIMULATIONS

f_c	Carrier center frequency	2.5 GHz
$p_{j,\max}$	Max. transmit power of UL user j	10 dBm
α_{BU}	Path loss exponent for direct paths	3.9
$P_{\max}^{\mathrm{DL}}$	Max. transmit power of FD BS	30 dBm
α_{BR}	Path loss exponent	2.1
α_{RU}	Path loss exponent	2.3
η	SI cancellation coefficient	-85 dB [27]
$\sigma_{n_k}^2$	Secondary DL user noise power	-100 dB
$\sigma_{n_{\mathrm{U}}}^2$	Secondary FD BS noise power	-110 dBm
G_i	Secondary FD BS antenna gain	5 dBi
p_{tol_i}	Interference tolerance	-90 dBm
G_{SI}	Rician factor for SI channels	5 dB
C_0	Path loss at 1 m	40 dB
K_{Rician}	Rician factor for IRS channels	5
$\varepsilon_{\mathrm{SCA}}$	SCA error tolerance	0.01
$\varepsilon_{\mathrm{BCD}}$	BCD error tolerance	0.01
χ	Penalty factor	10^3
ω_j^{UL}, ω_k^{DL}	Weights of UL and DL users	1

B. Baseline Schemes

For comparison, we consider four baseline schemes. For baseline scheme 1, zero-forcing beamforming (ZF-BF) is employed at the FD BS for both DL and UL transmissions and the phases of the IRS are generated in a random manner. In particular, the directions of both the DL beamformer $\mathbf{w}_k$ for desired user k and UL beamformer $\mathbf{v}_j$ for desired user j are fixed and lie in the null spaces of all the other DL user channels and all the other UL user channels, respectively. Then, by optimizing the DL and UL transmit powers, i.e., $p_k^{\mathrm{DL}} \in \mathbb{R}$ and p_j, we solve the problem in (13) subject to power constraints C1 and C2 and interference leakage constraint $\overline{\mathrm{C4}}$ by applying **Algorithm 1**.[14] For baseline scheme 2, we assume that the considered FD CR network does not employ an IRS.[15] Then, we optimize DL beamforming vectors $\mathbf{w}_k$, UL beamforming vectors $\mathbf{v}_j$, and the transmit powers of the UL users for maximization of the system spectral efficiency subject to constraints C1, C2, and $\overline{\mathrm{C4}}$ in (13). For baseline scheme 3,

[12] In practice, IRSs are usually deployed at favourable locations. As a result, we assume that the reflected signals suffer from a less severe path loss compared to the signals directly received from the BS.

[13] In this article, the IRS is intended to serve the users located in the area of the secondary network. Thus, the IRS is deployed at a location that is favorable for the secondary network. As a result, we assume that the link between the primary transmitter and the IRS suffers from a more severe path loss compared to the link between the secondary FD BS and the IRS.

[14] The optimization problem resulting for baseline scheme 1 is still non-convex due to the non-convex objective function in (13).

[15] For baseline scheme 2, we solve (43) and (44) by applying **Algorithm 3** with $\mathbf{\Psi} = \mathbf{0}$.

TABLE II
COMPUTATIONAL COMPLEXITY COMPARISON

Scheme	Computational complexity per iteration.
Proposed scheme	$\mathcal{O}\Big(\log(\frac{1}{\varepsilon_{\mathrm{SCA}}})\big(3IN_{\mathrm{T}}^3+9I^2N_{\mathrm{T}}^2+2I(M+1)^3+4I^2(M+1)^2+35I^3\big)\Big)$
Baseline scheme 1	$\mathcal{O}\Big(2I(K+J)^{3.5}+IK^{3.5}+IJ^{3.5}\Big)$ [42]
Baseline scheme 2	$\mathcal{O}\Big(\log(\frac{1}{\varepsilon_{\mathrm{SCA}}})\big(3IN_{\mathrm{T}}^3+9I^2N_{\mathrm{T}}^2+27I^3\big)\Big)$
Baseline scheme 3	$\mathcal{O}\Big(\log(\frac{1}{\varepsilon_{\mathrm{SCA}}})\big(3IN_{\mathrm{T}}^3+9I^2N_{\mathrm{T}}^2+4I(M+1)^3+8I^2(M+1)^2+43I^3\big)\Big)$
Baseline scheme 4	$\mathcal{O}\Big(\log(\frac{1}{\varepsilon_{\mathrm{SCA}}})\big(3IN_{\mathrm{T}}^3+9I^2N_{\mathrm{T}}^2+27I^3\big)\Big)$

we assume that the secondary BS operates in the HD mode where the UL reception and the DL transmission are realized in two orthogonal time slots of equal duration. As a result, both CCI and SI do not exist. In particular, for the first time slot, the DL spectral efficiency is maximized by jointly optimizing $\mathbf{w}_k$ and $\mathbf{\Psi}$ subject to constraints C1, C3, and $\overline{\text{C4}}$ in (13).[16] Then, for the second time slot, we maximize the UL spectral efficiency by optimizing UL beamforming vector $\mathbf{v}_j$, phase shift matrix $\mathbf{\Psi}$, and the transmit powers of UL users, i.e., p_j taking into account constraints C2, C3, and $\overline{\text{C4}}$ in (13). For a fair comparison, the resulting total spectral efficiency obtained for baseline scheme 3 is multiplied by a factor of one half due to the orthogonal time slots needed for separating the UL and DL transmissions. For baseline scheme 4, we assume that the IRS employs random phase shifts. Then, we optimize the DL beamforming vectors $\mathbf{w}_k$, the UL beamforming vectors $\mathbf{v}_j$, and the transmit powers of the UL users for maximization of the system spectral efficiency subject to constraints C1, C2, and $\overline{\text{C4}}$ in (13).

Furthermore, to reveal the tradeoff between the computational complexity and the achievable system performance, the computational complexities of the proposed scheme and the four baseline schemes are provided in Table II shown at the top of next page. While the proposed scheme entails a higher computational complexity compared to baseline schemes 1, 2, and 4, our simulation results in Figures 4-8 reveal that the proposed scheme also achieves a significantly higher performance.

C. Convergence of Algorithm 3

In Figure 3, we investigate the convergence of the proposed BCD algorithm for different numbers of PUs I, secondary UL users J, secondary DL users K, antenna elements N_{T}, and IRS reflecting elements M. In particular, we consider three cases: Case 1 with $N_{\mathrm{T}}=M=6$, $I=K=2$, and $J=3$; Case 2 with $N_{\mathrm{T}}=M=6$, $I=K=4$, and $J=5$; Case 3 with $N_{\mathrm{T}}=M=10$, $I=K=4$, and $J=5$. We can observe that for all three cases, the proposed algorithm monotonically converges to a stationary point. Specifically, for Case 1, the proposed algorithm converges within 10 iterations of **Algorithm 3**. For Case 2, the proposed algorithm needs considerably more iterations (roughly 30 iterations of

[16]For maximization of the DL spectral efficiency, we obtain $\mathbf{w}_k$ and $\mathbf{\Psi}$ by applying **Algorithm 3** with $p_j=0$ and $\mathbf{v}_j=\mathbf{0}$, $\forall j\in J$. Similarly, for maximization of the UL spectral efficiency, we obtain p_j, $\mathbf{v}_j$, and $\mathbf{\Psi}$ by applying **Algorithm 3** with $\mathbf{w}_k=\mathbf{0}$, $\forall k\in K$.

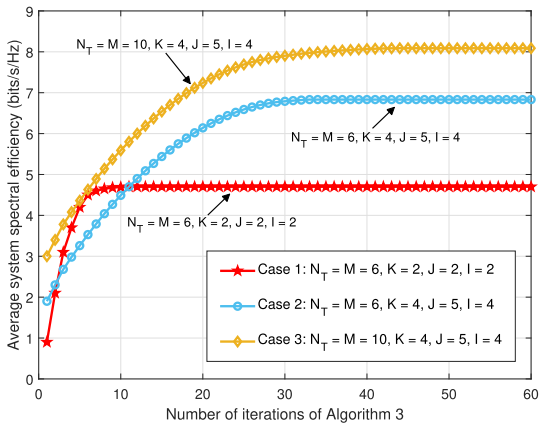

Fig. 3. Convergence of the proposed BCD algorithm for different values of N_{T}, M, I, J, and K with $p_{\mathrm{tol}_i}=-90$ dBm, $\upsilon^2=10\%$, and $P_{\max}^{\mathrm{DL}}=30$ dBm.

Algorithm 3) to converge since the larger number of users leads to more optimization variables and constraints in (11). Compared to Case 2, for Case 3, the proposed algorithm needs around 10 extra iterations for convergence since the larger values of N_{T} and M enlarge the size of the solution space of the considered problem significantly. We also note that the number of iterations required for the proposed algorithm to converge is more sensitive to the number of users than to the number of antennas and reflecting elements.

D. Average System Spectral Efficiency Versus Maximum DL Transmit Power

In Figure 4, we study the average system spectral efficiency versus the maximum DL transmit power, $P_{\max}^{\mathrm{DL}}$, for different resource allocation schemes. As expected, the system spectral efficiency increases monotonically with $P_{\max}^{\mathrm{DL}}$. Moreover, we observe that the proposed scheme outperforms all baseline schemes. In fact, compared to the baseline schemes, the significant performance improvement achieved by the proposed resource allocation scheme is enabled by the joint optimization of $\mathbf{\Phi}$, $\mathbf{w}_k$, p_j, and $\mathbf{v}_j$. On the one hand, the proposed scheme can create a more favorable radio propagation environment by optimizing the phase shift matrix of the IRS. On the other hand, it can fully exploit the DoFs introduced by the multiplexing of multiple UL and DL users on the same spectral resource via FD, which improves the spectral efficiency of the CR network. On the contrary, the four baseline schemes yield a dramatically lower system spectral efficiency. Specifically,

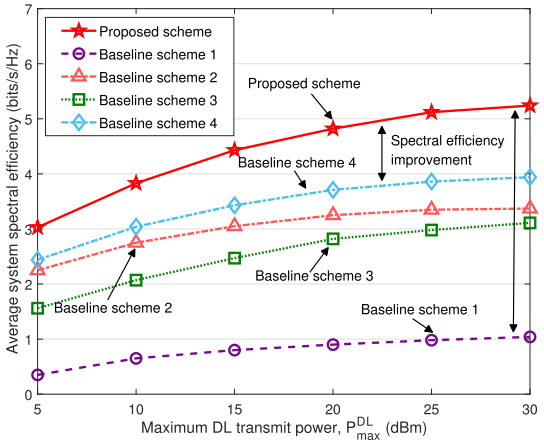

Fig. 4. Average system spectral efficiency (bits/s/Hz) versus maximum downlink transmit power (dBm) for different resource allocation schemes for $N_{\mathrm{T}} = 8$, $M = 8$, $I = 2$, $J = 3$, $K = 2$, $p_{\mathrm{tol}_i} = -90$ dBm, and $v^2 = 10\%$.

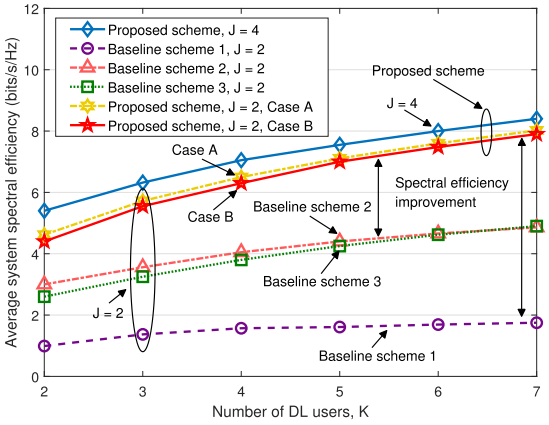

Fig. 5. Average system spectral efficiency (bits/s/Hz) versus number of downlink users for different resource allocation schemes for $N_{\mathrm{T}} = 8$, $M = 8$, $I = 2$, $v^2 = 10\%$, $p_{\mathrm{tol}_i} = -90$ dBm, and $P_{\max}^{\mathrm{DL}} = 30$ dBm.

for baseline scheme 1, the FD BS is unable to fully exploit the DoFs available for resource allocation because of the fixed beamforming vector. Although the multiuser interference (MUI) is mitigated by ZF-BF, both the CCI and the remaining SI become more serious as $P_{\max}^{\mathrm{DL}}$ increases which limits the system spectral efficiency. For baseline scheme 2, since there is no IRS available, there are no DoFs for customizing a favorable radio propagation environment for enhancing the desired signal and suppressing the interference at the PUs. For baseline scheme 3, although orthogonal DL and UL transmissions completely avoid CCI and SI, the resulting strictly suboptimal use of the DL and UL time resources leads to a significant loss of spectral efficiency. Baseline scheme 4 achieves a considerable system spectral efficiency improvement compared to baseline scheme 2. The reasons behind this are twofold. On the one hand, the IRS facilitates a higher received power for both the secondary users and the secondary FD BS because of the reflected path established by the IRS. On the other hand, the beamforming vectors for both UL and DL transmission are optimized to match the cascaded channels of the reflected paths, i.e., $\mathbf{h}_{\mathrm{R},j}^H \mathbf{\Psi} \mathbf{F}$ and $\mathbf{g}_{\mathrm{R},k}^H \mathbf{\Psi} \mathbf{F}$, respectively, which potentially improves the performance of the secondary network. Nevertheless, the proposed scheme still outperforms baseline scheme 4 by a significant margin due to the joint optimization of all available resources.

E. Average System Spectral Efficiency Versus Number of Secondary Users

Figure 5 depicts the average system spectral efficiency versus the number of secondary DL users for different resource allocation schemes. As can be seen from Figure 5, as K grows, the system spectral efficiency achieved with the proposed scheme and baseline schemes 1-3 increase since all schemes are able to exploit multiuser diversity. Similarly, we observe that the performance of the proposed scheme improves when the number of UL users, J, increases. However, compared to the proposed scheme, the system spectral efficiency for the baseline schemes are significantly lower. In particular, due to the partially fixed beamforming pattern of baseline scheme 1, the increasing CCI and SI associated with larger K cannot be mitigated which results in a substantially lower system spectral efficiency. For baseline scheme 2, since the IRS is not utilized, the system is unable to mitigate the growing MUI in UL and DL introduced by the increasing number of DL users K. For baseline scheme 3, the achieved system spectral efficiency is still lower compared to the proposed scheme due to the inefficient utilization of radio spectrum caused by the HD BS. Furthermore, in Figure 5, we verify the accuracy of modeling the interference caused by the primary transmitter as additional AWGN. Based on the resource allocation policy obtained by applying **Algorithm 3**, we compare the average system spectral efficiency for two cases: For Case A, we evaluate the performance of the system by modelling the interference from the primary network, i.e., $(\mathbf{f}^{\mathrm{UL}} + \mathbf{F}^H \mathbf{\Psi} \mathbf{f}^{\mathrm{P-I}}) \sum_{n \in \mathcal{I}} \sqrt{p_n^{\mathrm{P}}} d_n^{\mathrm{P}}$ and $(f_{\mathrm{D},k}^{\mathrm{DL}} + \mathbf{g}_{\mathrm{R},k}^H \mathbf{\Psi} \mathbf{f}^{\mathrm{P-I}}) \sum_{n \in \mathcal{I}} \sqrt{p_n^{\mathrm{P}}} d_n^{\mathrm{P}}$, as additional AWGNs $\mathbf{z}^{\mathrm{UL}} \sim \mathcal{CN}(0, \sigma_{z_0}^2 \mathbf{I}_{N_{\mathrm{T}}})$ and $z_k^{\mathrm{DL}} \sim \mathcal{CN}(0, \sigma_{z_k}^2)$, $\forall k \in \mathcal{K}$, respectively. For Case B, the interference from the primary network is modelled exactly as $(\mathbf{f}^{\mathrm{UL}} + \mathbf{F}^H \mathbf{\Psi} \mathbf{f}^{\mathrm{P-I}}) \sum_{n \in \mathcal{I}} \sqrt{p_n^{\mathrm{P}}} d_n^{\mathrm{P}}$ and $(f_{\mathrm{D},k}^{\mathrm{DL}} + \mathbf{g}_{\mathrm{R},k}^H \mathbf{\Psi} \mathbf{f}^{\mathrm{P-I}}) \sum_{n \in \mathcal{I}} \sqrt{p_n^{\mathrm{P}}} d_n^{\mathrm{P}}$ for performance evaluation, as described in Section V-A. As can been seen from Figure 5, the performance difference between Case A and Case B is very small. This suggests that modelling the interference caused by the primary transmitter as additional AWGN is indeed appropriate.

F. Average System Spectral Efficiency Versus Number of Antenna/IRS Elements

In Figure 6, we investigate the average system spectral efficiency versus the number of antenna/IRS elements. Specifically, to reveal the performance gain achieved by deploying an IRS, for the proposed scheme two cases are considered: Case 1 with a fixed number of antennas at the secondary BS ($N_{\mathrm{T}} = 4$) and increasing M and Case 2 with a fixed number of phase shifters ($M = 4$) and increasing N_{T}. We observe that

TABLE III
COMPARISON BETWEEN THE ACTUAL INTERFERENCE AND ITS UPPER BOUND

Terms	$\sum \frac{1}{3}\lvert a+b+c\rvert^2$	$\sum(\lvert a\rvert^2+\lvert b\rvert^2+\lvert c\rvert^2)$
$a=\Delta\mathbf{l}_{\mathrm{D},i}^H\mathbf{w}_k,\ b=\Delta\mathbf{l}_{\mathrm{R},i}^H\mathbf{\Psi}\mathbf{F}\mathbf{w}_k,\ c=\bar{\mathbf{l}}_{\mathrm{D},i}^H\mathbf{w}_k+\bar{\mathbf{l}}_{\mathrm{R},i}^H\mathbf{\Psi}\mathbf{F}\mathbf{w}_k$	-91.1 dBm	-90.9 dBm
$a=\sqrt{p_j}\Delta e_{i,j},\ b=\sqrt{p_j}\Delta\mathbf{l}_{\mathrm{R},i}^H\mathbf{\Psi}\mathbf{h}_{\mathrm{R},j},\ c=\sqrt{p_j}e_{i,j}+\bar{\mathbf{l}}_{\mathrm{R},i}^H\mathbf{\Psi}\mathbf{h}_{\mathrm{R},j}$	-98.1 dBm	-97.7 dBm
Total interference	-90.3 dBm	-90 dBm

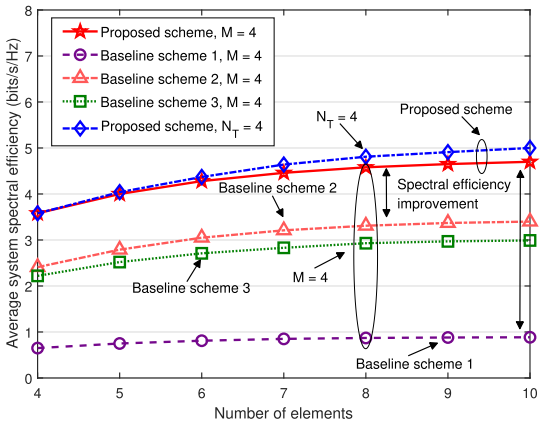

Fig. 6. Average system spectral efficiency (bits/s/Hz) versus number of elements for different resource allocation schemes for $K=2$, $I=2$, $J=3$, $\upsilon^2=10\%$, $p_{\mathrm{tol}_i}=-90$ dBm, and $P_{\max}^{\mathrm{DL}}=30$ dBm.

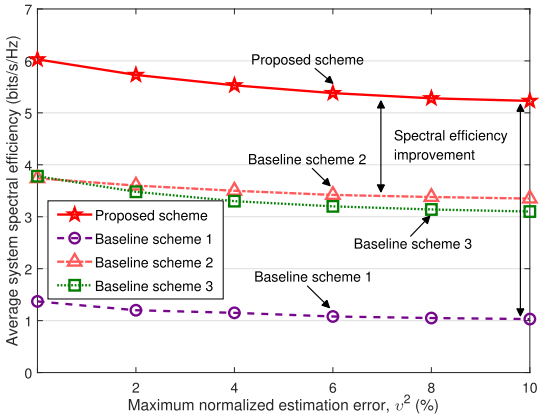

Fig. 7. Average system spectral efficiency (bits/s/Hz) versus maximum normalized channel estimation error, υ^2, for different schemes for $N_{\mathrm{T}}=M=8$, $K=I=2$, $J=3$, $p_{\mathrm{tol}_i}=-90$ dBm, and $P_{\max}^{\mathrm{DL}}=30$ dBm.

increasing the number of elements in Case 1 results in a larger performance gain compared to Case 2. The reason behind this is twofold. On the one hand, as the number of reflectors at the IRS increases, there are more DoFs for customizing favorable BS-IRS-user channels which improves both the UL and the DL beamforming gain. On the other hand, the additional IRS elements can reflect more power of the signal transmitted by the secondary FD BS which results in a power gain. Moreover, as can be seen from Figure 6, the average system spectral efficiency for the proposed scheme and the three baseline schemes improve as the number of antennas, N_{T}, at the FD BS increases. This can be explained by the fact that the extra DoFs provided by the additional antennas facilitates a higher beamforming resolution for both DL transmission and UL reception which lead to higher received SINRs. Yet, as N_{T} increases, the channel hardening effect leads to a diminishing growth rate of the system spectral efficiency. Figure 6 also shows that the average system spectral efficiency of the proposed scheme increases faster with N_{T} than the average system spectral efficiency of the baseline schemes thanks to the proposed optimization framework which exploits the system resources efficiently. Furthermore, for the parameter values adopted in Figure 6 and $N_{\mathrm{T}}=4$ and $M=10$, we also verify the tightness of the inequality used to safely approximate constraint C4 in (12). The corresponding numerical results, which have been obtained by averaging over different channel realizations, are provided in Table III shown at the top of this page. As can be seen from Table III, the difference between the actual interference and the upper bound is only 0.3 dB. This indicates that the proposed safe approximation is relatively tight.

G. Average System Spectral Efficiency versus Maximum Normalized Channel Estimation Error

In Figure 7, we study the average system spectral efficiency versus the maximum normalized channel estimation error. As expected, the average system spectral efficiency decreases with increasing υ^2. This is due to the fact that, as υ^2 increases, the secondary BS becomes less flexible and more conservative in resource allocation. In particular, the BS has to allocate more DoFs to satisfy the interference leakage constraint C4. As a result, fewer DoFs are available for suppressing the SI and facilitating accurate DL beamforming at the FD BS which degrades the system performance. Besides, over the entire range of υ^2, the proposed scheme significantly outperforms baseline schemes 1-3. This unveils that by jointly optimizing all available DoFs, the proposed scheme can mitigate the interference leakage more efficiently than the three baseline schemes, even in the presence of CSI uncertainty. Besides, compared to the proposed scheme and baseline scheme 3, we observe that baseline scheme 1 and baseline scheme 2 are less sensitive to channel estimation errors in the considered range. For baseline scheme 1, the random phase shift pattern of the IRS already results in a significant performance loss and increasing υ^2 from 0 to 10% only leads to a small additional loss. For baseline scheme 2, since the IRS is not deployed, only the imperfect knowledge of the CSI of the direct paths affects the performance, which leads to a smaller degradation.

H. Outage Probability Versus Maximum Interference Leakage Tolerance

Figure 8 shows the outage probability of the users in the primary network versus the maximum interference leakage

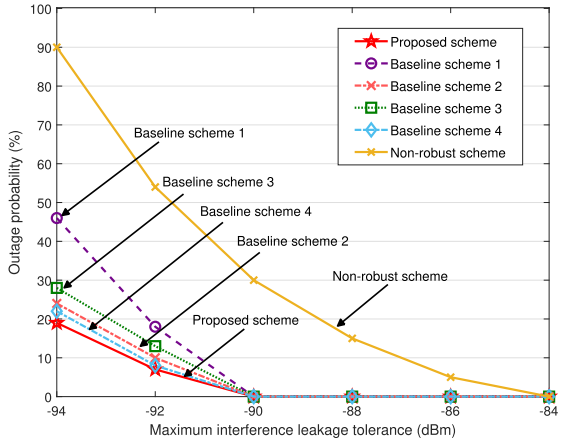

Fig. 8. Outage probability (%) versus maximum interference leakage tolerance (dBm) for different resource allocation schemes for $N_{\mathrm{T}} = 8$, $M = 8$, $K = 2$, $I = 2$, $J = 3$, $\upsilon^2 = 10\%$, and $P_{\max}^{\mathrm{DL}} = 30$ dBm.

tolerance for different resource allocation schemes. The outage probability is defined as the probability that the interference leakage from the secondary network to the i-th PU is higher than a predefined target interference leakage tolerance p_{tar_i}. For comparison, we also study the outage probability of a non-robust scheme. Specifically, for the non-robust scheme, we solve a problem similar to (11) but treat the estimated CSI of the PUs as perfect CSI. Then, using the actual CSI of the PUs, we check if the interference leakage constraint C4 in (11) is satisfied. As can be observed from Figure 8, both the proposed scheme and baseline schemes 1-4 yield a significant outage probability reduction compared to the non-robust scheme. Moreover, as we set the maximum interference leakage tolerance to $p_{\mathrm{tol}_i} = -90$ dBm, the outage probabilities of the proposed scheme and all baseline schemes decrease to zero for target interference leakage tolerances $p_{\mathrm{tar}_i} \leq -90$ dBm. In contrast, the non-robust scheme still suffers from outages. These results underline the robustness of the proposed scheme against imperfect CSI.

VI. Conclusion

In this article, we proposed to integrate an IRS into a multiuser FD CR system to simultaneously improve the system performance of the secondary network and effectively mitigate the interference caused to the PUs. In particular, the system spectral efficiency of the secondary network was maximized by jointly optimizing the DL transmit beamforming vectors and the UL receive beamforming vectors at the FD BS, the UL transmit power of the UL users, and the phase shift matrix at the IRS. We considered the robust design of IRS-assisted FD CR systems taking into account the imperfect knowledge of the CSI of the PUs. Since the resulting interference leakage tolerance constraint is an obstacle to efficient resource allocation algorithm design, we proposed a safe approximation of the original optimization problem. To tackle the non-convexity of the resulting design problem, we developed a BCD algorithm to solve the approximated problem in an alternating manner. In particular, the design of the DL transmit beamformers and UL transmit power was tackled by SCA and SDR, and the optimal UL receive beamformers were derived in closed form. The unit modulus constrained optimization problem introduced by the IRS was first transformed to a rank-constrained problem and then addressed by applying a penalty method and SCA. The proposed BCD algorithm is guaranteed to converge to a stationary point of the approximated optimization problem. Simulation results not only revealed the significant system spectral efficiency improvement achieved by the proposed scheme compared to four baseline schemes but also verified its robustness against the imperfect knowledge of the CSI of the PUs. Moreover, our results illustrated that IRSs are an efficient means to mitigate the various forms of interference in FD CR systems.

Finally, we note that the system model considered in this article can serve as a starting point for studying the impact of practical constraints in IRS-assisted FD CR systems. Potential future research topics in this direction include IRS-assisted FD CR systems with hardware impairments and discrete phase shifts.

Appendix

A. Proof of Theorem 1

To start with, we recast the relaxed version of (43) in equivalent form as (73) which is shown at the bottom of the page. Here, $\widehat{\phi}_k$ and $\widehat{\psi}_j$ are slack variables and Ξ collects all terms which are not relevant for the proof. Note that the problem in (73) is jointly convex with respect to all optimization variables and the Slater's condition is satisfied for (73) [37]. Therefore, strong duality holds, i.e., the gap between the optimal value of (73) and that of its dual problem is zero [37]. Specifically, the Lagrangian function of (73) in terms of beamforming matrix $\mathbf{W}_k$ is given as follows

$$\mathcal{L} = \xi \sum_{k\in\mathcal{K}} \mathrm{Tr}(\mathbf{W}_k) - \sum_{k\in\mathcal{K}} \mathrm{Tr}\Big(\big(\nabla_{\mathbf{W}_k}\widehat{g}_1 + \nabla_{\mathbf{W}_k}\widehat{g}_2\big)^H \mathbf{W}_k \Big) - \sum_{i\in\mathcal{I}} \mathrm{Tr}\big(\mathbf{S}_{\widehat{\mathrm{C4b}}_i}(\mathbf{W}_k, \beta_i, \gamma_i, \kappa_i)\mathbf{T}_{\widehat{\mathrm{C4b}}_i}\big) - \sum_{k\in\mathcal{K}} \mathrm{Tr}(\mathbf{W}_k\mathbf{Y}_k)$$

$$\begin{aligned}
&\underset{\substack{\mathbf{W}_k, p_j, \beta_i, \gamma_i, \tau_i, \\ \delta_i, \iota_i, \kappa_i, \widehat{\phi}_k, \widehat{\psi}_j}}{\text{minimize}} \quad -\sum_{k\in\mathcal{K}} \log_2(\widehat{\phi}_k + \sigma_{\mathrm{n}_k}^2) - \sum_{j\in\mathcal{J}} \log_2(\widehat{\psi}_j) - \sum_{k\in\mathcal{K}} \mathrm{Tr}\Big(\big(\nabla_{\mathbf{W}_k}\widehat{g}_1 + \nabla_{\mathbf{W}_k}\widehat{g}_2\big)^H \mathbf{W}_k \Big) + \Xi \\
&\text{s.t. } \mathrm{C1}, \mathrm{C2}, \widehat{\mathrm{C4}}\mathrm{a}, \widehat{\mathrm{C4}}\mathrm{b}, \widehat{\mathrm{C4}}\mathrm{c}, \widehat{\mathrm{C4}}\mathrm{d}, \mathrm{C5}, \ \ \mathrm{C10}\text{: } \widehat{\phi}_k \leq \sum_{r\in\mathcal{K}} \mathrm{Tr}(\widehat{\mathbf{g}}_k\widehat{\mathbf{g}}_k^H\mathbf{W}_r) + \sum_{j\in\mathcal{J}} p_j \left|\varphi_{j,k}\right|^2, \quad \forall k, \\
&\mathrm{C11}\text{: } \widehat{\psi}_j \leq \sum_{t\in\mathcal{J}} p_t \mathrm{Tr}(\widehat{\mathbf{h}}_j\widehat{\mathbf{h}}_j^H\mathbf{v}_j\mathbf{v}_j^H) + \mathrm{Tr}\big(\eta\mathbf{v}_j\mathbf{v}_j^H \mathrm{Diag}\big(\sum_{k\in\mathcal{K}} \mathbf{S}\mathbf{W}_k\mathbf{S}^H\big)\big) + \sigma_{\mathrm{U}}^2 \left\|\mathbf{v}_j\right\|^2, \quad \forall j.
\end{aligned} \tag{73}$$

$$+\sum_{i\in\mathcal{I}}\widehat{\beta}_i\sum_{r\in\mathcal{K}}\mathrm{Tr}(\widehat{\mathbf{l}}_i\widehat{\mathbf{l}}_i^H\mathbf{W}_r)-\sum_{k\in\mathcal{K}}\widehat{\zeta}_k\sum_{r\in\mathcal{K}}\mathrm{Tr}(\widehat{\mathbf{g}}_k\widehat{\mathbf{g}}_k^H\mathbf{W}_r)$$
$$-\sum_{i\in\mathcal{I}}\mathrm{Tr}\big(\mathbf{S}_{\widehat{\mathrm{C4c}}_i}(\mathbf{W}_k,p_j,\boldsymbol{\Psi},\gamma_i,\tau_i,\delta_i)\mathbf{T}_{\widehat{\mathrm{C4c}}_i}\big)$$
$$-\sum_{j\in\mathcal{J}}\widehat{\varsigma}_j\mathrm{Tr}\big(\eta\mathbf{v}_j\mathbf{v}_j^H\mathrm{Diag}\big(\sum_{k\in\mathcal{K}}\mathbf{S}\mathbf{W}_k\mathbf{S}^H\big)\big)+\Upsilon. \tag{74}$$

Here, we have introduced Υ to collect all terms that do not involve $\mathbf{W}_k$. The scalar Lagrange multipliers ξ, $\widehat{\beta}_i$, $\widehat{\zeta}_k$, and $\widehat{\varsigma}_j \geq 0$ are associated with constraints C1, $\widehat{\mathrm{C4}}$d, C10, and C11, respectively. The positive semidefinite Lagrange multiplier matrices $\mathbf{T}_{\widehat{\mathrm{C4b}}_i} \in \mathbb{C}^{(N_\mathrm{T}+1)\times(N_\mathrm{T}+1)}$, $\mathbf{T}_{\widehat{\mathrm{C4c}}_i} \in \mathbb{C}^{(M+1)\times(M+1)}$, and $\mathbf{Y}_k \in \mathbb{C}^{N_\mathrm{T}\times N_\mathrm{T}}$ are associated with constraints $\widehat{\mathrm{C4}}$b, $\widehat{\mathrm{C4}}$c, and C5, respectively. The dual problem of (73) is given by

$$\underset{\substack{\mathbf{T}_{\widehat{\mathrm{C4b}}_i},\mathbf{T}_{\widehat{\mathrm{C4c}}_i},\mathbf{Y}_k\succeq\mathbf{0},\\ \xi,\widehat{\beta}_i,\widehat{\zeta}_k,\widehat{\varsigma}_j\geq 0}}{\text{maximize}}\ \underset{\substack{\mathbf{W}_k,p_j,\beta_i,\gamma_i,\tau_i,\\ \delta_i,\iota_i,\kappa_i,\widehat{\phi}_k,\widehat{\psi}_j}}{\text{minimize}}\ \mathcal{L}. \tag{75}$$

Next, by checking the Karush-Kuhn-Tucker (KKT) conditions with respect to $\mathbf{W}_k$, we investigate the structure of the optimal $\mathbf{W}_k^\dagger$ of (75). Specifically, for $\mathbf{W}_k^\dagger$, we have

$$\text{K1: } \xi^\dagger,\widehat{\beta}_i^\dagger,\widehat{\zeta}_k^\dagger,\widehat{\varsigma}_j^\dagger\geq 0,\quad \mathbf{T}^\dagger_{\widehat{\mathrm{C4b}}_i},\mathbf{T}^\dagger_{\widehat{\mathrm{C4c}}_i},\mathbf{Y}_k^\dagger\succeq\mathbf{0}, \tag{76}$$

$$\text{K2: } \mathbf{Y}_k^\dagger\mathbf{W}_k^\dagger=\mathbf{0},\quad \text{K3: } \nabla_{\mathbf{W}_k^\dagger}\mathcal{L}=\mathbf{0}, \tag{77}$$

where $\xi^\dagger$, $\widehat{\beta}_i^\dagger$, $\zeta_c^\dagger$, $\mathbf{T}^\dagger_{\widehat{\mathrm{C4b}}_i}$, $\mathbf{T}^\dagger_{\widehat{\mathrm{C4c}}_i}$, and $\mathbf{Y}_k^\dagger$ are the optimal Lagrange multipliers for (75). Note that there exists at least one $\xi^\dagger > 0$ since constraint C1 is active for optimal $\mathbf{W}_k^\dagger$. To facilitate the proof, K3 in (77) is explicitly expressed as follows

$$\mathbf{Y}_k^\dagger=\xi^\dagger\mathbf{I}_{N_\mathrm{T}}-\boldsymbol{\Delta}_k^\dagger, \tag{78}$$

where $\boldsymbol{\Delta}_k^\dagger$ is given by

$$\boldsymbol{\Delta}_k^\dagger=\nabla_{\mathbf{W}_k}\widehat{g}_1(\mathbf{W}_k^\dagger)+\nabla_{\mathbf{W}_k}\widehat{g}_2(\mathbf{W}_k^\dagger)-\sum_{i\in\mathcal{I}}\mathbf{E}_i^H\mathbf{T}^\dagger_{\widehat{\mathrm{C4b}}_i}\mathbf{E}_i$$
$$-\sum_{i\in\mathcal{I}}\mathbf{C}^H\boldsymbol{\Psi}\mathbf{F}\mathbf{T}^\dagger_{\widehat{\mathrm{C4c}}_i}\mathbf{F}^H\boldsymbol{\Psi}^H\mathbf{C}-\sum_{i\in\mathcal{I}}\widehat{\beta}_i^\dagger\widehat{\mathbf{l}}_i\widehat{\mathbf{l}}_i^H$$
$$+\sum_{k\in\mathcal{K}}\widehat{\zeta}_k^\dagger\widehat{\mathbf{g}}_k\widehat{\mathbf{g}}_k^H+\sum_{j\in\mathcal{J}}\widehat{\varsigma}_j^\dagger\eta\mathbf{v}_j\mathbf{v}_j^H\mathrm{Diag}(\mathbf{S}\mathbf{S}^H). \tag{79}$$

Next, by unveiling the structure of matrix $\mathbf{Y}_k^\dagger$, we show that the optimal $\mathbf{W}^\dagger$ always satisfies $\mathrm{Rank}(\mathbf{W}_k^\dagger)\leq 1$. Denote the maximum eigenvalue of matrix $\boldsymbol{\Delta}_k^\dagger$ as $\nu^{\max}_{\boldsymbol{\Delta}_k^\dagger}\in\mathbb{R}$. We note that due to the randomness of the channels, the probability of having multiple eigenvalues with the same value $\nu^{\max}_{\boldsymbol{\Delta}_k^\dagger}$ is zero. Reviewing (78), if $\nu^{\max}_{\boldsymbol{\Delta}_k^\dagger}>\xi^\dagger$, then $\mathbf{Y}_k^\dagger\succeq\mathbf{0}$ does not hold which contradicts K1. On the other hand, if $\nu^{\max}_{\boldsymbol{\Delta}_k^\dagger}\leq\xi^\dagger$, then $\mathbf{Y}_k^\dagger$ is a positive semidefinite matrix with $\mathrm{Rank}(\mathbf{Y}_k^*)\geq N_\mathrm{T}-1$. Considering K2, this leads to $\mathrm{Rank}(\mathbf{W}_k^\dagger)\leq 1$. Next, we construct a bounded optimal solution based on the above discussion. Specifically, we construct a unit-norm vector $\mathbf{e}^{\max}_{\boldsymbol{\Delta}_k^\dagger}\in\mathbb{C}^{N_\mathrm{T}\times 1}$ which lies in the null space of $\mathbf{Y}_k^\dagger$, i.e., $\mathbf{Y}_k^\dagger\mathbf{e}^{\max}_{\boldsymbol{\Delta}_k^\dagger}=\mathbf{0}$. Let $\mathbf{e}^{\max}_{\boldsymbol{\Delta}_k^\dagger}$ be the unit-norm eigenvector associated with the principal eigenvalue $\nu^{\max}_{\boldsymbol{\Delta}_k^\dagger}$ of matrix $\boldsymbol{\Delta}_k^\dagger$. Thus, the optimal $\mathbf{W}_k^*$ can be expressed as $\mathbf{W}_k^\dagger=\varpi\mathbf{e}^{\max}_{\boldsymbol{\Delta}_k^\dagger}(\mathbf{e}^{\max}_{\boldsymbol{\Delta}_k^\dagger})^H$. Here, parameter ϖ can be tuned such that the DL transmit power constraint C1 is satisfied. ■

B. Proof of Theorem 2

To start with, we define the objective function and the optimal solution of problem (65) as $\widetilde{F}(\boldsymbol{\Theta})$ and $\boldsymbol{\Theta}^\dagger$, respectively. Then, for any feasible $\boldsymbol{\Theta}$, we have the following inequality:

$$\widetilde{F}(\boldsymbol{\Theta}^\dagger)\leq\widetilde{F}(\boldsymbol{\Theta}). \tag{80}$$

We further define the objective function of problem (67) as $\widetilde{G}(\boldsymbol{\Theta};\chi)$. Assuming $\boldsymbol{\Theta}_q$ minimizes $\widetilde{G}(\cdot;\chi_q)$ with penalty factor χ_q for each q, we have the following inequality:

$$\begin{aligned}\widetilde{F}(\boldsymbol{\Theta}_q)+\chi_q\big(\|\boldsymbol{\Theta}_q\|_*-\|\boldsymbol{\Theta}_q\|_2\big)&=\widetilde{G}(\boldsymbol{\Theta}_q;\chi_q)\\ &\leq\widetilde{F}(\boldsymbol{\Theta}^\dagger)+\chi_q\big(\|\boldsymbol{\Theta}^\dagger\|_*-\|\boldsymbol{\Theta}^\dagger\|_2\big)=\widetilde{G}(\boldsymbol{\Theta}^\dagger;\chi_q)\\ &\overset{(a)}{=}\widetilde{F}(\boldsymbol{\Theta}^\dagger),\end{aligned} \tag{81}$$

where equality (a) holds due to the fact that any optimal solution of (65), i.e., $\boldsymbol{\Theta}^\dagger$, fulfills $\|\boldsymbol{\Theta}^\dagger\|_*-\|\boldsymbol{\Theta}^\dagger\|_2\leq 0$. Then, we rearrange the inequality in (81) and obtain the following inequality:

$$\|\boldsymbol{\Theta}_q\|_*-\|\boldsymbol{\Theta}_q\|_2\leq\frac{1}{\chi_q}\big(\widetilde{F}(\boldsymbol{\Theta}^\dagger)-\widetilde{F}(\boldsymbol{\Theta}_q)\big). \tag{82}$$

Recall that if $\overline{\boldsymbol{\Theta}}$ is a limit point of the sequence $\{\boldsymbol{\Theta}_q\}$, we can find an infinite subsequence $\mathcal{Q}$ such that

$$\lim_{q\in\mathcal{Q}}\boldsymbol{\Theta}_q=\overline{\boldsymbol{\Theta}}. \tag{83}$$

Then, as $q\in\mathcal{Q}$, $q\to\infty$, we take the limit on both sides of (82) and obtain the following relation chain:

$$\begin{aligned}\|\overline{\boldsymbol{\Theta}}\|_*-\|\overline{\boldsymbol{\Theta}}\|_2&\overset{(b)}{=}\lim_{q\in\mathcal{Q}}\|\boldsymbol{\Theta}_q\|_*-\|\boldsymbol{\Theta}_q\|_2\\ &\leq\lim_{q\in\mathcal{Q}}\frac{1}{\chi_q}\big(\widetilde{F}(\boldsymbol{\Theta}^\dagger)-\widetilde{F}(\boldsymbol{\Theta}_q)\big)\overset{(c)}{=}0,\end{aligned} \tag{84}$$

where equality (b) holds because of the continuity property of norm functions and equality (c) holds due to $\chi_q\to\infty$. Thus, we have that $\|\overline{\boldsymbol{\Theta}}\|_*-\|\overline{\boldsymbol{\Theta}}\|_2=0$. As a result, $\overline{\boldsymbol{\Theta}}$ is a feasible solution of problem (65).

On the other hand, for any $\chi_q\geq 0$, we take the limit of (81) as $i\in\mathcal{Q}$, $q\to\infty$, which leads to the inequality:

$$\widetilde{F}(\overline{\boldsymbol{\Theta}})\overset{(d)}{\leq}\widetilde{F}(\overline{\boldsymbol{\Theta}})+\lim_{q\in\mathcal{Q}}\chi_q(\|\boldsymbol{\Theta}_q\|_*-\|\boldsymbol{\Theta}_q\|_2)\leq\widetilde{F}(\boldsymbol{\Theta}^\dagger), \tag{85}$$

where inequality (d) is due to the nonnegativity of the term $\|\boldsymbol{\Theta}_q\|_*-\|\boldsymbol{\Theta}_q\|_2$. As $\overline{\boldsymbol{\Theta}}$ is a feasible point whose objective value is no larger than that of the optimal solution $\boldsymbol{\Theta}^\dagger$, we conclude that $\overline{\boldsymbol{\Theta}}$ is also an optimal solution of problem (65), as claimed. This completes the proof.

REFERENCES

[1] D. Xu, X. Yu, and R. Schober, "Resource allocation for intelligent reflecting surface-assisted cognitive radio networks," 2020, *arXiv:2001.11729*. [Online]. Available: http://arxiv.org/abs/2001.11729

[2] V. W. Wong, R. Schober, D. W. K. Ng, and L.-C. Wang, *Key Technology for 5G Wireless Systerms*. Cambridge, U.K.: Cambridge Univ. Press, 2017.

[3] P. Kolodzy, *Spectrum Policy Task Force Report*. Washington, DC, USA: Federal Communications Commission, 2002.

[4] D. Datla, A. M. Wyglinski, and G. J. Minden, "A spectrum surveying framework for dynamic spectrum access networks," *IEEE Trans. Veh. Technol.*, vol. 58, no. 8, pp. 4158–4168, Oct. 2009.

[5] H. Islam, Y.-C. Liang, and A. T. Hoang, "Joint power control and beamforming for cognitive radio networks," *IEEE Trans. Wireless Commun.*, vol. 7, no. 7, pp. 2415–2419, Jul. 2008.

[6] D. W. K. Ng, E. S. Lo, and R. Schober, "Multiobjective resource allocation for secure communication in cognitive radio networks with wireless information and power transfer," *IEEE Trans. Veh. Technol.*, vol. 65, no. 5, pp. 3166–3184, May 2016.

[7] A. Sabharwal, P. Schniter, D. Guo, D. W. Bliss, S. Rangarajan, and R. Wichman, "In-band full-duplex wireless: Challenges and opportunities," *IEEE J. Sel. Areas Commun.*, vol. 32, no. 9, pp. 1637–1652, Sep. 2014.

[8] W. Afifi and M. Krunz, "Incorporating self-interference suppression for full-duplex operation in opportunistic spectrum access systems," *IEEE Trans. Wireless Commun.*, vol. 14, no. 4, pp. 2180–2191, Apr. 2015.

[9] S. Xiao, X. Zhou, G. Y. Li, and W. Guo, "Robust resource allocation in full-duplex cognitive radio networks," in *Proc. IEEE Global Commun. Conf. (GLOBECOM)*, Washington, DC, USA, Dec. 2016, pp. 1–7.

[10] Y. Sun, D. W. K. Ng, N. Zlatanov, and R. Schober, "Robust resource allocation for full-duplex cognitive radio systems," in *Proc. 24th Eur. Signal Process. Conf. (EUSIPCO)*, Budapest, Hungary, Aug. 2016, pp. 773–777.

[11] G. Zheng, I. Krikidis, and B. O. Ottersten, "Full-duplex cooperative cognitive radio with transmit imperfections," *IEEE Trans. Wireless Commun.*, vol. 12, no. 5, pp. 2498–2511, May 2013.

[12] M. D. Renzo *et al.*, "Smart radio environments empowered by reconfigurable AI meta-surfaces: An idea whose time has come," *EURASIP J. Wireless Commun. Netw.*, vol. 2019, no. 1, pp. 1–20, May 2019.

[13] Q. Wu, and R. Zhang, "Intelligent reflecting surface enhanced wireless network via joint active and passive beamforming," *IEEE Trans. Wireless Commun.*, vol. 18, no. 11, pp. 5394–5409, Nov. 2019.

[14] X. Yu, D. Xu, and R. Schober, "MISO wireless communication systems via intelligent reflecting surfaces : (Invited Paper)," in *Proc. IEEE/CIC Int. Conf. Commun. China (ICCC)*, Changchun, China, Aug. 2019, pp. 1–6.

[15] D. Xu, X. Yu, Y. Sun, D. W. K. Ng, and R. Schober, "Resource allocation for secure IRS-assisted multiuser MISO systems," in *Proc. IEEE Globecom Workshops (GC Wkshps)*, Waikoloa, HI, USA, Dec. 2019, pp. 1–6.

[16] C. Pan *et al.*, "Intelligent reflecting surface aided MIMO broadcasting for simultaneous wireless information and power transfer," 2019, *arXiv:1908.04863*. [Online]. Available: http://arxiv.org/abs/1908.04863

[17] S. Zhang and R. Zhang, "Capacity characterization for intelligent reflecting surface aided MIMO communication," *IEEE J. Sel. Areas Commun.*, vol. 38, no. 8, pp. 1823–1838, Aug. 2020.

[18] J. Zhang, E. Bjornson, M. Matthaiou, D. W. K. Ng, H. Yang, and D. J. Love, "Prospective multiple antenna technologies for beyond 5G," *IEEE J. Sel. Areas Commun.*, vol. 38, no. 8, pp. 1637–1660, Aug. 2020.

[19] Q. Wu and R. Zhang, "Towards smart and reconfigurable environment: Intelligent reflecting surface aided wireless network," *IEEE Commun. Mag.*, vol. 58, no. 1, pp. 106–112, Jan. 2020.

[20] T. J. Cui, M. Q. Qi, X. Wan, J. Zhao, and Q. Cheng, "Coding metamaterials, digital metamaterials and programmable metamaterials," *Light, Sci. Appl.*, vol. 3, no. 10, p. e218, Oct. 2014.

[21] Y. Yang, S. Zhang, and R. Zhang, "IRS-enhanced OFDM: Power allocation and passive array optimization," in *Proc. IEEE Global Commun. Conf. (GLOBECOM)*, Waikoloa, HI, USA, Dec. 2019, pp. 1–6.

[22] X. Yu, D. Xu, and R. Schober, "Enabling secure wireless communications via intelligent reflecting surfaces," in *Proc. IEEE Global Commun. Conf. (GLOBECOM)*, Dec. 2019, pp. 1–6.

[23] P. Tseng, "Convergence of a block coordinate descent method for nondifferentiable minimization," *J. Optim. Theory Appl.*, vol. 109, no. 3, pp. 475–494, Jun. 2001.

[24] Q. T. Dinh and M. Diehl, "Local convergence of sequential convex programming for nonconvex optimization," in *Recent Advances in Optimization and its Applications in Engineering*. Berlin, Germany: Springer, 2010.

[25] A. Ben-Tal and M. Zibulevsky, "Penalty/Barrier multiplier methods for convex programming problems," *SIAM J. Optim.*, vol. 7, no. 2, pp. 347–366, May 1997.

[26] Y. Liu, Z. Ding, M. Elkashlan, and J. Yuan, "Nonorthogonal multiple access in large-scale underlay cognitive radio networks," *IEEE Trans. Veh. Tech.*, vol. 65, no. 12, pp. 10152–10157, Apr. 2016.

[27] D. Bharadia, E. Mcmilin, and S. Katti, "Full duplex radios," *ACM SIGCOMM Comput. Commun. Rev.*, vol. 43, no. 4, pp. 375–386, Sep. 2013.

[28] A. Ghosh, J. Zhang, J. G. Andrews, and R. Muhamed, *Fundamentals LTE*. London, U.K.: Pearson, 2010.

[29] L. Zhang, Y.-C. Liang, Y. Xin, and H. V. Poor, "Robust cognitive beamforming with partial channel state information," *IEEE Trans. Wireless Commun.*, vol. 8, no. 8, pp. 4143–4153, Aug. 2009.

[30] Z. Wang, L. Liu, and S. Cui, "Channel estimation for intelligent reflecting surface assisted multiuser communications: Framework, algorithms, and analysis," *IEEE Trans. Wireless Commun.*, early access, Jun. 30, 2020, doi: 10.1109/TWC.2020.3004330.

[31] J. Wang and D. P. Palomar, "Worst-case robust MIMO transmission with imperfect channel knowledge," *IEEE Trans. Signal Process.*, vol. 57, no. 8, pp. 3086–3100, Aug. 2009.

[32] Q.-U.-A. Nadeem, H. Alwazani, A. Kammoun, A. Chaaban, M. Debbah, and M.-S. Alouini, "Intelligent reflecting surface-assisted multi-user MISO communication: Channel estimation and beamforming design," *IEEE Open J. Commun. Soc.*, vol. 1, pp. 661–680, 2020.

[33] B. P. Day, A. R. Margetts, D. W. Bliss, and P. Schniter, "Full-duplex MIMO relaying: Achievable rates under limited dynamic range," in *Proc. 6th Asilomar Conf. Signals, Syst. Comput.*, Nov. 2012, pp. 1290–1294.

[34] Y. Sun, D. W. K. Ng, J. Zhu, and R. Schober, "Multi-objective optimization for robust power efficient and secure full-duplex wireless communication systems," *IEEE Trans. Wireless Commun.*, vol. 15, no. 8, pp. 5511–5526, Aug. 2016.

[35] A. Masmoudi and T. Le-Ngoc, "Channel estimation and self-interference cancelation in full-duplex communication systems," *IEEE Trans. Veh. Technol.*, vol. 66, no. 1, pp. 321–334, Jan. 2017.

[36] Q. Li, W.-K. Ma, and A. M.-C. So, "A safe approximation approach to secrecy outage design for MIMO wiretap channels," *IEEE Signal Process. Lett.*, vol. 21, no. 1, pp. 118–121, Jan. 2014.

[37] S. Boyd and L. Vandenberghe, *Convex Optimation*. Cambridge, U.K.: Cambridge Univ. Press, 2004.

[38] M. Grant and S. Boyd. (Mar. 2017). *CVX: MATLAB Software for Disciplined Convex Programming, Version 2.1*. [Online]. Available: http://cvxr.com/cvx

[39] A. Gershman, N. Sidiropoulos, S. Shahbazpanahi, M. Bengtsson, and B. Ottersten, "Convex optimization-based beamforming," *IEEE Signal Process. Mag.*, vol. 27, no. 3, pp. 62–75, May 2010.

[40] Z.-Q. Luo, W.-K. Ma, A. So, Y. Ye, and S. Zhang, "Semidefinite relaxation of quadratic optimization problems," *IEEE Signal Process. Mag.*, vol. 27, no. 3, pp. 20–34, May 2010.

[41] K. Yang, T. Jiang, Y. Shi, and Z. Ding, "Federated learning based on Over-the-Air computation," in *Proc. IEEE Int. Conf. Commun. (ICC)*, Shanghai, China, May 2019, pp. 1–6.

[42] I. Pólik and T. Terlaky, "Interior point methods for nonlinear optimization," in *Nonlinear Optimizatio*. Berlin, Germany: Springer, 2010, pp. 215–276.

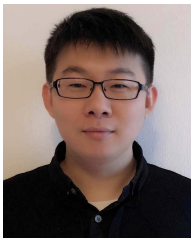

Dongfang Xu (Student Member, IEEE) received the B.S. degree in communication engineering from Shandong University, Jinan, China, in 2014, and the M.S. degree in communication and multimedia engineering from Friedrich-Alexander-Universität Erlangen-Nürnberg, Erlangen, Germany, in 2017, where he is currently pursuing the Ph.D. degree in electrical engineering. His research interests include convex and nonconvex optimization, unmanned aerial vehicle communications, and physical layer security.

Xianghao Yu (Member, IEEE) received the B.Eng. degree in information engineering from Southeast University, Nanjing, China, in 2014, and the Ph.D. degree in electronic and computer engineering from The Hong Kong University of Science and Technology (HKUST), Hong Kong, in 2018. He is currently a Humboldt Post-Doctoral Research Fellow with the Institute for Digital Communications, Friedrich-Alexander-University Erlangen-Nürnberg (FAU), Erlangen, Germany. He has coauthored the book *Stochastic Geometry Analysis of Multi-Antenna Wireless Networks* (Springer, 2019). His research interests include millimeter wave communications, intelligent reflecting surface-assisted communications, MIMO systems, mathematical optimization, and stochastic geometry.

Dr. Yu received the IEEE Global Communications Conference (GLOBECOM) 2017 Best Paper Award, the 2018 IEEE Signal Processing Society Young Author Best Paper Award, and the IEEE GLOBECOM 2019 Best Paper Award.

Yan Sun (Member, IEEE) received the B.S. degree in communication engineering from PLA Information Engineering University, Zhengzhou, China, in 2011, the M.S. degree in telecommunication engineering from Xidian University, Xi'an, China, in 2014, and the Ph.D. degree in electrical engineering from Friedrich-Alexander-University Erlangen-Nürnberg (FAU), Erlangen, Germany, in 2019. His research interests include convex and non-convex optimization, UAV communications, and AI-aided air-interface.

Dr. Sun received the IEEE Student Travel Grant for attending the IEEE Global Telecommunication Conference (GLOBECOM) 2016 and the IEEE International Conference on Acoustics, Speech and Signal Processing (ICASSP) 2017. He was also honored as an Exemplary Reviewer of the IEEE TRANSACTION ON COMMUNICATIONS in 2017 and 2018, the Best Reviewer of the IEEE TRANSACTION ON WIRELESS COMMUNICATIONS in 2017, and an Exemplary Reviewer of the IEEE COMMUNICATION LETTER for 2016 and 2017.

Derrick Wing Kwan Ng (Senior Member, IEEE) received the bachelor's (Hons.) and M.Phil. degrees in electronic engineering from The Hong Kong University of Science and Technology (HKUST) in 2006 and 2008, respectively, and the Ph.D. degree from The University of British Columbia (UBC) in 2012. He was a Senior Post-Doctoral Fellow with the Institute for Digital Communications, Friedrich-Alexander-University Erlangen-Nürnberg (FAU), Germany. He is currently a Senior Lecturer and a Scientia Fellow with the University of New South Wales, Sydney, Australia. His research interests include convex and non-convex optimization, physical layer security, IRS-assisted communication, UAV-assisted communication, wireless information and power transfer, and green (energy-efficient) wireless communications.

Dr. Ng received the Australian Research Council (ARC) Discovery Early Career Researcher Award 2017, the Best Paper Awards at the IEEE TCGCC Best Journal Paper Award 2018, INISCOM 2018, the IEEE International Conference on Communications (ICC) 2018, the IEEE International Conference on Computing, Networking and Communications (ICNC) 2016, the IEEE Wireless Communications and Networking Conference (WCNC) 2012, the IEEE Global Telecommunication Conference (GLOBECOM) 2011, and the IEEE Third International Conference on Communications and Networking in China 2008. He has been serving as an Editorial Assistant to the Editor-in-Chief of IEEE TRANSACTIONS ON COMMUNICATIONS from January 2012 to December 2019. He is currently serving as an Editor for IEEE TRANSACTIONS ON COMMUNICATIONS, IEEE TRANSACTIONS ON WIRELESS COMMUNICATIONS, and an Area Editor for IEEE OPEN JOURNAL of the COMMUNICATIONS SOCIETY. Also, he is listed as a Highly Cited Researcher by Clarivate Analytics in 2018 and 2019.

Robert Schober (Fellow, IEEE) received the Diplom (Univ.) and Ph.D. degrees in electrical engineering from the Friedrich-Alexander-University Erlangen-Nürnberg (FAU), Germany, in 1997 and 2000, respectively. From 2002 to 2011, he was a Professor and a Canada Research Chair with the University of British Columbia (UBC), Vancouver, Canada. Since January 2012, he has been an Alexander von Humboldt Professor and the Chair of digital communication with FAU. His research interests include communication theory, wireless communications, and statistical signal processing.

Dr. Schober is a fellow of the Canadian Academy of Engineering and of the Engineering Institute of Canada. He received several awards for his work, including the 2002 Heinz Maier Leibnitz Award of the German Science Foundation (DFG), the 2004 Innovations Award of the Vodafone Foundation for Research in Mobile Communications, the 2006 UBC Killam Research Prize, the 2007 Wilhelm Friedrich Bessel Research Award of the Alexander von Humboldt Foundation, the 2008 Charles McDowell Award for Excellence in Research from UBC, the 2011 Alexander von Humboldt Professorship, the 2012 NSERC E.W.R. Stacie Fellowship, and the 2017 Wireless Communications Recognition Award by the IEEE Wireless Communications Technical Committee. From 2012 to 2015, he served as Editor-in-Chief for IEEE TRANSACTIONS ON COMMUNICATIONS. He currently serves as a member for the Editorial Board of the PROCEEDINGS OF THE IEEE and as the VP Publications for the IEEE Communication Society (ComSoc). Since 2017, he has been listed as a Highly Cited Researcher by the Web of Science.

Anhang D

Publication 3

[J3] **D. Xu**, V. Jamali, X. Yu, D. W. K. Ng and R. Schober, "Optimal Resource Allocation Design for Large IRS-Assisted SWIPT Systems: A Scalable Optimization Framework," in IEEE Transactions on Communications, vol. 70, no. 2, pp. 1423-1441, Feb. 2022, doi:10.1109/TCOMM.2022.3140467.[1]

[1]© 2022 IEEE. Reprinted, with permission, from D. Xu, V. Jamali, X. Yu, D. W. K. Ng, and R. Schober, "Optimal resource allocation design for large IRS-assisted SWIPT systems: A scalable optimization framework," *IEEE Trans. Commun.*, Feb. 2022.

Optimal Resource Allocation Design for Large IRS-Assisted SWIPT Systems: A Scalable Optimization Framework

Dongfang Xu, *Graduate Student Member, IEEE*, Vahid Jamali, *Member, IEEE*, Xianghao Yu, *Member, IEEE*, Derrick Wing Kwan Ng, *Fellow, IEEE*, and Robert Schober, *Fellow, IEEE*

***Abstract*— In this paper, we study the optimal resource allocation algorithm design for large intelligent reflecting surface (IRS)-assisted simultaneous wireless information and power transfer (SWIPT) systems. To facilitate efficient system design for large IRSs, instead of jointly optimizing all the IRS elements, we partition the IRS into several tiles and employ a scalable optimization framework comprising an offline design stage and an online optimization stage. In the offline stage, the IRS elements of each tile are jointly designed to support a set of different phase shift configurations, referred to as transmission modes, while the best transmission mode is selected from the set for each tile in the online stage. Given a transmission mode set, we aim to minimize the total base station (BS) transmit power by jointly optimizing the beamforming and the transmission mode selection policy taking into account the quality-of-service requirements of information decoding and non-linear energy harvesting receivers, respectively. Although the resource allocation algorithm design is formulated as a non-convex combinatorial optimization problem, we solve it optimally by applying the branch-and-bound (BnB) approach which entails a high computational complexity. To strike a balance between optimality and computational complexity, we also develop an efficient suboptimal algorithm capitalizing on the penalty method and successive convex approximation. Our simulation results show that the proposed designs enable considerable power savings compared to several baseline schemes. Moreover, our results reveal that by properly adjusting the numbers of tiles and transmission modes, the proposed scalable optimization framework indeed facilitates online design for large IRSs. Besides, our results confirm that the advocated physics-based model and scalable optimization framework enable a flexible trade-off between performance and complexity, which is vital for realizing the performance gains promised by large IRS-assisted communication systems in practice.**

***Index Terms*— Branch and bound approach, optimal resource allocation, intelligent reflecting surface, scalable optimization.**

I. Introduction

NEXT-GENERATION wireless networks are envisioned to offer sustainable high data-rate communication services. To satisfy this demand, radio frequency (RF) transmission-enabled simultaneous wireless information and power transfer (SWIPT) has been proposed as a promising technique for prolonging the lifetime of energy-constrained communication systems [2], [3]. However, as the signal attenuation associated with the path loss increases with the transmission distance, the received power may not be adequate to ensure stable operation of power-hungry devices, unless they are located very close to the wireless energy transmitter [3]. Moreover, due to the random nature of wireless channels, the performance of SWIPT systems can be severely degraded when the radio propagation environment is unfavorable. Indeed, these issues can potentially jeopardize the provision of high data-rate and sustainable communication services creating a performance bottleneck for SWIPT systems.

To overcome these challenges, intelligent reflecting surfaces (IRSs) have been recently advocated for application in SWIPT systems [4]–[7]. In particular, exploiting their programmability, the IRS elements can be adjusted to reflect the incident signal with a certain desired phase shift according to the channel conditions [4], [8]. As a result, IRSs can be intelligently configured to enhance the received power by constructively combining the signals reflected by different IRS elements at the desired energy harvesting receivers (ERs) or alternatively destructively amalgamating the undesired

Manuscript received August 27, 2021; revised December 2, 2021; accepted December 28, 2021. Date of publication January 5, 2022; date of current version February 17, 2022. Dongfang Xu is supported by the Chinese Scholarship Council (CSC). Derrick Wing Kwan Ng is supported by funding from the UNSW Digital Grid Futures Institute, UNSW, Sydney, under a cross-disciplinary fund scheme and by the Australian Research Council's Discovery Project (DP210102169). Robert Schober's work was supported in part by the German Science Foundation through projects SCHO 831/12-1, SCHO 831/15-1, and SFB 1483 - Project-ID 442419336, EmpkinS. An earlier version of this paper was presented in part at the IEEE Wireless Communications and Networking Conference (WCNC) 2021 [DOI: 10.1109/WCNC49053.2021.9417357]. The associate editor coordinating the review of this article and approving it for publication was M. Bennis. *(Corresponding author: Xianghao Yu.)*

Dongfang Xu and Robert Schober are with the Institute for Digital Communications, Friedrich-Alexander-University Erlangen-Nürnberg (FAU), 91058 Erlangen, Germany (e-mail: dongfang.xu@fau.de; robert.schober@fau.de).

Vahid Jamali is with the Department of Electrical Engineering, Princeton University, Princeton, NJ 08544 USA (e-mail: jamali@princeton.edu).

Xianghao Yu is with the Department of Electronic and Computer Engineering, The Hong Kong University of Science and Technology, Hong Kong (e-mail: eexyu@ust.hk).

Derrick Wing Kwan Ng is with the School of Electrical Engineering and Telecommunications, University of New South Wales, Sydney, NSW 2052, Australia (e-mail: w.k.ng@unsw.edu.au).

Color versions of one or more figures in this article are available at https://doi.org/10.1109/TCOMM.2022.3140467.

Digital Object Identifier 10.1109/TCOMM.2022.3140467

interference at the information decoding receivers (IRs). This flexibility allows the system designer to customize a favorable radio propagation environment for performance improvement [5]. Moreover, since IRSs comprise passive components with low-power consumption, adding an IRS to the communication infrastructure does not lead to a significant additional energy burden [6], [7]. Inspired by these advantages, several works have considered the combination of IRS and SWIPT [9]–[11]. For instance, the authors of [9] studied the joint design of the beamforming vector at the base station (BS) and the discrete phase shift patterns of the IRS elements for minimization of the BS transmit power in an IRS-aided SWIPT system. Also, in [10], the authors considered an IRS-enabled multiple-input multiple-output (MIMO) SWIPT system and developed an alternating optimization (AO)-based algorithm for maximization of the system spectral efficiency while providing reliable wireless power transfer service to multiple ERs. Besides, the authors of [11] proposed to jointly optimize the phase shift matrix of the IRS and the beamforming vectors at the BS for security provisioning in an IRS-aided SWIPT system. However, the authors of [9] and [10] adopted an overly-simplified energy harvesting (EH) model, in which the harvested power of the ERs is linearly proportional to the received RF power. In fact, according to practical field measurements [12], [13], the linear EH model is only accurate when the received RF power is constant. However, due to the combination of the signals from the direct link and the reflected link, which are both fading, the received RF power at the ERs in IRS-assisted SWIPT systems usually has a larger dynamic range than that in conventional SWIPT systems. As a result, the schemes proposed in [9] and [10] may not provide satisfactory wireless power charging service for practical ERs. On the other hand, the authors of [9]–[11] adopted an element-wise optimization framework for IRS design such that the computational complexity of the developed optimization algorithms scales with the number of IRS elements. Hence, these algorithms may not be efficient and scalable for online optimization of large IRSs.

Nevertheless, in practice, the number of IRS phase shift elements deployed in future wireless systems is expected to be large. On the one hand, since the phase shifters are usually sub-wavelength elements, a typical rectangular IRS naturally consists of hundreds of elements due to its highly integrated architecture [14]–[16]. For instance, the authors in [15] designed and manufactured a 80 cm $\times$ 30 cm experimental IRS system comprising 1,100 phase shift elements, while an 1 m $\times$ 1 m large IRS prototype composed of 10,000 phase shift elements was demonstrated in [16]. On the other hand, even in free space propagation environments, the equivalent path loss of the BS-IRS-receiver link is in general much larger than that of the unobstructed direct link due to the double-path loss effect [17]. Hence, to fully realize the potential of IRSs, it is necessary to deploy a large number of phase shift elements such that the severe end-to-end path loss of the cascaded IRS channel can be compensated [18], [19]. However, with the commonly adopted element-wise optimization framework, both the computational complexity of the existing algorithms, e.g., [10], [20], [21], and the required signaling overhead grow with the number of IRS elements. As a result, with the element-wise optimization framework, online design of large IRSs may not be feasible in practice, which constitutes a bottleneck for unleashing the full potential of IRSs in wireless communication systems. Therefore, it is necessary to develop an efficient and scalable optimization framework that paves the way to real-time online design for practical IRSs. To address this issue, recently, the authors of [22] developed a physics-based IRS model and a corresponding tile and transmission mode (TT)-based optimization framework. In particular, they proposed to partition the set of IRS elements into several subsets, referred to as tiles, and modeled the impact of each tile on the effective end-to-end wireless channel taking into account the incident angle, the reflection angle, and the polarization of the electromagnetic wave. Subsequently, they developed a scalable optimization framework comprising an offline design stage and an online optimization stage. In the offline stage, the IRS elements of each tile are jointly designed to support a set of different transmission modes, where each transmission mode effectively corresponds to a given configuration of the phase shifts. To facilitate efficient online design, the authors of [22] proposed a transmission mode pre-selection criterion to refine the offline transmission mode set. Then, in the online stage, the best transmission mode is selected from the refined set according to the design objective. With this new optimization framework, the computational complexity needed for designing large IRSs scales with two design parameters, namely, the number of tiles and the size of the refined transmission mode set. To illustrate this, the authors of [22] considered a multi-user IRS-assisted multiple-input single-output (MISO) communication system and developed two efficient algorithms based on respectively AO and greedy approaches for minimization of the BS transmit power subject to quality-of-service (QoS) constraints for multiple IRs. However, these algorithms are not applicable for the IRS-assisted SWIPT systems considered in this paper due to the coexistence of IRs and ERs and the non-linearity of practical EH models. Moreover, both the AO-based algorithm and the three-step greedy algorithm developed in [22] are suboptimal algorithms, while optimal algorithms for the TT-based optimization framework have not been investigated in the literature, yet. Furthermore, the authors of [22] took into account neither user fairness nor the specific nature of the underlying resource allocation problem for transmission mode pre-selection. As a result, the schemes proposed in [22] may not be able to fully exploit the benefits of TT-based IRS optimization. Besides, the impact of the two tunable parameters, i.e., the number of tiles and the number of the transmission modes, on the computational complexity of the optimization algorithms and the performance of the IRS-assisted system has not be comprehensively investigated in [22].

In this paper, we address the above issues. The contributions of this paper can be summarized as follows:

- We formulate the optimal resource allocation algorithm design for large IRS-assisted SWIPT systems as a non-convex optimization problem which is based on a realistic non-linear EH model for the ERs and a physics-based IRS model.

- We study a TT-based scalable two-stage optimization framework comprising an offline design stage and an online optimization stage. To facilitate efficient online design of IRS-assisted SWIPT systems, we develop two new transmission mode pre-selection criteria to refine the offline transmission mode set.
- Based on the refined transmission mode set, we jointly optimize the BS beamforming and IRS transmission mode selection policy for minimization of the total transmit power under QoS constraints for both the IRs and the ERs. Although the resulting problem is a non-convex mixed-integer optimization problem, we solve it optimally by exploiting a branch-and-bound (BnB) approach and obtain the optimal online joint beamforming and transmission mode selection strategy.
- Since the optimal scheme entails a high computational complexity, we develop a computationally efficient suboptimal algorithm by capitalizing on the penalty method, successive convex approximation (SCA), and semidefinite relaxation (SDR). This algorithm asymptotically converges to a locally optimal solution of the considered problem.
- Simulation results show that the performance of the proposed suboptimal scheme closely approaches that of the proposed optimal scheme. Moreover, our results reveal that the proposed optimal and suboptimal schemes entail much lower power consumption compared to three baseline schemes. Furthermore, our results unveil that by properly tuning the number of tiles and the number of the transmission modes, we can strike a balance between computational complexity and system performance. Besides, we verify that the proposed scalable optimization framework indeed facilitates the efficient online optimization of large IRSs.

The remainder of this paper is organized as follows. In Section II, we introduce the considered IRS-assisted SWIPT system model. In Section III, we first present the adopted TT-based optimization framework, and then develop several transmission mode pre-selection criteria and formulate the online resource allocation optimization problem for the considered system. The optimal and suboptimal online joint beamforming and transmission mode selection algorithm designs are provided in Sections IV. In Section V, simulation results are presented, and Section VI concludes the paper.

Notation: In this paper, boldface lower case and boldface capital letters denote vectors and matrices, respectively. $\mathbf{1}_L$ denote the all-ones vector of length L. $\mathbb{C}^{N\times M}$ denotes the space of $N \times M$ complex-valued matrices. $\mathbb{H}^N$ denotes the set of all N-dimensional complex Hermitian matrices. $\mathbf{I}_N$ refers to the $N \times N$ identity matrix. $|\cdot|$ and $||\cdot||_2$ denote the absolute value of a complex scalar and the l_2-norm of a vector, respectively. $\mathbf{A}^H$ stands for the conjugate transpose of matrix $\mathbf{A}$. $\mathbf{A} \succeq \mathbf{0}$ indicates that $\mathbf{A}$ is a positive semidefinite matrix. $\mathrm{Rank}(\mathbf{A})$ and $\mathrm{Tr}(\mathbf{A})$ denote the rank and the trace of matrix $\mathbf{A}$, respectively. $\exp(x)$ represents the exponential function of a real-valued scalar x. $\mathcal{E}\{\cdot\}$ denotes statistical expectation. $\sim$ and $\triangleq$ stand for "distributed as" and "defined as", respectively. The distribution of a circularly symmetric complex Gaussian random variable with mean μ and variance σ^2 is denoted by $\mathcal{CN}(\mu, \sigma^2)$. $\mathbf{x}^*$ denotes the optimal value of optimization variable $\mathbf{x}$. The gradient vector of function $L(\mathbf{x})$ with respect to $\mathbf{x}$ is denoted by $\nabla_{\mathbf{x}} L(\mathbf{x})$.

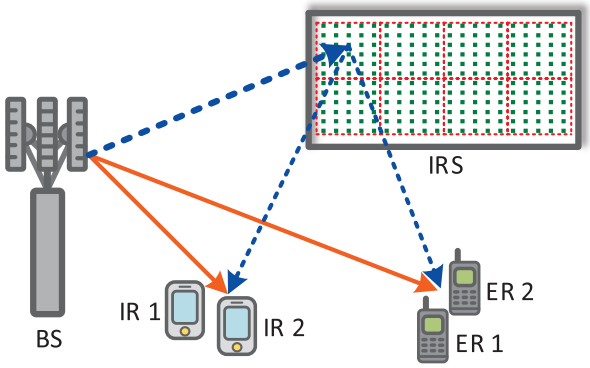

Fig. 1. An IRS-aided SWIPT system comprising one multi-antenna base station (BS), $K = 2$ information decoding receivers (IRs), and $J = 2$ energy harvesting receivers (ERs). To facilitate efficient online design, the large IRS is partitioned into $T = 8$ tiles of equal size, as indicated by the red-colored dotted boxes. The direct links and the reflected links between the base station and the receivers are denoted by orange solid lines and blue dashed lines, respectively.

II. System Model

We consider an IRS-assisted SWIPT system. The system comprises a BS, K IRs, and J ERs, cf. Figure 1. In particular, the BS is equipped with N_{T} antennas while all receivers are single-antenna devices. Based on the received signal, the IRs decode the message transmitted by the BS, while the ERs harvest the received power. To enhance the system performance, a large IRS comprising M phase shift elements is deployed to assist the BS in providing SWIPT services for the two sets of receivers. For notational simplicity, we define sets $\mathcal{J} = \{1, \cdots, J\}$ and $\mathcal{K} = \{1, \cdots, K\}$ to collect the indices of the ERs and IRs, respectively.

A. Signal Model

In a given scheduling time slot, the BS transmit signal is given by

$$\mathbf{x} = \sum_{k\in\mathcal{K}} \mathbf{w}_k d_k + \mathbf{v}, \tag{1}$$

where $\mathbf{w}_k \in \mathbb{C}^{N_{\mathrm{T}}\times 1}$ and $d_k \in \mathbb{C}$ denote the beamforming vector for IR k and the corresponding information symbol, respectively. Without loss of generality, we assume $\mathcal{E}\{|d_k|^2\} = 1, \forall k \in \mathcal{K}$. Moreover, $\mathbf{v}$ is generated as a Gaussian pseudo-random sequence which is utilized to provide wireless power transfer service for ERs and is known to both the IRs and ERs [3], [23]. In particular, $\mathbf{v}$ is modeled as

$$\mathbf{v} \sim \mathcal{CN}(\mathbf{0}, \mathbf{V}), \tag{2}$$

where $\mathbf{V} \succeq \mathbf{0}$, $\mathbf{V} \in \mathbb{H}^{N_{\mathrm{T}}}$, denotes the covariance matrix of the pseudo-random energy signal.

In each scheduling time slot, the received signals at IR k and ER j are given by

$$y_{\mathrm{I},k} = \underbrace{\mathbf{h}_{\mathrm{I},k}^H \mathbf{w}_k d_k}_{\text{desired signal}} + \underbrace{\mathbf{h}_{\mathrm{I},k}^H \sum_{r\in\mathcal{K}\setminus\{k\}} \mathbf{w}_r d_r}_{\text{multiuser interference}} + \underbrace{\mathbf{h}_{\mathrm{I},k}^H \mathbf{v}}_{\text{energy signal}} + n_{\mathrm{I},k}, \quad (3)$$

$$y_{\mathrm{E},j} = \mathbf{h}_{\mathrm{E},j}^H \left(\sum_{k\in\mathcal{K}} \mathbf{w}_k d_k + \mathbf{v} \right) + n_{\mathrm{E},j}, \quad (4)$$

respectively. Here, variables $n_{\mathrm{I},k} \sim \mathcal{CN}(0, \sigma_{\mathrm{I}_k}^2)$ and $n_{\mathrm{E},j} \sim \mathcal{CN}(0, \sigma_{\mathrm{E}_j}^2)$ denote the additive white Gaussian noise with variance $\sigma_{\mathrm{I}_k}^2$ and $\sigma_{\mathrm{E}_j}^2$ at IR k and ER j, respectively. Moreover, vectors $\mathbf{h}_{\mathrm{I},k}$ and $\mathbf{h}_{\mathrm{E},j}$ respectively denote the effective BS-IR$_k$ and BS-ER$_j$ channels which are the superpositions of the channels of the direct and IRS-assisted links, i.e.,

$$\mathbf{h}_{\mathrm{I},k} = \mathbf{h}_{\mathrm{I},k,\mathrm{R}} + \mathbf{h}_{\mathrm{I},k,\mathrm{D}} \quad \text{and} \quad \mathbf{h}_{\mathrm{E},j} = \mathbf{h}_{\mathrm{E},j,\mathrm{R}} + \mathbf{h}_{\mathrm{E},j,\mathrm{D}}. \quad (5)$$

Here, $\mathbf{h}_{\mathrm{I},k,\mathrm{R}}$ and $\mathbf{h}_{\mathrm{E},j,\mathrm{R}}$ are the IRS-assisted BS-IR$_k$ and BS-ER$_j$ channels, respectively, and $\mathbf{h}_{\mathrm{I},k,\mathrm{D}}$ and $\mathbf{h}_{\mathrm{E},j,\mathrm{D}}$ denote the channels of the corresponding direct links. Further details regarding the adopted channel models are presented in Section III-A. Besides, to investigate the maximum achievable performance, similar to [24], [25], we assume that the perfect channel state information (CSI) of the entire system is available at the BS.[1]

B. Non-Linear Energy Harvesting Model

Most existing works on IRS-assisted SWIPT systems adopted a linear EH model [10], [28]. However, this model is not accurate as the RF energy conversion efficiency depends on the input RF power level of the EH circuit. To capture this effect, in this paper, we adopt the non-linear EH model proposed in [29]. In particular, the energy harvested by ER j, i.e., Υ_j^{EH}, is modeled by

$$\Upsilon_j^{\mathrm{EH}} = \frac{\Lambda_j - a_j \Xi_j}{1 - \Xi_j}, \quad \Xi_j = \frac{1}{1 + \exp(\varrho_j c_j)}, \quad (6)$$

$$\Lambda_j = \frac{a_j}{1 + \exp\left(-\varrho_j \left(P_j^{\mathrm{ER}} - c_j\right)\right)}, \quad (7)$$

where Λ_j is a logistic function whose input is the received RF power P_j^{ER} at ER j, and constant Ξ_j ensures a zero-input/zero-output response. Besides, a_j, c_j, and ϱ_j are constant parameters that depend on the employed EH circuit. Given the schematic of the EH circuit, these parameters can be easily determined via some standard curve fitting method [29].

III. A Scalable Optimization Framework for IRS-Assisted SWIPT Systems

In this section, we first present the adopted IRS model which enables a scalable optimization of large IRSs. To facilitate an efficient online design for larger IRSs, we also develop two new transmission mode pre-selection criteria for large IRS-assisted SWIPT systems. At last, after introducing the adopted performance metrics, we formulate the resource allocation design as an optimization problem.

A. End-to-End IRS Channel Model Based on TT Framework

In the following, we adapt the TT-based optimization framework recently developed in [22] to the considered IRS-assisted SWIPT system. We first briefly present the general form of the TT-based framework and then specialize it to the case where a physics-based model is used to characterize the wireless channel and the IRS. Finally, we discuss why this framework enables scalable optimization.

1) TT Framework: In practice, optimizing the individual phase shift elements may not be affordable for online design of large IRSs. To address this issue, in the TT framework, *i)* the large IRS is partitioned into T tiles of equal sizes[2] and *ii)* a set of S phase shift configurations for all IRS elements of each tile is designed offline [22], [30]. Throughout this paper, we refer to the phase shift configurations as transmission modes and employ the same set of transmission modes for all IRS tiles. Let $\mathbf{h}_{\mathrm{I},k,s,t,\mathrm{R}}$ and $\mathbf{h}_{\mathrm{E},j,s,t,\mathrm{R}}$ denote the end-to-end BS-IR$_k$ and BS-ER$_j$ channels of tile t, respectively, which are realized by transmission mode s. Then, $\mathbf{h}_{\mathrm{I},k,\mathrm{R}}$ and $\mathbf{h}_{\mathrm{E},j,\mathrm{R}}$ are given by, respectively,

$$\mathbf{h}_{\mathrm{I},k,\mathrm{R}} = \sum_{\substack{s\in\mathcal{S},\\ t\in\mathcal{T}}} b_{s,t} \mathbf{h}_{\mathrm{I},k,s,t,\mathrm{R}} \quad \text{and} \quad \mathbf{h}_{\mathrm{E},j,\mathrm{R}} = \sum_{\substack{s\in\mathcal{S},\\ t\in\mathcal{T}}} b_{s,t} \mathbf{h}_{\mathrm{E},j,s,t,\mathrm{R}}, \quad (8)$$

where sets $\mathcal{S} = \{1, \cdots, S\}$ and $\mathcal{T} = \{1, \cdots, T\}$ collect the indices of the transmission modes and tiles, respectively. Furthermore, $b_{s,t} \in \{0, 1\}$ is a binary variable with $b_{s,t} = 1$ if tile t employs transmission mode s, $\forall s \in \mathcal{S}, \forall t \in \mathcal{T}$; otherwise it is equal to zero. Constraint $\sum_{s\in\mathcal{S}} b_{s,t} = 1$, $\forall t$, has to hold since only one transmission mode can be selected for each tile. Note that for a given set of transmission modes, channel vectors $\mathbf{h}_{\mathrm{I},k,s,t,\mathrm{R}}$ and $\mathbf{h}_{\mathrm{E},j,s,t,\mathrm{R}}$ are fixed. However, unlike conventional systems, we can choose among S^T possible end-to-end IRS-assisted channels by optimizing $b_{s,t}$.

For ease of presentation and without loss of generality, we model the direct link via a virtual tile indexed by $t = 0$ and rewrite $\mathbf{h}_{\mathrm{I},k,\mathrm{D}}$ as $\mathbf{h}_{\mathrm{I},k,\mathrm{D}} = \sum_{s\in\mathcal{S}} b_{s,0} \mathbf{h}_{\mathrm{I},k,s,0}$ with $\mathbf{h}_{\mathrm{I},k,s,0} = \mathbf{h}_{\mathrm{I},k,\mathrm{D}}$, $\forall s$. By doing so, we can simplify the notation by dropping the subscripts R and D in all the channel vectors. We note that for ER j, channel vector $\mathbf{h}_{\mathrm{E},j,\mathrm{D}}$ can be defined in a similar manner as $\mathbf{h}_{\mathrm{I},j,\mathrm{D}}$. As a result, the effective end-to-end BS-IR$_k$ and BS-ER$_j$ channels can be

[1] We note that the channel estimation schemes developed for IRS-assisted systems, e.g., [26], [27], can also be applied for the tile-based IRS considered in this paper. For example, the effective end-to-end channel between the BS and information decoding receiver k, i.e., $\mathbf{h}_{\mathrm{I},k,s,t}$, can be estimated by employing the ON/OFF channel estimation protocol proposed in [26], where $\mathbf{h}_{\mathrm{I},k,s,t}$, $t = 1, \cdots, T$, are estimated one-by-one by switching one tile of the IRS on at a time. As a result, the CSI of the considered large IRS-assisted SWIPT systems can be accurately estimated.

[2] T is a tunable parameter and one can determine its value based on the specific system requirements. For instance, if low complexity of the online optimization algorithms is important, a relatively small value of T is favorable. On the other hand, if high performance is the main concern, the large IRS should be partitioned into a large number of tiles. Similarly, we can also tune the value of S to adjust the tradeoff between system performance and complexity.

rewritten as, respectively,

$$\mathbf{h}_{\mathrm{I},k} = \sum_{\substack{s\in\mathcal{S},\\ t\in\widehat{\mathcal{T}}}} b_{s,t}\mathbf{h}_{\mathrm{I},k,s,t} \quad \text{and} \quad \mathbf{h}_{\mathrm{E},j} = \sum_{\substack{s\in\mathcal{S},\\ t\in\widehat{\mathcal{T}}}} b_{s,t}\mathbf{h}_{\mathrm{E},j,s,t}, \quad (9)$$

where $\widehat{\mathcal{T}} = \mathcal{T} \cup \{0\}$.

2) Physics-Based Model: We assume that the wireless environment consists of multiple scatterers, where each scatterer contributes a single propagation path [22], [31]. Hence, the signal transmitted by the BS will arrive at the IRS via multiple paths, and the signal reflected by the IRS will arrive at a given receiver via multiple paths. To fully unleash the potential of the IRS, it is crucial to reflect the signal along strong paths in order to ensure sufficient link budget especially when the direct links suffer from severe shadowing. Motivated by this discussion, instead of modeling the IRS tiles in terms of the reflection coefficients of all individual reflecting elements, we model the tile for each transmission mode in terms of its response for all angles of arrival (AoAs) corresponding to the paths in the BS-IRS link and angles of departure (AoDs) corresponding to the paths in the IRS-receiver link. In particular, for tile t employing transmission mode s, the effective end-to-end channel between the BS and IR k, i.e., $\mathbf{h}_{\mathrm{I},k,s,t}$, is given by [22]

$$\mathbf{h}_{\mathrm{I},k,s,t}^H = \mathbf{1}_{\mathrm{I},k,\mathrm{R}}^H \mathbf{C}_{\mathrm{I},k,\mathrm{R}} \mathbf{R}_{\mathrm{I},k,s,t} \mathbf{C}_{\mathrm{T}} \mathbf{D}_{\mathrm{T}}, \quad \forall t \in \mathcal{T}. \quad (10)$$

Here, $\mathbf{1}_{\mathrm{I},k,\mathrm{R}} \in \mathbb{C}^{L_{\mathrm{I},k,\mathrm{R}}\times 1}$ is an all-ones vector, and $\mathbf{D}_{\mathrm{T}} \in \mathbb{C}^{L_{\mathrm{T}}\times N_{\mathrm{T}}}$ is a matrix representing the BS antenna array response of the BS-IRS link. L_{T} and $L_{\mathrm{I},k,\mathrm{R}}$ denote the numbers of scatterers of the BS-IRS and IRS-IR$_k$ links, respectively. Moreover, diagonal matrices $\mathbf{C}_{\mathrm{T}} \in \mathbb{C}^{L_{\mathrm{T}}\times L_{\mathrm{T}}}$ and $\mathbf{C}_{\mathrm{I},k,\mathrm{R}} \in \mathbb{C}^{L_{\mathrm{I},k,\mathrm{R}}\times L_{\mathrm{I},k,\mathrm{R}}}$ contain the channel coefficients which capture the joint impact of path loss, shadowing, and small-scale fading on the BS-IRS and IRS-IR$_k$ links, respectively. Furthermore, matrix $\mathbf{R}_{\mathrm{I},k,s,t} \in \mathbb{C}^{L_{\mathrm{I},k,\mathrm{R}}\times L_{\mathrm{T}}}$ denotes the response function of tile t applying the s-th transmission mode evaluated at the AoAs of the BS-IRS link and the AoDs of the IRS-IR$_k$ link. We note that for each channel realization, $\mathbf{R}_{\mathrm{I},k,s,t}$ is fixed for a given transmission mode and depends on the channel AoAs and AoDs, see [22, Eq. (26)] and [32, Eq. (5)]. In other words, different transmission modes realize different $\mathbf{R}_{\mathrm{I},k,s,t}$ and consequently different end-to-end channels $\mathbf{h}_{\mathrm{I},k,s,t}$.

Remark 1: We note that the physics-based model in (10) is a more general and more accurate model compared to the widely adopted conventional IRS model [24], [33], [34]. On the one hand, by setting T equal to the number of IRS elements M and mapping the entire phase shift domain to the transmission mode set, the conventional IRS model can be regarded as a special case of the IRS model considered in this paper. On the other hand, unlike the conventional IRS model, which over-optimistically assumes a constant gain for all signals reflected by the IRS, the physics-based model takes into account the impact of the incident and reflection angles of the impinging electromagnetic waves on the reflected signals when determining the corresponding gain.

Assuming a scatterer-based wireless environment, the channel vector of the direct link between the BS and IR$_k$ is given by [22]

$$\mathbf{h}_{\mathrm{I},k,0}^H = \mathbf{1}_{\mathrm{I},k,\mathrm{D}}^H \mathbf{C}_{\mathrm{I},k,\mathrm{D}} \mathbf{D}_{\mathrm{I},k,\mathrm{D}}, \quad (11)$$

where $\mathbf{1}_{\mathrm{I},k,\mathrm{D}} \in \mathbb{C}^{L_{\mathrm{I},k,\mathrm{D}}\times 1}$ is an all-ones vector, $\mathbf{D}_{\mathrm{I},k,\mathrm{D}} \in \mathbb{C}^{L_{\mathrm{I},k,\mathrm{D}}\times N_{\mathrm{T}}}$ is a matrix containing the BS antenna array vectors of the BS-IR$_k$ direct link, $\mathbf{C}_{\mathrm{I},k,\mathrm{D}} \in \mathbb{C}^{L_{\mathrm{I},k,\mathrm{D}}\times L_{\mathrm{I},k,\mathrm{D}}}$ is a diagonal matrix whose diagonal entries are the channel coefficients of the scatterers in the BS-IR$_k$ direct link, and $L_{\mathrm{I},k,\mathrm{D}}$ denotes the number of scatterers of the BS-IR$_k$ direct link. The BS-ER$_j$ channel realized via tile t for transmission mode s, i.e., $\mathbf{h}_{\mathrm{E},j,s,t}$, and the BS-ER$_j$ direct channel $\mathbf{h}_{\mathrm{E},j,0}$ are modeled similar to $\mathbf{h}_{\mathrm{I},k,s,t}$ and $\mathbf{h}_{\mathrm{I},k,0}$ in (10) and (11), respectively.

Remark 2: We note that this paper focuses on slowly time-varying fading channels such that the coherence time of the considered system is larger than the duration of a scheduling frame. Moreover, we assume the perfect CSI of all channels is available at the BS and the AoAs and AoDs of the scatterers are known for resource allocation design. On the other hand, in practice, channel estimation errors and AoA and AoD estimation errors (caused, e.g., by mobile scatterers) are unavoidable. To mitigate the impact of these errors, the algorithms developed in this paper can be extended by applying concepts from robust optimization, e.g., [3], [35], [36]. However, this is beyond the scope of this paper but constitutes an interesting topic for future work.

3) Two-Stage Scalable Optimization Framework: IRS optimization based on (8) and (10) is performed in two stages, namely an offline stage and an online stage. *i)* In the offline stage, the set of transmission modes is designed which determines the set of potential end-to-end channels that each tile can create for a given channel realization. *ii)* In the online stage, the best transmission mode is chosen for each tile depending on the design objective of the considered systems. The scalability of this TT framework stems from the fact that the computational complexity for online IRS optimization is untied from the number of IRS elements M, but scales with the number of tiles T and the number of transmission modes S which are design parameters and can be adjustable to trade performance for complexity. The authors of [22] and [32] have studied the offline transmission mode design and developed a corresponding simple pre-selection criterion, and the proposed transmission mode sets are also applicable to the IRS-assisted SWIPT systems considered here. Therefore, in this paper, we focus our attention on the online algorithm design as well as novel transmission mode pre-selection criteria. We emphasize that the transmission mode pre-selection criteria and the online optimization algorithms developed in this paper are applicable for any offline transmission mode set. In Figure 2, we illustrate the key steps of the adopted scalable optimization framework. The green and blue colored boxes indicate the main foci of the paper.

B. Transmission Mode Pre-Selection for Online Optimization

In this paper, we employ the offline transmission mode set that is generated according to [22, Section III-A] for online

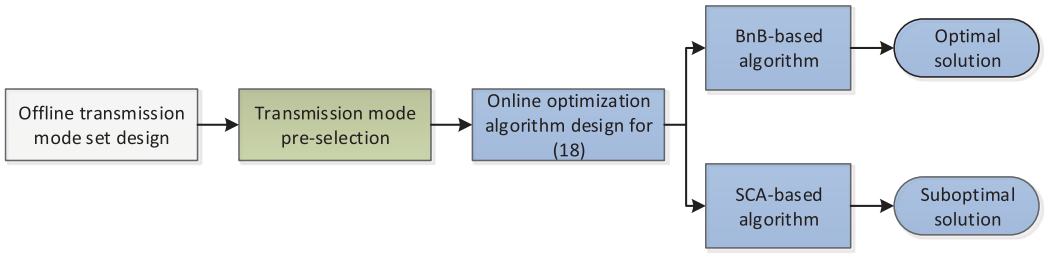

Fig. 2. Illustration of key steps of the proposed scalable optimization framework.

optimization of the considered system. However, it has been shown in [22], that for a given radio propagation environment, not all the elements in the offline transmission mode set will contribute to a system performance enhancement. Hence, instead of directly employing the offline transmission mode set for online resource allocation, it is advisable to first refine the transmission mode set to facilitate a more computationally efficient online optimization. To this end, in the following, we first present the simple transmission mode pre-selection criterion proposed in [22]. Then, we develop two new criteria that take into account user fairness and the specific characteristics of SWIPT systems, respectively.

For the effective end-to-end channel in (10), a given channel realization does not only depend on the channel coefficients of the links but also on the locations of the scatterers. Since the number of scatterers is limited and the locations of the scatterers are fixed, the IRS can exploit only a limited number of AoAs and AoDs to receive the signals from the BS and to reflect the signals to the receivers. As a result, only a limited number of transmission modes are suitable candidates for reflecting the signal impinging from one of the scatterers/BS to one of the other scatterers/receivers [22], [32]. Thus, for a given BS-receiver pair, the Euclidean norm of the channel vector, i.e., $\|\mathbf{h}_{\mathrm{I},k,s,t}\|_2$ or $\|\mathbf{h}_{\mathrm{E},j,s,t}\|_2$, is non-negligible only for a few of the transmission modes contained in the offline transmission mode set. Thus, to facilitate online optimization for practically large IRS-assisted SWIPT systems, we propose to first pre-select a subset of the transmission modes from the set generated in the offline design stage.

The authors of [22] developed a simple and straightforward transmission mode pre-selection criterion which chooses the transmission modes that yield the largest effective end-to-end channel gain, i.e., the largest Euclidean norm of the channel vector. In particular, the desired refined transmission mode set can be obtained as follows

$$\text{Criterion 1: } \mathcal{S}_{\mathrm{R}_1} = \Bigg\{ s | \exists (r,i,t) : \|\mathbf{h}_{r,i,s,t}\|_2 \geq \delta_1, \begin{Bmatrix} r=\mathrm{I},\ i \in \mathcal{K} \\ r=\mathrm{E},\ i \in \mathcal{J} \end{Bmatrix}, t \in \mathcal{T} \Bigg\}, \quad (12)$$

where $\delta_1 > 0$ is a tunable threshold which can be used to adjust the size of set $\mathcal{S}_{\mathrm{R}_1}$. Although Criterion 1 is simple to implement, it does not take into account user fairness and may lead to a biased refined transmission mode set that is favorable only for one IR or one ER. In fact, if the channel state of one receiver is much better than that of the other receivers, it is possible that most of the phase-shift configurations in the refined transmission mode set are only favorable for this receiver. To circumvent this issue, we can construct an improved transmission mode set by pre-selecting a few favorable phase-shift configurations for each receiver. Specifically, the transmission mode set for a given receiver is constructed as follows

$$\text{Criterion 2: } \mathcal{S}_{\mathrm{R}_{2,r,i}} = \left\{ s \mid \exists t : \|\mathbf{h}_{r,i,s,t}\|_2 \geq \delta_{2,r,i}, t \in \mathcal{T} \right\}, \begin{cases} r=\mathrm{I},\ i \in \mathcal{K} \\ r=\mathrm{E},\ i \in \mathcal{J} \end{cases}, \quad (13)$$

where $\delta_{2,r,i} > 0$ is a parameter to adjust the size of set $\mathcal{S}_{\mathrm{R}_{2,r,i}}$ and the total set in this case is given by $\mathcal{S}_{\mathrm{R}_2} = \bigcup_{r,i} \mathcal{S}_{\mathrm{R}_{2,r,i}}$.

Apart from the aforementioned criteria, one can also pre-select transmission modes based on the specific resource allocation optimization objective. Considering the fact that in SWIPT systems, the ERs usually require much higher received powers than the IRs, we can refine the transmission mode set by keeping those transmission modes that are favorable for the ERs, which facilitates minimization of the BS transmit power while providing satisfactory service for both IRs and ERs. This can be achieved by imposing weights on the effective end-to-end channels of the ERs. To this end, the transmission mode set for receiver i is constructed based on the following weight criterion

$$\text{Criterion 3: } \mathcal{S}_{\mathrm{R}_3} = \{ s \mid \exists (r,i,t) : p_{r,i,s,t} \geq \delta_1, t \in \mathcal{T} \}, \quad (14)$$

where variable $p_{r,i,s,t}$ is defined as

$$p_{r,i,s,t} = \begin{cases} \omega \|\mathbf{h}_{r,i,s,t}\|_2, & r=\mathrm{E}, \quad \forall i \in \mathcal{J} \\ \|\mathbf{h}_{r,i,s,t}\|_2, & r=\mathrm{I}, \quad \forall i \in \mathcal{K} \end{cases}. \quad (15)$$

Here, $\omega > 1$ is the weight factor to be used to prioritize the ERs such that the resulting set is more favorable for ERs. For $\omega = 1$, Criterion 3 is identical to Criterion 1. Note that which one of the three transmission mode pre-selection criteria is adopted does not affect the online resource allocation algorithm design.

C. Optimization Problem Formulation

The received signal-to-noise-plus-interference ratio (SINR) of IR k, i.e., Γ_k is given by[3]

$$\Gamma_k = \frac{\left|\mathbf{h}_{\mathrm{I},k}^H \mathbf{w}_k\right|^2}{\mathbf{h}_{\mathrm{I},k}^H \big(\sum\limits_{r\in\mathcal{K}\setminus\{k\}} \mathbf{w}_r \mathbf{w}_r^H + \mathbf{V}\big)\mathbf{h}_{\mathrm{I},k} + \sigma_{\mathrm{I}_k}^2}. \tag{16}$$

Furthermore, the received RF power at ER j, i.e., P_j^{ER}, is given by

$$P_j^{\mathrm{ER}} = \mathbf{h}_{\mathrm{E},j}^H \left(\sum_{k\in\mathcal{K}} \mathbf{w}_k \mathbf{w}_k^H + \mathbf{V} \right) \mathbf{h}_{\mathrm{E},j}. \tag{17}$$

In this paper, we aim to minimize the total transmit power at the BS while satisfying the QoS requirements of the IRs and the EH requirements of the ERs.[4] In particular, for a given refined transmission mode set[5] $\mathcal{S}_{\mathrm{R}}$, the joint optimal beamforming and transmission mode selection policy, i.e., $\{\mathbf{w}_k, \mathbf{V}, b_{s,t}\}$, is obtained by solving the following optimization problem[6]

$$\begin{aligned} \underset{\mathbf{V}\in\mathbb{H}^{N_{\mathrm{T}}},\mathbf{w}_k,b_{s,t}}{\text{minimize}} \; & \sum_{k\in\mathcal{K}} \|\mathbf{w}_k\|_2^2 + \mathrm{Tr}(\mathbf{V}) \\ \text{s.t. C1: } & \Gamma_k \geq \Gamma_{\mathrm{req}_k}, \quad \forall k, \text{C2: } \Upsilon_j^{\mathrm{EH}} \geq E_{\mathrm{req}_j}, \quad \forall j, \\ & \text{C3: } \mathbf{V} \succeq \mathbf{0}, \; \text{C4: } b_{s,t} \in \{0,1\}, \quad \forall s \in \mathcal{S}_{\mathrm{R}}, \quad \forall t \in \widehat{\mathcal{T}}, \\ & \text{C5: } \sum_{s\in\mathcal{S}_{\mathrm{R}}} b_{s,t} = 1, \quad \forall t \in \widehat{\mathcal{T}}. \end{aligned} \tag{18}$$

Here, Γ_{req_k} in constraint C1 is the pre-defined minimum required SINR of IR k. Constraint C2 indicates that the minimum harvested power at ER j should be greater than a given threshold E_{req_j}. Constraint C3 and $\mathbf{V} \in \mathbb{H}^{N_{\mathrm{T}}}$ restrict matrix $\mathbf{V}$ to be a positive semidefinite Hermitian matrix such that it is a valid covariance matrix. Constraints C4 and C5 are imposed since only one transmission mode can be selected for each tile.

The problem in (18) is a mixed-integer non-convex optimization problem. Although (18) is still challenging to solve due to the non-convexity stemming from the coupling of the optimization variables, the fractional function in constraint C1, and the binary selection constraint in C4, we sidestep the unit-modulus constraint of the optimization problems formulated in [9]–[11] based on the conventional element-wise optimization framework. This allows us to leverage the plethora of algorithms developed for integer programming problems to preserve joint optimality rather than solely relying on AO-based algorithms. Therefore, in the next section, we develop a BnB-based algorithm to obtain the globally optimal solution of problem (18) which serves as a performance benchmark. Since the BnB-based algorithm entails a high computational complexity, we also develop a suboptimal scheme which has only polynomial time computational complexity.

IV. Solution of the Problem

In this section, we first tackle the coupling of the optimization variables by employing the Big-M formulation [37]. Then, a BnB-based algorithm is proposed to solve the optimization problem in (18) optimally leading to an iterative resource allocation algorithm. In each iteration, a non-convex optimization problem is solved optimally by SDR. Subsequently, we develop a suboptimal solution based on SCA which asymptotically converges to a locally optimal solution of the considered optimization problem in polynomial time.

A. Problem Transformation

To facilitate resource allocation algorithm design, we first handle the coupling of the optimization variables by defining $\mathbf{W}_k = \mathbf{w}_k \mathbf{w}_k^H, \; \forall k$. Considering the channel vectors $\mathbf{h}_{\mathrm{I},k}$ and $\mathbf{h}_{\mathrm{E},j}$ defined in (9), we note that (16) and (17) contain cross-terms $b_{s,t} b_{p,q}, \; \forall s,p \in \mathcal{S}_{\mathrm{R}}, \; \forall t,q \in \widehat{\mathcal{T}}$. For handling this coupling, we define new optimization variable $\beta_{s,t,p,q} = b_{s,t} b_{p,q}$. Since $b_{s,t}$ and $b_{p,q}$ are binary variables, we apply the Big-M formulation to represent $\beta_{s,t,p,q} = b_{s,t} b_{p,q}$ equivalently in terms of the following convex constraints

$$\text{C6a: } 0 \leq \beta_{s,t,p,q} \leq 1, \text{C6b: } \beta_{s,t,p,q} \leq b_{s,t}, \tag{19}$$

$$\text{C6c: } \beta_{s,t,p,q} \leq b_{p,q}, \text{C6d: } \beta_{s,t,p,q} \geq b_{s,t} + b_{p,q} - 1. \tag{20}$$

Then, we insert $\mathbf{h}_{\mathrm{I},k}$ and $\mathbf{h}_{\mathrm{E},j}$ defined in (9) back into (16) and (17) and rewrite the SINR of IR k and the received RF power at ER j as follows, respectively,

$$\Gamma_k = \frac{\sum\limits_{\substack{s\in\mathcal{S}_{\mathrm{R}},\\ t\in\widehat{\mathcal{T}}}} \sum\limits_{\substack{p\in\mathcal{S}_{\mathrm{R}},\\ q\in\widehat{\mathcal{T}}}} \beta_{s,t,p,q} \mathbf{h}_{\mathrm{I},k,s,t}^H \mathbf{W}_k \mathbf{h}_{\mathrm{I},k,p,q}}{\sum\limits_{\substack{s\in\mathcal{S}_{\mathrm{R}},\\ t\in\widehat{\mathcal{T}}}} \sum\limits_{\substack{p\in\mathcal{S}_{\mathrm{R}},\\ q\in\widehat{\mathcal{T}}}} \beta_{s,t,p,q} \mathbf{h}_{\mathrm{I},k,s,t}^H \left(\sum\limits_{\substack{r\in\mathcal{K},\\ r\neq k}} \mathbf{W}_r + \mathbf{V} \right) \mathbf{h}_{\mathrm{I},k,p,q} + \sigma_{\mathrm{I}_k}^2}, \tag{21}$$

$$P_j^{\mathrm{ER}} = \sum_{\substack{s\in\mathcal{S}_{\mathrm{R}},\\ t\in\widehat{\mathcal{T}}}} \sum_{\substack{p\in\mathcal{S}_{\mathrm{R}},\\ q\in\widehat{\mathcal{T}}}} \beta_{s,t,p,q} \mathbf{h}_{\mathrm{E},j,s,t}^H \left(\sum_{k\in\mathcal{K}} \mathbf{W}_k + \mathbf{V} \right) \mathbf{h}_{\mathrm{E},j,p,q}. \tag{22}$$

[3]Since the pseudo-random energy signal $\mathbf{v}$ is perfectly known at all receivers in principle, it is possible to cancel the interference at the IRs. In this case, the energy signal-induced interference at IR k, i.e., $\mathbf{h}_{\mathrm{I},k}^H \mathbf{V} \mathbf{h}_{\mathrm{I},k}$, is absent in the expression for the SINR in (16) [23]. On the other hand, applying interference cancellation increases receiver complexity, of course. Without loss of generality, in this paper, we assume that the IRs do not cancel the energy signal-induced interference. Nevertheless, we note that with proper modifications the algorithms developed in this paper are also applicable to the case where cancellation of the energy signal-induced interference is possible.

[4]In practice, apart from the IRs and ERs considered in this paper, SWIPT systems may comprise another type of receiver, i.e., hybrid information and EH receivers [3]. In particular, according to a given power splitting ratio, hybrid receivers split the received signal into two parts, one for EH and one for information decoding. We note that for hybrid information and EH receivers with a given fixed power splitting ratio, the problem formulation for resource allocation is essentially identical to (18). As a result, the proposed optimal and suboptimal resource allocation algorithms can also be applied to IRS-assisted SWIPT system employing hybrid information and EH receivers.

[5]For notational simplicity, in the remainder of the paper, we omit the subscripts of the refined transmission mode sets and use $\mathcal{S}_{\mathrm{R}}$ and S_{R} to denote the set employed for online resource allocation and its cardinality, respectively.

[6]In practice, the total transmit power, i.e., $\sum\limits_{k\in\mathcal{K}} \|\mathbf{w}_k\|^2 + \mathrm{Tr}(\mathbf{V})$, has to be smaller than or equal to the maximum possible transmit power of the BS, i.e., $P^{\max}$. However, since, in this paper, the objective of resource allocation is to minimize the total transmit power of the BS, imposing such a constraint in the problem formulation is not necessary. In fact, after solving the considered optimization problem in (18), we can check if the corresponding objective function value is smaller than or equal to $P^{\max}$. If this is not the case, then the obtained solution cannot be realized.

We note that there are still coupled optimization variables in (21) and (22), i.e., $\beta_{s,t,p,q}\mathbf{W}_k$ and $\beta_{s,t,p,q}\mathbf{V}$. To overcome this difficulty, we again apply the Big-M formulation. In particular, we define new optimization variables $\widehat{\mathbf{W}}_{k,s,t,p,q} = \beta_{s,t,p,q}\mathbf{W}_k$ and $\widehat{\mathbf{V}}_{s,t,p,q} = \beta_{s,t,p,q}\mathbf{V}$ to decompose the product terms by imposing the following additional convex constraints[7]:

$$\text{C7a: } \widehat{\mathbf{W}}_{k,s,t,p,q} \preceq \beta_{s,t,p,q}P^{\max}\mathbf{I}_{N_\mathrm{T}}, \tag{23}$$

$$\text{C7b: } \widehat{\mathbf{W}}_{k,s,t,p,q} \succeq \mathbf{W}_k - (1-\beta_{s,t,p,q})P^{\max}\mathbf{I}_{N_\mathrm{T}}, \tag{24}$$

$$\text{C7c: } \widehat{\mathbf{W}}_{k,s,t,p,q} \preceq \mathbf{W}_k, \text{C7d: } \widehat{\mathbf{W}}_{k,s,t,p,q} \succeq \mathbf{0}, \tag{25}$$

$$\text{C8a: } \widehat{\mathbf{V}}_{s,t,p,q} \preceq \beta_{s,t,p,q}P^{\max}\mathbf{I}_{N_\mathrm{T}}, \tag{26}$$

$$\text{C8b: } \widehat{\mathbf{V}}_{s,t,p,q} \succeq \mathbf{V} - (1-\beta_{s,t,p,q})P^{\max}\mathbf{I}_{N_\mathrm{T}}, \tag{27}$$

$$\text{C8c: } \widehat{\mathbf{V}}_{s,t,p,q} \preceq \mathbf{V}, \text{C8d: } \widehat{\mathbf{V}}_{s,t,p,q} \succeq \mathbf{0}. \tag{28}$$

Then, constraints C1 and C2 can be respectively recast as constraints $\widehat{\text{C1}}$ and $\widehat{\text{C2}}$, as shown at the bottom of the page. Here, constant C_{req_j} in $\widehat{\text{C2}}$ is defined as $C_{\mathrm{req}_j} = (\frac{a_j}{E_{\mathrm{req}_j}(1-\Xi_j)+a_j\Xi_j} - 1)\exp(-\varrho_j c_j)$.

Then, we recast the optimization problem in (18) as follows

$$\begin{aligned}\underset{\substack{\mathbf{W}_k,\widehat{\mathbf{W}}_{k,s,t,p,q}\in\mathbb{H}^{N_\mathrm{T}},\\ \mathbf{V},\widehat{\mathbf{V}}_{s,t,p,q}\in\mathbb{H}^{N_\mathrm{T}},\\ b_{s,t},\beta_{s,t,p,q}}}{\text{minimize}} & \sum_{\substack{s\in\mathcal{S}_\mathrm{R},\\ t\in\widehat{\mathcal{T}}}}\sum_{\substack{p\in\mathcal{S}_\mathrm{R},\\ q\in\widehat{\mathcal{T}}}} \mathrm{Tr}\left(\sum_{k\in\mathcal{K}}\widehat{\mathbf{W}}_{k,s,t,p,q}+\widehat{\mathbf{V}}_{s,t,p,q}\right)\\ \text{s.t. } & \widehat{\text{C1}}, \widehat{\text{C2}}, \text{C3-C5}, \text{C6a-C6d}, \text{C7a-C7d},\\ & \text{C8a-C8d}, \text{C9: } \mathrm{Rank}(\mathbf{W}_k) \le 1, \quad \forall k,\end{aligned} \tag{31}$$

where $\mathbf{W}_k \in \mathbb{H}^{N_\mathrm{T}}$ and the rank-one constraint C9 are imposed to guarantee that $\mathbf{W}_k = \mathbf{w}_k\mathbf{w}_k^H$ holds after optimization. We note that the binary constraint in C4 and rank-one constraint C9 are still obstacles to solving problem (31). Nevertheless, in the next subsection, we develop a BnB-based algorithm to optimally solve (31).

B. Optimal Resource Allocation Scheme

The BnB approach is a promising systematic partial enumeration strategy to optimally solve discrete and combinatorial optimization problems. Given an optimization problem with a finite number of binary optimization variables, BnB-based algorithms are guaranteed to terminate at the globally optimal solution in a finite number of iterations [40]. BnB algorithms have been widely adopted to optimally solve communication resource allocation problems involving binary variables such as optimal user scheduling [41] and optimal subcarrier assignment [42]. Thanks to the series of transformations applied in Section IV-A, the reformulated equivalent problem in (31) is in the canonical form that allows the application of the BnB concept to develop an optimal algorithm.[8] The basic principle of BnB-based algorithms is to exploit a tree traversal where the feasible set of the main problem is mapped to the root. BnB-based algorithms explore all branches of the tree, where each node of the tree represents a subset of the solution set. For each node, a subproblem based on the corresponding subset is formulated and both an upper bound and a lower bound are constructed. These bounds are then utilized to check the optimality of a given subproblem. A node is discarded if it cannot produce a better solution than the current best solution found by the algorithm. Based on a predefined node selection strategy, the tree traversal proceeds by selecting and branching one node into two new nodes in each iteration of the BnB-based algorithm. As the tree structure continues to expand, the feasible set is progressively partitioned into smaller subsets and the current best solution is updated leading to improved objective values in the course of the iterations. Following the above procedure, the gap between the upper bound and the lower bound gradually vanishes in each iteration and the BnB-based algorithm converges to the globally optimal solution of the considered optimization problem. In this subsection, we present the construction of the bounds, the partition rule, and the branching strategy for the problem in (31), and then develop the optimal resource allocation algorithm.

1) Lower and Upper Bounds: We denote the search space of the proposed BnB-based algorithm as $\mathcal{B}$, where $\mathcal{B}$ is the product of ST binary sets. In particular, $\mathcal{B}$ is given by $\mathcal{B} = \prod_{s\in\mathcal{S}_\mathrm{R}}\prod_{t\in\mathcal{T}}\mathcal{B}_{s,t}$, where $\mathcal{B}_{s,t} \triangleq \{0,1\}$, $\forall s,\ t$. Then, we define a continuous optimization variable $0 \le \widetilde{b}_{s,t} \le 1$ and rewrite optimization problem (31) as a binary-optimization-variable-relaxed optimization problem in (32), as shown at the bottom of the next page. Here, the new optimization variables $\widetilde{\beta}_{s,t,p,q}$, $\widetilde{\mathbf{W}}_{k,s,t,p,q}$, and $\widetilde{\mathbf{V}}_{s,t,p,q}$ are defined as $\widetilde{\beta}_{s,t,p,q} = \widetilde{b}_{s,t}\widetilde{b}_{p,q}$,

[7]Here, $P^{\max}$ is used only to establish an upper bound for the new optimization variables $\widehat{\mathbf{W}}_{k,s,t,p,q}$ and $\widehat{\mathbf{V}}_{s,t,p,q}$ [38], [39]. Replacing $P^{\max}$ with an arbitrarily large constant serves the same purpose.

[8]Note that the proposed scalable optimization framework allows us to flexibly tune T and S_R, which determines the number of optimization variables $b_{s,t}$. On the other hand, the number of nodes in the BnB search tree is proportional to the number of optimization variables $b_{s,t}$. As a result, the choice of T and S_R directly influences the complexity of the proposed BnB-based optimal algorithm. This dependence facilitates the efficient online design of large IRS-assisted wireless systems. Note that other global optimization algorithms, such as McCormick envelope algorithm [43], may also be considered for optimally solving the considered optimization problem in (18).

$$\widehat{\text{C1}}\text{:}\frac{1}{\Gamma_{\mathrm{req}_k}}\sum_{\substack{s\in\mathcal{S}_\mathrm{R},\\ t\in\widehat{\mathcal{T}}}}\sum_{\substack{p\in\mathcal{S}_\mathrm{R},\\ q\in\widehat{\mathcal{T}}}}\mathrm{Tr}\big(\mathbf{h}_{\mathrm{I},k,p,q}\mathbf{h}_{\mathrm{I},k,s,t}^H\widehat{\mathbf{W}}_{k,s,t,p,q}\big) - \sum_{\substack{s\in\mathcal{S}_\mathrm{R},\\ t\in\widehat{\mathcal{T}}}}\sum_{\substack{p\in\mathcal{S}_\mathrm{R},\\ q\in\widehat{\mathcal{T}}}}\mathrm{Tr}\Big(\mathbf{h}_{\mathrm{I},k,p,q}\mathbf{h}_{\mathrm{I},k,s,t}^H\big(\sum_{\substack{r\in\mathcal{K}\\ r\neq k}}\widehat{\mathbf{W}}_{r,s,t,p,q}+\widehat{\mathbf{V}}_{s,t,p,q}\big)\Big) \ge \sigma_{\mathrm{I}_k}^2, \tag{29}$$

$$\widehat{\text{C2}}\text{:}C_{\mathrm{req}_j} \ge \exp\Big(-\varrho_j\sum_{\substack{s\in\mathcal{S}_\mathrm{R},\\ t\in\widehat{\mathcal{T}}}}\sum_{\substack{p\in\mathcal{S}_\mathrm{R},\\ q\in\widehat{\mathcal{T}}}}\mathrm{Tr}\big(\mathbf{h}_{\mathrm{E},j,p,q}\mathbf{h}_{\mathrm{E},j,s,t}^H\big(\sum_{k\in\mathcal{K}}\widehat{\mathbf{W}}_{k,s,t,p,q}+\widehat{\mathbf{V}}_{s,t,p,q}\big)\big)\Big), \forall j, \tag{30}$$

$\widetilde{\mathbf{W}}_{k,s,t,p,q} = \widetilde{\beta}_{s,t,p,q}\mathbf{W}_k$, and $\widetilde{\mathbf{V}}_{s,t,p,q} = \widetilde{\beta}_{s,t,p,q}\mathbf{V}$, respectively. We note that constraint C4 is a continuous relaxation of binary constraint C4. In general, solving the optimization problem in (32) may yield a non-binary solution. As a result, the optimal solution of the constraint-relaxed problem in (32), i.e., $(\widetilde{b}^*_{s,t}, \mathbf{W}^*_k, \mathbf{V}^*)$, provides a lower bound for (31) which is denoted by $F_{\rm L}(\widetilde{b}^*_{s,t}, \mathbf{W}^*_k, \mathbf{V}^*)$. However, to optimally solve (32), we still need to circumvent the non-convexity stemming from the unit-rank constraint C9. For handling this issue, we employ SDR and remove constraint C9. The rank-relaxed version of (32) is a convex optimization problem and can be efficiently solved by standard solvers such as CVX [44]. Next, we show the tightness of the relaxation by introducing the following theorem.

Theorem 1: For given $\Gamma_{{\rm req}_k} > 0$, the optimal solution $\mathbf{W}^*_k$ of the relaxed problem (32) always satisfies ${\rm Rank}\,(\mathbf{W}^*_k) = 1$, $\forall k$.

Proof: Please refer to the Appendix. ■

On the other hand, we can also obtain an upper bound of (31) based on the solution produced by (32). In particular, by relaxing the binary constraint and optimally solving the relaxed version of (32), we obtain the optimal solution $\widetilde{b}^*_{s,t}$, where $0 \le \widetilde{b}^*_{s,t} \le 1$, $\forall s,\ t$. Then, based on $\widetilde{b}^*_{s,t}$, we construct a binary solution for the optimization problem in (31) by rounding each $\widetilde{b}^*_{s,t}$ to either 0 or 1. In particular, for $\forall t \in \mathcal{T}$, we round the variable $\widetilde{b}^*_{s,t}$ with index $s^\dagger$ to 1, where $s^\dagger$ is given by

$$s^\dagger = \arg\max_{s\in\mathcal{S}_{\rm R}} \widetilde{b}^*_{s,t}, \quad \forall t \in \mathcal{T}. \tag{33}$$

Then, we set all the other $\widetilde{b}^*_{s,t}$ to 0, $\forall t \in \mathcal{T}$, and denote the rounded solution by $\overline{b}_{s,t}$. We note that given the optimal solution $\mathbf{W}^*_k$ and $\mathbf{V}^*$ of (32), the rounded solution $\overline{b}_{s,t}$ may violate the constraints of (31) and cause infeasibility. Hence, we insert the rounded solution $\overline{b}_{s,t}$ back into (31) and solve the rank-relaxed version of (31) for the optimal solution $\mathbf{W}^{**}_k$ and $\mathbf{V}^{**}$.[9] Then, we can obtain the corresponding upper bound of the objective function value $F_{\rm U}(\overline{b}_{s,t}, \mathbf{W}^{**}_k, \mathbf{V}^{**})$. Now, we have acquired both a lower bound and an upper bound for the optimization problem in (31).

2) Partitioning Rule and Branching Strategy: In each iteration of the BnB algorithm, we select a node in the search tree and branch the corresponding parent problem into two new subproblems, where we use superscript (j) to denote the iteration index of the optimization variables. In particular, among all available nodes, we select the node associated with the smallest lower bound and partition its set according to the Euclidean distance between $\widetilde{b}_{s,t}$ and its rounded version $\overline{b}_{s,t}$. Specifically, in the j-th iteration, we branch the node with index (s^*, t^*), where (s^*, t^*) is given by

$$(s^*, t^*) = \arg\max_{s,t} \left|\widetilde{b}^{(j)}_{s,t} - \overline{b}^{(j)}_{s,t}\right|. \tag{34}$$

Accordingly, the feasible set of b_{s^*,t^*}, i.e., $\mathcal{B}^{(j)}_{s^*,t^*}$, is further divided into two new subsets $(\mathcal{B}^{(j)}_{s^*,t^*})_l$ and $(\mathcal{B}^{(j)}_{s^*,t^*})_r$, which are associated with $b^{(j)}_{s^*,t^*} = 0$ and $b^{(j)}_{s^*,t^*} = 1$, respectively. Then, in the j-th iteration, we focus on the following two subproblems $\mathcal{P}_i$

$$\begin{aligned}\mathcal{P}_i:\ &\underset{\substack{\mathbf{W}_k, \widehat{\mathbf{W}}_{k,s,t,p,q}\in\mathbb{H}^{N_{\rm T}},\\ \mathbf{V}, \widehat{\mathbf{V}}_{s,t,p,q}\in\mathbb{H}^{N_{\rm T}},\\ b_{s,t}, \widehat{\beta}_{s,t,p,q}}}{\text{minimize}} \sum_{\substack{s\in\mathcal{S}_{\rm R},\\ t\in\widehat{\mathcal{T}}}}\sum_{\substack{p\in\mathcal{S}_{\rm R},\\ q\in\widehat{\mathcal{T}}}} {\rm Tr}\left(\sum_{k\in\mathcal{K}} \widehat{\mathbf{W}}_{k,s,t,p,q} + \widehat{\mathbf{V}}_{s,t,p,q}\right)\\ &\text{s.t. C1, C2, C3, C5, C6a-C6d, C7a-C7d, C8a-C8d,}\\ &\quad \overline{\text{C4}}\text{: } b^{(j)}_{s,t} \in \mathcal{B}^{(j)}_{s,t},\ \forall s\in\mathcal{S}_{\rm R}\backslash\{s^*\},\ t\in\mathcal{T}\backslash\{t^*\},\\ &\quad \text{C10: } b^{(j)}_{s^*,t^*} = i,\end{aligned} \tag{35}$$

[9] Since the optimal solution of (32), i.e., $\widetilde{b}^*_{s,t}$, and its rounded version $\overline{b}_{s,t}$ generally lead to different optimal beamforming policies, we denote the optimal beamforming policy associated with $\overline{b}_{s,t}$ by $(\mathbf{W}^{**}_k, \mathbf{V}^{**})$ to avoid ambiguity.

$$\begin{aligned}&\underset{\substack{\mathbf{W}_k, \widetilde{\mathbf{W}}_{k,s,t,p,q}\in\mathbb{H}^{N_{\rm T}},\\ \mathbf{V}, \widetilde{\mathbf{V}}_{s,t,p,q}\in\mathbb{H}^{N_{\rm T}},\\ \widetilde{b}_{s,t},\ \widetilde{\beta}_{s,t,p,q}}}{\text{minimize}} \quad F_{\rm L}(\widetilde{b}_{s,t}, \mathbf{W}_k, \mathbf{V}) \triangleq \sum_{\substack{s\in\mathcal{S}_{\rm R},\\ t\in\widehat{\mathcal{T}}}}\sum_{\substack{p\in\mathcal{S}_{\rm R},\\ q\in\widehat{\mathcal{T}}}} {\rm Tr}\left(\sum_{k\in\mathcal{K}} \widetilde{\mathbf{W}}_{k,s,t,p,q} + \widetilde{\mathbf{V}}_{s,t,p,q}\right)\\ &\text{s.t. C3, C9,}\\ &\widetilde{\text{C1}}\text{:}\frac{1}{\Gamma_{{\rm req}_k}} \sum_{\substack{s,p\in\mathcal{S}_{\rm R},\\ t,q\in\widetilde{\mathcal{T}}}} {\rm Tr}\big(\mathbf{h}_{{\rm I},k,p,q}\mathbf{h}^H_{{\rm I},k,s,t}\widetilde{\mathbf{W}}_{k,s,t,p,q}\big) - \sum_{\substack{s,p\in\mathcal{S}_{\rm R},\\ t,q\in\widetilde{\mathcal{T}}}} {\rm Tr}\Big(\mathbf{h}_{{\rm I},k,p,q}\mathbf{h}^H_{{\rm I},k,s,t}\big(\sum_{r\in\mathcal{K}\backslash\{k\}} \widetilde{\mathbf{W}}_{r,s,t,p,q} + \widetilde{\mathbf{V}}_{s,t,p,q}\big)\Big) \ge \sigma^2_{{\rm I}_k},\ \forall k,\\ &\widetilde{\text{C2}}\text{:}C_{{\rm req}_j} \ge \exp\Big(-\varrho_j \sum_{\substack{s,p\in\mathcal{S}_{\rm R},\\ t,q\in\widetilde{\mathcal{T}}}} {\rm Tr}\big(\mathbf{h}_{{\rm E},j,p,q}\mathbf{h}^H_{{\rm E},j,s,t}(\sum_{k\in\mathcal{K}} \widetilde{\mathbf{W}}_{k,s,t,p,q} + \widetilde{\mathbf{V}}_{s,t,p,q})\big)\Big),\quad \forall j, \widetilde{\text{C4}}\text{: } 0 \le \widetilde{b}_{s,t} \le 1,\quad \forall s,\ t,\\ &\widetilde{\text{C5}}\text{: } \sum_{s\in\mathcal{S}_{\rm R}} \widetilde{b}_{s,t} = 1,\quad \forall t, \widetilde{\text{C6a}}\text{: } 0 \le \widetilde{\beta}_{s,t,p,q} \le 1, \widetilde{\text{C6b}}\text{: } \widetilde{\beta}_{s,t,p,q} \le \widetilde{b}_{s,t}, \widetilde{\text{C6c}}\text{: } \widetilde{\beta}_{s,t,p,q} \le \widetilde{b}_{p,q},\\ &\widetilde{\text{C6d}}\text{: } \widetilde{\beta}_{s,t,p,q} \ge \widetilde{b}_{s,t} + \widetilde{b}_{p,q} - 1, \widetilde{\text{C7a}}\text{: } \widetilde{\mathbf{W}}_{k,s,t,p,q} \preceq \widetilde{\beta}_{s,t,p,q}P^{\max}\mathbf{I}_{N_{\rm T}}, \widetilde{\text{C7b}}\text{: } \widetilde{\mathbf{W}}_{k,s,t,p,q} \preceq \mathbf{W}_k,\\ &\widetilde{\text{C7c}}\text{: } \widetilde{\mathbf{W}}_{k,s,t,p,q} \succeq \mathbf{W}_k - (1-\widetilde{\beta}_{s,t,p,q})P^{\max}\mathbf{I}_{N_{\rm T}}, \widetilde{\text{C7d}}\text{: } \widetilde{\mathbf{W}}_{k,s,t,p,q} \succeq \mathbf{0}, \widetilde{\text{C8a}}\text{: } \widetilde{\mathbf{V}}_{s,t,p,q} \preceq \widetilde{\beta}_{s,t,p,q}P^{\max}\mathbf{I}_{N_{\rm T}},\\ &\widetilde{\text{C8b}}\text{: } \widetilde{\mathbf{V}}_{s,t,p,q} \succeq \mathbf{V} - (1-\widetilde{\beta}_{s,t,p,q})P^{\max}\mathbf{I}_{N_{\rm T}}, \widetilde{\text{C8c}}\text{: } \widetilde{\mathbf{V}}_{s,t,p,q} \preceq \mathbf{V}, \widetilde{\text{C8d}}\text{: } \widetilde{\mathbf{V}}_{s,t,p,q} \succeq \mathbf{0},\end{aligned} \tag{32}$$

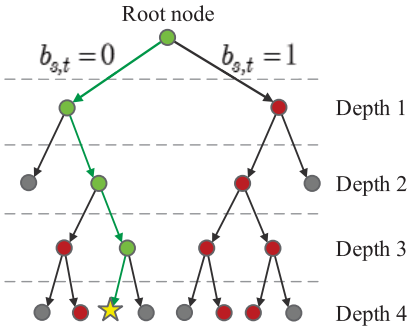

Fig. 3. An illustration of the BnB search tree for $S_{\mathrm{R}}=2$ and $T=2$. The green arrows and dots correspond to the path to the optimal node (yellow star). The red and grey dots correspond to non-optimal feasible nodes and discarded nodes, respectively.

where $i \in \{0,1\}$. We note that constraint $\overline{\mathrm{C4}}$ contains both the transmission mode selection variables determined in the previous iterations and the undetermined binary optimization variables to be optimized in the future iterations, which makes (35) a non-convex optimization problem. By relaxing the undetermined binary $b_{s,t}$ to continuous optimization variables in $[0,1]$, we solve a relaxed version of (35) to obtain the optimal solution and the corresponding objective function value. Then, based on the optimal solution, we determine the rounded solution according to (33). Subsequently, we solve (31) by inserting the rounded solution and compute the corresponding objective function value. Based on these objective function values, we can respectively update the upper bound and lower bound in each iteration. In Figure 3, we provide an example for the BnB search tree for $T=2$ and $S_{\mathrm{R}}=2$. Firstly, the root node branches into two new nodes associated with $b_{s,t}=0$ and $b_{s,t}=1$. In each iteration, the search tree is expanded by adding two new nodes while it is pruned by discarding those nodes (grey dots) that are worse than the current upper bound. We note that the branching procedure is exhaustive due to the limited depth of the search tree and the finite number of nodes at each depth. As a result, the BnB algorithm always terminates within a finite number of iterations.

The BnB-based algorithm for optimally solving optimization problem (31) is summarized in **Algorithm 1**. In each iteration of the BnB-based algorithm, we denote the sets and the solutions associated with the two partitioned child nodes by subscripts l and r, respectively, to distinguish them from those associated with the parent node. The aforementioned set partitioning, node branching, and bound updating steps are repeatedly performed such that the difference between the lower bound and the upper bound of (31) decreases until it is less than a pre-defined error tolerance. It is known that BnB-based algorithms are guaranteed to converge to an $\varepsilon_{\mathrm{BnB}}$-optimal solution within a finite number of iterations [40], where $\varepsilon_{\mathrm{BnB}}$ is the maximum error tolerance. The proof of convergence for the adopted BnB algorithm follows directly from [45]. The developed BnB-based algorithm can serve as a performance benchmark for any suboptimal algorithm. However, the computational complexity of the BnB-based algorithm scales exponentially with the number of transmission modes and the number of tiles. To strike a balance between optimality and computational complexity, in the next subsection, we develop an SCA-based algorithm which determines a suboptimal solution of the considered optimization problem in (18) in polynomial time.[10]

Algorithm 1 BnB-Based Algorithm

1: Solve (32) to obtain optimal solution $(\widetilde{b}^*_{s,t})^{(1)}$ and compute lower bound $L^{(1)}=F_{\mathrm{L}}\big((\widetilde{b}^*_{s,t})^{(1)},(\mathbf{W}^*_k)^{(1)},(\mathbf{V}^*)^{(1)}\big)$. Compute the rounded binary solution $(\overline{b}_{s,t})^{(1)}$ according to (33) and obtain the corresponding upper bound $U^{(1)}=F_{\mathrm{U}}\big((\overline{b}_{s,t})^{(1)},(\mathbf{W}^{**}_k)^{(1)},(\mathbf{V}^{**})^{(1)}\big)$. Initialize the search tree $\mathcal{T}_{\mathrm{BnB}}$ by adding the root node associated with $\mathcal{B}^{(1)}$ and $(\widetilde{b}^*_{s,t})^{(1)}$. Set convergence tolerance $0<\varepsilon_{\mathrm{BnB}}\ll 1$ and iteration index $j=1$.
2: **repeat**
3: Select the node corresponding to the smallest lower bound $F_{\mathrm{L}}\big((\widetilde{b}^*_{s,t})^{(j)},(\mathbf{W}^*_k)^{(j)},(\mathbf{V}^*)^{(j)}\big)$
4: Partition the feasible set associated with the selected node into two subsets $(\mathcal{B}_{s^*,t^*})^{(j)}_l$ and $(\mathcal{B}_{s^*,t^*})^{(j)}_r$ according to (34)
5: Solve the relaxed version of the two subproblems $\mathcal{P}_0$ and $\mathcal{P}_1$ in (35) to obtain optimal solutions $(\widetilde{b}_{s^*,t^*}=0,\widetilde{b}^*_{s,t})^{(j)}_l$ and $(\widetilde{b}_{s^*,t^*}=1,\widetilde{b}^*_{s,t})^{(j)}_r$, $\forall s\in\mathcal{S}_{\mathrm{R}}\setminus\{s^*\}$, $t\in\mathcal{T}\setminus\{t^*\}$, and store the corresponding objective function values
6: Compute the rounded solutions based on $\Big\{(\widetilde{b}_{s^*,t^*}=0,\widetilde{b}^*_{s,t})^{(j)}_l,(\widetilde{b}_{s^*,t^*}=1,\widetilde{b}^*_{s,t})^{(j)}_r\Big\}$ and obtain $\Big\{(\overline{b}_{s,t})^{(j)}_l,(\overline{b}_{s,t})^{(j)}_r\Big\}$
7: Solve the problem in (31) based on $(\overline{b}_{s,t})^{(j)}_l$ and $(\overline{b}_{s,t})^{(j)}_r$ and store the corresponding objective function values
8: Expand the tree $\mathcal{T}_{\mathrm{BnB}}$ by adding the two new nodes associated with $(\mathcal{B}_{s^*,t^*})^{(j)}_l$ and $(\widetilde{b}_{s^*,t^*}=0,\widetilde{b}^*_{s,t})^{(j)}_l$ and $(\mathcal{B}_{s^*,t^*})^{(j)}_r$ and $(\widetilde{b}_{s^*,t^*}=1,\widetilde{b}^*_{s,t})^{(j)}_r$, respectively
9: Among all existing nodes in $\mathcal{T}_{\mathrm{BnB}}$, update $L^{(j)}$ and $U^{(j)}$ as the smallest upper bound $F_{\mathrm{U}}\big((\overline{b}_{s,t})^{(j)},(\mathbf{W}^{**}_k)^{(j)},(\mathbf{V}^{**})^{(j)}\big)$ and lower bound $F_{\mathrm{L}}\big((\widetilde{b}^*_{s,t})^{(j)},(\mathbf{W}^*_k)^{(j)},(\mathbf{V}^*)^{(j)}\big)$, respectively
10: Set $j=j+1$
11: **until** $\frac{U^{(j-1)}-L^{(j-1)}}{L^{(j-1)}}\leq\varepsilon_{\mathrm{BnB}}$
12: Output the optimal solution $(\overline{b}_{s,t})^{(j-1)}$ and the corresponding beamforming policy $\big((\mathbf{W}^{**}_k)^{(j-1)},(\mathbf{V}^{**})^{(j-1)}\big)$

C. Suboptimal Resource Allocation Scheme

We start with the non-convex optimization problem in (31). To facilitate efficient resource allocation algorithm design,

[10]We note that, in the literature, optimization problems involving coupled variables are often tackled by AO-based algorithms. However, AO-based algorithms cannot guarantee the joint optimality of the optimization variables and may get stuck in saddle points [46]. To preserve the joint optimality, we develop an SCA-based algorithm which is guaranteed to converge to a locally optimal solution of (18).

we first rewrite constraint C4 equivalently as follows:

$$\text{C4a: } \sum_{\substack{s\in\mathcal{S}_{\mathrm{R}},\\ t\in\widehat{\mathcal{T}}}} b_{s,t}-b_{s,t}^2\le 0 \text{ and C4b: } 0\le b_{s,t}\le 1,\quad \forall s,t. \tag{36}$$

We note that constraint C4a involves a difference of convex (d.c.) functions and hence is still non-convex with respect to $b_{s,t}$. To circumvent this obstacle, we employ the penalty method [47] and recast (31) as follows:

$$\begin{aligned}\underset{\substack{\mathbf{W}_k,\widehat{\mathbf{W}}_{k,s,t,p,q}\in\mathbb{H}^{N_{\mathrm{T}}},\\ \mathbf{V},\widehat{\mathbf{V}}_{s,t,p,q}\in\mathbb{H}^{N_{\mathrm{T}}},\\ b_{s,t},\beta_{s,t,p,q}}}{\text{minimize}}\ & \sum_{\substack{s\in\mathcal{S}_{\mathrm{R}},\\ t\in\widehat{\mathcal{T}}}}\sum_{\substack{p\in\mathcal{S}_{\mathrm{R}},\\ q\in\widehat{\mathcal{T}}}}\mathrm{Tr}\Bigg(\sum_{k\in\mathcal{K}}\widehat{\mathbf{W}}_{k,s,t,p,q}+\widehat{\mathbf{V}}_{s,t,p,q}\Bigg)\\ &+\chi\sum_{\substack{s\in\mathcal{S}_{\mathrm{R}},\\ t\in\widehat{\mathcal{T}}}}(b_{s,t}-b_{s,t}^2)\\ \text{s.t. }& \widehat{\mathrm{C1}},\widehat{\mathrm{C2}},\mathrm{C3},\mathrm{C4b},\mathrm{C5},\mathrm{C6a\text{-}C8d},\mathrm{C9},\end{aligned} \tag{37}$$

where $\chi\gg 0$ is a constant penalty factor which ensures that $b_{s,t}$ is binary. Next, we reveal the equivalence between problem (37) and problem (31) in the following theorem [47].

Theorem 2: Denote the optimal solution of problem (37) as $(b_{s,t})_i$ with penalty factor $\chi=\chi_i$. When χ_i is sufficiently large, i.e., $\chi=\chi_i\to\infty$, every limit point $(b_{s,t})$ of the sequence $\{(b_{s,t})_i\}$ is an optimal solution of problem (31).

Proof: The optimization problem in (37) has a similar structure as [48, Problem (27)] and Theorem 2 can be proved following the same steps as in [48, Appendix C]. Due to the limited space, we omit the detailed proof of Theorem 2 for brevity. ■

We note that the objective function of (37) is in the canonical form of a difference of convex programming problem, which facilitates the application of SCA. In particular, for a given feasible point $b_{s,t}^{(m)}$ found in the m-th iteration of the SCA procedure, we construct a global underestimator of $b_{s,t}^2$ as follows

$$b_{s,t}^2\ge 2b_{s,t}b_{s,t}^{(m)}-(b_{s,t}^{(m)})^2,\quad \forall s,t. \tag{38}$$

The optimization problem solved in the $(m+1)$-th iteration of the proposed algorithm is given by

$$\begin{aligned}\underset{\substack{\mathbf{W}_k,\widehat{\mathbf{W}}_{k,s,t,p,q}\in\mathbb{H}^{N_{\mathrm{T}}},\\ \mathbf{V},\widehat{\mathbf{V}}_{s,t,p,q}\in\mathbb{H}^{N_{\mathrm{T}}},\\ b_{s,t},\beta_{s,t,p,q}}}{\text{minimize}}\ & f(\mathbf{W}_k,\mathbf{V},b_{s,t})\\ \text{s.t. }& \widehat{\mathrm{C1}},\widehat{\mathrm{C2}},\mathrm{C3},\mathrm{C4b},\mathrm{C5\text{-}C9},\end{aligned} \tag{39}$$

where $f(\mathbf{W}_k,\mathbf{V},b_{s,t})$ is defined as

$$\begin{aligned}f(\mathbf{W}_k,\mathbf{V},b_{s,t})=&\sum_{\substack{s\in\mathcal{S}_{\mathrm{R}},\\ t\in\widehat{\mathcal{T}}}}\sum_{\substack{p\in\mathcal{S}_{\mathrm{R}},\\ q\in\widehat{\mathcal{T}}}}\mathrm{Tr}\left(\sum_{k\in\mathcal{K}}\widehat{\mathbf{W}}_{k,s,t,p,q}+\widehat{\mathbf{V}}_{s,t,p,q}\right)\\ &+\chi\sum_{\substack{s\in\mathcal{S}_{\mathrm{R}},\\ t\in\widehat{\mathcal{T}}}}\Big(b_{s,t}-2b_{s,t}b_{s,t}^{(m)}+(b_{s,t}^{(m)})^2\Big).\end{aligned} \tag{40}$$

We note that the only non-convex constraint in (39) is the unit-rank constraint C9. To overcome this, we omit constraint C9 by applying SDR. Following similar steps as in the Appendix, we can prove that the solution of the relaxed problem yields a rank-one beamforming matrix. As a result, the rank-relaxed version of (39) becomes a standard convex optimization problem which can be solved by convex program solvers such as CVX [44]. The overall algorithm is summarized in **Algorithm 2**. In each iteration of **Algorithm 2**, the objective function in (39) is monotonically decreasing. Moreover, as $\chi\to\infty$, the proposed algorithm asymptotically converges to a locally optimal solution of (31) in polynomial time.

Algorithm 2 SCA-Based Algorithm

1: Set initial point $\mathbf{W}_k^{(1)}$, $\mathbf{V}^{(1)}$, $\widehat{\mathbf{W}}_{k,s,t,p,q}^{(1)}$, $\widehat{\mathbf{V}}_{s,t,p,q}^{(1)}$, $b_{s,t}^{(1)}$, $\beta_{s,t,p,q}^{(1)}$, iteration index $m=1$, and convergence tolerance $0<\varepsilon_{\mathrm{SCA}}\ll 1$.
2: **repeat**
3: For given $\mathbf{W}_k^{(m)}$, $\mathbf{V}^{(m)}$, $\widehat{\mathbf{W}}_{k,s,t,p,q}^{(m)}$, $\widehat{\mathbf{V}}_{s,t,p,q}^{(m)}$, $b_{s,t}^{(m)}$, $\beta_{s,t,p,q}^{(m)}$ obtain an intermediate solution $\mathbf{W}_k^{(m+1)}$, $\mathbf{V}^{(m+1)}$, $\widehat{\mathbf{W}}_{k,s,t,p,q}^{(m+1)}$, $\widehat{\mathbf{V}}_{s,t,p,q}^{(m+1)}$, $b_{s,t}^{(m+1)}$, $\beta_{s,t,p,q}^{(m+1)}$ by solving the relaxed version of problem (39)
4: Set $m=m+1$
5: **until** $\frac{f(\mathbf{W}_k^{(m-1)},\mathbf{V}^{(m-1)},b_{s,t}^{(m-1)})-f(\mathbf{W}_k^{(m)},\mathbf{V}^{(m)},b_{s,t}^{(m)})}{f(\mathbf{W}_k^{(m)},\mathbf{V}^{(m)},b_{s,t}^{(m)})}\le\varepsilon_{\mathrm{SCA}}$

Remark 3: In the literature, the commonly adopted optimization framework for IRSs aims at jointly optimizing the continuous [49] or discrete [24] phase shifts of the IRS elements. Advanced algorithms based on AO [10], inner approximation (IA) [20], and SCA [21] have been developed to tackle the resulting IRS optimization problems. Nevertheless, the computational complexity of these algorithms is typically proportional to at least the cubic power of the number of IRS elements, i.e., M. Furthermore, since the number of served ERs and IRs is typically substantially smaller than the number of IRS elements, the overall computational complexity of resource allocation optimization algorithm is dominated by M. Moreover, for a large IRS-assisted system, the number of phase shift elements typically exceeds 500. Hence, the online element-wise IRS optimization design becomes prohibitive for practically large IRSs. In contrast, by adopting the proposed TT-based optimization framework and employing **Algorithm 2**, the computational complexity of IRS optimization scales with the number of tiles and the size of the refined transmission mode set specified in Section III-B, i.e., T and S_{R}, instead of the number of IRS elements M. In particular, the (worst case) per iteration computational complexity of **Algorithm 2** is given by $\mathcal{O}\Big((K+1)S_{\mathrm{R}}^2T^2N_{\mathrm{T}}^3+\big((K+1)S_{\mathrm{R}}^2T^2\big)^2N_{\mathrm{T}}^2+\big((K+1)S_{\mathrm{R}}^2T^2\big)^3\Big)$, where $\mathcal{O}(\cdot)$ is the big-O notation [50, Theorem 3.12]. Hence, by properly adjusting the number of tiles and the number of transmission modes, the computational complexity of the developed algorithm becomes affordable for the optimization of large IRSs.

V. Simulation Results

In this section, we evaluate the performance of the proposed resource allocation schemes via simulations.

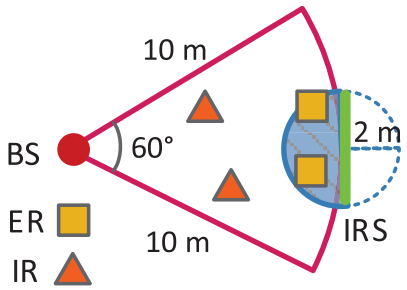

Fig. 4. Simulation setup for an IRS-assisted SWIPT system, which consists of $K = 2$ IRs and $J = 2$ ERs.

TABLE I
SIMULATION PARAMETERS

Carrier center frequency, f_c	2.4 GHz
Bandwidth, B	200 kHz
Min. required SINR at each IR, Γ_{req}	10 dB
Min. required energy at each ER, E_{req}	10 μW
BS antenna gain, G_i	10 dBi
EH parameters, a_j, c_j, ϱ_j	20, 6400, 0.003
Numbers of scatterers in each link	6
Noise power at receivers, $\sigma_{\mathrm{I}_k}^2$, $\sigma_{\mathrm{E}_j}^2$	-100 dBm
Convergence tolerance, $\varepsilon_{\mathrm{BnB}}$, $\varepsilon_{\mathrm{SCA}}$	10^{-2}
Penalty factor, χ	10^3

A. Simulation Setup

Figure 4 illustrates the schematic of the simulated multiuser MISO SWIPT system. We focus on the resource allocation algorithm design for one sector of a cell with a radius of 10 m. The BS is equipped with $N_{\mathrm{T}} = 8$ antennas, unless otherwise specified.[11] Unless specified otherwise, we assume that there are $K = 2$ IRs randomly and uniformly distributed in the considered SWIPT system. To enhance the system performance, we consider a rectangular IRS comprising $M = 600$ elements. The IRS is located at the edge of the sector and is 10 m away from the BS. There are $J = 2$ ERs randomly and uniformly distributed within the charging zone between the BS and the IRS, which is a semicircular area (blue area) with the IRS at its center and a radius of 2 m, cf. Figure 4. To facilitate computationally efficient resource allocation algorithm design, we partition the 600 IRS elements into T tiles of equal size, where each tile comprises $600/T$ phase shift elements. We jointly design the elements of each tile offline to generate a set of transmission modes. Following a similar approach as in [22, Section III-A], for all tiles, we generate a transmission mode set which is the product of a reflection codebook with 121 elements and a wavefront phase codebook with 2 elements.[12] Then, we employ the three mode pre-selection criteria proposed in Section III-B and obtain the corresponding refined transmission mode sets. For a fair comparison, we adjust parameters δ_1, $\delta_{2,r,i}$, and ω such that the refined transmission mode sets for all criteria have the same size S_{R}. In the following, unless otherwise specified, we pre-select the transmission modes based on Criterion 1. Moreover, we assume that the channel coefficients contained in $\mathbf{C}_{\mathrm{T}}$, $\mathbf{C}_{\mathrm{R}_k}$, and $\mathbf{C}_{\mathrm{D}_k}$ are impaired by free space path loss, shadowing, and Rayleigh fading. The path loss exponent is assumed to be 2 for all channels while the path loss at a reference distance of 1 m is set as $(\frac{c}{4\pi f_c})^2 = 40$ dB [48]. Assuming the direct links are severely shadowed, the shadowing attenuations are -30 dB and 0 dB for the direct links and the reflected links, respectively. The AoAs and AoDs at the BS and the IRS are uniformly distributed random variables and are generated as follows: the azimuth angles and polarizations of the incident signal are uniformly distributed in the interval $[0, 2\pi]$. The elevation angles of the IRS and the BS are uniformly distributed in the range of $[0, \pi/4]$ while the elevation angles of all users are uniformly distributed in the interval $[0, \pi]$. The simulation results shown in this section have been averaged over different channel realizations and the adopted parameter values are listed in Table I.

B. Baseline Schemes

To investigate the effectiveness of the algorithms developed in this paper, we consider three baseline schemes. For baseline scheme 1, a transmission mode is randomly chosen from the refined transmission mode set and is assigned to each tile while the BS adopts an isotropic radiation pattern for $\mathbf{V}$. Then, we optimize the beamforming vector $\mathbf{w}_k$ and the power allocated to the covariance matrix of the energy signal $\mathbf{V}$ for minimization of the total transmit power. For baseline scheme 2, the IRS employs random phase shifts. Then, we jointly optimize the beamforming vector $\mathbf{w}_k$ and the covariance matrix of the energy signal $\mathbf{V}$ for minimization of the BS total transmit power. For baseline scheme 3, for each tile, we select the transmission mode corresponding to the channel vector with the largest Euclidean norm directly from the offline transmission mode set, and the BS employs maximum ratio transmission with respect to the corresponding channel vector, i.e., $\mathbf{w}_k = \frac{\sqrt{p_k}\mathbf{h}_{\mathrm{I},k}}{\|\mathbf{h}_{\mathrm{I},k}\|_2}$, where p_k is the power allocated to IR k. Then, the transmit power at the BS is minimized by optimizing the power allocated to each IR and the covariance matrix of the energy signal.

C. Convergence of the Proposed Algorithms

In Figure 5, we investigate the convergence behavior of the proposed algorithms for different IRS models. For $T = 3$ and $S_{\mathrm{R}} = 8$, we observe that the upper bound and lower bound of the proposed optimal scheme monotonically converge to the same objective function value confirming the optimality of the proposed optimal scheme. Yet, the average number of iterations needed for achieving convergence is around 1,000. This is due to the fact that the computational complexity of the proposed optimal algorithm increases exponentially with T and S_{R}. Moreover, Figure 5 also confirms that the proposed

[11] In general, the maximum number of IRs and ERs that can be served depends on the number of the antennas at the BS. As a result, throughout this section, we set $K + J \leq N_{\mathrm{T}}$ such that the QoS of the IRs and ERs can be guaranteed.

[12] The reflection codebook enables the tile to reflect an incident signal with the desired phase shift, while the wavefront phase codebook facilitates the combination of the signals that arrive from different tiles at the receivers in a constructive or destructive manner.

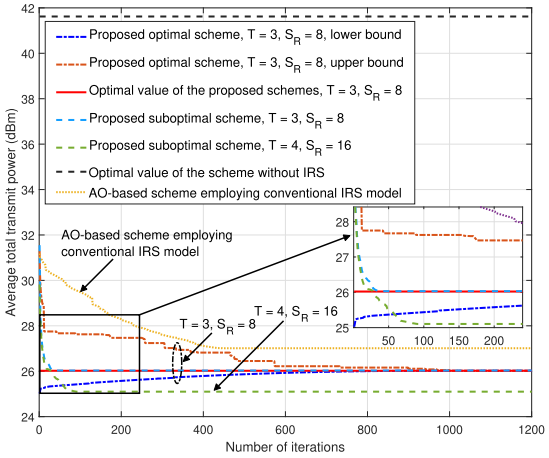

Fig. 5. Convergence behavior of different algorithms for $K = J = 2$, $N_{\mathrm{T}} = 10$, $\varepsilon_{\mathrm{BnB}} = 10^{-4}$, $\varepsilon_{\mathrm{SCA}} = 10^{-4}$, $\Gamma_{\mathrm{req}} = 10$ dB, and $E_{\mathrm{req}} = 5$ μW.

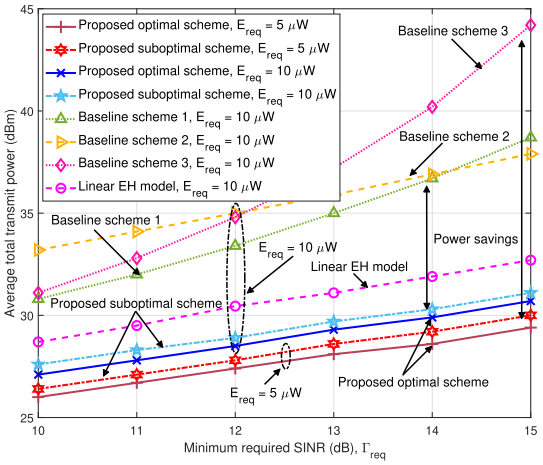

Fig. 6. Average total transmit power (dBm) versus minimum required SINR at IRs for different schemes with $K = J = 2$, $N_{\mathrm{T}} = 8$, $T = 3$, and $S_{\mathrm{R}} = 8$.

suboptimal scheme achieves a close-to-optimal performance while enjoying a polynomial time computational complexity. For the suboptimal scheme, we also consider an IRS with $T = 4$ and $S_{\mathrm{R}} = 16$. As we increase the number of tiles and enlarge the size of the refined transmission mode set (from $T = 3$ and $S_{\mathrm{R}} = 8$ to $T = 4$ and $S_{\mathrm{R}} = 16$), the total transmit power required for the proposed suboptimal scheme is reduced by roughly 1 dB. Correspondingly, the suboptimal scheme requires approximately 40 additional iterations to converge for $T = 4$ and $S_{\mathrm{R}} = 16$ compared to $T = 3$ and $S_{\mathrm{R}} = 8$. This confirms that by reconfiguring the tiles and resizing the refined transmission mode set, we can flexibly adjust the trade-off between system performance and the number of iterations required for convergence which is desirable in practice. On the other hand, we also investigate the performance of an AO-based scheme employing the conventional IRS model. In particular, we apply the AO-based algorithm reported in [48] to jointly optimize the phase shifts of all IRS elements and the transmit beamformers for minimization of the BS transmit power under the same QoS requirements for the ERs and IRs as for the proposed schemes. As can be seen from Figure 5, for the considered large IRS with 600 elements, the AO-based algorithm for the conventional IRS model requires more than 400 iterations to converge which is substantially more than the proposed suboptimal algorithm. This is due to the fact that by adopting the element-wise optimization framework, the search space of the AO-based algorithm scales with the large number of phase shift elements. Meanwhile, we also observe that the AO-based algorithm for the conventional IRS model leads to a higher power consumption (roughly 1 dB) compared to the proposed schemes with $T = 3$ and $S_{\mathrm{R}} = 8$. The reason behind this is two-fold. First, the conventional IRS model over-optimistically assumes a unit gain for the reflected signal, which neither takes into account the limited number of scatterers nor captures the impact of the physical characteristics of the IRS channels, e.g., the incident and reflected angles and the polarization of the waves. As a result, the conventional IRS model may not be able to efficiently enhance the propagation conditions of practical low-rank channels induced by a limited number of scatterers. Second, the AO-based algorithm converges only to a stationary point [46] while our proposed suboptimal algorithm yields a close-to-optimal performance. For comparison, we also show the performance of a conventional SWIPT system without IRS. In this case, the beamforming vectors and the covariance matrix of the energy signal are jointly designed for minimization of the total transmit power. As can be seen from Figure 5, this scheme requires a significantly higher transmit power compared to the proposed optimal and suboptimal schemes (roughly 16 dB more). This indicates that IRSs are indeed a powerful tool to enhance the performance of SWIPT systems. Furthermore, for the parameters adopted in Figure 5, in Table II, we provide the average runtime needed for convergence[13] of the proposed optimal and suboptimal schemes as well as the AO-based scheme. To facilitate the presentation, we normalize the average convergence runtime of the proposed optimal and suboptimal schemes with respect to that of the commonly adopted AO-based scheme. As can be observed from Table II, the AO-based scheme, which is based on the conventional IRS model, requires a significantly longer runtime compared to the proposed schemes, which are based on the physics-based IRS model, indicating a higher complexity and slower convergence. Moreover, by tuning T and S_{R}, the convergence runtime of the proposed schemes can be adjusted, which facilitates the efficient online optimization for the design of practically large IRSs.

D. Total Transmit Power Versus Minimum Required SINR

In Figure 6, we investigate the average total transmit power versus the minimum required SINR, $\Gamma_{\mathrm{req}} = \Gamma_{\mathrm{req}_k}$, $\forall k$, at the IRs for different resource allocation schemes. Since the AO-based scheme employing the conventional IRS model has a prohibitively high complexity for the considered large IRS and worse performance compared to our proposed schemes, we do not consider it in Figure 6. We can observe from

[13]These simulations were carried out on a computer equipped with an Intel Core i7-3770 processor with a base frequency of 3.40 GHz.

TABLE II
COMPARISON OF THE AVERAGE CONVERGENCE RUNTIME RATIO OF DIFFERENT SCHEMES

Scheme	Avg. runtime ratio (%)
Proposed optimal scheme with $T = 3$ and $S_{\mathrm{R}} = 8$	32.6
Proposed suboptimal scheme with $T = 3$ and $S_{\mathrm{R}} = 8$	2.3
Proposed suboptimal scheme with $T = 4$ and $S_{\mathrm{R}} = 16$	11.9
AO-based scheme for conventional IRS model with $M = 600$	100

Figure 6 that the required total transmit powers of the proposed optimal and suboptimal schemes as well as the three baseline schemes grow with Γ_{req}. This is attributed to the fact that to satisfy a more stringent minimum SINR requirement, Γ_{req}, the BS has to transmit with higher power. However, the proposed optimal and suboptimal schemes achieve significant power savings compared with the three baseline schemes. This reveals the effectiveness of the proposed schemes in jointly optimizing the beamforming vectors and the transmission mode selection. Besides, we observe that for a smaller E_{req}, the total transmit power for the proposed optimal and suboptimal schemes decreases. This is due to the fact that the BS has to allocate less power to the energy signal when the minimum EH requirement is less stringent. Moreover, we also show results for a scheme that is based on the overly-simplified linear EH model for the ERs. In particular, in this case, we solve a problem similar to (18) except that the harvested energy is assumed to be linearly proportional to the received RF power. Then, we take the obtained solution back into the actual system with non-linear EH and check if the QoS requirement of the ERs is satisfied. If the obtained solution is infeasible, we increase the transmit power until constraint C2 in (18) is fulfilled. As can be observed from Figure 6, to satisfy the QoS requirement of the ERs, the scheme based on the linear EH model consumes more power than the proposed schemes which are based on the non-linear EH model. This is due to the fact that in systems with practical non-linear EH circuits, the beamforming policy optimized for the linear EH model causes some mismatch and underutilization of resources.

E. Total Transmit Power Versus Size of Refined Transmission Mode Set

Figure 7 depicts the average total transmit power versus the size of the refined transmission mode set, S_{R}, for different resource allocation schemes. By adjusting parameter δ_1 in Criterion 1, we select more transmission modes and increase the size of the refined transmission mode set as desired. As can be seen from the figure, the average total transmit powers of the proposed optimal and suboptimal schemes decrease with the size of the refined transmission mode set, i.e., S_{R}. This is due to the fact that as S_{R} grows, additional transmission modes are included in the refined transmission mode set, which can be exploited for customizing a more favorable wireless channel and to potentially reduce the BS transmit power at the expense of a higher computational complexity. We note that for practical IRSs (usually comprising more than 500 phase shift elements), algorithms developed under the conventional element-wise optimization framework,

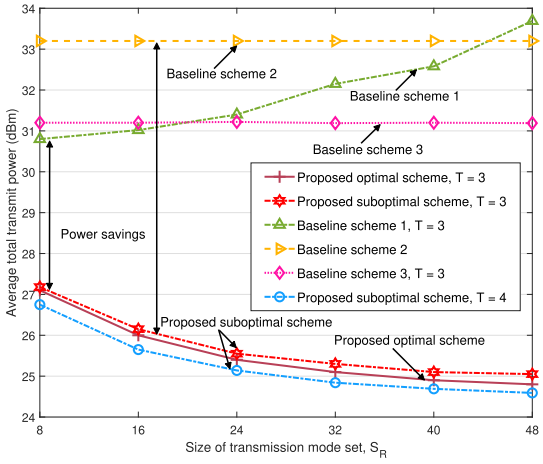

Fig. 7. Average total transmit power (dBm) versus the size of the refined transmission mode set for different schemes with $K = J = 2$, $N_{\mathrm{T}} = 8$, $\Gamma_{\mathrm{req}} = 10$ dB, and $E_{\mathrm{req}} = 10$ μW.

e.g., AO and IA, become prohibitively complex, while the values of T and S_{R} for the proposed scheme can still be properly chosen to allow for efficient online optimization. Moreover, unlike the proposed optimal and suboptimal schemes, the average total transmit power of baseline scheme 1 dramatically increases with S_{R}. In fact, as the refined transmission mode set becomes larger, the random transmission mode selection in baseline scheme 1 is more likely to choose a transmission mode yielding a small effective channel gain, which potentially degrades the received power of the desired signal. As a result, the BS has to consume more power to satisfy the QoS requirements of the receivers. In contrast, the average total transmit powers of baseline schemes 2 and 3 are almost independent of S_{R}. Yet, the reasons behind this are rather different. In particular, instead of selecting a predefined transmission mode, baseline scheme 2 applies an IRS with randomly generated phase shifts. Hence, the performance of baseline scheme 2 does not depend on the size of the refined transmission mode set. As for baseline scheme 3, the transmission mode selection strategy is based on the offline transmission mode set and identical for all tiles regardless of the size of the refined transmission mode set.

F. Total Transmit Power Versus Number of Receivers

In Figure 8, we study the average total transmit power versus the number of IRs, K, for different resource allocation schemes. For ease of presentation, we focus on the proposed suboptimal scheme as it closely approaches the performance of the proposed optimal scheme but entails a much lower

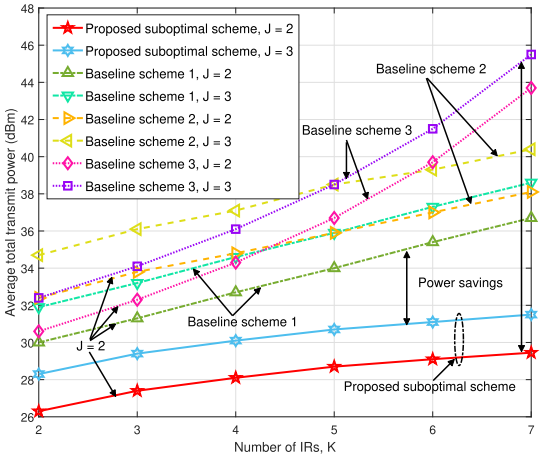

Fig. 8. Average total transmit power (dBm) versus the number of IRs for different schemes with $N_{\mathrm{T}} = 10$, $T = 3$, $S_{\mathrm{R}} = 8$, $\Gamma_{\mathrm{req}} = 10$ dB, and $E_{\mathrm{req}} = 10$ μW.

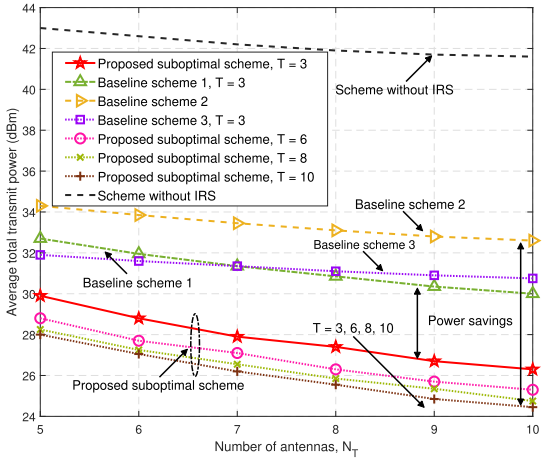

Fig. 9. Average total transmit power (dBm) versus the number of antennas for different schemes with $K = J = 2$, $S_{\mathrm{R}} = 8$, $\Gamma_{\mathrm{req}} = 10$ dB, and $E_{\mathrm{req}} = 10$ μW.

computational complexity. As expected, the total transmit power increases with the number of receivers. The reason for this is two-fold. First, to meet the additional minimum SINR and EH requirements introduced by the additional receivers, a higher transmit power at the BS is necessary. Secondly, as the number of receivers increases, the BS has to dedicate more degrees of freedom (DoFs) to effectively managing the more severe multiuser interference such that the BS is less capable of reducing the total transmit power. Moreover, we observe that the average total transmit powers for all considered baseline schemes are substantially higher than that of the proposed suboptimal scheme. In particular, baseline scheme 1 yields a much higher power consumption compared to the proposed scheme due to the randomly selected transmission mode and the fixed energy signal radiation pattern. As for baseline scheme 2, due to the random phase shift pattern of the IRS, the DoFs offered by the IRS cannot be fully exploited for establishing a beneficial radio propagation environment to facilitate power-efficient resource allocation. As for baseline scheme 3, since the transmission modes for all tiles are identical and the beamforming policy is partially fixed, performance is sacrificed in exchange for a simpler implementation.

G. Total Transmit Power Versus Number of Antennas

Figure 9 illustrates the average total transmit power versus the number of antennas at the BS, N_{T}, for different resource allocation schemes. It is expected that the average total transmit power decreases as the number of antennas grows since additional DoFs can be exploited for beamforming design when more antennas are available at the BS. Moreover, compared with the three baseline schemes, the proposed suboptimal scheme provides substantial power savings due to its ability to fully utilize the resources available in the system. On the other hand, we also study the impact of the numbers of tiles on performance. As can be seen from Figure 9, the proposed suboptimal scheme consumes less power when the IRS is divided into more tiles. Yet, as we further increase T from 8 to 10, the power reduction becomes marginal (approximately 0.2 dB). In fact, a small number of tiles is sufficient to preserve most of the maximum possible performance gain enabled by the IRS. In other words, for large IRS, it is not necessary nor computationally efficient to jointly optimize all phase shift elements, as is done in the conventional element-wise optimization framework adopted in the literature. Furthermore, we also show the performance of a system without IRS. The average total transmit power of this system also decreases with increasing numbers of transmit antennas. This is due to the fact that the BS can exploit the additional DoFs introduced by the extra antennas to facilitate a more precise beamforming. On the other hand, compared with the IRS-assisted system, the system without IRS requires a significantly higher transmit power as it cannot benefit from the significant passive beamforming gain offered by the IRS. This confirms the effectiveness of deploying IRSs to enhance the performance of SWIPT systems.

H. Impact of Transmission Mode Pre-Selection

Figure 10 illustrates the average total transmit power versus the weight factor of Criterion 3 for transmission mode pre-selection. We observe that the average total transmit power for the proposed suboptimal scheme employing Criterion 3 first decreases with weight factor ω ($1 \leq \omega \leq 4$). Specifically, as the weight factor increases, more transmission modes that favor the effective channel vectors of the ERs, i.e., $\|\mathbf{h}_{\mathrm{E},j,s,t}\|_2$, are included in the refined transmission mode set. Also, in typical SWIPT systems, the ERs usually require much higher received powers compared to the IRs. As a result, refined transmission mode sets constructed with larger ω enable the configuration of wireless propagation environments that are more favorable for the ERs, which potentially results in power savings. Yet, as we further increase ω, the power consumption of the BS starts to increase. This is due to the fact that very large weight factors ($\omega > 4$) lead to the construction of severely biased transmission mode sets that are favorable for the ERs but lead to poor channel conditions for the IRs. Hence, the BS is forced to consume more power to

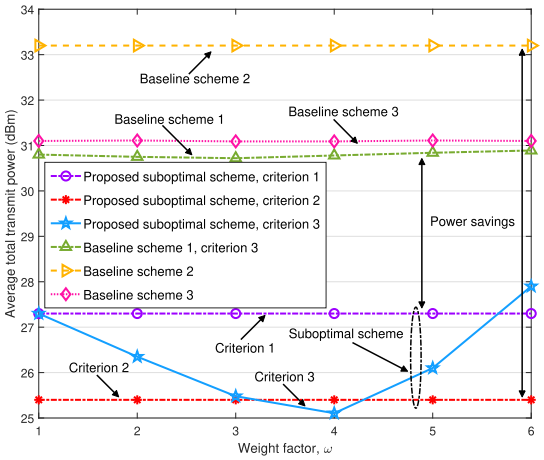

Fig. 10. Average total transmit power (dBm) versus the weight factor of Criterion 3 for different schemes with $K = J = 2$, $N_{\mathrm{T}} = 8$, $T = 3$, $S_{\mathrm{R}} = 8$, $\Gamma_{\mathrm{req}} = 10$ dB, and $E_{\mathrm{req}} = 10$ μW.

compensate for the severe signal attenuation, which outweighs the power gain resulting from customizing favorable channels for the ERs. In contrast, though also employing Criterion 3 to refine the transmission mode set, baseline scheme 1 is not sensitive to ω. This is due to the fact that its transmission mode selection policy is fixed instead of being optimized over the refined transmission mode set. On the other hand, we also show the performance of the proposed suboptimal scheme employing transmission mode pre-selection Criteria 2 and 3, which do not depend on ω. In particular, Criterion 2 leads to a lower transmit power compared to Criterion 1. In fact, since Criterion 1 only focuses on the magnitude of the channel, it may construct a biased transmission mode set when one receiver enjoys much better channel conditions than the other receivers. In this case, the BS is forced to increase the transmit power to satisfy the QoS requirements of the receivers with poor channel conditions. On the contrary, Criterion 2 generates individual transmission mode sets for all receivers and promotes a wireless propagation environment that is favorable for all receivers, which potentially leads to less transmit power consumption compared with Criterion 1.

VI. Conclusion

In this paper, we studied the resource allocation algorithm design for large IRS-assisted SWIPT systems. Compared with existing works assuming an overly simplified system model, we adopted a physics-based IRS model and a non-linear EH model which can better capture the properties of practical IRS-assisted SWIPT systems. To facilitate the efficient system design for large IRSs, we partition the IRS into several tiles and adopt a TT-based optimization framework which comprises an offline transmission mode set design stage and an online optimization stage. To further reduce the computational complexity of IRS online design, we proposed two new transmission mode pre-selection criteria. Given the refined transmission mode set, we focused on the joint online optimization of the transmit beamforming vectors, the covariance matrix of the energy signal, and the transmission mode selection for minimization of the BS transmit power while satisfying the QoS requirements of the IRs and the ERs. To tackle the formulated combinatorial optimization problem, we first proposed a BnB-based optimization algorithm which yields the globally optimal solution of the considered optimization problem. Since the optimal scheme entails a high computational complexity, we also developed a computationally efficient SCA-based algorithm which asymptotically converges to a locally optimal solution. Simulation results showed that the proposed schemes do not only yield considerable power savings compared with three baseline schemes but also allow us to flexibly strike a balance between system performance and computational complexity by adjusting the number of tiles and transmission modes. Moreover, the adopted physics-based IRS model can effectively leverage the wave AoA and AoD and polarization that are not explicitly modeled by the conventional IRS model. Furthermore, in combination with the physics-based IRS model, the proposed TT-based framework was shown to be crucial for realizing real-time online design of wireless systems assisted by large IRS.

Appendix

To start with, we rewrite the relaxed version of problem (32) equivalently as follows:

$$\begin{aligned}
&\underset{\substack{\mathbf{W}_k,\widetilde{\mathbf{W}}_{k,s,t,p,q}\in\mathbb{H}^{N_{\mathrm{T}}},\\ \mathbf{V},\widetilde{\mathbf{V}}_{s,t,p,q}\in\mathbb{H}^{N_{\mathrm{T}}},\\ \widetilde{b}_{s,t},\widetilde{\beta}_{s,t,p,q},\theta_j}}{\text{minimize}} \ \sum_{\substack{s\in\mathcal{S}_{\mathrm{R}},\\ t\in\widehat{\mathcal{T}}}}\sum_{\substack{p\in\mathcal{S}_{\mathrm{R}},\\ q\in\widehat{\mathcal{T}}}} \mathrm{Tr}\Bigg(\sum_{k\in\mathcal{K}}\widetilde{\mathbf{W}}_{k,s,t,p,q}+\widetilde{\mathbf{V}}_{s,t,p,q}\Bigg)\\
&\quad \text{s.t. } \widetilde{\mathrm{C1}}, \mathrm{C3}, \widetilde{\mathrm{C4}}, \widetilde{\mathrm{C5}}, \widetilde{\mathrm{C6a}}\text{-}\widetilde{\mathrm{C6d}}, \widetilde{\mathrm{C7a}}\text{-}\widetilde{\mathrm{C7d}}, \widetilde{\mathrm{C8a}}\text{-}\widetilde{\mathrm{C8d}},\\
&\qquad \widetilde{\mathrm{C2a}}\text{: } C_{\mathrm{req}_j} \geq \exp\left(-\varrho_j\theta_j\right), \quad \forall j,\\
&\qquad \widetilde{\mathrm{C2b}}\text{: } \theta_j \geq \sum_{\substack{s\in\mathcal{S}_{\mathrm{R}},\\ t\in\widehat{\mathcal{T}}}}\sum_{\substack{p\in\mathcal{S}_{\mathrm{R}},\\ q\in\widehat{\mathcal{T}}}} \mathrm{Tr}\Big(\mathbf{g}_{p,q,j}\mathbf{g}_{s,t,j}^H\big(\sum_{k\in\mathcal{K}}\widetilde{\mathbf{W}}_{k,s,t,p,q}\\
&\qquad\qquad + \widetilde{\mathbf{V}}_{s,t,p,q}\big)\Big), \quad \forall j. \qquad (41)
\end{aligned}$$

Note that the optimization problem in (41) is jointly convex with respect to the optimization variables and satisfies Slater's constraint qualification. Thus, strong duality holds for (41). Moreover, since $\widetilde{\mathbf{W}}_{k,s,t,p,q} = \widetilde{\beta}_{s,t,p,q}\mathbf{W}_k$ always holds, we express the Lagrangian function of (41) in terms of $\mathbf{W}_k$ as follows

$$\begin{aligned}
\mathcal{L} = \sum_{k\in\mathcal{K}}\Big(&\mathrm{Tr}\Big(\sum_{\substack{s,p\in\mathcal{S}_{\mathrm{R}},\\ q,t\in\widehat{\mathcal{T}}}}\widetilde{\beta}_{s,t,p,q}\mathbf{W}_k\Big)\\
&+\mathrm{Tr}\Big(\sum_{\substack{s,p\in\mathcal{S}_{\mathrm{R}},\\ q,t\in\widehat{\mathcal{T}}}}\widetilde{\beta}_{s,t,p,q}\mathbf{U}_{k,s,t,p,q}\mathbf{W}_k\Big)\\
&-\eta_k\mathrm{Tr}\Big(\sum_{\substack{s,p\in\mathcal{S}_{\mathrm{R}},\\ q,t\in\widehat{\mathcal{T}}}}\widetilde{\beta}_{s,t,p,q}\mathbf{h}_{\mathrm{I},k,p,q}\mathbf{h}_{\mathrm{I},k,s,t}^H\mathbf{W}_k\Big)\\
&-\mathrm{Tr}\Big(\sum_{\substack{s,p\in\mathcal{S}_{\mathrm{R}},\\ q,t\in\widehat{\mathcal{T}}}}\widetilde{\beta}_{s,t,p,q}\mathbf{Z}_{k,s,t,p,q}\mathbf{W}_k\Big)\\
&+\sum_{\substack{s,p\in\mathcal{S}_{\mathrm{R}},\\ q,t\in\widehat{\mathcal{T}}}}(1-\widetilde{\beta}_{s,t,p,q})\mathrm{Tr}(\mathbf{X}_{k,s,t,p,q}\mathbf{W}_k)
\end{aligned}$$

$$
\begin{aligned}
&- \sum_{\substack{s,p\in\mathcal{S}_{\mathrm{R}},\\ q,t\in\widehat{\mathcal{T}}}} (1-\widetilde{\beta}_{s,t,p,q})\mathrm{Tr}(\mathbf{Y}_{k,s,t,p,q}\mathbf{W}_k)\\
&+\eta_k\Gamma_k^{\mathrm{req}} \sum_{r\in\mathcal{K}\setminus\{k\}} \mathrm{Tr}\Big(\sum_{\substack{s,p\in\mathcal{S}_{\mathrm{R}},\\ q,t\in\widehat{\mathcal{T}}}} \widetilde{\beta}_{s,t,p,q}\mathbf{h}_{\mathrm{I},k,p,q}\mathbf{h}_{\mathrm{I},k,s,t}^H\mathbf{W}_k\Big)\\
&+\sum_{j\in\mathcal{J}}\zeta_j\mathrm{Tr}\Big(\sum_{\substack{s,p\in\mathcal{S}_{\mathrm{R}},\\ q,t\in\widehat{\mathcal{T}}}} \widetilde{\beta}_{s,t,p,q}\mathbf{h}_{\mathrm{E},j,p,q}\mathbf{h}_{\mathrm{E},j,s,t}^H\mathbf{W}_k\Big)\Big)+\Phi.
\end{aligned}
\tag{42}
$$

Here, Φ comprises the terms that do not involve $\mathbf{W}_k$. The scalar Lagrange multipliers η_k and $\zeta_j \geq 0$ are associated with constraint $\widetilde{\mathrm{C1}}$ and $\widetilde{\mathrm{C2b}}$, respectively. The positive semidefinite Lagrange multiplier matrices $\mathbf{U}_{k,s,t,p,q}$, $\mathbf{X}_{k,s,t,p,q}$, $\mathbf{Y}_{k,s,t,p,q}$, and $\mathbf{Z}_{k,s,t,p,q} \in \mathbb{C}^{N_{\mathrm{T}}\times N_{\mathrm{T}}}$ are associated with constraints $\widetilde{\mathrm{C7a}}$, $\widetilde{\mathrm{C7b}}$, $\widetilde{\mathrm{C7c}}$, and $\widetilde{\mathrm{C7d}}$. Note that there always exist $\widetilde{\beta}^*_{s,t,p,q} > 0$. Next, by examining the KKT conditions with respect to $\mathbf{W}_k$, we investigate the structure of the optimal beamforming matrix. In particular, we have

$$
\begin{aligned}
&\mathrm{K1}: \ \eta_k^*, \zeta_j^* \geq 0,\\
&\qquad \mathbf{U}_{k,s,t,p,q}^*, \mathbf{X}_{k,s,t,p,q}^*, \mathbf{Y}_{k,s,t,p,q}^*, \mathbf{Z}_{k,s,t,p,q}^* \succeq \mathbf{0}, \qquad (43)\\
&\mathrm{K2}: \sum_{\substack{s\in\mathcal{S}_{\mathrm{R}},p\in\mathcal{S}_{\mathrm{R}},\\ t\in\widehat{\mathcal{T}} \quad q\in\widehat{\mathcal{T}}}} \widetilde{\beta}^*_{s,t,p,q}\mathbf{Z}^*_{k,s,t,p,q}\mathbf{W}_k^* = \mathbf{0}, \qquad (44)\\
&\mathrm{K3}: \ \nabla_{\mathbf{W}_k}\mathcal{L}(\mathbf{W}_k^*) = \mathbf{0}, \qquad (45)
\end{aligned}
$$

where η_k^*, ζ_j^*, $\mathbf{U}^*_{k,s,t,p,q}$, $\mathbf{X}^*_{k,s,t,p,q}$, $\mathbf{Y}^*_{k,s,t,p,q}$, and $\mathbf{Z}^*_{k,s,t,p,q}$ are the optimal values corresponding to $\mathbf{W}_k^*$ and $\widetilde{\beta}^*_{s,t,p,q}$. Note that $\widetilde{\beta}^*_{s,t,p,q} \geq 0$, $\mathbf{W}_k^* \succeq \mathbf{0}$, and $\mathbf{Z}^*_{k,s,t,p,q} \succeq \mathbf{0}$, and we have $\widetilde{\beta}^*_{s,t,p,q}\mathbf{Z}^*_{k,s,t,p,q}\mathbf{W}_k^* = \mathbf{0}$. Then, assuming $\widetilde{\beta}^*_{s^\circ,t^\circ,p^\circ,q^\circ} = 1$, we explicitly write $\nabla_{\mathbf{W}_k}\mathcal{L}(\mathbf{W}_k^*)$ in K3 as follows

$$
\mathbf{Z}^*_{k,s^\circ,t^\circ,p^\circ,q^\circ} = \sum_{s\in\mathcal{S}_{\mathrm{R}},t\in\widehat{\mathcal{T}}} \sum_{p\in\mathcal{S}_{\mathrm{R}},q\in\widehat{\mathcal{T}}} \widetilde{\beta}^*_{s,t,p,q}\mathbf{I}_{N_{\mathrm{T}}} - \mathbf{\Delta}_k^*, \tag{46}
$$

where $\mathbf{\Delta}_k^*$ is given by

$$
\begin{aligned}
\mathbf{\Delta}_k^* = &\sum_{\substack{s,p\in\mathcal{S}_{\mathrm{R}},\\ q,t\in\widehat{\mathcal{T}}}} \widetilde{\beta}^*_{s,t,p,q}\Big(\eta_k^*\mathbf{h}_{\mathrm{I},k,p,q}\mathbf{h}_{\mathrm{I},k,s,t}^H\\
&-\widetilde{\beta}^*_{s,t,p,q}\sum_{r\in\mathcal{K}\setminus\{k\}}\eta_r^*\Gamma_r^{\mathrm{req}}\mathbf{h}_{\mathrm{I},r,p,q}\mathbf{h}_{\mathrm{I},r,s,t}^H\\
&-\widetilde{\beta}^*_{s,t,p,q}\sum_{j\in\mathcal{J}}\zeta_j^*\mathbf{h}_{\mathrm{E},j,p,q}\mathbf{h}_{\mathrm{E},j,s,t}^H - \widetilde{\beta}^*_{s,t,p,q}\mathbf{U}^*_{k,s,t,p,q}\\
&+(1-\widetilde{\beta}^*_{s,t,p,q})\big(\mathbf{Y}^*_{k,s,t,p,q}-\mathbf{X}^*_{k,s,t,p,q}\big)\Big)\\
&+\sum_{\substack{s\in\mathcal{S}_{\mathrm{R}}\setminus\{s^\circ\},p\in\mathcal{S}_{\mathrm{R}}\setminus\{p^\circ\},\\ t\in\widehat{\mathcal{T}}\setminus\{t^\circ\} \quad q\in\widehat{\mathcal{T}}\setminus\{q^\circ\}}} \sum \widetilde{\beta}^*_{s,t,p,q}\mathbf{Z}^*_{k,s,t,p,q}.
\end{aligned}
\tag{47}
$$

Then, using similar arguments as in [51, Appendix A], it can be shown that $\mathbf{Z}^*_{k,s^\circ,t^\circ,p^\circ,q^\circ}$ in (46) satisfies $\mathrm{Rank}(\mathbf{Z}^*_{k,s^\circ,t^\circ,p^\circ,q^\circ}) \geq N_{\mathrm{T}} - 1$. Recalling $\mathbf{Z}^*_{k,s^\circ,t^\circ,p^\circ,q^\circ}\mathbf{W}_k^* = \mathbf{0}$, for each IR k, we can always obtain an optimal $\mathbf{W}_k^*$ with a unit rank. This completes the proof.

REFERENCES

[1] D. Xu, X. Yu, V. Jamali, D. W. K. Ng, and R. Schober, "Resource allocation for large IRS-assisted SWIPT systems with non-linear energy harvesting model," in *Proc. IEEE Wireless Commun. Netw. Conf. (WCNC)*, Mar. 2021, pp. 1–7.

[2] V. W. Wong, R. Schober, D. W. K. Ng, and L.-C. Wang, *Key Technologies for 5G Wireless Systems*. Cambridge, U.K.: Cambridge Univ. Press, 2017.

[3] D. W. K. Ng, E. S. Lo, and R. Schober, "Robust beamforming for secure communication in systems with wireless information and power transfer," *IEEE Trans. Wireless Commun.*, vol. 13, no. 8, pp. 4599–4615, Aug. 2014.

[4] C. Huang *et al.*, "Holographic MIMO surfaces for 6G wireless networks: Opportunities, challenges, and trends," *IEEE Wireless Commun.*, vol. 27, no. 5, pp. 118–125, Oct. 2020.

[5] C. Pan *et al.*, "Reconfigurable intelligent surfaces for 6G systems: Principles, applications, and research directions," 2020, *arXiv:2011.04300*.

[6] Q. Wu and R. Zhang, "Towards smart and reconfigurable environment: Intelligent reflecting surface aided wireless network," *IEEE Commun. Mag.*, vol. 58, no. 1, pp. 106–112, Jan. 2020.

[7] M. D. Renzo *et al.*, "Smart radio environments empowered by reconfigurable intelligent surfaces: How it works, state of research, and the road ahead," *IEEE J. Sel. Areas Commun.*, vol. 38, no. 11, pp. 2450–2525, Nov. 2020.

[8] T. J. Cui, M. Q. Qi, X. Wan, J. Zhao, and Q. Cheng, "Coding metamaterials, digital metamaterials and programmable metamaterials," *Light, Sci. Appl.*, vol. 3, no. 10, p. e218, Oct. 2014.

[9] Q. Wu and R. Zhang, "Joint active and passive beamforming optimization for intelligent reflecting surface assisted SWIPT under QoS constraints," *IEEE J. Sel. Areas Commun.*, vol. 38, no. 8, pp. 1735–1748, Aug. 2020.

[10] C. Pan *et al.*, "Intelligent reflecting surface aided MIMO broadcasting for simultaneous wireless information and power transfer," *IEEE J. Sel. Areas Commun.*, vol. 38, no. 8, pp. 1719–1734, Aug. 2020.

[11] W. Sun, Q. Song, L. Guo, and J. Zhao, "Secrecy rate maximization for intelligent reflecting surface aided SWIPT systems," in *Proc. IEEE/CIC Int. Conf. Commun. China (ICCC)*, Aug. 2020, pp. 1–6.

[12] C. R. Valenta and G. D. Durgin, "Harvesting wireless power: Survey of energy-harvester conversion efficiency in far-field, wireless power transfer systems," *IEEE Microw. Mag.*, vol. 15, no. 4, pp. 108–120, Jun. 2014.

[13] T. Le, K. Mayaram, and T. Fiez, "Efficient far-field radio frequency energy harvesting for passively powered sensor networks," *IEEE J. Solid-State Circuits*, vol. 43, no. 5, pp. 1287–1302, May 2008.

[14] Q. Ma and T. J. Cui, "Information metamaterials: Bridging the physical world and digital world," *PhotoniX*, vol. 1, no. 1, pp. 1–32, Dec. 2020.

[15] X. Pei *et al.*, "RIS-aided wireless communications: Prototyping, adaptive beamforming, and indoor/outdoor field trials," *IEEE Trans. Commun.*, vol. 69, no. 12, pp. 8627–8640, Dec. 2021.

[16] X. Wan *et al.*, "Reconfigurable sum and difference beams based on a binary programmable metasurface," *IEEE Antennas Wireless Propag. Lett.*, vol. 20, no. 3, pp. 381–385, Mar. 2021.

[17] M. Di Renzo, F. Habibi Danufane, X. Xi, J. de Rosny, and S. Tretyakov, "Analytical modeling of the path-loss for reconfigurable intelligent surfaces—Anomalous mirror or scatterer?" in *Proc. IEEE 21st Int. Workshop Signal Process. Adv. Wireless Commun. (SPAWC)*, May 2020, pp. 1–5.

[18] Q. Wu *et al.*, "Intelligent reflecting surface aided wireless communications: A tutorial," *IEEE Trans. Commun.*, vol. 69, no. 5, pp. 3313–3351, May 2021.

[19] E. Björnson, Ö. Özdogan, and E. G. Larsson, "Reconfigurable intelligent surfaces: Three myths and two critical questions," *IEEE Commun. Mag.*, vol. 58, no. 12, pp. 90–96, Dec. 2020.

[20] X. Yu, D. Xu, D. W. K. Ng, and R. Schober, "IRS-assisted green communication systems: Provable convergence and robust optimization," *IEEE Trans. Commun.*, vol. 69, no. 9, pp. 6313–6329, Sep. 2021.

[21] Q. Wu, X. Zhou, and R. Schober, "IRS-assisted wireless powered NOMA: Is dynamic passive beamforming really needed?" *IEEE Wireless Commun. Lett.*, vol. 10, no. 7, pp. 1493–1497, Jul. 2021.

[22] M. Najafi, V. Jamali, R. Schober, and H. V. Poor, "Physics-based modeling and scalable optimization of large intelligent reflecting surfaces," *IEEE Trans. Commun.*, vol. 69, no. 4, pp. 2673–2691, Apr. 2021.

[23] J. Xu, L. Liu, and R. Zhang, "Multiuser MISO beamforming for simultaneous wireless information and power transfer," *IEEE Trans. Signal Process.*, vol. 62, no. 18, pp. 4798–4810, Sep. 2014.

[24] Q. Q. Wu and R. Zhang, "Beamforming optimization for wireless network aided by intelligent reflecting surface with discrete phase shifts," *IEEE Trans. Commun.*, vol. 68, no. 3, pp. 1838–1851, May 2020.
[25] G. Zhou, C. Pan, H. Ren, K. Wang, and A. Nallanathan, "Intelligent reflecting surface aided multigroup multicast miso communication systems," *IEEE Trans. Signal Process.*, vol. 68, pp. 3236–3251, 2020.
[26] D. Mishra and H. Johansson, "Channel estimation and low-complexity beamforming design for passive intelligent surface assisted MISO wireless energy transfer," in *Proc. IEEE Int. Conf. Acoust., Speech Signal Process. (ICASSP)*, Brighton, U.K., May 2019, pp. 4659–4663.
[27] Q.-U.-A. Nadeem, H. Alwazani, A. Kammoun, A. Chaaban, M. Debbah, and M.-S. Alouini, "Intelligent reflecting surface-assisted multi-user MISO communication: Channel estimation and beamforming design," *IEEE Open J. Commun. Soc.*, vol. 1, pp. 661–680, 2020.
[28] Y. Tang, G. Ma, H. Xie, J. Xu, and X. Han, "Joint transmit and reflective beamforming design for IRS-assisted multiuser MISO SWIPT systems," in *Proc. IEEE Int. Conf. Commun.*, Jun. 2020, pp. 1–6.
[29] E. Boshkovska, D. W. K. Ng, N. Zlatanov, and R. Schober, "Practical non-linear energy harvesting model and resource allocation for SWIPT systems," *IEEE Commun. Lett.*, vol. 19, no. 12, pp. 2082–2085, Dec. 2015.
[30] X. Yu, V. Jamali, D. Xu, D. W. K. Ng, and R. Schober, "Smart and reconfigurable wireless communications: From IRS modeling to algorithm design," 2021, *arXiv:2103.07046*.
[31] A. Alkhateeb, O. El Ayach, G. Leus, and R. W. Heath, Jr., "Channel estimation and hybrid precoding for millimeter wave cellular systems," *IEEE J. Sel. Topics Signal Process.*, vol. 8, no. 5, pp. 831–846, Oct. 2014.
[32] V. Jamali, M. Najafi, R. Schober, and H. V. Poor, "Power efficiency, overhead, and complexity tradeoff of IRS codebook design—Quadratic phase-shift profile," *IEEE Commun. Lett.*, vol. 25, no. 6, pp. 2048–2052, Jun. 2021.
[33] S. Hu, Z. Wei, Y. Cai, C. Liu, D. W. K. Ng, and J. Yuan, "Robust and secure sum-rate maximization for multiuser MISO downlink systems with self-sustainable IRS," *IEEE Trans. Commun.*, vol. 69, no. 10, pp. 7032–7049, Oct. 2021.
[34] X. Mu, Y. Liu, L. Guo, J. Lin, and N. Al-Dhahir, "Exploiting intelligent reflecting surfaces in NOMA networks: Joint beamforming optimization," *IEEE Trans. Wireless Commun.*, vol. 19, no. 10, pp. 6884–6898, Oct. 2020.
[35] Y. Sun, D. W. K. Ng, J. Zhu, and R. Schober, "Multi-objective optimization for robust power efficient and secure full-duplex wireless communication systems," *IEEE Trans. Wireless Commun.*, vol. 15, no. 8, pp. 5511–5526, Aug. 2016.
[36] Q. Zhang, W. Saad, and M. Bennis, "Millimeter wave communications with an intelligent reflector: Performance optimization and distributional reinforcement learning," *IEEE Trans. Wireless Commun.*, early access, Sep. 3, 2021, doi: 10.1109/TWC.2021.3107520.
[37] I. Griva, S. G. Nash, and A. Sofer, *Linear and Nonlinear Optimization*, vol. 108. Philadelphia, PA, USA: SIAM, 2009.
[38] M. Cococcioni and L. Fiaschi, "The big-M method with the numerical infinite M," *Optim. Lett.*, vol. 15, no. 7, pp. 2455–2468, Sep. 2020.
[39] Y. Sun, D. W. K. Ng, J. Zhu, and R. Schober, "Robust and secure resource allocation for full-duplex MISO multicarrier NOMA systems," *IEEE Trans. Commun.*, vol. 66, no. 9, pp. 4119–4137, Sep. 2018.
[40] R. Horst and H. Tuy, *Global Optimization: Deterministic Approaches*. Berlin, Germany: Springer, 2013.
[41] Z. Wei, D. W. K. Ng, J. Yuan, and H. M. Wang, "Optimal resource allocation for power-efficient MC-NOMA with imperfect channel state information," *IEEE Trans. Commun.*, vol. 65, no. 9, pp. 3944–3961, Sep. 2017.
[42] Y. B. Lin, T. H. Chiu, and Y. T. Su, "Optimal and near-optimal resource allocation algorithms for OFDMA networks," *IEEE Trans. Wireless Commun.*, vol. 8, no. 8, pp. 4066–4077, Aug. 2009.
[43] A. Mitsos, B. Chachuat, and P. I. Barton, "McCormick-based relaxations of algorithms," *SIAM J. Optim.*, vol. 20, no. 2, pp. 573–601, Jan. 2009.
[44] M. Grant and S. Boyd. (Jan. 2020). *CVX: MATLAB Software for Disciplined Convex Programming, Version 2.1*. [Online]. Available: http://cvxr.com/cvx
[45] C. D. Maranas and C. A. Floudas, "Global optimization in generalized geometric programming," *Comput. Chem. Eng.*, vol. 21, no. 4, pp. 351–369, Dec. 1997.
[46] J. C. Bezdek and R. J. Hathaway, "Some notes on alternating optimization," in *Proc. AFSS Int. Conf. Fuzzy Syst.* Berlin, Germany: Springer, 2002, pp. 288–300.
[47] A. Ben-Tal and M. Zibulevsky, "Penalty/barrier multiplier methods for convex programming problems," *SIAM J. Optim.*, vol. 7, no. 2, pp. 347–366, May 1997.
[48] X. Yu, D. Xu, Y. Sun, D. W. K. Ng, and R. Schober, "Robust and secure wireless communications via intelligent reflecting surfaces," *IEEE J. Sel. Areas Commun.*, vol. 38, no. 11, pp. 2637–2652, Nov. 2020.
[49] Q. Wu and R. Zhang, "Intelligent reflecting surface enhanced wireless network via joint active and passive beamforming," *IEEE Trans. Wireless Commun.*, vol. 18, no. 11, pp. 5394–5409, Nov. 2019.
[50] I. Pólik and T. Terlaky, "Interior point methods for nonlinear optimization," in *Nonlinear Optimization*. Berlin, Germany: Springer, 2010, pp. 215–276.
[51] D. Xu *et al.*, "Resource allocation for IRS-assisted full-duplex cognitive radio systems," *IEEE Trans. Commun.*, vol. 68, no. 12, pp. 7376–7394, Dec. 2020.

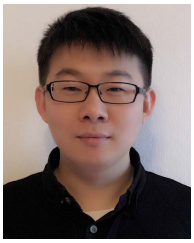

Dongfang Xu (Graduate Student Member, IEEE) received the B.S. degree in communication engineering from Shandong University, Jinan, China, in 2014, and the M.S. degree in communication and multimedia engineering from the Friedrich-Alexander University of Erlangen-Nuremberg (FAU), Germany, in 2017, where he is currently pursuing the Ph.D. degree in electrical engineering. He was a co-recipient of the IEEE Global Communications Conference (GLOBECOM) 2019 Best Paper Award and an Exemplary Reviewer of IEEE TRANSACTIONS ON COMMUNICATIONS in 2020.

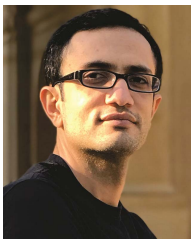

Vahid Jamali (Member, IEEE) received the B.Sc. and M.Sc. degrees (Hons.) in electrical engineering from the K. N. Toosi University of Technology, Tehran, Iran, in 2010 and 2012, respectively, and the Ph.D. degree (Hons.) from the Friedrich-Alexander-University (FAU) of Erlangen-Nürnberg, Erlangen, Germany, in 2019. In 2017, he was a Visiting Research Scholar with Stanford University, CA, USA. He is currently a Post-Doctoral Research Fellow with the Department of Electrical and Computer Engineering, Princeton University. His research interests include wireless and molecular communications and multiuser information theory. He has served as a member of the technical program committee for several IEEE conferences. He has received several awards for his publications and research work, including the Best Paper Awards from the IEEE ICC in 2016, the ACM NanoCOM in 2019, the Asilomar CSSC in 2020, and the IEEE WCNC in 2021; the Doctoral Research Grant from the German Academic Exchange Service (DAAD) in 2017; the Best Ph.D. Thesis Presentation Award from the IEEE WCNC in 2018; the Best Journal Paper Award (Literaturpreis) from the German Information Technology Society (ITG) in 2020; and the Postdoctoral Research Fellowship by the German Research Foundation (DFG) in 2020. He is an Associate Editor of the IEEE COMMUNICATIONS LETTERS, IEEE OPEN JOURNAL OF THE COMMUNICATIONS SOCIETY, and *Physical Communication* journal (Elsevier).

Xianghao Yu (Member, IEEE) received the B.Eng. degree in information engineering from Southeast University, Nanjing, China, in 2014, and the Ph.D. degree in electronic and computer engineering from The Hong Kong University of Science and Technology (HKUST), Hong Kong, China, in 2018.

He was a Humboldt Post-Doctoral Research Fellow at the Institute for Digital Communications, Friedrich-Alexander-University Erlangen-Nuremberg (FAU), Erlangen, Germany. He is currently a Research Assistant Professor with the Department of Electronic and Computer Engineering, HKUST. He has coauthored the book titled *Stochastic Geometry Analysis of Multi-Antenna Wireless Networks* (Springer, 2019). His research interests include millimeter wave communications, intelligent reflecting surface-assisted communications, and wireless artificial intelligence. He has received the IEEE Global Communications Conference (GLOBECOM) 2017 Best Paper Award, the 2018 IEEE Signal Processing Society Young Author Best Paper Award, and the IEEE GLOBECOM 2019 Best Paper Award. He was also recognized as an Exemplary Reviewer of the IEEE TRANSACTIONS ON WIRELESS COMMUNICATIONS in 2017 and 2018.

Derrick Wing Kwan Ng (Fellow, IEEE) received the bachelor's (Hons.) and Master of Philosophy (M.Phil.) degrees in electronic engineering from The Hong Kong University of Science and Technology (HKUST) in 2006 and 2008, respectively, and the Ph.D. degree from The University of British Columbia (UBC) in November 2012.

He was a Senior Post-Doctoral Fellow at the Institute for Digital Communications, Friedrich-Alexander-University Erlangen-Nürnberg (FAU), Germany. He is currently working as a Scientia Associate Professor at the University of New South Wales, Sydney, Australia. His research interests include convex and non-convex optimization, physical layer security, IRS-assisted communication, UAV-assisted communication, wireless information and power transfer, and green (energy-efficient) wireless communications. He has been listed as a Highly Cited Researcher by Clarivate Analytics since 2018. He has received the Australian Research Council (ARC) Discovery Early Career Researcher Award 2017 and the Best Paper Awards at the WCSP 2020 and 2021, IEEE TCGCC Best Journal Paper Award 2018, INISCOM 2018, IEEE International Conference on Communications (ICC) 2018 and 2021, IEEE International Conference on Computing, Networking and Communications (ICNC) 2016, IEEE Wireless Communications and Networking Conference (WCNC) 2012, the IEEE Global Telecommunication Conference (GLOBECOM) 2011 and 2021, and the IEEE Third International Conference on Communications and Networking in China 2008. He has been serving as an Editorial Assistant to the Editor-in-Chief for the IEEE TRANSACTIONS ON COMMUNICATIONS from January 2012 to December 2019. He is serving as an Editor for the IEEE TRANSACTIONS ON COMMUNICATIONS and the IEEE TRANSACTIONS ON WIRELESS COMMUNICATIONS. He is serving as an Area Editor for the IEEE OPEN JOURNAL OF THE COMMUNICATIONS SOCIETY.

Robert Schober (Fellow, IEEE) received the Diploma (Univ.) and Ph.D. degrees in electrical engineering from the Friedrich-Alexander University of Erlangen-Nuremberg (FAU), Germany, in 1997 and 2000, respectively.

From 2002 to 2011, he was a Professor and a Canada Research Chair at The University of British Columbia (UBC), Vancouver, Canada. Since January 2012, he has been an Alexander von Humboldt Professor and the Chair for digital communication at FAU. His research interests fall into the broad areas of communication theory, wireless communications, and statistical signal processing. Since 2017, he has been listed as a Highly Cited Researcher by the Web of Science. He is a fellow of the Canadian Academy of Engineering and the Engineering Institute of Canada. He has received several awards for his work, including the 2002 Heinz Maier-Leibnitz Award of the German Science Foundation (DFG), the 2004 Innovations Award of the Vodafone Foundation for Research in Mobile Communications, the 2006 UBC Killam Research Prize, the 2007 Wilhelm Friedrich Bessel Research Award of the Alexander von Humboldt Foundation, the 2008 Charles McDowell Award for Excellence in Research from UBC, the 2011 Alexander von Humboldt Professorship, the 2012 NSERC E. W. R. Stacie Fellowship, and the 2017 Wireless Communications Recognition Award by the IEEE WIRELESS COMMUNICATIONS Technical Committee. From 2012 to 2015, he served as the Editor-in-Chief for the IEEE TRANSACTIONS ON COMMUNICATIONS. He currently serves as a member of the Editorial Board for the PROCEEDINGS OF THE IEEE and a VP for the Publications of the IEEE Communication Society (ComSoc).

Anhang E

Publication 4

[C1] **D. Xu**, X. Yu, Y. Sun, D. W. K. Ng and R. Schober, "Resource Allocation for Secure IRS-Assisted Multiuser MISO Systems," 2019 IEEE Globecom Workshops (GC Wkshps), 2019, pp. 1-6, doi:10.1109/GCWkshps45667.2019.9024490.[1]

[1]© 2019 IEEE. Reprinted, with permission, from D. Xu, X. Yu, Y. Sun, D. W. K. Ng, and R. Schober, "Resource allocation for secure IRS-assisted multiuser MISO systems," in *Proc. IEEE Global Commun. Conf. Wkshps.*, Dec. 2019, pp. 1-6.

Resource Allocation for Secure IRS-assisted Multiuser MISO Systems

Dongfang Xu†, Xianghao Yu†, Yan Sun†, Derrick Wing Kwan Ng§, and Robert Schober†
†Friedrich-Alexander-Universität Erlangen-Nürnberg, Germany, §The University of New South Wales, Australia

***Abstract*—In this paper, we study resource allocation design for secure communication in intelligent reflecting surface (IRS)-assisted multiuser multiple-input single-output (MISO) communication systems. To enhance physical layer security, artificial noise (AN) is transmitted from the base station (BS) to deliberately impair the channel of an eavesdropper. In particular, we jointly optimize the phase shift matrix at the IRS and the beamforming vectors and AN covariance matrix at the BS for maximization of the system sum secrecy rate. To handle the resulting non-convex optimization problem, we develop an efficient suboptimal algorithm based on alternating optimization, successive convex approximation, semidefinite relaxation, and manifold optimization. Our simulation results reveal that the proposed scheme substantially improves the system sum secrecy rate compared to two baseline schemes.**

I. Introduction

Recently, intelligent reflecting surface (IRS)-assisted wireless communication systems have received considerable attention as a promising approach for providing cost-effective and power-efficient high data-rate communication services for the fifth-generation and beyond wireless communication systems [1]–[7]. Consisting of a set of small reflecting elements, IRSs can be easily and flexibly deployed on building facades and interior walls, improving communication service coverage [1]. Compared to conventional relays and distributed antenna systems [8], passive reflectors embedded in IRSs require little operational power which makes them suitable for deployment in energy-constrained systems. Furthermore, due to their programmability and reconfigurability, IRSs can be adjusted on-demand such that a favourable radio propagation environment is obtained to improve system performance [1]. As a result, several initial works have addressed technical issues regarding the design of IRS-assisted communication systems. For instance, the authors in [3] investigated the joint transmit beamforming and phase shift matrix design for maximization of the total received power of the user of an IRS-enhanced single-user system. In [5], two computationally efficient suboptimal algorithms were developed for maximization of the spectral efficiency achieved by an IRS-assisted multiple-input single-output (MISO) communication system. However, these works did not consider security and the obtained results may not be applicable to systems where communication security is a concern.

Recently, physical layer security has emerged as a promising technology to facilitate secure communication in wireless systems [9]. By configuring multiple antennas at the base station (BS), beamforming can be employed to degrade the channel quality of eavesdroppers. In [10], a transmit beamforming algorithm was designed to achieve communication secrecy in a MISO wireless system. Furthermore, the authors of [11] proposed two algorithms to maximize the secrecy rate in an IRS-assisted MISO wireless system. In [12], the authors jointly optimized the beamforming vectors at the BS and the phase shifts at the IRS for maximization of the secrecy rate of a legitimate user. However, in [11] and [12], artificial noise (AN) is not employed for security enhancement. Nevertheless, AN transmission is an effective approach to improve physical layer security [13]. Moreover, [11] and [12] focused on the case of maximizing the secrecy rate of a single user and the proposed schemes may not be able to guarantee secure communication for multiuser IRS-assisted systems. The authors of [14] investigated the resource allocation algorithm design for maximization of the minimum secrecy rate among several legitimate users of an IRS-assisted multiuser MISO system. However, in [14] the unit modulus constraint introduced by the reflectors of the IRS was approximated by a convex constraint, which simplifies the optimization problem considerably and may lead to a performance loss. Therefore, the design of efficient resource allocation algorithms for maximization of the sum secrecy rate of IRS-assisted multiuser communication systems employing AN to impair eavesdroppers and imposing a unit modulus constraint for the IRS reflectors remains an open issue.

Motivated by the above discussions, in this paper, we investigate the joint design of the phase shift matrix at the IRS and the downlink (DL) beamforming vectors and the AN covariance matrix at the BS for maximizing the system sum secrecy rate.

II. System Model

In this section, after introducing the notations used in this paper, we present the system model adopted for IRS-assisted communication.

A. Notations

In this paper, we use boldface capital and lower case letters to represent matrices and vectors, respectively. $\mathbb{R}^{N\times M}$ and $\mathbb{C}^{N\times M}$ denote the space of $N \times M$ real-valued and complex-valued matrices, respectively. $\mathbb{H}^N$ denotes the set of all N-dimensional complex Hermitian matrices. $\mathbf{I}_N$ indicates an $N \times N$ identity matrix. $|\cdot|$ and $||\cdot||_2$ denote the absolute value of a complex scalar and the l_2-norm of a vector, respectively. $\mathbf{x}^T$, and $\mathbf{x}^H$ stand for the transpose and the conjugate transpose of vector $\mathbf{x}$, respectively. $\mathbf{A} \succeq \mathbf{0}$ indicates that $\mathbf{A}$ is a positive semidefinite matrix. $\mathrm{Rank}(\mathbf{A})$, $\mathrm{Tr}(\mathbf{A})$, and $[\mathbf{A}]_{i,i}$ denote the rank, the trace, and the (i,i)-entry of matrix $\mathbf{A}$, respectively. x_i denotes the i-th element of vector $\mathbf{x}$. $\mathrm{diag}(\mathbf{x})$ represents the $N \times N$ diagonal matrix with diagonal elements $x_1, \cdots, x_N$. $\mathrm{unt}(\mathbf{x})$ represents an N-dimensional vector with elements $\frac{x_1}{|x_1|}, \cdots, \frac{x_N}{|x_N|}$. $\mathbf{A} \circ \mathbf{B}$ represents the Hadamard product of matrices $\mathbf{A}$ and $\mathbf{B}$. $\Re\{\cdot\}$ extracts the real value of a complex variable. $\mathcal{E}\{\cdot\}$ denotes statistical expectation. $\triangleq$ and $\sim$ stand for "defined as" and "distributed as", respectively. The distribution of a circularly symmetric complex Gaussian random variable with mean μ and variance σ^2 is denoted by $\mathcal{CN}(\mu, \sigma^2)$. $[x]^+$ stands for $\max\{0, x\}$. The gradient vector of function $f(\mathbf{x})$ with respect to $\mathbf{x}$ is denoted by $\nabla_{\mathbf{x}} f(\mathbf{x})$.

B. IRS-assisted Multiuser Wireless Communication System

We consider an IRS-assisted multiuser DL communication system which comprises a BS, an eavesdropper, an IRS, and a set of desired users, indexed by $\mathcal{K} \triangleq \{1, \cdots, K\}$, as illustrated

978-1-7281-0960-2/19/$31.00 ©2019 IEEE

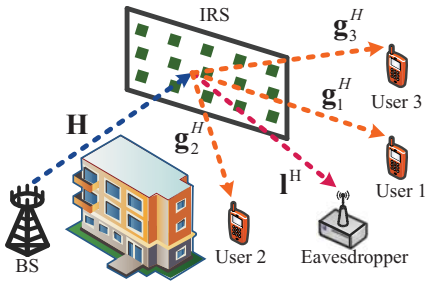

Fig. 1. An intelligent reflecting surface (IRS)-assisted secure communication system with one eavesdropper and $K = 3$ desired users. The direct links from the BS to the users and the eavesdropper are blocked by a building.

in Figure 1. The BS is equipped with $N_{\mathrm{T}} > 1$ antennas, while both the desired users and the eavesdropper are single-antenna devices. Moreover, a passive IRS is deployed to achieve secure communication between the BS and the users. The IRS employs M phase shifters, indexed by $\mathcal{M} \triangleq \{1, \cdots, M\}$, and can be programmed and reconfigured via a controller. Furthermore, perfect channel state information (CSI) of the whole system is assumed to be available at the BS for resource allocation design[1]. Besides, we assume that the direct links from the BS to the users and the eavesdropper are unavailable due to unfavorable propagation conditions (e.g., blockage by a building).

In each scheduling time slot, the BS transmits a signal vector $\mathbf{x} \in \mathbb{C}^{N_{\mathrm{T}}}$ to the K users. In particular, the signal vector, which comprises K information signals and AN, is given by

$$\mathbf{x} = \sum_{k\in\mathcal{K}} \mathbf{w}_k s_k + \mathbf{z}, \tag{1}$$

where $\mathbf{w}_k \in \mathbb{C}^{N_{\mathrm{T}}}$ and $s_k \in \mathbb{C}$ denote the beamforming vector for the k-th user and the corresponding information bearing signal, respectively. We assume $\mathcal{E}\{|s_k|^2\} = 1, \forall k \in \mathcal{K}$, without loss of generality. Moreover, to guarantee secure communication, an AN vector $\mathbf{z} \in \mathbb{C}^{N_{\mathrm{T}}}$ is generated and transmitted by the BS to impair the eavesdropper. In particular, we model $\mathbf{z}$ as a complex Gaussian random vector with zero mean and covariance matrix $\mathbf{Z} \in \mathbb{H}^{N_{\mathrm{T}}}$, $\mathbf{Z} \succeq \mathbf{0}$.

The signals received by user k and the eavesdropper via the reflection at the IRS are given by

$$y_k = \mathbf{g}_k^H \mathbf{\Phi} \mathbf{H} (\sum_{k\in\mathcal{K}} \mathbf{w}_k s_k + \mathbf{z}) + n_k, \tag{2}$$

$$y_e = \mathbf{l}^H \mathbf{\Phi} \mathbf{H} (\sum_{k\in\mathcal{K}} \mathbf{w}_k s_k + \mathbf{z}) + n_e, \tag{3}$$

respectively, where $\mathbf{g}_k \in \mathbb{C}^M$ and $\mathbf{l} \in \mathbb{C}^M$ denote the channel vectors between the IRS and user k and between the IRS and the eavesdropper, respectively. $\mathbf{\Phi} = \mathrm{diag}\left(e^{j\phi_1}, \cdots, e^{j\phi_M}\right)$ denotes the phase shift matrix of the IRS, where $\phi_m, \forall m \in \mathcal{M}$, represents the phase shift of the m-th reflector of the IRS [3]. The channel matrix between the BS and the IRS is denoted by $\mathbf{H} \in \mathbb{C}^{M\times N_{\mathrm{T}}}$. Besides, $n_k \sim \mathcal{CN}(0, \sigma_{n_k}^2)$ and $n_e \sim \mathcal{CN}(0, \sigma_{n_e}^2)$ are the additive white Gaussian noise samples at user k and the eavesdropper, respectively.

III. Optimization Problem Formulation

In this section, we first define the adopted system performance metric and then formulate the resource allocation optimization problem for the considered system.

[1]In practice, the BS may not be able to obtain perfect CSI. Hence, the results in this paper serve as a theoretical system performance benchmark.

A. Achievable Rate and Secrecy Rate

The achievable rate (bits/s/Hz) of user k is given by $R_k = \log_2(1 + \Gamma_k)$, where

$$\Gamma_k = \frac{\left|\mathbf{g}_k^H \mathbf{\Phi} \mathbf{H} \mathbf{w}_k\right|^2}{\sum\limits_{r\in\mathcal{K}\setminus\{k\}} \left|\mathbf{g}_k^H \mathbf{\Phi} \mathbf{H} \mathbf{w}_r\right|^2 + \mathrm{Tr}(\mathbf{H}^H \mathbf{\Phi}^H \mathbf{g}_k \mathbf{g}_k^H \mathbf{\Phi} \mathbf{H} \mathbf{Z}) + \sigma_{n_k}^2}. \tag{4}$$

In this paper, we impose a worst-case assumption regarding the capabilities of the eavesdropper for resource allocation algorithm design to ensure secure communication [13]. Specifically, we assume that the eavesdropper is capable of canceling all multiuser interference before decoding the desired information. Therefore, the channel capacity between the BS and the eavesdropper for wiretapping user k is given by

$$C_k^{\mathrm{E}} = \log_2\Big(1 + \frac{\left|\mathbf{l}^H \mathbf{\Phi} \mathbf{H} \mathbf{w}_k\right|^2}{\mathrm{Tr}(\mathbf{H}^H \mathbf{\Phi}^H \mathbf{l}\mathbf{l}^H \mathbf{\Phi} \mathbf{H} \mathbf{Z}) + \sigma_{n_e}^2}\Big). \tag{5}$$

The achievable secrecy rate between the BS and user k is given by $R_k^{\mathrm{Sec}} = \left[R_k - C_k^{\mathrm{E}}\right]^+$ [15].

B. Optimization Problem Formulation

We aim to maximize the system sum secrecy rate by optimizing $\mathbf{w}_k$, $\mathbf{Z}$, and $\mathbf{\Phi}$. The corresponding optimization problem is formulated as

$$\begin{aligned} \underset{\mathbf{w}_k, \mathbf{Z}\in\mathbb{H}^{N_{\mathrm{T}}}, \mathbf{\Phi}}{\text{maximize}} \quad & \sum_{k\in\mathcal{K}} \left[R_k - C_k^{\mathrm{E}}\right]^+ \\ \text{s.t.} \quad & \text{C1:} \sum_{k\in\mathcal{K}} \left\|\mathbf{w}_k\right\|^2 + \mathrm{Tr}(\mathbf{Z}) \le P_{\max}, \\ & \text{C2:} \left|[\mathbf{\Phi}]_{m,m}\right| = 1, \forall m, \quad \text{C3:} \ \mathbf{Z} \succeq \mathbf{0}. \end{aligned} \tag{6}$$

Constraint C1 limits the maximum BS transmit power allowance to $P_{\max}$. Besides, the operator $[\cdot]^+$ has no impact on the optimal solution and hence is omitted in the following for notational simplicity[2].

We note that it is very arduous to obtain the globally optimal solution of (6), due to the coupling of the optimization variables and the unit modulus constraint in C2. Therefore, we develop a resource allocation algorithm based on alternating optimization [16] to obtain a suboptimal solution of (6) in the next section.

IV. Solution of the Problem

In this section, we aim to design a computationally efficient suboptimal algorithm for handling (6) via alternating optimization. For notational simplicity, we first define $\mathbf{G}_k = \mathrm{diag}(\mathbf{g}_k^H)\mathbf{H}$, $\mathbf{L} = \mathrm{diag}(\mathbf{l}^H)\mathbf{H}$, $\mathbf{W}_k = \mathbf{w}_k\mathbf{w}_k^H$. Moreover, we define a new optimization variable $\mathbf{u} = \left[e^{j\phi_1}, \cdots, e^{j\phi_M}\right]^T$. Then, we rewrite the received SINRs at user k as follows:

$$\Gamma_k = \frac{\mathrm{Tr}(\mathbf{W}_k \mathbf{G}_k^H \mathbf{u}\mathbf{u}^H \mathbf{G}_k)}{\sum\limits_{r\in\mathcal{K}\setminus\{k\}} \mathrm{Tr}(\mathbf{W}_r \mathbf{G}_k^H \mathbf{u}\mathbf{u}^H \mathbf{G}_k) + \mathrm{Tr}(\mathbf{Z}\mathbf{G}_k^H \mathbf{u}\mathbf{u}^H \mathbf{G}_k) + \sigma_{n_k}^2}. \tag{7}$$

Moreover, the channel capacity for the eavesdropper with respect to the message of user k in (5) can be rewritten as

$$C_k^{\mathrm{E}} = \log_2\Big(1 + \frac{\mathrm{Tr}(\mathbf{W}_k \mathbf{L}^H \mathbf{u}\mathbf{u}^H \mathbf{L})}{\mathrm{Tr}(\mathbf{Z}\mathbf{L}^H \mathbf{u}\mathbf{u}^H \mathbf{L}) + \sigma_{n_e}^2}\Big). \tag{8}$$

[2]It can be proved that at the optimal solution, if the achievable secrecy rate of user k is non-positive, the proposed algorithm would turn off the transmission of user k and reallocate the available power to other users.

$$F_1=-\sum_{k\in\mathcal{K}}\log_2\Big(\sum_{r\in\mathcal{K}}\mathrm{Tr}(\mathbf{W}_r\mathbf{G}_k^H\mathbf{u}\mathbf{u}^H\mathbf{G}_k)+\mathrm{Tr}(\mathbf{Z}\mathbf{G}_k^H\mathbf{u}\mathbf{u}^H\mathbf{G}_k)+\sigma_{n_k}^2\Big),\ F_2=-K\log_2\Big(\mathrm{Tr}(\mathbf{Z}\mathbf{L}^H\mathbf{u}\mathbf{u}^H\mathbf{L})+\sigma_{n_e}^2\Big), \tag{9}$$

$$G_1=-\sum_{k\in\mathcal{K}}\log_2\Big(\sum_{r\in\mathcal{K}\setminus\{k\}}\mathrm{Tr}(\mathbf{W}_r\mathbf{G}_k^H\mathbf{u}\mathbf{u}^H\mathbf{G}_k)+\mathrm{Tr}(\mathbf{Z}\mathbf{G}_k^H\mathbf{u}\mathbf{u}^H\mathbf{G}_k)+\sigma_{n_k}^2\Big),\ G_2=-\sum_{k\in\mathcal{K}}\log_2\Big(\mathrm{Tr}(\mathbf{W}_k\mathbf{L}^H\mathbf{u}\mathbf{u}^H\mathbf{L})+\mathrm{Tr}(\mathbf{Z}\mathbf{L}^H\mathbf{u}\mathbf{u}^H\mathbf{L})+\sigma_{n_e}^2\Big) \tag{10}$$

Now, to facilitate the application of alternating optimization, we first recast (6) in equivalent form as follows:

$$\begin{aligned}&\underset{\mathbf{Z}\in\mathbb{H}^{N_\mathrm{T}},\mathbf{W},\mathbf{u}}{\text{minimize}}\quad f=F_1+F_2-G_1-G_2 \qquad (11)\\ \text{s.t.}\quad &\text{C1:}\sum_{k\in\mathcal{K}}\mathrm{Tr}(\mathbf{W}_k)+\mathrm{Tr}(\mathbf{Z})\le P_{\max},\\ &\text{C2: } |u_m|=1,\ \forall m, \qquad \text{C3: } \mathbf{Z}\succeq\mathbf{0},\\ &\text{C4: } \mathbf{W}_k\succeq\mathbf{0},\ \forall k, \qquad \text{C5: } \mathrm{Rank}(\mathbf{W}_k)\le 1,\ \forall k,\end{aligned}$$

where $\mathbf{W}\in\mathbb{C}^{K\times N_\mathrm{T}}$ are the collection of all $\mathbf{W}_k$, and F_1, F_2, G_1, and G_2 are shown at the bottom of this page. Moreover, u_m is the m-th element of $\mathbf{u}$, and $\mathbf{W}_k\in\mathbb{H}^{N_\mathrm{T}}$, $\mathbf{W}_k\succeq\mathbf{0}$, and $\mathrm{Rank}(\mathbf{W}_k)\le 1$ in (11) are imposed to ensure that $\mathbf{W}_k=\mathbf{w}_k\mathbf{w}_k^H$ holds after optimization.

By employing alternating optimization, we iteratively optimize $\{\mathbf{W},\mathbf{Z}\}$ and $\mathbf{u}$ with the other one fixed. In particular, for a given $\mathbf{u}$, we solve (11) by employing successive convex approximation (SCA) [17] and semidefinite relaxation (SDR) [15]. Then, for given $\mathbf{W}$ and $\mathbf{Z}$, we solve for $\mathbf{u}$ by applying manifold optimization [18].

A. SCA and SDR

For a given $\mathbf{u}$, the optimization problem in (11) can be rewritten as

$$\begin{aligned}&\underset{\mathbf{Z}\in\mathbb{H}^{N_\mathrm{T}},\mathbf{W}}{\text{minimize}}\quad F_1+F_2-G_1-G_2 \qquad (12)\\ &\text{s.t.}\qquad \text{C1, C3-C5.}\end{aligned}$$

To facilitate the application of SCA, we first construct global underestimators of G_1 and G_2, respectively [17]. In particular, for any feasible point $\mathbf{W}^i$ and $\mathbf{Z}^i$, the differentiable convex function $G_1(\mathbf{W},\mathbf{Z})$ satisfies the following inequality:

$$\begin{aligned}G_1(\mathbf{W},\mathbf{Z})&\ge G_1(\mathbf{W}^i,\mathbf{Z}^i)\\ &+\mathrm{Tr}\Big(\big(\nabla_{\mathbf{W}}G_1(\mathbf{W}^i,\mathbf{Z}^i)\big)^H(\mathbf{W}-\mathbf{W}^i)\Big)\\ &+\mathrm{Tr}\Big(\big(\nabla_{\mathbf{Z}}G_1(\mathbf{W}^i,\mathbf{Z}^i)\big)^H(\mathbf{Z}-\mathbf{Z}^i)\Big)\\ &\triangleq \widetilde{G_1}(\mathbf{W},\mathbf{Z},\mathbf{W}^i,\mathbf{Z}^i), \qquad (13)\end{aligned}$$

where the right hand side term in (13) is a global underestimation of $G_1(\mathbf{W},\mathbf{Z})$. Similarly, a global underestimation of $G_2(\mathbf{W},\mathbf{Z})$ at feasible point $\mathbf{W}^i$ and $\mathbf{Z}^i$ can be constructed as follows

$$\begin{aligned}\widetilde{G_2}(\mathbf{W},\mathbf{Z},\mathbf{W}^i,\mathbf{Z}^i)&\triangleq G_2(\mathbf{W}^i,\mathbf{Z}^i)\\ &+\mathrm{Tr}\Big(\big(\nabla_{\mathbf{W}}G_2(\mathbf{W}^i,\mathbf{Z}^i)\big)^H(\mathbf{W}-\mathbf{W}^i)\Big)\\ &+\mathrm{Tr}\Big(\big(\nabla_{\mathbf{Z}}G_2(\mathbf{W}^i,\mathbf{Z}^i)\big)^H(\mathbf{Z}-\mathbf{Z}^i)\Big). \qquad (14)\end{aligned}$$

Therefore, for any given $\mathbf{W}^i$ and $\mathbf{Z}^i$, an upper bound of (12) can be obtained by solving the following optimization problem:

$$\begin{aligned}&\underset{\mathbf{Z}\in\mathbb{H}^{N_\mathrm{T}},\mathbf{W}}{\text{minimize}}\quad F_1+F_2-\widetilde{G_1}-\widetilde{G_2} \qquad (15)\\ &\text{s.t.}\qquad \text{C1, C3-C5.}\end{aligned}$$

We note that the remaining non-convexity of (15) stems from the rank-one constraint C5. To tackle this issue, we remove constraint C5 by applying SDR where the relaxed version of (15) can be efficiently solved via convex problem solvers such as CVX [19]. In the following theorem, we reveal the tightness of SDR.

Theorem 1: If $\mathrm{P}_{\max}>0$, an optimal beamforming matrix $\mathbf{W}_k$ satisfying $\mathrm{Rank}(\mathbf{W}_k)\le 1$ can always be obtained.

Proof: Please refer to the Appendix. ■

We note that the minimum of (15) serves as an upper bound of (12). By employing the algorithm summarized in **Algorithm 1**, we can iteratively tighten the upper bound and obtain a sequence of solutions $\mathbf{W}$ and $\mathbf{Z}$. It can be shown that the objective function in (15) is non-increasing in each iteration, and the developed algorithm is guaranteed to converge to a locally optimal solution of (12) [17].

Algorithm 1 Successive Convex Approximation-Based Algorithm

1: Initialize iteration index $i=1$.
2: **repeat**
3: Solve (15) for given $\mathbf{W}^i$ and $\mathbf{Z}^i$ and store the intermediate solution $\mathbf{W},\mathbf{Z}$
4: Set $i=i+1$ and $\mathbf{W}^i=\mathbf{W}$ and $\mathbf{Z}^i=\mathbf{Z}$
5: **until** convergence
6: $\mathbf{W}^*=\mathbf{W}^i$ and $\mathbf{Z}^*=\mathbf{Z}^i$

B. Oblique Manifold Optimization

For given $\mathbf{W}_k$ and $\mathbf{Z}$, we can rewrite (11) as:

$$\begin{aligned}&\underset{\mathbf{u}}{\text{minimize}}\quad F_1+F_2-G_1-G_2 \qquad (16)\\ &\text{s.t.}\qquad \text{C2: } [\mathbf{u}\mathbf{u}^H]_{m,m}=1,\ \forall m.\end{aligned}$$

We note that it is very challenging to solve (16) optimally due to the non-convex unit modulus constraint C2. In the literature, the unit modulus constraint is often handled by SDR and Gaussian randomization [3] which leads to a suboptimal solution. Yet, the objective function may not be monotonically non-increasing in each iteration when this approach is applied. Thus, the corresponding algorithm cannot guarantee convergence. In contrast, in this paper, we develop a manifold optimization-based algorithm which is guaranteed to converge to a suboptimal solution. Moreover, unlike [14] where the unit modulus constraint was relaxed, in this paper, the unit modulus constraint is handled directly by exploiting manifold optimization theory [18]. We note that constraint C2 defines an oblique manifold [18] which can be characterized by

$$\mathcal{O}=\left\{\mathbf{u}\in\mathbb{C}^M \mid [\mathbf{u}\mathbf{u}^H]_{m,m}=1,\ \forall m\in\mathcal{M}\right\}. \qquad (17)$$

We note that constraint C2 is automatically satisfied when optimizing $\mathbf{u}$ over the oblique manifold. Now, we introduce some definitions which are commonly used in Riemannian manifold optimization [18].

The *tangent space* of the oblique manifold $\mathcal{O}$ at point $\mathbf{u}_j$ is defined as the space which contains all tangent vectors of the oblique manifold $\mathcal{O}$ at point $\mathbf{u}_j$, cf. Figure 2(a). Specifically, each tangent vector is a vector that is a tangent to the oblique

manifold $\mathcal{O}$ at point $\mathbf{u}_j$ [18]. The tangent space for $\mathcal{O}$ at $\mathbf{u}_j$ is given by

$$T_{\mathbf{u}_j}\mathcal{O} = \left\{\mathbf{v} \in \mathbb{C}^M \mid [\mathbf{v}\mathbf{u}_j^H]_{m,m} = 0,\ \forall m \in \mathcal{M}\right\}, \quad (18)$$

where $\mathbf{v}$ is a tangent vector at $\mathbf{u}_j$. Among all tangent vectors, the one that yields the fastest increase of the objective function is defined as the *Riemannian gradient*, i.e., $\text{grad}_{\mathbf{u}_j} f$. The Riemannian gradient of function f at point $\mathbf{u}_j$ is calculated based on the orthogonal projection of the Euclidean gradient $\nabla_{\mathbf{u}_j} f$ onto tangent space $T_{\mathbf{u}_j}\mathcal{O}$ [20]. In particular, $\text{grad}_{\mathbf{u}_j} f$ is given by

$$\text{grad}_{\mathbf{u}_j} f = \nabla_{\mathbf{u}_j} f - \Re\left\{\nabla_{\mathbf{u}_j} f \circ (\mathbf{u}_j^T)^H\right\} \circ \mathbf{u}_j, \quad (19)$$

where $\nabla_{\mathbf{u}_j} f$ is obtained as [21]

$$\begin{aligned}\nabla_{\mathbf{u}_j} f = &\frac{K\mathbf{L}(\mathbf{Z}^H + \mathbf{Z})\mathbf{L}^H\mathbf{u}_j}{(\ln 2)F_2(\mathbf{u}_j)} \\ &+ \frac{\sum\limits_{k\in\mathcal{K}}\sum\limits_{r\in\mathcal{K}}\left[\mathbf{G}_k(\mathbf{W}_r^H + \mathbf{W}_r + \mathbf{Z}^H + \mathbf{Z})\mathbf{G}_k^H\mathbf{u}_j\right]}{(\ln 2)F_1(\mathbf{u}_j)} \\ &- \frac{\sum\limits_{k\in\mathcal{K}}\sum\limits_{r\in\mathcal{K}\setminus\{k\}}\left[\mathbf{G}_k(\mathbf{W}_r^H + \mathbf{W}_r + \mathbf{Z}^H + \mathbf{Z})\mathbf{G}_k^H\mathbf{u}_j\right]}{(\ln 2)G_1(\mathbf{u}_j)} \\ &- \frac{\sum\limits_{k\in\mathcal{K}}\mathbf{L}(\mathbf{W}_k^H + \mathbf{W}_k + \mathbf{Z}^H + \mathbf{Z})\mathbf{L}^H\mathbf{u}_j}{(\ln 2)G_2(\mathbf{u}_j)}. \end{aligned} \quad (20)$$

After obtaining the Riemannian gradient $\text{grad}_{\mathbf{u}_j} f$, we can exploit the optimization approaches designed for the Euclidean space to tackle manifold optimization problems. In particular, we employ the conjugate gradient (CG) method [22], where the update rule of the search direction in the Euclidean space is given by

$$\boldsymbol{\mu}_{j+1} = -\nabla_{\mathbf{u}_{j+1}} f + \alpha_j \boldsymbol{\mu}_j. \quad (21)$$

Here, $\boldsymbol{\mu}_j$ denotes the search direction at $\mathbf{u}_j$ and α_j is chosen as the Polak-Ribière parameter to achieve fast convergence [22]. However, since vectors $\boldsymbol{\mu}_j$ and $\boldsymbol{\mu}_{j+1}$ in (21) lie in $T_{\mathbf{u}_j}\mathcal{O}$ and $T_{\mathbf{u}_{j+1}}\mathcal{O}$, respectively, they cannot be integrated directly over different tangent spaces. To circumvent this problem, we introduce an operation called *transport* which maps $\boldsymbol{\mu}_j$ from tangent space $T_{\mathbf{u}_j}\mathcal{O}$ to tangent space $T_{\mathbf{u}_{j+1}}\mathcal{O}$ [23]. In particular, the vector transport for oblique manifold $\mathcal{O}$, as shown in cf. Figure 2(b), is given by

$$\begin{aligned}\mathcal{T}_{\mathbf{u}_j\to\mathbf{u}_{j+1}}(\boldsymbol{\mu}_j) \triangleq T_{\mathbf{u}_j}\mathcal{O} \mapsto T_{\mathbf{u}_{j+1}}\mathcal{O}: \\ \boldsymbol{\mu}_j \mapsto \boldsymbol{\mu}_j - \Re\left\{\boldsymbol{\mu}_j \circ (\mathbf{u}_{j+1}^T)^H\right\} \circ \mathbf{u}_{j+1}. \end{aligned} \quad (22)$$

Similar to (21), the search direction of the Riemannian gradient in (19) can be updated based on the following equation:

$$\boldsymbol{\mu}_{j+1} = -\text{grad}_{\mathbf{u}_{j+1}} f + \alpha_j \mathcal{T}_{\mathbf{u}_j\to\mathbf{u}_{j+1}}(\boldsymbol{\mu}_j). \quad (23)$$

Algorithm 2 Oblique Manifold Optimization-Based Algorithm

1: Set iteration index $j = 1$, convergence tolerance ε, step size δ_j, and initial point $\mathbf{u}_1$
2: Calculate the Riemannian gradient according to (19)
3: **repeat**
4: Choose the step size δ_j according to [18, p. 62]
5: Find $\mathbf{u}_{j+1}$ by retraction in (24)
6: Update Riemannian gradient $\text{grad}_{\mathbf{u}_{j+1}} f$ by using (19)
7: Calculate the vector transport $\mathcal{T}_{\mathbf{u}_j\to\mathbf{u}_{j+1}}(\boldsymbol{\mu}_j)$ by using (22)
8: Choose Polak-Ribière parameter α_j according to [18, Eq. 8.24]
9: Calculate conjugate search direction $\boldsymbol{\mu}_{j+1}$ by using (23)
10: Set $j = j + 1$
11: **until** $\left\|\text{grad}_{\mathbf{u}_j} f\right\| \le \varepsilon$
12: Set $\boldsymbol{\Phi} = \text{diag}\left((\mathbf{u}_{j+1}^T)^H\right)$

Algorithm 3 Alternating Optimization Algorithm

1: Set iteration index $t = 1$, the initial point $\mathbf{u}^{(1)}$, convergence tolerance ϵ, maximum iteration number $T_{\max}$.
2: **repeat**
3: Solve (12) via **Algorithm 1** for given $\mathbf{u}^{(t)}$ and store the optimal solution $\mathbf{W}^{(t)}$ and $\mathbf{Z}^{(t)}$
4: Solve (16) via **Algorithm 2** for given $\mathbf{W}^{(t)}$ and $\mathbf{Z}^{(t)}$ and store the solution $\mathbf{u}^{(t+1)}$
5: Set $t = t + 1$
6: **until** $\left|f^{(t+1)} - f^{(t)}\right| \le \epsilon$
7: Obtain the solution by $\mathbf{W}^* = \mathbf{W}^{(t)}$, $\mathbf{Z}^* = \mathbf{Z}^{(t)}$, and $\mathbf{u}^* = \mathbf{u}^{(t)}$

After determining the search direction $\boldsymbol{\mu}_j$ at $\mathbf{u}_j$, we introduce another operation called *retraction* to determine the destination on the oblique manifold [23]. In other words, by applying retraction, we map a vector in the tangent space $T_{\mathbf{u}_j}\mathcal{O}$ onto the manifold $\mathcal{O}$, cf. Figure 2(c). In particular, for a given point $\mathbf{u}_j$ on manifold $\mathcal{O}$, the retraction for step size δ_j and search direction $\boldsymbol{\mu}_j$ are given as

$$\mathcal{R}_{\mathbf{u}_j}(\delta_j\boldsymbol{\mu}_j) \triangleq T_{\mathbf{u}_j}\mathcal{O} \mapsto \mathcal{O}: \delta_j\boldsymbol{\mu}_j \mapsto \text{unt}(\delta_j\boldsymbol{\mu}_j). \quad (24)$$

The problem in (16) can be tackled by applying the proposed algorithm summarized in **Algorithm 2**. Since **Algorithm 2** is a gradient-based algorithm, the objective function in (16) is monotonically non-increasing in each iteration. Hence, **Algorithm 2** is guaranteed to converge to a stationary point of (16) [22].

The proposed alternating optimization algorithm is summarized in **Algorithm 3**. Recall that the objective function is monotonically non-increasing after each iteration of both **Algorithm 1** and **Algorithm 2**. Therefore, the proposed alternating optimization algorithm is guaranteed to converge to a

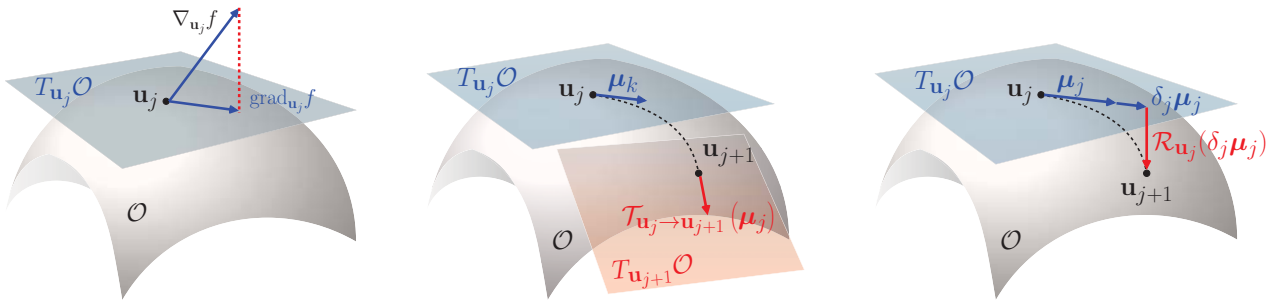

(a) Tangent space and Riemannian gradient. (b) Vector transport. (c) Retraction.

Fig. 2. An illustration of major definitions in Riemannian manifold optimization.

TABLE I
SYSTEM PARAMETERS

System bandwidth and carrier center frequency	200 kHz and 2.4 GHz
Noise powers, $\sigma_{n_k}^2$ and $\sigma_{n_e}^2$	-110 dBm
BS maximum transmit power, $P_{\max}$	40 dBm
Convergence tolerances, ϵ and ε	10^{-3}

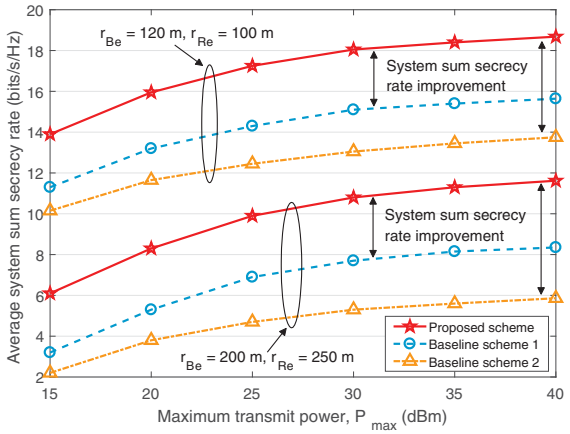

Fig. 3. Average system sum secrecy rate (bits/s/Hz) versus maximum transmit power (dBm) with $K = 3$, $N_{\mathrm{T}} = 6$, and $M = 6$.

suboptimal solution of (11).

V. Simulation Results

We investigate the system performance of the proposed resource allocation scheme via simulations. Table I summarizes the parameters used in our simulation. In particular, the BS is at the center of a single cell with radius 500 meters. One sector of the cell happens to be blocked by buildings and there are K users randomly and uniformly distributed within this sector. An IRS is deployed to provide communication service for the users in this sector. We focus on the resource allocation design to achieve secure communication in this sector. Moreover, we also adopt two baseline schemes for comparison. For baseline scheme 1, we adopt an IRS with random phase ϕ_m, $\forall m \in \mathcal{M}$ [1], and jointly optimize $\mathbf{w}_k$ and $\mathbf{Z}$. For baseline scheme 2, the BS does not generate AN (as in [11] and [14]) and an IRS is employed for security provisioning. In this case, we jointly optimize only $\mathbf{w}_k$ and $\mathbf{\Phi}$ to achieve secure communication. r_{Be} and r_{Re} denote the distance from the BS to the eavesdropper and the distance from the IRS to the eavesdropper, respectively.

In Figure 3, we study the average system sum secrecy rate versus the maximum transmit power. As expected, the system sum secrecy rates for the proposed scheme and the two baseline schemes increase monotonically with increasing $P_{\max}$. Moreover, we can see that the proposed scheme outperforms the baseline schemes. In fact, by jointly optimizing $\mathbf{\Phi}$, $\mathbf{w}_k$, and $\mathbf{Z}$, the proposed scheme can simultaneously facilitates a more favourable radio propagation environment for the users and impair the eavesdropper. In contrast, the two baseline schemes achieve significantly lower system sum secrecy rates, due to the random phase of the IRS for baseline scheme 1 and the lack of AN for baseline scheme 2. Besides, we can observe from Figure 3 that the geometry of the network (i.e., the values of r_{Be} and r_{Re}) has a significant impact on the system sum secrecy rate.

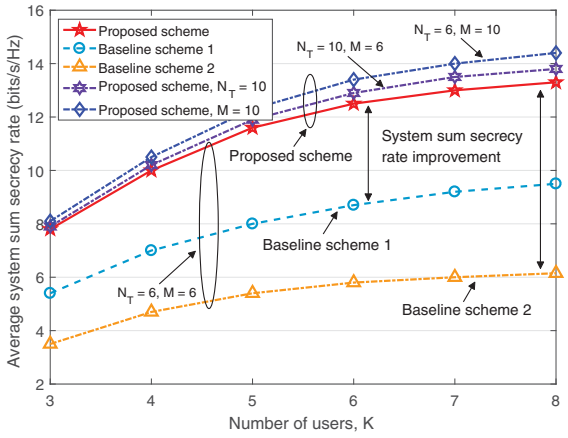

Fig. 4. Average system sum secrecy secrecy rate (bits/s/Hz) versus number of users with $P_{\max} = 20$ dBm, $r_{\mathrm{Be}} = 200$ m, and $r_{\mathrm{Re}} = 250$ m.

This indicates that the location of the IRS needs to be chosen carefully for achieving the best possible system performance.

Figure 4 shows the average system sum secrecy rate versus the number of legitimate users with $P_{\max} = 20$ dBm, $N_{\mathrm{T}} = 6$, and $M = 6$. We observe that the system sum secrecy rates achieved by the proposed scheme and the two baseline schemes monotonically increase with K. This is due to the fact that both the proposed scheme and the two baseline schemes are able to exploit multiuser diversity. To investigate the performance gain attained by deploying IRSs, we show the system sum secrecy rate of the proposed scheme for two additional cases: Case 1 with $N_{\mathrm{T}} = 10$ and $M = 6$ and Case 2 with $N_{\mathrm{T}} = 6$ and $M = 10$. We observe that Case 2 results in a larger performance gain over the system with the default parameters ($N_{\mathrm{T}} = 6$ and $M = 6$) compared to Case 1. The reasons behind this are two-fold. On the one hand, the extra phase shifters can reflect more power of the signal received from the BS which leads to a power gain. On the other hand, they also provide higher flexibility in resource allocation which improves the beamforming gain for the IRS-user links.

VI. Conclusion

In this paper, we proposed an efficient resource allocation algorithm to achieve secure communication in IRS-assisted multiuser MISO systems. AN is injected by the BS to enhance physical layer security. Due to the non-convexity of the formulated optimization problem, we developed an alternating optimization algorithm with guaranteed convergence. Our simulation results reveal that the proposed scheme can significantly enhance the security of IRS-assisted wireless communication systems compared to the two baseline schemes, which respectively do not optimize the IRS phase shift matrix or do not exploit AN.

Appendix- Proof of Theorem 1

We note that if $R_k - C_k^{\mathrm{E}} \leq 0$, the proposed algorithm would stop transmitting information to user k and allocate the corresponding power to other users. In this case, the optimal beamforming vector for user k is $\mathbf{w}_k^* = \mathbf{0}$ which implies $\mathrm{Rank}(\mathbf{W}_k^*) = 0$. Next, for the case where $P_{\max} > 0$ and $R_k - C_k^{\mathrm{E}} > 0$, we show that the optimal beamforming matrix $\mathbf{W}_k^*$ is indeed a rank-one matrix. To start with, we rewrite (15)

in the following equivalent form:

$$\underset{\mathbf{W}_k,\mathbf{Z}\in\mathbb{H}^{N_\mathrm{T}},\eta,\tau_k,\iota}{\text{minimize}} \quad \eta \tag{25}$$

$$\text{s.t.} \quad \text{C1, C3, C4, C6: } \overline{F_1}+\overline{F_2}-\widetilde{G_1}-\widetilde{G_2}\le\eta,$$

$$\text{C7: } \tau_k \ge \sum_{r\in\mathcal{K}} \mathrm{Tr}(\mathbf{W}_r\mathbf{G}_k^H\mathbf{u}\mathbf{u}^H\mathbf{G}_k)+\mathrm{Tr}(\mathbf{Z}\mathbf{G}_k^H\mathbf{u}\mathbf{u}^H\mathbf{G}_k),$$

$$\text{C8: } \iota \ge \mathrm{Tr}(\mathbf{Z}\mathbf{L}^H\mathbf{u}\mathbf{u}^H\mathbf{L}),$$

where $\overline{F_1}=-\sum_{k\in\mathcal{K}}\log_2(\tau_k+\sigma_{n_k}^2)$ and $\overline{F_2}=-\sum_{k\in\mathcal{K}}\log_2(\iota+\sigma_{n_e}^2)$, and τ_k and ι are auxiliary optimization variables.

Problem (25) is jointly convex with respect to all optimization variables. Moreover, it can be verified that Slater's condition holds [21]. Therefore, strong duality holds, i.e., we can obtain the optimal solution of (25) by solving the dual problem [21]. The Lagrangian function of (25) in terms of beamforming matrix $\mathbf{W}_k$ is given by

$$\begin{aligned}\mathcal{L}=&\,\xi\sum_{k\in\mathcal{K}}\mathrm{Tr}(\mathbf{W}_k)-\sum_{k\in\mathcal{K}}\mathrm{Tr}(\mathbf{W}_k\mathbf{Y}_k)\\&+\kappa\mathrm{Tr}\Big(\big[\nabla_{\mathbf{W}}G_1(\mathbf{W}^i,\mathbf{Z}^i)+\nabla_{\mathbf{W}}G_2(\mathbf{W}^i,\mathbf{Z}^i)\big]^H(\mathbf{W}-\mathbf{W}^i)\Big)\\&-\lambda_k\sum_{r\in\mathcal{K}}\mathrm{Tr}(\mathbf{W}_r\mathbf{G}_k^H\mathbf{u}\mathbf{u}^H\mathbf{G}_k)+\Upsilon,\end{aligned} \tag{26}$$

where Υ denotes the collection of the optimization variables of the primal and dual problems and constant terms that are not relevant to the proof. ξ, κ, and λ_k denote the scalar Lagrange multipliers associated with constraints C1, C6, and C7. $\mathbf{Y}_k\in\mathbb{C}^{N_\mathrm{T}\times N_\mathrm{T}}$ is the Lagrange multiplier matrix associated with constraint C4. The dual problem of (15) is given by

$$\underset{\substack{\mathbf{Y}_k\succeq\mathbf{0},\\ \xi,\kappa,\lambda_k\ge0}}{\text{maximize}} \ \underset{\substack{\mathbf{W}_k,\mathbf{Z}\in\mathbb{H}^{N_\mathrm{T}},\\ \eta,\tau_k,\iota}}{\text{minimize}} \ \mathcal{L}(\mathbf{W}_k,\mathbf{Z},\eta,\mathbf{Y}_k,\xi,\kappa,\lambda_k). \tag{27}$$

Then, we investigate the structure of the optimal $\mathbf{W}_k^*$ of dual problem (15) by applying the Karush-Kuhn-Tucker (KKT) conditions. In particular, the KKT conditions associated with $\mathbf{W}_k^*$ are as follows

$$\text{K1:}\xi^*,\kappa^*,\lambda_k^*\ge0,\mathbf{Y}_k^*\succeq\mathbf{0},\ \text{K2:}\mathbf{Y}_k^*\mathbf{W}_k^*=\mathbf{0},\ \text{K3:}\nabla_{\mathbf{W}_k^*}\mathcal{L}=\mathbf{0}, \tag{28}$$

where ξ^*, κ^*, λ_k^*, and $\mathbf{Y}_k^*$ denote the optimal Lagrange multipliers for dual problem (27), and $\nabla_{\mathbf{W}_k^*}\mathcal{L}$ represents the gradient vector of (26) with respect to $\mathbf{W}_k^*$. To facilitate the proof, we rewrite K3 explicitly as follows

$$\mathbf{Y}_k^*=\xi^*\mathbf{I}_{N_\mathrm{T}}-\mathbf{\Delta}, \tag{29}$$

where $\mathbf{\Delta}$ is given by

$$\begin{aligned}\mathbf{\Delta}\ =&\,\lambda^*\mathbf{G}_k^H\mathbf{u}\mathbf{u}^H\mathbf{G}_k\\&-\kappa^*\Big(\nabla_{\mathbf{W}}G_1(\mathbf{W}^i,\mathbf{Z}^i)+\nabla_{\mathbf{W}}G_2(\mathbf{W}^i,\mathbf{Z}^i)\Big).\end{aligned} \tag{30}$$

Next, by revealing the structure of matrix $\mathbf{Y}_k^*$, we prove that the optimal beamforming matrix $\mathbf{W}^*$ is indeed a rank-one matrix. To start with, we first denote the maximum eigenvalue of matrix $\mathbf{\Delta}$ as $\nu_{\mathbf{\Delta}}^{\max}\in\mathbb{R}$. We note that the case where multiple eigenvalues have the same value $\nu_{\mathbf{\Delta}}^{\max}$ occurs with probability zero, due to the randomness of the channels. Reviewing (29), if $\nu_{\mathbf{\Delta}}^{\max}>\xi^*$, then $\mathbf{Y}_k^*$ cannot be a positive semidefinite matrix which contradicts K1. On the other hand, if $\nu_{\mathbf{\Delta}}^{\max}<\xi^*$, then $\mathbf{Y}_k^*$ must be a positive definite matrix with full rank. In this case, considering K2, $\mathbf{W}_k^*$ is forced to be $\mathbf{0}$ which is obviously not the optimal solution for $P_{\max}>0$ and $R_k-C_k^\mathrm{E}>0$. In addition, we note that there exists at least one optimal solution with $\xi^*>0$ such that constraint C1 is met with equality. Therefore, for the optimal solution, the equality $\nu_{\mathbf{\Delta}}^{\max}=\xi^*$ must hold which results in $\mathrm{Rank}(\mathbf{Y}_k^*)=N_\mathrm{T}-1$. Next, we construct a bounded optimal solution based on the above discussion. In particular, we construct a unit-norm vector $\mathbf{e}_{\mathbf{\Delta}}^{\max}\in\mathbb{C}^{N_\mathrm{T}}$ which lies in the null space of $\mathbf{Y}_k^*$, i.e., $\mathbf{Y}_k^*\mathbf{e}_{\mathbf{\Delta}}^{\max}=\mathbf{0}$. We note that $\mathbf{e}_{\mathbf{\Delta}}^{\max}$ denotes the eigenvector of matrix $\mathbf{\Delta}$ corresponding to the maximum eigenvalue $\nu_{\mathbf{\Delta}}^{\max}$ with unit norm. Therefore, for $P_{\max}>0$ and $R_k-C_k^\mathrm{E}>0$, the optimal beamforming matrix $\mathbf{W}_k^*$ is indeed a rank-one matrix which can be expressed as $\mathbf{W}_k^*=\zeta\mathbf{e}_{\mathbf{\Delta}}^{\max}(\mathbf{e}_{\mathbf{\Delta}}^{\max})^H$, where ζ is a parameter to adjust $\mathbf{W}_k^*$ such that constraint C1 is satisfied with equality. ■

REFERENCES

[1] M. Di Renzo *et al.*, "Smart radio environments empowered by AI reconfigurable meta-surfaces: An idea whose time has come," *arXiv preprint arXiv:1903.08925*, 2019.

[2] S. Hu, F. Rusek, and O. Edfors, "Beyond massive MIMO: The potential of data transmission with large intelligent surfaces," *IEEE Trans. Signal Process.*, vol. 66, no. 10, pp. 2746–2758, Mar. 2018.

[3] Q. Wu and R. Zhang, "Intelligent reflecting surface enhanced wireless network: Joint active and passive beamforming design," in *Proc. IEEE Global Commun.*, Dec. 2018, pp. 1–6.

[4] Q. Wu and R. Zhang, "Beamforming optimization for intelligent reflecting surface with discrete phase shifts," in *ICASSP 2019 - 2019 IEEE International Conference on Acoustics, Speech and Signal Processing (ICASSP)*, May 2019, pp. 7830–7833.

[5] X. Yu, D. Xu, and R. Schober, "MISO wireless communication systems via intelligent reflecting surfaces," *arXiv preprint arXiv:1904.12199*, 2019.

[6] M. Najafi and R. Schober, "Intelligent reflecting surfaces for free space optical communications," *arXiv preprint arXiv:1905.01094*, 2019.

[7] Q. Wu and R. Zhang, "Towards smart and reconfigurable environment: Intelligent reflecting surface aided wireless network," *arXiv preprint arXiv:1905.00152*, 2019.

[8] H. Zhu, S. Karachontzitis, and D. Toumpakaris, "Low-complexity resource allocation and its application to distributed antenna systems," *IEEE Wireless Commun.*, vol. 17, no. 3, pp. 44–50, Jun. 2010.

[9] Y. Sun, D. W. K. Ng, J. Zhu, and R. Schober, "Robust and secure resource allocation for full-duplex MISO multicarrier NOMA systems," *IEEE Trans. Commun.*, vol. 66, no. 9, pp. 4119–4137, Sep. 2018.

[10] F. Zhu, F. Gao, T. Zhang, K. Sun, and M. Yao, "Physical-layer security for full duplex communications with self-interference mitigation," *IEEE Trans. Wireless Commun.*, vol. 15, no. 1, pp. 329–340, Jan. 2016.

[11] X. Yu, D. Xu, and R. Schober, "Enabling secure wireless communications via intelligent reflecting surfaces," *arXiv preprint arXiv:1904.09573*, 2019.

[12] H. Shen, W. Xu, S. Gong, Z. He, and C. Zhao, "Secrecy rate maximization for intelligent reflecting surface assisted multi-antenna communications," *arXiv preprint arXiv:1905.10075*, 2019.

[13] Y. Sun, D. W. K. Ng, and R. Schober, "Resource allocation for secure full-duplex radio systems," in *21th International ITG Workshop on Smart Antennas*, Mar. 2017, pp. 1–6.

[14] J. Chen, Y. Liang, Y. Pei, and H. Guo, "Intelligent reflecting surface: A programmable wireless environment for physical layer security," *arXiv preprint arXiv:1905.03689*, 2019.

[15] Y. Sun, D. W. K. Ng, J. Zhu, and R. Schober, "Multi-objective optimization for robust power efficient and secure full-duplex wireless communication systems," *IEEE Trans. Wireless Commun.*, vol. 15, no. 8, pp. 5511–5526, Apr. 2016.

[16] J. C. Bezdek and R. J. Hathaway, "Some notes on alternating optimization," in *AFSS Int. Conf. on Fuzzy Systems*. Springer, 2002, pp. 288–300.

[17] Q. T. Dinh and M. Diehl, "Local convergence of sequential convex programming for nonconvex optimization," in *Recent Advances in Optimization and its Applications in Engineering*. Springer, 2010.

[18] P.-A. Absil, R. Mahony, and R. Sepulchre, *Optimization algorithms on matrix manifolds*. Princeton University Press, 2009.

[19] M. Grant and S. Boyd, "CVX: Matlab software for disciplined convex programming, version 2.1," *Available at http://cvxr.com/cvx*, Mar. 2017.

[20] S. Gallot, D. Hulin, and J. Lafontaine, *Riemannian geometry*. Springer, 1990, vol. 3.

[21] S. Boyd and L. Vandenberghe, *Convex optimization*. Cambridge university press, 2004.

[22] M. Avriel, *Nonlinear programming: analysis and methods*. Courier Corporation, 2003.

[23] X. Yu, J. Shen, J. Zhang, and K. B. Letaief, "Alternating minimization algorithms for hybrid precoding in millimeter wave MIMO systems," *IEEE J. Sel. Area Signal Process.*, vol. 10, no. 3, pp. 485–500, Apr. 2016.

Anhang F

Publication 5

[C2] **D. Xu**, X. Yu, D. W. Kwan Ng and R. Schober, "Resource Allocation for Active IRS-Assisted Multiuser Communication Systems," 2021 55th Asilomar Conference on Signals, Systems, and Computers, 2021, pp. 113-119, doi:10.1109/IEEECONF53345.2021.9723093.[1]

[1]©2021 IEEE. Reprinted, with permission, from D. Xu, X. Yu, D. W. K. Ng, and R. Schober, "Resource allocation for active IRS-assisted multiuser communication systems," in *Proc. Asilomar Conf. on Signals, Systems, and Computers*, Oct. 2021, pp. 113-119.

2021 55th Asilomar Conference on Signals, Systems, and Computers | 978-1-6654-5828-3/21/$31.00 ©2021 IEEE | DOI: 10.1109/IEEECONF53345.2021.9723093

Resource Allocation for Active IRS-Assisted Multiuser Communication Systems

Dongfang Xu*, Xianghao Yu§, Derrick Wing Kwan Ng‡, and Robert Schober*
*Friedrich-Alexander-University Erlangen-Nürnberg, Germany
§Dept. of ECE, The Hong Kong University of Science and Technology, Hong Kong
‡The University of New South Wales, Australia

***Abstract*—Intelligent reflecting surfaces (IRSs) are emerging as promising enablers for the next generation of wireless communication systems, because of their ability to customize favorable radio propagation environments. However, with the conventional passive architecture, IRSs can only adjust the phase of the incident signals limiting the achievable beamforming gain. To fully unleash the potential of IRSs, in this paper, we consider a more general IRS architecture, i.e., active IRSs, which can adapt the phase and amplify the magnitude of the reflected incident signal simultaneously with the support of an additional power source. To realize green communication in active IRS-assisted multiuser systems, we jointly optimize the reflection matrix at the IRS and the beamforming vector at the base station (BS) for the minimization of the BS transmit power. The resource allocation algorithm design is formulated as an optimization problem taking into account the maximum power budget of the active IRS and the quality-of-service (QoS) requirements of the users. To handle the non-convex design problem, we develop a novel and computationally efficient algorithm based on the bilinear transformation and inner approximation methods. The proposed algorithm is guaranteed to converge to a locally optimal solution of the considered problem. Simulation results illustrate the effectiveness of the proposed scheme compared to two baseline schemes. Moreover, the results unveil that deploying active IRSs is a promising approach to enhance the system performance compared to conventional passive IRSs, especially when strong direct links exist.**

I. Introduction

Future wireless communication systems are envisioned to provide high data-rate communication services [1]. Inspired by recent advances in electromagnetic metamaterials, revolutionary new metasurfaces, called intelligent reflecting surfaces (IRSs) have been proposed for deployment in conventional communication networks to satisfy this demand [2]. In particular, comprising a number of programmable elements, IRSs can be smartly adapted to the channel conditions so as to proactively customize the radio propagation environment for enhancing the system performance [3]. Moreover, due to the passive nature of the reflecting elements, e.g., diodes and phase shifters, the power required for maintaining the IRS operation is typically very small [2]. Furthermore, commonly fabricated as thin rectangular surfaces, IRSs can be flexibly deployed coexisting with existing infrastructure and smoothly integrate into conventional communication systems.

These favorable properties have motivated numerous works to study IRSs for performance enhancement of conventional communication systems [4]–[6]. Yet, in practice, the end-to-end path loss of the BS-IRS-receiver link is in general much larger than that of the unobstructed direct link due to the double path loss effect [7]. Hence, employing passive IRSs may not effectively enhance the system performance. To compensate for the severe double path loss in the cascaded IRS channel, one has to adopt a large passive IRS comprising hundreds if not thousands of phase shift elements to achieve a significant passive beamforming gain [7], [8]. However, deploying a large number of passive IRS elements significantly increases the signaling overhead for channel estimation and the complexity of IRS optimization [4]–[6], which makes the design of IRS-assisted wireless systems challenging in practice. To circumvent these issues, the authors of [9] recently proposed a new IRS structure, namely, active IRSs. In particular, equipped with reflection-type amplifiers [10], [11], active IRSs can not only reflect the incident signals by manipulating the programmable IRS elements, but also amplify the reflected signal with the support of an extra power supply. We note that active IRSs are fundamentally different from full-duplex amplify-and-forward (FD-AF) relays in terms of hardware architecture and the mode of transmission. Specifically, equipped with radio frequency (RF) chains, FD-AF relays are able to receive the incident signal and then transmit it after amplification at the expense of self-interference. This process introduces a delay incurred by the signal processing at the relay. In contrast, equipped with low-power reflection-type amplifiers, active IRSs reflect and amplify the incident signal instantaneously, and the resulting delay between the direct link and the reflected link is negligibly small compared to the symbol duration [4]. Moreover, the signals received at different relay antennas are jointly amplified via an amplification matrix. In contrast, for active IRSs, the signals received at different IRS elements are individually amplified. On the other hand, compared to conventional passive IRSs, active IRSs can effectively compensate the double path loss effect without significantly complicating the IRS design [9]. To illustrate this, the authors of [9] studied the joint transmit and reflect beamforming design for maximization of the spectral efficiency of an active IRS-assisted multiuser communication system. The resource allocation algorithm design was formulated as a series of quadratic constraint quadratic programming (QCQP) problems which were tackled in an

alternating manner. In fact, to realize the potential gains facilitated by active IRSs, the appropriate amount of power has to be assigned to each element of the active IRS from the limited available power. As a result, compared to systems assisted by conventional passive IRSs, it is more important to delicately design the BS beamforming such that the power consumption of the whole system is still affordable and the quality-of-service (QoS) requirements of the users can be satisfied. Alternating optimization (AO)-based optimization frameworks cannot effectively handle the aforementioned power minimization problem. In particular, such problems cannot be easily transformed to standard QCQP or second-order cone program (SOCP) problems with convex constraints that can be efficiently solved by employing AO-based algorithms [4], [9]. Moreover, by dividing the coupled optimization variables into disjoint groups, AO-based algorithms inevitably eliminate the joint optimality of the BS beamforming vectors, the IRS amplification factor matrix, and the IRS phase shift matrix in the considered power minimization problem, which may lead to unsatisfactory performance [12]. Besides, for the considered power minimization problem, the monotonicity of the objective value during AO cannot be guaranteed because of the required Gaussian randomization [6].

Motivated by the above discussion, in this paper, we investigate the resource allocation algorithm design for active IRS-assisted communication systems, where the active IRS can amplify the reflected signal exploiting an additional power source. To this end, we aim to minimize the transmit power of the BS by jointly designing the BS beamformers and the IRS reflection matrix, taking into account the QoS requirements of the users and the maximum power budget of the active IRS. Since the optimization variables are highly coupled in the resulting non-convex optimization problem, the corresponding globally optimal solution is challenging to obtain. As a compromise, by capitalizing on bilinear transformation, inner approximation, and semidefinite relaxation, we develop a novel iterative algorithm, which enjoys low computational complexity. The proposed algorithm is guaranteed to converge to a locally optimal solution of the considered problem. Our simulation results reveal that active IRSs are a promising solution to fully exploit the potential of IRS-assisted wireless systems, especially when non-negligible direct links exist.

Notation: Vectors and matrices are denoted by boldface lower case and boldface capital letters, respectively. $\mathbb{R}_{+}^{N\times M}$ and $\mathbb{C}^{N\times M}$ denote the spaces of $N \times M$ positive real-valued matrices and complex-valued matrices, respectively. $\Re\{\cdot\}$ extracts the real part of a complex number. $|\cdot|$ and $||\cdot||$ denote the absolute value of a complex scalar and the Euclidean norm of its argument, respectively. $\mathbf{I}_N$ refers to the identity matrix of dimension N. $\mathbb{H}^N$ denotes the set of complex Hermitian matrices of dimension N. $\mathbf{A}^H$ refers to the conjugate transpose of matrix $\mathbf{A}$. $\mathbf{A} \succeq \mathbf{0}$ indicates that $\mathbf{A}$ is a positive semidefinite matrix. $||\mathbf{A}||_F$, $\mathrm{Tr}(\mathbf{A})$, and $\mathrm{Rank}(\mathbf{A})$ denote the Frobenius norm, the trace, and the rank of matrix $\mathbf{A}$, respectively. $\mathrm{diag}(\mathbf{a})$ represents a diagonal matrix whose main diagonal elements are extracted from vector $\mathbf{a}$; $\mathrm{Diag}(\mathbf{A})$ denotes a vector whose elements are extracted from the main diagonal elements of matrix $\mathbf{A}$. $\mathcal{E}\{\cdot\}$ represents statistical expectation. $\triangleq$ and $\sim$ refer to "defined as" and "distributed as", respectively. $\mathcal{CN}(\mu, \sigma^2)$ indicates the distribution of a circularly symmetric complex Gaussian random variable with mean μ and variance σ^2. $\mathbf{X}^*$ refers to the optimal value of optimization variable $\mathbf{X}$.

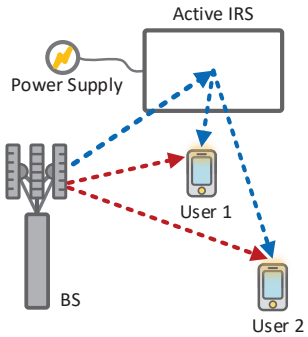

Fig. 1. An active IRS-assisted communication system consist of one multi-antenna BS and $K = 2$ users. The active IRS is supported by a power supply. The direct links and reflected links between the BS and the users are denoted by red dashed lines and blue dash lines, respectively.

II. System Model

We consider an active IRS-assisted multiuser multiple-input single-output (MISO) communication system, cf. Figure 1. The BS is equipped with N_{T} antennas while all K users are single-antenna devices. To enhance the performance of the considered system, an active IRS is employed to assist the information transmission from the BS to the users. In particular, the active IRS is composed of M elements and is supported by an additional power source. Equipped with an integrated active reflection-type amplifier, each IRS element can not only smartly alter the phase of the incident signals, but also amplify the reflected signal for effective beamforming. To establish a performance upper bound for the considered system, we assume that the perfect channel state information (CSI) of the entire system is available at the BS. The CSI can be acquired with one of the existing channel estimation schemes proposed for IRS-assisted wireless systems [13], [14]. To simplify the notation, we collect the indices of the users and IRS elements in sets $\mathcal{K} = \{1, \cdots, K\}$ and $\mathcal{M} = \{1, \cdots, M\}$, respectively.

In each scheduled time slot, the signal vector $\mathbf{x}$ transmitted by the BS is constructed as follows

$$\mathbf{x} = \sum_{k\in\mathcal{K}} \mathbf{w}_k b_k, \tag{1}$$

where $\mathbf{w}_k \in \mathbb{C}^{N_{\mathrm{T}}\times 1}$ and $b_k \in \mathbb{C}$ denote the beamforming vector for user k and the corresponding information symbol. We assume $\mathcal{E}\{|b_k|^2\} = 1$, $\forall k \in \mathcal{K}$, without loss of generality.

Employing reflection-type amplifiers [10] driven by a common power supply, the signal reflected and amplified by the active IRS is given by

$$\mathbf{y} = \mathbf{A}\boldsymbol{\Theta}\mathbf{G}\mathbf{x} + \underbrace{\mathbf{A}\boldsymbol{\Theta}\mathbf{d}}_{\text{dynamic noise}} + \underbrace{\mathbf{s}}_{\text{static noise}}, \tag{2}$$

where $\mathbf{A} \triangleq \text{diag}(a_1, \cdots, a_M) \in \mathbb{R}_+^{M\times M}$ and $\boldsymbol{\Theta} \triangleq \text{diag}(e^{j\psi_1}, \cdots, e^{j\psi_M}) \in \mathbb{C}^{M\times M}$ denote the amplification factor matrix and the phase shift matrix of the active IRS, respectively. Matrix $\mathbf{G} \in \mathbb{C}^{M\times N_\text{T}}$ denotes the channel between the BS and the IRS. Moreover, we observe from (2) that the noises at the IRS can be divided into two categories, i.e., dynamic noise and static noise [9]. In particular, the dynamic noise is generated due to the power amplification [11], where $\mathbf{d} \in \mathbb{C}^{N_\text{T}\times 1}$ is modelled as additive white Gaussian noise (AWGN) with variance σ_d^2, i.e., $\mathbf{d} \sim \mathcal{CN}(\mathbf{0}_{N_\text{T}}, \sigma_d^2\mathbf{I}_{N_\text{T}})$ [9]. The static noise $\mathbf{s} \in \mathbb{C}^{N_\text{T}\times 1}$ is modelled as AWGN with variance σ_s^2, i.e., $\mathbf{s} \sim \mathcal{CN}(\mathbf{0}_{N_\text{T}}, \sigma_s^2\mathbf{I}_{N_\text{T}})$, and it is not affected by $\mathbf{A}$ and its power is usually negligibly small compared to that of the dynamic noise $\mathbf{A}\boldsymbol{\Theta}\mathbf{d}$ [15].

The received signal at user k is given by

$$r_k = \underbrace{(\mathbf{h}_{\text{D},k}^H + \mathbf{h}_{\text{R},k}^H\mathbf{A}\boldsymbol{\Theta}\mathbf{G})\mathbf{w}_k b_k}_{\text{desired signal}} + \underbrace{\mathbf{h}_{\text{R},k}^H\mathbf{A}\boldsymbol{\Theta}\mathbf{d}}_{\text{dynamic noise introduced by IRS}} + \underbrace{(\mathbf{h}_{\text{D},k}^H + \mathbf{h}_{\text{R},k}^H\mathbf{A}\boldsymbol{\Theta}\mathbf{G})\sum_{\substack{r\in\mathcal{K}\\ r\neq k}}\mathbf{w}_r b_r}_{\text{multiuser interference}} + \underbrace{n_k}_{\text{noise at user } k}, \tag{3}$$

where $\mathbf{h}_{\text{D},k} \in \mathbb{C}^{N_\text{T}\times 1}$ and $\mathbf{h}_{\text{R},k} \in \mathbb{C}^{M\times 1}$ denote the channel vectors of the BS-user k link (direct link) and the IRS-user k link (reflected link), respectively. n_k represents the AWGN at the user k with zero mean and variance $\sigma_{n_k}^2$, i.e., $n_k \sim \mathcal{CN}(0, \sigma_{n_k}^2)$.

III. Problem Formulation

The received signal-to-interference-plus-noise ratio (SINR) of user k is given by

$$\Gamma_k = \frac{\left|(\mathbf{h}_{\text{D},k}^H + \mathbf{h}_{\text{R},k}^H\mathbf{A}\boldsymbol{\Theta}\mathbf{G})\mathbf{w}_k\right|^2}{\sum\limits_{\substack{r\in\mathcal{K}\\ r\neq k}}\left|(\mathbf{h}_{\text{D},k}^H+\mathbf{h}_{\text{R},k}^H\mathbf{A}\boldsymbol{\Theta}\mathbf{G})\mathbf{w}_r\right|^2 + \sigma_d^2\left\|\mathbf{h}_{\text{R},k}^H\mathbf{A}\boldsymbol{\Theta}\right\|^2 + \sigma_{n_k}^2}. \tag{4}$$

In this paper, we aim to minimize the BS transmit power while satisfying the QoS requirements of the users and the maximum power allowance of the active IRS. In particular, the joint design of the BS beamforming vectors, the IRS amplification factor matrix, and the IRS phase shift matrix, i.e., $\{\mathbf{w}_k, \mathbf{A}, \boldsymbol{\Theta}\}$, is obtained by solving the following optimization problem

$$\begin{aligned} \underset{\mathbf{w}_k,\mathbf{A},\boldsymbol{\Theta}}{\text{minimize}} \quad & \sum_{k\in\mathcal{K}}\|\mathbf{w}_k\|^2 \\ \text{s.t.} \quad & \text{C1: } \Gamma_{\text{req}_k} \le \Gamma_k, \ \forall k, \\ & \text{C2: } \sum_{k\in\mathcal{K}}\|\mathbf{A}\boldsymbol{\Theta}\mathbf{G}\mathbf{w}_k\|^2 + \sigma_d^2\|\mathbf{A}\boldsymbol{\Theta}\|_F^2 \le P_\text{A}. \end{aligned} \tag{5}$$

Here, Γ_{req_k} in constraint C1 is the minimum required SINR of user k. Constraint C2 indicates that the amplification power of the active IRS should be less than or equal to the maximum power allowance P_A. We note that the optimization problem in (5) is non-convex due to the coupled optimization variables and the fractional constraint C1. Next, by employing the bilinear transformation and IA, we develop a iterative low-complexity algorithm which is guaranteed to converge to a locally optimal solution of the problem in (5).

Remark 1: Compared to passive IRS design, though active IRS design sidesteps the unit-modulus constraint, it also introduces the additional non-convex constraint C2 which aggravates the coupling between the optimization variables. In fact, for resource allocation design for IRS-assisted systems, the coupling between the optimization variables is an unavoidable obstacle. For passive IRSs, such obstacle is commonly tackled by employing AO-based algorithms [9], [16] or IA-based algorithms [6]. However, employing AO-based algorithms destroys the joint optimality of the optimization variables, which may lead to unsatisfactory system performance. Moreover, it has been shown in [6] that for power minimization problems, the commonly adopted AO-based algorithm with Gaussian randomization is not guaranteed to generate a monotonically decreasing sequence of the objective function values during the iterations. On the other hand, when directly applying IA, the matrix $\boldsymbol{\Theta} = \text{diag}(e^{j\psi_1}, \cdots, e^{j\psi_M})$ at the IRS is first transformed into a vector $\mathbf{v} = [e^{j\psi_1}, \cdots, e^{j\psi_M}]^H$ [16]. Then, a new optimization variable $\mathbf{V}$ is defined as $\mathbf{V} = \mathbf{v}\mathbf{v}^H$, which imposes three additional constraints on the considered optimization problem, i.e., $\mathbf{V} \succeq \mathbf{0}$, $\text{Diag}(\mathbf{V}) = \mathbf{1}$, and a non-convex constraint $\text{Rank}(\mathbf{V}) = 1$. In the literature, the rank-one constraint is usually removed by employing SDR. However, by doing so, the rank of the obtained solution is in general larger than one [17]. Alternatively, $\text{Rank}(\mathbf{V}) = 1$ can be equivalently transformed into a difference of norm functions, and then be tackled by a penalty-based algorithm [18]. However, since the penalty factor cannot be infinitely large in practice, such an approach can only guarantee a suboptimal solution. To circumvent these obstacles, in this paper, for active IRSs, we employ bilinear transformation and IA and develop a low-complexity iterative algorithm which is guaranteed to converge to a locally optimal solution of the optimization problem in (5) [19].

IV. Solution of the Optimization problem

A. Bilinear Transformation

Note that matrices $\mathbf{A}$ and $\boldsymbol{\Theta}$ in (5) always appear in product form. Hence, we rewrite the product term $\mathbf{A}\boldsymbol{\Theta}$ as $\boldsymbol{\Psi} = \text{diag}(a_1e^{j\psi_1}, \cdots, a_Me^{j\psi_M}) \in \mathbb{C}^{M\times M}$. Then, the quadratic term $\sigma_d^2\left\|\mathbf{h}_{\text{R},k}^H\mathbf{A}\boldsymbol{\Theta}\right\|^2$ in constraint C1 can be rewritten as follows

$$\sigma_d^2\left\|\mathbf{h}_{\text{R},k}^H\mathbf{A}\boldsymbol{\Theta}\right\|^2 = \sigma_d^2\text{Tr}(\boldsymbol{\Psi}^H\mathbf{H}_{\text{R},k}\boldsymbol{\Psi}), \tag{6}$$

where $\mathbf{H}_{\text{R},k} \in \mathbb{C}^{M\times M}$ is defined as $\mathbf{H}_{\text{R},k} = \mathbf{h}_{\text{R},k}\mathbf{h}_{\text{R},k}^H$. To facilitate the application of the IA algorithm, we de-

fine $\mathbf{W}_k = \mathbf{w}_k\mathbf{w}_k^H$, $\forall k$, and rewrite the quadratic term $\left|(\mathbf{h}_{\mathrm{D},k}^H + \mathbf{h}_{\mathrm{R},k}^H\mathbf{\Psi}\mathbf{G})\mathbf{w}_r\right|^2$ in constraint C1 as follows

$$\begin{aligned}
&\left|(\mathbf{h}_{\mathrm{D},k}^H + \mathbf{h}_{\mathrm{R},k}^H\mathbf{\Psi}\mathbf{G})\mathbf{w}_r\right|^2 \\
=\ & \mathbf{h}_{\mathrm{D},k}^H\mathbf{W}_r\mathbf{h}_{\mathrm{D},k} + \mathbf{h}_{\mathrm{R},k}^H\mathbf{\Psi}\mathbf{G}\mathbf{W}_r\mathbf{G}^H\mathbf{\Psi}^H\mathbf{h}_{\mathrm{R},k} \\
+\ & 2\Re\left\{\mathbf{h}_{\mathrm{D},k}^H\mathbf{W}_r\mathbf{G}^H\mathbf{\Psi}^H\mathbf{h}_{\mathrm{R},k}\right\} \\
=\ & \mathrm{Tr}\left(\begin{bmatrix}\mathbf{h}_{\mathrm{R},k}\\ \mathbf{h}_{\mathrm{D},k}\end{bmatrix}\begin{bmatrix}\mathbf{h}_{\mathrm{R},k}^H & \mathbf{h}_{\mathrm{D},k}^H\end{bmatrix}\begin{bmatrix}\mathbf{0} & \mathbf{\Psi}\mathbf{G}\mathbf{W}_r^H\\ \mathbf{W}_r\mathbf{G}^H\mathbf{\Psi}^H & \mathbf{0}\end{bmatrix}\right) \\
+\ & \mathrm{Tr}(\mathbf{H}_{\mathrm{D},k}\mathbf{W}_r) + \mathrm{Tr}(\mathbf{\Psi}\mathbf{G}\mathbf{W}_r\mathbf{G}^H\mathbf{\Psi}^H\mathbf{H}_{\mathrm{R},k}), \qquad (7)
\end{aligned}$$

where $\mathbf{H}_{\mathrm{D},k} \in \mathbb{C}^{N_{\mathrm{T}}\times N_{\mathrm{T}}}$ is defined as $\mathbf{H}_{\mathrm{D},k} = \mathbf{h}_{\mathrm{D},k}\mathbf{h}_{\mathrm{D},k}^H$. Then, we recast the optimization problem in (5) equivalently as follows

$$\begin{aligned}
\underset{\mathbf{\Psi},\mathbf{W}_k\in\mathbb{H}^{N_{\mathrm{T}}}}{\text{minimize}} \quad & \sum_{k\in\mathcal{K}}\mathrm{Tr}(\mathbf{W}_k) \\
\text{s.t.}\ \ & \text{C1: } \Gamma_k \geq \Gamma_{\mathrm{req}_k},\ \forall k, \\
& \text{C2: } \sum_{k\in\mathcal{K}}\mathrm{Tr}(\mathbf{\Psi}\mathbf{G}\mathbf{W}_k\mathbf{G}^H\mathbf{\Psi}^H) + \sigma_d^2\mathrm{Tr}(\mathbf{\Psi}\mathbf{\Psi}^H) \leq P_{\mathrm{A}}, \\
& \text{C3: } \mathbf{W}_k \succeq \mathbf{0},\ \forall k, \quad \text{C4: } \mathrm{Rank}(\mathbf{W}_k) \leq 1,\ \forall k. \qquad (8)
\end{aligned}$$

We note that the coupling between $\mathbf{W}_k$ and $\mathbf{\Psi}$ in constraints C1 and C2 and the rank-one constraint C4 are obstacles to solving (8). Next, we take the term $\mathrm{Tr}(\mathbf{\Psi}\mathbf{G}\mathbf{W}_r\mathbf{G}^H\mathbf{\Psi}^H\mathbf{H}_{\mathrm{R},k})$ as an example to illustrate how to construct a convex subset for the non-convex constraint C1. Note the fact that for arbitrary matrices $\mathbf{C}$ and $\mathbf{D}$ having the same dimensions, we have $\mathrm{Tr}(\mathbf{C}\mathbf{D}) = \frac{1}{2}\left\|\mathbf{C}+\mathbf{D}\right\|_F^2 - \frac{1}{2}\mathrm{Tr}(\mathbf{C}^H\mathbf{C}) - \frac{1}{2}\mathrm{Tr}(\mathbf{D}^H\mathbf{D})$. Hence, we first rewrite the coupling term $\mathrm{Tr}(\mathbf{\Psi}\mathbf{G}\mathbf{W}_r\mathbf{G}^H\mathbf{\Psi}^H\mathbf{H}_{\mathrm{R},k})$ as follows

$$\begin{aligned}
&\mathrm{Tr}(\mathbf{\Psi}\mathbf{G}\mathbf{W}_r\mathbf{G}^H\mathbf{\Psi}^H\mathbf{H}_{\mathrm{R},k}) \\
=\ & \frac{1}{2}\left\|\mathbf{\Psi} + \mathbf{G}\mathbf{W}_r\mathbf{G}^H\mathbf{\Psi}^H\mathbf{H}_{\mathrm{R},k}\right\|_F^2 - \frac{1}{2}\mathrm{Tr}(\mathbf{\Psi}^H\mathbf{\Psi}) \\
& -\frac{1}{2}\mathrm{Tr}(\mathbf{H}_{\mathrm{R},k}^H\mathbf{\Psi}\mathbf{G}\mathbf{W}_r^H\mathbf{G}^H\mathbf{G}\mathbf{W}_r\mathbf{G}^H\mathbf{\Psi}^H\mathbf{H}_{\mathrm{R},k}). \qquad (9)
\end{aligned}$$

We note that the right-hand side term of (9) contains a bilinear function of optimization variables $\mathbf{W}_r$ and $\mathbf{\Psi}$, i.e., $\mathbf{G}\mathbf{W}_r\mathbf{G}^H\mathbf{\Psi}^H\mathbf{H}_{\mathrm{R},k}$, which is still non-convex. To circumvent this challenge, we further define a new optimization variable $\mathbf{Z}_r = \mathbf{W}_r\mathbf{G}^H\mathbf{\Psi}^H$, where $\mathbf{Z}_r \in \mathbb{C}^{N_{\mathrm{T}}\times M}$. Then, we introduce the following lemma to transform the constraint $\mathbf{Z}_r = \mathbf{W}_r\mathbf{G}^H\mathbf{\Psi}^H$ to a more tractable form.

Lemma 1: The equality constraint $\mathbf{Z}_r = \mathbf{W}_r\mathbf{G}^H\mathbf{\Psi}^H$ is equivalent to the following inequality constraints:

$$\text{C5: } \begin{bmatrix}\mathbf{U}_r & \mathbf{Z}_r & \mathbf{W}_r\mathbf{G}^H\\ \mathbf{Z}_r^H & \mathbf{V}_r & \mathbf{\Psi}\\ \mathbf{G}\mathbf{W}_r^H & \mathbf{\Psi}^H & \mathbf{I}_M\end{bmatrix} \succeq \mathbf{0},\ \forall r\in\mathcal{K}, \qquad (10)$$

$$\text{C6: } \mathrm{Tr}\left(\mathbf{U}_r - \mathbf{W}_r\mathbf{G}^H\mathbf{G}\mathbf{W}_r^H\right) \leq 0,\ \forall r\in\mathcal{K}, \qquad (11)$$

where $\mathbf{U}_r \in \mathbb{C}^{N_{\mathrm{T}}\times N_{\mathrm{T}}}$ and $\mathbf{V}_r \in \mathbb{C}^{M\times M}$ are auxiliary optimization variables.

Proof: The equality constraint $\mathbf{Z}_r = \mathbf{W}_r\mathbf{G}^H\mathbf{\Psi}^H$ has a similar structure as the constraint in [20, Eq. (3)] and Lemma 1 can be proved by closely following the same steps as in [20, Appendix A]. Due to the space limitation, we omit the detailed proof of Lemma 1.

B. Inner Approximation

After employing the proposed bilinear transformation, we can rewrite the right-hand side term of (9) as follows

$$\begin{aligned}
&\frac{1}{2}\left\|\mathbf{\Psi} + \mathbf{G}\mathbf{Z}_r\mathbf{H}_{\mathrm{R},k}\right\|_F^2 - \frac{1}{2}\mathrm{Tr}\left(\mathbf{\Psi}^H\mathbf{\Psi}\right) \\
&-\frac{1}{2}\mathrm{Tr}\left(\mathbf{H}_{\mathrm{R},k}^H\mathbf{Z}_r^H\mathbf{G}^H\mathbf{G}\mathbf{Z}_r\mathbf{H}_{\mathrm{R},k}\right). \qquad (12)
\end{aligned}$$

We note that the quadratic terms $\mathrm{Tr}(\mathbf{\Psi}^H\mathbf{\Psi})$ and $\mathrm{Tr}(\mathbf{H}_{\mathrm{R},k}^H\mathbf{Z}_r^H\mathbf{G}^H\mathbf{G}\mathbf{Z}\mathbf{H}_{\mathrm{R},k})$ are obstacles for efficient algorithm design. To handle this issue, we construct respective global underestimators for these terms by employing their first-order Taylor approximations via the iterative IA approach. In particular, we have

$$\mathrm{Tr}\left(\mathbf{\Psi}^H\mathbf{\Psi}\right) \geq \mathrm{Tr}\left(\left(2\mathbf{\Psi}^{(j)}\right)^H\mathbf{\Psi}\right) - \left\|\mathbf{\Psi}^{(j)}\right\|_F^2, \qquad (13)$$

$$\begin{aligned}
&\mathrm{Tr}\left(\mathbf{H}_{\mathrm{R},k}^H\mathbf{Z}_r^H\mathbf{G}^H\mathbf{G}\mathbf{Z}_r\mathbf{H}_{\mathrm{R},k}\right) \\
&\geq \mathrm{Tr}\left(\left(2\mathbf{H}_{\mathrm{R},k}^H\mathbf{G}^H\mathbf{G}\mathbf{Z}_r^{(j)}\mathbf{H}_{\mathrm{R},k}\right)^H\mathbf{Z}_r\right) - \left\|\mathbf{G}\mathbf{Z}_r^{(j)}\mathbf{H}_{\mathrm{R},k}\right\|_F^2, \qquad (14)
\end{aligned}$$

where $\mathbf{\Psi}^{(j)}$ and $\mathbf{Z}_r^{(j)}$ are intermediate solutions obtained in the j-th iteration and superscript j denotes the iteration index of the optimization variables. Moreover, by applying steps similar to (7), (9), (13), and (14), we construct an upper bound for the term $-\left|(\mathbf{h}_{\mathrm{D},k}^H + \mathbf{h}_{\mathrm{R},k}^H\mathbf{A}\mathbf{\Theta}\mathbf{G})\mathbf{w}_k\right|^2$ in constraint C1. As a result, a convex subset of constraint C1 is obtained in constraint $\overline{\text{C1}}$ which is shown at the top of the next page. Here, $\widetilde{\mathbf{h}}_k^H \in \mathbb{C}^{1\times(M+N_{\mathrm{T}})}$ is defined as $\widetilde{\mathbf{h}}_k^H = [\mathbf{h}_{\mathrm{R},k}^H\ \mathbf{h}_{\mathrm{D},k}^H]$. Similarly, constraint C2 can be approximated by the following convex constraint:

$$\begin{aligned}
\overline{\text{C2}}\text{: } & \sum_{k\in\mathcal{K}}\left[\frac{1}{2}\left\|\mathbf{\Psi} + \mathbf{G}\mathbf{Z}_k\right\|_F^2 - \mathrm{Tr}\left(\left(\mathbf{G}^H\mathbf{G}\mathbf{Z}_k^{(j)}\right)^H\mathbf{Z}_k\right)\right] \\
& -K\left[\mathrm{Tr}\left(\left(\mathbf{\Psi}^{(j)}\right)^H\mathbf{\Psi}\right) - \frac{1}{2}\left\|\mathbf{\Psi}^{(j)}\right\|_F^2 - \frac{1}{2}\left\|\mathbf{G}\mathbf{Z}_k^{(j)}\right\|_F^2\right] \\
& +\sigma_d^2\mathrm{Tr}(\mathbf{\Psi}\mathbf{\Psi}^H) \leq P_{\mathrm{A}}. \qquad (16)
\end{aligned}$$

On the other hand, we note that constraint C6 is in the canonical form of a difference of convex functions which is a non-convex constraint. To tackle this obstacle, again, we construct a global underestimator of $\mathrm{Tr}(\mathbf{W}_r\mathbf{G}^H\mathbf{G}\mathbf{W}_r^H)$. Specifically, we have

$$\begin{aligned}
&\mathrm{Tr}(\mathbf{W}_r\mathbf{G}^H\mathbf{G}\mathbf{W}_r^H) \\
&\geq -\left\|\mathbf{W}_r^{(j)}\mathbf{G}^H\right\|_F^2 + 2\mathrm{Tr}\left((\mathbf{G}^H\mathbf{G}\mathbf{W}_r^{(j)})^H\mathbf{W}_r\right). \qquad (17)
\end{aligned}$$

Then, constraint C6 can be approximated by the following convex constraint:

$$\begin{aligned}
\overline{\text{C6}}\text{: } & \mathrm{Tr}\left(\mathbf{U}_r\right) + \left\|\mathbf{W}_r^{(j)}\mathbf{G}^H\right\|_F^2 \\
& -2\mathrm{Tr}\left((\mathbf{G}^H\mathbf{G}\mathbf{W}_r^{(j)})^H\mathbf{W}_r\right) \leq 0,\ \forall r\in\mathcal{K}. \qquad (18)
\end{aligned}$$

Therefore, the optimization problem to be solved in the $(j+1)$-th iteration of the IA-based algorithm is given by

$$\underset{\substack{\mathbf{\Psi},\mathbf{W}_k\in\mathbb{H}^{N_{\mathrm{T}}},\\ \mathbf{Z}_k,\mathbf{U}_k,\mathbf{V}_k}}{\text{minimize}} \quad F(\mathbf{W}_k) \triangleq \sum_{k\in\mathcal{K}}\mathrm{Tr}(\mathbf{W}_k)$$

$$\overline{\text{C1}}\text{: } \frac{\Gamma_{\text{req}_k}}{2}\sum_{r\in\mathcal{K}\setminus\{k\}}\|\boldsymbol{\Psi}+\mathbf{G}\mathbf{Z}_r\mathbf{H}_{\text{R},k}\|_F^2-[\Gamma_{\text{req}_k}(K-1)-1]\left[\text{Tr}\left(\left(\boldsymbol{\Psi}^{(j)}\right)^H\boldsymbol{\Psi}\right)-\frac{1}{2}\left\|\boldsymbol{\Psi}^{(j)}\right\|_F^2\right]-\text{Tr}(\mathbf{H}_{\text{D},k}\mathbf{W}_k)$$
$$-\Gamma_{\text{req}_k}\sum_{r\in\mathcal{K}\setminus\{k\}}\left[\text{Tr}\left(\left(\mathbf{H}_{\text{R},k}^H\mathbf{G}^H\mathbf{G}\mathbf{Z}_r^{(j)}\mathbf{H}_{\text{R},k}\right)^H\mathbf{Z}_r\right)-\frac{1}{2}\left\|\mathbf{G}\mathbf{Z}_r^{(j)}\mathbf{H}_{\text{R},k}\right\|_F^2\right]-\frac{1}{2}\left\|\mathbf{G}\mathbf{Z}_k^{(j)}\mathbf{H}_{\text{R},k}\right\|_F^2$$
$$+\Gamma_{\text{req}_k}\left(\sum_{r\in\mathcal{K}\setminus\{k\}}\text{Tr}(\mathbf{H}_{\text{D},k}\mathbf{W}_r)+\sigma_d^2\text{Tr}(\boldsymbol{\Psi}^H\mathbf{H}_{\text{R},k}\boldsymbol{\Psi})+\sigma_{n_k}^2\right)-\frac{1}{2}\|\boldsymbol{\Psi}+\mathbf{G}\mathbf{Z}_k\mathbf{H}_{\text{R},k}\|_F^2$$
$$+\text{Tr}\left(\left(\mathbf{H}_{\text{R},k}^H\mathbf{G}^H\mathbf{G}\mathbf{Z}_k^{(j)}\mathbf{H}_{\text{R},k}\right)^H\mathbf{Z}_k\right)+\text{Tr}\left(\widetilde{\mathbf{h}}_k\widetilde{\mathbf{h}}_k^H\begin{bmatrix}\mathbf{0} & \Gamma_{\text{req}_k}\sum\limits_{r\in\mathcal{K}\setminus\{k\}}\mathbf{Z}_r^H-\mathbf{Z}_k^H\\ \Gamma_{\text{req}_k}\sum\limits_{r\in\mathcal{K}\setminus\{k\}}\mathbf{Z}_r-\mathbf{Z}_k & \mathbf{0}\end{bmatrix}\right)\leq 0,\forall k. \quad (15)$$

Algorithm 1 IA-based Algorithm

1: Set initial point $\mathbf{W}_k^{(j)}$, $\boldsymbol{\Psi}^{(j)}$, $\mathbf{Z}_k^{(j)}$, $\mathbf{U}_k^{(j)}$, $\mathbf{V}_k^{(j)}$, iteration index $j=1$, and error tolerance $0<\epsilon\ll 1$.
2: **repeat**
3: For given $\mathbf{W}_k^{(j)}$, $\boldsymbol{\Psi}^{(j)}$, $\mathbf{Z}_k^{(j)}$, $\mathbf{U}_k^{(j)}$, $\mathbf{V}_k^{(j)}$, obtain the intermediate solution $\mathbf{W}_k^{(j+1)}$, $\boldsymbol{\Psi}^{(j+1)}$, $\mathbf{Z}_k^{(j+1)}$, $\mathbf{U}_k^{(j+1)}$, $\mathbf{V}_k^{(j+1)}$ by solving the rank constraint-relaxed version of problem (19)
4: Set $j=j+1$
5: **until** $\frac{F(\mathbf{W}_k^{(j-1)})-F(\mathbf{W}_k^{(j)})}{F(\mathbf{W}_k^{(j)})}\leq\epsilon$

$$\text{s.t.}\quad \overline{\text{C1}},\overline{\text{C2}},\text{C3},\text{C4},\text{C5},\overline{\text{C6}}. \quad (19)$$

We note that the only obstacle to efficiently solving (19) is the rank-one constraint C4. To convexify the optimization problem in (19), we apply SDR and remove constraint C4 from the formulation. Then, the resulting relaxed version of (19) becomes a standard convex optimization problem which can be optimally solved by convex program solvers such as CVX [21]. Next, we introduce the following theorem to reveal the tightness of SDR.

Theorem 1: Given any positive Γ_{req_k}, the optimal beamforming matrix obtained from (19), i.e., $\mathbf{W}_k^*$, is always a rank-one matrix.

Proof: Problem (19) has a similar structure as [6, Problem (17)] and Theorem 1 can be proved following the same steps as in [6, Appendix]. The detailed proof of Theorem 1 is omitted for brevity. ■

We summarize the proposed algorithm in **Algorithm 1**. Note that the objective function of (19) is monotonically non-increasing in each iteration of **Algorithm 1**. Moreover, according to [19, Theorem 1], the proposed algorithm is guaranteed to converge to a locally optimal solution of (5) in polynomial time. The per iteration computational complexity of **Algorithm 1** is given by $\mathcal{O}\Big(\log(1/\epsilon)\big((3K+1)^3+(3K+1)^2N_{\text{T}}^2+(3K+1)N_{\text{T}}^3+(2K+1)^3+(2K+1)^2M^2+(2K+1)M^3\big)\Big)$, where $\mathcal{O}(\cdot)$ is the big-O notation [22, Theorem 3.12] and ϵ is the convergence tolerance of **Algorithm 1**.

TABLE I
SYSTEM SIMULATION PARAMETERS.

f_c	Carrier center frequency	2.4 GHz
σ_k^2	Noise power at the users	-114 dBm
σ_d^2	Dynamic noise power	-100 dBm [9]
ϵ	Convergence tolerance	10^{-3}

V. Simulation Results

In this section, the system performance of the proposed resource allocation scheme is evaluated via simulations. The BS is equipped with $N_{\text{T}}=4$ antennas and serves one sector of a cell with a radius of R m, where $K=3$ users are randomly and uniformly distributed in this sector. The active IRS comprises M elements and is deployed at the edge of the sector. Moreover, the fading coefficients of all the channels are generated as independent and identically distributed Rician random variables with Rician factor 3 dB. In addition, the path loss exponents for the direct links and the reflected links between the BS and the users are α_{d} and α_{r}, respectively. For ease of presentation, we assume that the minimum required SINRs of all users are identical, i.e., $\Gamma_{\text{req}_k}=\Gamma_{\text{req}}$, $\forall k$. The adopted simulation parameter values are listed in Table I.

For comparison, we consider two baseline schemes. For baseline scheme 1, we assume that an IRS is not deployed. Then, we optimize the beamforming vector $\mathbf{w}_k$ for minimization of the transmit power at the BS. For baseline scheme 2, we divide the power available at the active IRS, P_{A}, equally among the IRS elements, i.e., $a_m=\sqrt{\frac{P_{\text{A}}}{M}}$, $\forall m\in\mathcal{M}$, and generate the phases of the IRS elements in a random manner. Moreover, we adopt zero-forcing (ZF) beamforming at the BS. Then, we solve a problem similar to problem (5), where we optimize the power allocated to user k, i.e., $p_k\in\mathbb{R}_+$.

A. Transmit Power Minimization

In Figure 2, we investigate the average BS transmit power versus the minimum required SINR of the users for a scenario where the direct links are severely shadowed ($\alpha_{\text{d}}=3.8$). We can observe from Figure 2 that the transmit power of the proposed scheme and the two baseline schemes

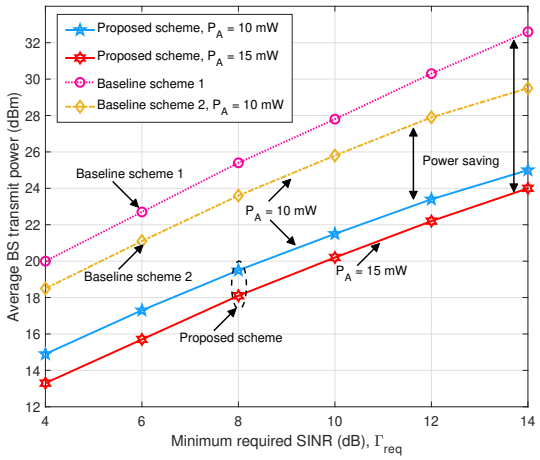

Fig. 2. Average BS transmit power (dBm) versus minimum required SINR of the users for $K = 3$, $N_{\mathrm{T}} = 4$, $M = 10$, $\alpha_{\mathrm{d}} = 3.8$, $\alpha_{\mathrm{r}} = 2.3$, and $R = 100$ m.

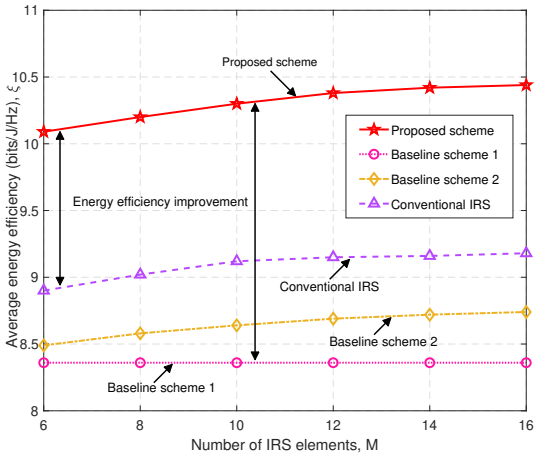

Fig. 3. Average energy efficiency versus the number of IRS elements with $K = 3$, $N_{\mathrm{T}} = 4$, $P_{\mathrm{A}} = 20$ mW, $\Gamma_{\mathrm{req}} = 10$ dB, $\alpha_{\mathrm{d}} = 2.9$, $\alpha_{\mathrm{r}} = 2.3$, and $R = 200$ m.

monotonically increases with Γ_{req}. This is attributed to the fact that to satisfy a more stringent minimum SINR requirement, the BS has to transmit with a higher power. Yet, the proposed scheme yields substantial power savings compared to the two baseline schemes even if we account for the total transmit power. For example, for $\Gamma_{\mathrm{req}} = 4$, the proposed scheme with $P_{\mathrm{A}} = 10$ mW consumes $10^{(1.5)} + 10 \approx 41.6$ mW, while baseline scheme 1 and baseline scheme 2 require 100 mW and 73.1 mW, respectively. In particular, for baseline scheme 1, since there is no IRS, there are no degrees of freedom (DoFs) available for customizing favorable wireless channels. As for baseline scheme 2, both the BS and the active IRS cannot fully exploit the DoFs available for resource allocation due to the partially fixed beamforming policy and the randomly generated IRS phase shifts, respectively. This highlights the effectiveness of the proposed scheme for jointly optimizing the beamformers at the BS and the active IRS elements. Moreover, as expected, increasing the maximum power allowance at the active IRS from 10 mW to 15 mW leads to further transmit power savings at the BS. This is because the additional power budget at the active IRS can be utilized to facilitate more accurate beamforming and to mitigate multiuser interference in a more effective manner.

B. Energy Efficiency Evaluation

To further investigate the performance of active IRSs, we also compare with a conventional IRS where the IRS elements just passively reflect the incident signals without amplification. In particular, we employ the IA-based algorithm developed in [6] and solve a problem similar to (5) but replacing constraint C2 with a unit-modulus constraint induced by the passive IRS. For a fair comparison, we adopt the energy efficiency (bits/J/Hz) as the performance metric which is defined as[1] [6, Eq. (19)]

$$\xi = \frac{\sum\limits_{k \in \mathcal{K}} \log_2(1 + \Gamma_k)}{\frac{1}{\eta} \sum\limits_{k \in \mathcal{K}} \|\mathbf{w}_k\|^2 + N_{\mathrm{T}} P_{\mathrm{T}} + P_{\mathrm{C}} + M P_{\mathrm{I}} + \frac{1}{\eta} P_{\mathrm{A}}}, \tag{20}$$

where $\eta = 0.5$ is the power amplifier efficiency, $P_{\mathrm{T}} = 100$ mW is the circuit power that maintains one BS antenna element operational, $P_{\mathrm{C}} = 85$ mW is the static circuit power of the BS [6], $P_{\mathrm{I}} = 2$ mW is the circuit power required to support one IRS element[2] [23], and $P_{\mathrm{A}} = 20$ mW is the power allowance of the active IRS [9]. Figure 3 illustrates the average energy efficiency versus the number of IRS elements for a scenario where the direct links are slightly shadowed ($\alpha_{\mathrm{d}} = 2.9$). As can be seen from Figure 3, the energy efficiencies of the proposed scheme, the scheme employing a conventional IRS, and baseline scheme 2 monotonically increase with the number of IRS elements. In particular, due to the low-power consumption of IRS phase shifters, deploying more IRS elements does not significantly increase the operational power of the IRS. Moreover, additional IRS elements introduce extra DoFs that can be exploited to proactively configure the wireless channel which yields transmit power savings. Besides, for the proposed scheme, additional IRS elements allow the active IRS to strike a balance between effectively mitigating the dynamic noise amplification and amplifying the desired signals. On the other hand, we observe that the proposed scheme outperforms the scheme employing a conventional passive IRS and the two baseline schemes. In particular, for the scenario where the direct links are slightly shadowed, deploying passive IRSs can not effectively enhance performance due to the double path loss effect. In contrast, the proposed scheme employing the active

[1]We set $P_{\mathrm{A}} = 0$ when computing the energy efficiency of the system with the conventional passive IRS.

[2]In this paper, we adopt the same P_{I} for passive and active IRS elements. Yet, in practice, depending on the specific hardware structure and components, active IRS elements may consume slightly more power for supporting the required amplifier [10].

IRS can simultaneously adjust the phase and the amplitude of the reflected signal to combat the double path loss effect, which yields a performance enhancement at the expense of supplying extra power to the IRS. This observation strongly motivates the application of active IRSs to further improve the system performance, especially when the direct links are not weak.

VI. Conclusion

In this paper, we investigated the deployment of active IRSs, where, unlike conventional passive IRSs, each IRS element is equipped with an amplifier, and studied the resulting resource allocation algorithm design problem for a multiuser communication system. In particular, we jointly optimized the beamforming vectors at the BS and the IRS parameters for minimization of the BS transmit power. To tackle the formulated non-convex optimization problem, we developed a novel low-complexity algorithm, based on the bilinear transformation and IA. The developed algorithm is guaranteed to converge to a locally optimal solution of the considered problem. Simulation results showed that the proposed scheme achieves considerable power savings compared to two baseline schemes. Moreover, our results revealed that active IRSs are a promising means to combat the performance degradation caused by the double path loss effect in IRS-assisted communication systems.

References

[1] V. W. S. Wong, R. Schober, D. W. K. Ng, and L. C. Wang, *Key Technologies for 5G Wireless Systems*. Cambridge University Press, 2017.

[2] T. Cui, M. Qi, X. Wan, J. Zhao, and Q. Cheng, "Coding metamaterials, digital metamaterials and programmable metamaterials," *Light: Science & Applications*, vol. 3, no. 10, p. e218, 2014.

[3] X. Yu, V. Jamali, D. Xu, D. W. K. Ng, and R. Schober, "Smart and reconfigurable wireless communications: From IRS modeling to algorithm design," *arXiv:2103.07046, accepted for publication in IEEE Wirel. Commun.*, 2021.

[4] Q. Wu and R. Zhang, "Intelligent reflecting surface enhanced wireless network via joint active and passive beamforming," *IEEE Trans. Wireless Commun.*, vol. 18, no. 11, pp. 5394–5409, Aug. 2019.

[5] C. Huang, A. Zappone, G. C. Alexandropoulos, M. Debbah, and C. Yuen, "Reconfigurable intelligent surfaces for energy efficiency in wireless communication," *IEEE Trans. Wireless Commun.*, vol. 18, no. 8, pp. 4157–4170, Aug. 2019.

[6] X. Yu, D. Xu, D. W. K. Ng, and R. Schober, "Power-efficient resource allocation for multiuser MISO systems via intelligent reflecting surfaces," in *Proc. IEEE Global Commun. Conf. (GLOBECOM)*, Taipei, Taiwan, Dec. 2020, pp. 1–6.

[7] M. Najafi, V. Jamali, R. Schober, and H. V. Poor, "Physics-based modeling and scalable optimization of large intelligent reflecting surfaces," *IEEE Trans. Commun.*, vol. 69, no. 4, pp. 2673–2691, Apr. 2021.

[8] D. Xu, V. Jamali, X. Yu, D. W. K. Ng, and R. Schober, "Optimal resource allocation design for large IRS-assisted SWIPT systems: A scalable optimization framework," *arXiv:2104.03346, under revision*, 2021.

[9] Z. Zhang, L. Dai, X. Chen, C. Liu, F. Yang, R. Schober, and H. V. Poor, "Active RIS vs. passive RIS: Which will prevail in 6G?" *arXiv:2103.15154*, 2021.

[10] J. Lončar, A. Grbic, and S. Hrabar, "Ultrathin active polarization-selective metasurface at x-band frequencies," *Physical Review B*, vol. 100, no. 7, p. 075131, 2019.

[11] C. You and R. Zhang, "Wireless communication aided by intelligent reflecting surface: Active or passive?" *arXiv:2106.10963*, 2021.

[12] J. C. Bezdek and R. J. Hathaway, "Some notes on alternating optimization," in *AFSS Int. Conf. on Fuzzy Systems*. Springer, 2002, pp. 288–300.

[13] L. Wei, C. Huang, G. C. Alexandropoulos, C. Yuen, Z. Zhang, and M. Debbah, "Channel estimation for RIS-empowered multi-user MISO wireless communications," *IEEE Trans. Commun.*, vol. 69, no. 6, pp. 4144–4157, Jun. 2021.

[14] Q. U. A. Nadeem, H. Alwazani, A. Kammoun, A. Chaaban, M. Debbah, and M. S. Alouini, "Intelligent reflecting surface-assisted multi-user MISO communication: Channel estimation and beamforming design," *IEEE Open J. Commun. Soc.*, vol. 1, pp. 661–680, Jun. 2020.

[15] J. Bousquet, S. Magierowski, and G. G. Messier, "A 4-ghz active scatterer in 130-nm CMOS for phase sweep amplify-and-forward," *IEEE Trans. Circuits Syst. I: Regular Papers*, vol. 59, no. 3, pp. 529–540, Mar. 2012.

[16] Q. Wu and R. Zhang, "Beamforming optimization for wireless network aided by intelligent reflecting surface with discrete phase shifts," *IEEE Trans. Commun.*, vol. 68, no. 3, pp. 1838–1851, Mar. 2020.

[17] Z. Q. Luo, W. K. Ma, A. M. C. So, Y. Ye, and S. Zhang, "Semidefinite relaxation of quadratic optimization problems," *IEEE Signal Process. Mag.*, vol. 27, no. 3, pp. 20–34, May 2010.

[18] D. Xu, X. Yu, Y. Sun, D. W. K. Ng, and R. Schober, "Resource allocation for IRS-assisted full-duplex cognitive radio systems," *IEEE Trans. Commun.*, vol. 68, no. 12, pp. 7376–7394, Dec. 2020.

[19] B. R. Marks and G. P. Wright, "A general inner approximation algorithm for nonconvex mathematical programs," *Operations research*, vol. 26, no. 4, pp. 681–683, 1978.

[20] U. Rashid, H. D. Tuan, H. H. Kha, and H. H. Nguyen, "Joint optimization of source precoding and relay beamforming in wireless MIMO relay networks," *IEEE Trans. Commun.*, vol. 62, no. 2, pp. 488–499, Feb. 2014.

[21] M. Grant and S. Boyd, "CVX: Matlab software for disciplined convex programming, version 2.1," *http://cvxr.com/cvx*, Jan. 2020.

[22] I. Pólik and T. Terlaky, "Interior point methods for nonlinear optimization," *Nonlinear Optimization*, pp. 215–276, 2010.

[23] X. Pei, H. Yin, L. Tan, L. Cao, Z. Li, K. Wang, K. Zhang, and E. Björnson, "RIS-aided wireless communications: Prototyping, adaptive beamforming, and indoor/outdoor field trials," *arXiv:2103.00534*, 2021.

Literaturverzeichnis

[1] G. L. Stuber, J. R. Barry, S. W. McLaughlin, L. Ye, M. A. Ingram, and T. Pratt, "Broadband MIMO-OFDM wireless communications," *Proc. IEEE*, vol. 92, no. 2, pp. 271–294, Feb. 2004.

[2] Cisco, "Cisco annual internet report (2018–2023) white paper," Jul. 2022.

[3] M. Shafi *et al.*, "5G: A tutorial overview of standards, trials, challenges, deployment, and practice," *IEEE J. Sel. Areas Commun.*, vol. 35, no. 6, pp. 1201–1221, Jun. 2017.

[4] X. You *et al.*, "Towards 6G wireless communication networks: Vision, enabling technologies, and new paradigm shifts," *Science China Information Sciences*, vol. 64, no. 1, pp. 1–74, Jan. 2021.

[5] M. Shafi *et al.*, "5G: A tutorial overview of standards, trials, challenges, deployment, and practice," *IEEE J. Sel. Areas Commun.*, vol. 35, no. 6, pp. 1201–1221, Jun. 2017.

[6] M. Xiao *et al.*, "Millimeter wave communications for future mobile networks," *IEEE J. Sel. Areas Commun.*, vol. 35, no. 9, pp. 1909–1935, Sept. 2017.

[7] X. Yu, J. Shen, J. Zhang, and K. B. Letaief, "Alternating minimization algorithms for hybrid precoding in millimeter wave MIMO systems," *IEEE J. Sel. Top. Signal Process.*, vol. 10, no. 3, pp. 485–500, Apr. 2016.

[8] H.-J. Song and T. Nagatsuma, "Present and future of terahertz communications," *IEEE Trans. Terahertz Sci. Technol.*, vol. 1, no. 1, pp. 256–263, Sept. 2011.

[9] B. Wang and R. K. J. Liu, "Advances in cognitive radio networks: A survey," *IEEE J. Sel. Top. Signal Process.*, vol. 5, no. 1, pp. 5–23, Feb. 2011.

[10] F. Liu, Y. Cui, C. Masouros, J. Xu, T. X. Han, Y. C. Eldar, and S. Buzzi, "Integrated sensing and communications: Towards dual-functional wireless networks for 6G and beyond," *IEEE J. Sel. Areas Commun.*, vol. 40, no. 6, pp. 1728–1767, Jun. 2022.

[11] Z. Wei, F. Liu, C. Masouros, N. Su, and A. P. Petropulu, "Toward multi-functional 6G wireless networks: Integrating sensing, communication, and security," *IEEE Commun. Mag.*, vol. 60, no. 4, pp. 65–71, Apr. 2022.

[12] D. Xu, X. Yu, D. W. K. Ng, A. Schmeink, and R. Schober, "Robust and secure resource allocation for ISAC systems: A novel optimization framework for variable-length snapshots," *IEEE Trans. Commun.*, vol. 70, no. 12, pp. 8196–8214, Dec. 2022.

[13] A. Sabharwal, P. Schniter, D. Guo, D. W. Bliss, S. Rangarajan, and R. Wichman, "In-band full-duplex wireless: challenges and opportunities," *IEEE J. Sel. Areas Commun.*, vol. 32, no. 9, pp. 1637–1652, Sept. 2014.

[14] Z. Ding, D. Xu, and R. S. H. V. Poor, "Hybrid NOMA offloading in multi-user MEC networks," *IEEE Trans. Wireless Commun.*, vol. 21, no. 7, pp. 5377–5391, Jul. 2022.

[15] B. Clerckx, Y. Mao, R. Schober, and H. V. Poor, "Rate-splitting unifying SDMA, OMA, NOMA, and multicasting in MISO broadcast channel: A simple two-user rate analysis," *IEEE Wireless Commun. Lett.*, vol. 9, no. 3, pp. 349–353, Mar. 2020.

[16] K. P. Valavanis and G. J. Vachtsevanos, *Handbook of Unmanned Aerial Vehicles*. Springer, 2015, vol. 2077.

[17] A. Birk, B. Wiggerich, H. Bülow, M. Pfingsthorn, and S. Schwertfeger, "Safety, security, and rescue missions with an unmanned aerial vehicle (UAV)," *J. Intell. Robot. Syst.*, vol. 64, no. 1, pp. 57–76, 2011.

[18] X. Lin, V. Yajnanarayana, S. D. Muruganathan, S. Gao, H. Asplund, H. Maattanen, M. Bergstrom, S. Euler, and Y. . E. Wang, "The sky is not the limit: LTE for unmanned aerial vehicles," *IEEE Commun. Mag.*, vol. 56, no. 4, pp. 204–210, Apr. 2018.

[19] Y. Liu, Z. Qin, Y. Cai, Y. Gao, G. Y. Li, and A. Nallanathan, "UAV communications based on non-orthogonal multiple access," *IEEE Wireless Commun.*, vol. 26, no. 1, pp. 52–57, Feb. 2019.

[20] T. Shima and S. Rasmussen, *UAV cooperative decision and control: challenges and practical approaches*. SIAM, 2009.

[21] B. Ahmed, H. Pota, and M. Garratt, "Flight control of a rotary wing UAV using backstepping," *Intern. J. of Robust and Nonlinear Control*, vol. 20, no. 6, pp. 639–658, 2010.

[22] D. Xu, Y. Sun, D. W. K. Ng, and R. Schober, "Robust resource allocation for UAV systems with UAV jittering and user location uncertainty," in *Proc. IEEE Global Commun. Conf. (GC Wkshps)*, Abu Dhabi, United Arab Emirates, Dec. 2018, pp. 1–6.

[23] L. Gupta, R. Jain, and G. Vaszkun, "Survey of important issues in UAV communication networks," *IEEE Commun. Surv. Tuts.*, vol. 18, no. 2, pp. 1123–1152, 2015.

[24] Y. Zeng and R. Zhang, "Energy-efficient UAV communication with trajectory optimization," *IEEE Trans. Wireless Commun.*, vol. 16, no. 6, pp. 3747–3760, Jun. 2017.

[25] J. M. Seddon and S. Newman, *Basic Helicopter Aerodynamics*. John Wiley & Sons, 2011, vol. 40.

[26] S. Hayat, E. Yanmaz, and R. Muzaffar, "Survey on unmanned aerial vehicle networks for civil applications: A communications viewpoint," *IEEE Commun. Surv. Tuts.*, vol. 18, no. 4, pp. 2624–2661, 2016.

[27] T. Cui, M. Qi, X. Wan, J. Zhao, and Q. Cheng, "Coding metamaterials, digital metamaterials and programmable metamaterials," *Light: Science & Applications*, vol. 3, no. 10, p. e218, 2014.

[28] X. Wan, Q. Xiao, Y. Zhang, Y. Li, J. Eisenbeis, J. Wang, Z. Huang, H. Liu, T. Zwick, and T. Cui, "Reconfigurable sum and difference beams based on a binary programmable metasurface," *IEEE Antennas Wirel. Propag. Lett.*, vol. 20, no. 3, pp. 381–385, Mar. 2021.

[29] X. Pei, H. Yin, L. Tan, L. Cao, Z. Li, K. Wang, K. Zhang, and E. Björnson, "RIS-aided wireless communications: Prototyping, adaptive beamforming, and indoor/outdoor field trials," *IEEE Trans. Commun.*, vol. 69, no. 12, pp. 8627–8640, 2021.

[30] C. You, B. Zheng, and R. Zhang, "Intelligent reflecting surface with discrete phase shifts: Channel estimation and passive beamforming," in *Proc. Intern. Conf. Commun. (ICC)*, Dublin, Ireland, 2020, pp. 1–6.

[31] X. Yu, V. Jamali, D. Xu, D. W. K. Ng, and R. Schober, "Smart and reconfigurable wireless communications: From IRS modeling to algorithm design," *IEEE Wireless Commun.*, vol. 28, no. 6, pp. 118–125, 2021.

[32] L. Dai, B. Wang, M. Wang, X. Yang, J. Tan, S. Bi, S. Xu, F. Yang, Z. Chen, M. D. Renzo, C. B. Chae, and L. Hanzo, "Reconfigurable intelligent surface-based wireless communications: Antenna design, prototyping, and experimental results," *IEEE Access*, vol. 8, pp. 45 913–45 923, Mar. 2020.

[33] E. Björnson, O. Özdogan, and E. G. Larsson, "Reconfigurable intelligent surfaces: Three myths and two critical questions," *IEEE Commun. Mag.*, vol. 58, no. 12, pp. 90–96, Dec. 2020.

[34] Q. Wu, S. Zhang, B. Zheng, C. You, and R. Zhang, "Intelligent reflecting surface aided wireless communications: A tutorial," *IEEE Trans. Commun.*, vol. 69, no. 5, pp. 3313–3351, May 2021.

[35] Y. Liu, X. Liu, X. Mu, T. Hou, J. Xu,, M. Di Renzo, and N. Al-Dhahir, "Reconfigurable intelligent surfaces: Principles and opportunities," *IEEE Commun. Surv. Tutor.*, vol. 23, no. 3, pp. 1546–1577, 2021.

[36] D. Xu, X. Yu, V. Jamali, D. W. K. Ng, and R. Schober, "Resource allocation for large IRS-assisted SWIPT systems with non-linear energy harvesting model," in *Proc. IEEE Wireless Commun. Netw. Conf. (WCNC)*, Nanjing, China, Mar. 2021, pp. 1–7.

[37] M. Najafi, V. Jamali, R. Schober, and H. V. Poor, "Physics-based modeling and scalable optimization of large intelligent reflecting surfaces," *IEEE Trans. Commun.*, vol. 69, no. 4, pp. 2673–2691, Apr. 2021.

[38] M. M. Azari, F. Rosas, K.-C. Chen, and S. Pollin, "Joint sum-rate and power gain analysis of an aerial base station," in *Proc. IEEE Globecom Workshops (GC Wkshps)*, Washington, DC, USA, Dec. 2016, pp. 1–6.

[39] Y. Zeng, J. Xu, and R. Zhang, "Energy minimization for wireless communication with rotary-wing UAV," *IEEE Trans. Wireless Commun.*, vol. 18, no. 4, pp. 2329–2345, Apr. 2019.

[40] Y. Sun, D. Xu, D. W. K. Ng, L. Dai, and R. Schober, "Optimal 3D-trajectory design and resource allocation for solar-powered UAV communication systems," *IEEE Trans. Commun.*, vol. 67, no. 6, pp. 4281–4298, Jun. 2019.

[41] M. Hua, Y. Wang, C. Li,, Y. Huang, and L. Yang, "Energy-efficient optimization for UAV-aided cellular offloading," *IEEE Wireless Commun. Lett.*, vol. 8, no. 3, pp. 769–772, Jun. 2019.

[42] S. A. Bortoff, "Path planning for uavs," in *Proc. IEEE American Control Conf. (ACC)*, vol. 1, no. 6, 2000, pp. 364–368.

[43] Q. Wu, Y. Zeng, and R. Zhang, "Joint trajectory and communication design for multi-UAV enabled wireless networks," *IEEE Trans. Wireless Commun.*, vol. 17, no. 3, pp. 2109–2121, Mar. 2018.

[44] X. Yuan, T. Yang, Y. Hu, J. Xu, and A. Schmeink, "Trajectory design for UAV-enabled multiuser wireless power transfer with nonlinear energy harvesting," *IEEE Trans. Wireless Commun.*, vol. 20, no. 2, pp. 1105–1121, Feb. 2021.

[45] D. Xu, Y. Sun, D. W. K. Ng, and R. Schober, "Multiuser MISO UAV communications in uncertain environments with no-fly zones: Robust trajectory and resource allocation design," *IEEE Trans. Commun.*, vol. 68, no. 5, pp. 3153–3172, May 2020.

[46] J. Xu, Y. Zeng, and R. Zhang, "UAV-enabled wireless power transfer: Trajectory design and energy optimization," *IEEE Trans. Wireless Commun.*, vol. 17, no. 8, pp. 5092–5106, Aug. 2018.

[47] H. He, S. Zhang, Y. Zeng, and R. Zhang, "Joint altitude and beamwidth optimization for UAV-enabled multiuser communications," *IEEE Commun. Lett.*, vol. 22, no. 2, pp. 344–347, Feb. 2018.

[48] Y. Gao, H. Tang, and B. L. X. Yuan, "Joint trajectory and power design for UAV-enabled secure communications with no-fly zone constraints," *IEEE Access*, vol. 7, pp. 44 459–44 470, 2019.

[49] R. Li, Z. Wei, L. Yang, D. W. K. Ng, N. Yang, J. Yuan, and J. An, "Joint trajectory and resource allocation design for UAV communication systems," in *Proc. IEEE Globecom Workshops (GC Wkshps)*. IEEE, 2018, pp. 1–6.

[50] Y. Hsu and R.-H. Gau, "Reinforcement learning-based collision avoidance and optimal trajectory planning in UAV communication networks," *IEEE Transactions Mob. Comput.*, vol. 21, no. 1, pp. 306–320, Jan. 2022.

[51] Worldwide Aviation Database, "OpenAIP," *http://maps.openaip.net/*, 2020.

[52] I. Griva, S. G. Nash, and A. Sofer, *Linear and Nonlinear Optimization*. SIAM, 2009, vol. 108.

[53] Q. Wu and R. Zhang, "Intelligent reflecting surface enhanced wireless network via joint active and passive beamforming," *IEEE Trans. Wireless Commun.*, vol. 18, no. 11, pp. 5394–5409, Aug. 2019.

[54] T. Jiang and Y. Shi, "Over-the-air computation via intelligent reflecting surfaces," in *Proc. IEEE Global Commun. Conf. (GLOBECOM)*, Waikoloa, HI, USA, Dec. 2019, pp. 1–6.

[55] Y. Tang, G. Ma, H. Xie, J. Xu, and X. Han, "Joint transmit and reflective beamforming design for IRS-assisted multiuser MISO SWIPT systems," in *Proc. Intern. Conf. Commun. (ICC)*, Dublin, Ireland, Jun., 2020, pp. 1–6.

[56] X. Yu, D. Xu, and R. Schober, "MISO wireless communication systems via intelligent reflecting surfaces," in *Proc. IEEE Int. Conf. Commun. China (ICCC)*, Changchun, China, May 2019, pp. 1–6.

[57] D. Xu, Y. Sun, D. W. K. Ng, and R. Schober, "Resource allocation for IRS-assisted full-duplex cognitive radio systems," *IEEE Trans. Commun.*, vol. 68, no. 12, pp. 7376–7394, Dec. 2020.

[58] X. Yu, D. Xu, D. W. K. Ng, and R. Schober, "Power-efficient resource allocation for multiuser MISO systems via intelligent reflecting surfaces," in *Proc. IEEE Global Commun. Conf. (GLOBECOM)*, Taipei, Taiwan, Dec. 2020, pp. 1–6.

[59] X. Yu, D. Xu, and R. Schober, "Optimal beamforming for miso communications via intelligent reflecting surfaces," in *Proc. IEEE 21st Intern. Workshop on Signal Processing Advances in Wireless Commun. (SPAWC)*, Atlanta, GA, USA, May 2020, pp. 1–5.

[60] X. Yu, D. Xu, Y. Sun, D. W. K. Ng, and R. Schober, "Robust and secure wireless communications via intelligent reflecting surfaces," *IEEE J. Sel. Areas Commun.*, vol. 38, no. 11, Nov. 2020.

[61] S. Shen, B. Clerckx, and R. Murch, "Modeling and architecture design of reconfigurable intelligent surfaces using scattering parameter network analysis," *IEEE Trans. Wireless Commun.*, vol. 21, no. 2, pp. 1229–1243, Feb. 2022.

[62] V. Jamali, M. Najafi, R. Schober, and H. V. Poor, "Power efficiency, overhead, and complexity tradeoff in IRS-assisted communications–quadratic phase-shift design," *IEEE Commun. Lett.*, vol. 25, no. 6, pp. 2048–2052, Jun. 2021.

[63] D. Xu, V. Jamali, X. Yu, D. W. K. Ng, and R. Schober, "Optimal resource allocation design for large IRS-assisted SWIPT systems: A scalable optimization framework," *IEEE Trans. Commun.*, vol. 70, no. 2, pp. 1423–1441, Feb. 2022.

[64] W. R. Ghanem, V. Jamali, M. Schellmann, H. Cao, J. Eiching, and R. Schober, "Optimization-based phase-shift codebook design for large IRSs," *arXiv:2203.01630*, 2022.

[65] Z. Zhang, L. Dai, X. Chen, C. Liu, F. Yang, R. Schober, and H. V. Poor, "Active RIS vs. passive RIS: Which will prevail in 6G?" *arXiv:2103.15154*, 2021.

[66] P. Zeng, D. Qiao, Q. Wu, and Y. Wu, "Throughput maximization for active intelligent reflecting surface-aided wireless powered communications," *IEEE Wireless Commun. Lett.*, vol. 11, no. 5, pp. 992–996, May 2022.

[67] S. Zhang and R. Zhang, "Intelligent reflecting surface aided multiple access: Capacity region and deployment strategy," in *IEEE 21st Intern. Workshop on Signal Processing Advances in Wireless Commun. (SPAWC)*, Atlanta, GA, USA, May 2020, pp. 1–5.

[68] X. Mu, Y. Liu, L. Guo, J. Lin, and R. Schober, "Joint deployment and multiple access design for intelligent reflecting surface assisted networks," *IEEE Trans. Wireless Commun.*, vol. 20, no. 10, pp. 6648–6664, Oct. 2021.

[69] X. Yu, D. Xu, and R. Schober, "Enabling secure wireless communications via intelligent reflecting surfaces," in *Proc. IEEE Global Commun. Conf. (GLOBECOM)*, Waikoloa, HI, USA, Dec. 2019, pp. 1–6.

[70] X. Yu, D. Xu, D. W. K. Ng, and R. Schober, "IRS-assisted green communication systems: Provable convergence and robust optimization," *IEEE Trans. Commun.*, vol. 69, no. 9, pp. 6313–6329, Sept. 2021.

[71] S. Hu, Z. Wei, Y. Cai, C. Liu, D. W. K. Ng, and J. Yuan, "Robust and secure sum-rate maximization for multiuser MISO downlink systems with self-sustainable IRS," *IEEE Trans. Commun.*, vol. 69, no. 10, pp. 7032–7049, Oct. 2021.

[72] G. Zhou, C. Pan, H. Ren, K. Wang, and A. Nallanathan, "A framework of robust transmission design for IRS-aided MISO communications with imperfect cascaded channels," *IEEE Trans. Signal Process.*, vol. 68, pp. 5092–5106, Aug. 2020.

[73] D. W. K. Ng, E. S. Lo, and R. Schober, "Robust beamforming for secure communication in systems with wireless information and power transfer," *IEEE Trans. Wireless Commun.*, vol. 13, no. 8, pp. 4599–4615, Apr. 2014.

[74] Q. Wu and R. Zhang, "Beamforming optimization for wireless network aided by intelligent reflecting surface with discrete phase shifts," *IEEE Trans. Commun.*, vol. 68, no. 3, pp. 1838–1851, Mar. 2020.

[75] Z. Ding, R. Schober, and H. V. Poor, "On the impact of phase shifting designs on IRS-NOMA," *IEEE Wireless Commun. Lett.*, vol. 9, no. 10, pp. 1596–1600, Oct. 2020.

[76] S. Gong, Z. Yang, C. Xing, J. An, and L. Hanzo, "Beamforming optimization for intelligent reflecting surface-aided SWIPT IoT networks relying on discrete phase shifts," *IEEE Internet Things J.*, vol. 8, no. 10, pp. 8585–8602, May 2021.

[77] D. Xu, X. Yu, Y. Sun, D. W. K. Ng, and R. Schober, "Resource allocation for secure IRS-assisted multiuser MISO systems," in *Proc. IEEE Global Commun. Conf. (GLOBECOM) Wkshps*, Waikoloa, HI, USA, Dec., 2019, pp. 1–6.

[78] D. Xu, X. Yu, D. W. K. Ng, and R. Schober, "Resource allocation for active IRS-assisted multiuser communication systems," in *Proc. Fifty-Fifth Asilomar Conf. Signals, Systems and Computers (ASILOMAR)*, Pacific Grove, CA, USA, Oct. 2021, pp. 113–119.

[79] Q. Ma and T. Cui, "Information metamaterials: bridging the physical world and digital world," *PhotoniX*, vol. 1, no. 1, pp. 1–32, 2020.

[80] Q. Wu and R. Zhang, "Joint active and passive beamforming optimization for intelligent reflecting surface assisted SWIPT under QoS constraints," *IEEE J. Sel. Areas Commun.*, vol. 38, no. 8, pp. 1735–1748, Aug. 2020.

[81] C. Pan, H. Ren, K. Wang, M. Elkashlan, A. Nallanathan, J. Wang, and L. Hanzo, "Intelligent reflecting surface aided MIMO broadcasting for simultaneous wireless information and power transfer," *IEEE J. Sel. Areas Commun.*, vol. 38, no. 8, pp. 1719–1734, Aug. 2020.

[82] H. Shen, W. Xu, S. Gong, Z. He, and C. Zhao, "Secrecy rate maximization for intelligent reflecting surface assisted multi-antenna communications," *IEEE Commun. Lett.*, vol. 23, no. 9, pp. 1488–1492, Sept. 2019.

[83] S. Boyd and L. Vandenberghe, *Convex Optimization*. Cambridge university press, 2004.

[84] D. P. Bertsekas, "Nonlinear programming," *Journal of the Operational Research Society*, vol. 48, no. 3, pp. 334–334, 1997.

[85] M. Grant, S. Boyd, and Y. Ye, "CVX: Matlab software for disciplined convex programming," 2009.

[86] J. Lofberg, "YALMIP : a toolbox for modeling and optimization in MATLAB," in *Proc. IEEE Int. Conf. Robot. Autom*, Taipei, Taiwan, 2004, pp. 284–289.

[87] R. T. Rockafellar, *Convex analysis*. Princeton university press, 1970, vol. 18.

[88] X. Su, S. Chan, and J. H. Manton, "Bandwidth allocation in wireless ad hoc networks: Challenges and prospects," *IEEE Commun. Mag.*, vol. 48, no. 1, pp. 80–85, Jan. 2010.

[89] F. Zhao, L. Wei, and H. Chen, "Optimal time allocation for wireless information and power transfer in wireless powered communication systems," *IEEE Trans. Veh. Tech.*, vol. 65, no. 3, pp. 1830–1835, Mar. 2016.

[90] J. Nocedal and S. J. Wright, "Quadratic programming," *Numerical optimization*, pp. 448–492, 2006.

[91] C. K. Ho and R. Zhang, "Optimal energy allocation for wireless communications with energy harvesting constraints," *IEEE Trans. Signal Process.*, vol. 60, no. 9, pp. 4808–4818, Sept. 2012.

[92] Y. Sun, D. W. K. Ng, Z. Ding, and R. Schober, "Optimal joint power and subcarrier allocation for full-duplex multicarrier non-orthogonal multiple access systems," *IEEE Trans. Commun.*, vol. 65, no. 3, pp. 1077–1091, Mar. 2017.

[93] Y. Sun, D. W. K. Ng, D. Xu, L. Dai, and R. Schober, "Resource allocation for solar powered UAV communication systems," in *IEEE 19st Intern. Workshop on Signal Processing Advances in Wireless Commun. (SPAWC)*, Kalamata, Greece, Jun. 2018, pp. 1–5.

[94] Y. Cai, Z. Wei, R. Li, D. W. K. Ng, and J. Yuan, "Energy-efficient resource allocation for secure UAV communication systems," in *Proc. IEEE Wireless Commun. Netw. Conf. (WCNC)*, Marrakesh, Morocco, Apr. 2019, pp. 1–8.

[95] Y. Nesterov, "Semidefinite relaxation and nonconvex quadratic optimization," *Optimization methods and software*, vol. 9, no. 1-3, pp. 141–160, 1998.

[96] Y. Sun, D. W. K. Ng, J. Zhu, and R. Schober, "Multi-objective optimization for robust power efficient and secure full-duplex wireless communication systems," *IEEE Trans. Wireless Commun.*, vol. 15, no. 8, pp. 5511–5526, Apr. 2016.

[97] R. Zhang, Y. C. Liang, C. C. Chai, and S. Cui, "Optimal beamforming for two-way multi-antenna relay channel with analogue network coding," *IEEE J. Sel. Areas Commun.*, vol. 27, no. 5, pp. 699–712, Jun. 2009.

[98] S. Hu, Z. Wei, Y. Cai, D. W. K. Ng, and J. Yuan, "Sum-rate maximization for multiuser MISO downlink systems with self-sustainable IRS," in *Proc. IEEE Global Commun. Conf. (GLOBECOM)*, Taipei, Taiwan, Dec. 2020, pp. 1–7.

[99] D. Xu, X. Yu, and R. Schober, "Resource allocation for intelligent reflecting surface-assisted cognitive radio networks," in *Proc. IEEE Intern. Workshop on Signal Processing Advances in Wireless Commun. (SPAWC)*, Atlanta, GA, USA, May 2020, pp. 1–5.

[100] Q. T. Dinh and M. Diehl, "Local convergence of sequential convex programming for nonconvex optimization," in *Recent Advances in Optimization and its Applications in Engineering*. Springer, 2010, pp. 93–102.

[101] Q. Wu and R. Zhang, "Towards smart and reconfigurable environment: Intelligent reflecting surface aided wireless network," *IEEE Commun. Mag.*, vol. 58, no. 1, pp. 106–112, Jan. 2020.

[102] J. C. Bezdek and R. J. Hathaway, "Some notes on alternating optimization," in *AFSS Int. Conf. on Fuzzy Systems*. Springer, 2002, pp. 288–300.

[103] H. Tuy, "Monotonic optimization: Problems and solution approaches," *SIAM Journal on Optimization*, vol. 11, no. 2, pp. 464–494, 2000.

[104] Y. Zhang, L. Qian, and J. Huang, "Monotonic optimization in communication and networking systems," *Foundations and Trends® in Networking*, vol. 7, no. 1, pp. 1–75, 2013.

[105] E. Björnson and E. Jorswieck, "Optimal resource allocation in coordinated multi-cell systems," *Foundations and Trends® in Communications and Information Theory*, vol. 9, no. 2–3, pp. 113–381, 2013.

[106] G. Laporte, "The traveling salesman problem: An overview of exact and approximate algorithms," *Eur. J. Oper. Res.*, vol. 59, no. 2, pp. 231–247, 1992.

[107] E. L. Lawler and D. E. Wood, "Branch-and-bound methods: A survey," *Operations research*, vol. 14, no. 4, pp. 699–719, 1966.

[108] R. Horst and H. Tuy, *Global Optimization: Deterministic Approaches*. Springer Science & Business Media, 2013.

[109] G. Raja, S. Anbalagan, A. Ganapathisubramaniyan, M. S. Selvakumar, A. K. Bashir, and S. Mumtaz, "Efficient and secured swarm pattern multi-UAV communication," *IEEE Trans. Veh. Tech.*, vol. 70, no. 7, pp. 7050–7058, Jul. 2021.

[110] X. Zhu, F. Qi, and Y. Feng, "Deep-learning-based multiple beamforming for 5G uav IoT networks," *IEEE Netw.*, vol. 34, no. 5, pp. 32–38, Sept. 2020.

[111] M. Di Renzo *et al.*, "Smart radio environments empowered by reconfigurable intelligent surfaces: How it works, state of research, and the road ahead," *IEEE J. Sel. Areas Commun.*, vol. 38, no. 11, pp. 2450–2525, Nov. 2020.